TESIS DE LA UNIVERSIDAD DE ZARAGOZA

2021 289

Isabel Ortiz de Solórzano García

On the synthesis of polymeric, inorganic and hybrid nanoparticles for controlled drug delivery applications. From a molecular level to a whole-body distribution

Director/es
Arruebo Gordo, Manuel
Sebastián Cabeza, Victor

ISSN 2254-7606

Prensas de la Universidad
Universidad Zaragoza

ISSN 2254-7606

Universidad Zaragoza
1542

Tesis Doctoral

ON THE SYNTHESIS OF POLYMERIC, INORGANIC AND HYBRID NANOPARTICLES FOR CONTROLLED DRUG DELIVERY APPLICATIONS. FROM A MOLECULAR LEVEL TO A WHOLE-BODY DISTRIBUTION

Autor

Isabel Ortiz de Solórzano García

Director/es

Arruebo Gordo, Manuel
Sebastián Cabeza, Victor

UNIVERSIDAD DE ZARAGOZA
Escuela de Doctorado

2019

"On the synthesis of polymeric, inorganic and hybrid nanoparticles for controlled drug delivery applications. From a molecular level to a whole-body distribution."

This thesis dissertation is submitted to the Department of Chemical Engineering and Environmental Technologies at the University of Zaragoza (Spain) in partial fulfillment of the requirements for the degree of Doctor

Isabel Ortiz de Solórzano García

Zaragoza, 2019

Departamento de Ingeniería Química y Tecnologías del Medio Ambiente
Universidad Zaragoza

Instituto Universitario de Investigación en Nanociencia de Aragón
Universidad Zaragoza

nanostructured films & particles

Dr. Manuel Arruebo Gordo and **Dr. Víctor Sebastián Cabeza,**

Professors at the University of Zaragoza in the Department of Chemical Engineering and Environmental Technologies and members of the Institute of Nanoscience of Aragon.

Inform that,

The Doctoral thesis entitled:

"On the synthesis of polymeric, inorganic and hybrid nanoparticles for controlled drug delivery applications. From a molecular level to a whole-body distribution."

has been written by Ms. **Isabel Ortiz de Solórzano García** under our supervision and has not been submitted in support of an application for another degree at this or any other University. This thesis has been carried out at the laboratories of the Institute of Nanoscience of Aragon and the Biomedical Research Institute of Aragon with the economic support of the research project: NANOHEDONISM "Photo-triggered On-demand Drug Delivery System for Chronic Pain" (ERC-2013-CoG-614715) funded by the European Research Council as part of their program IDEAS, ERC Consolidator Grant and thanks to the FPU predoctoral contract obtained by Ms. Isabel Ortiz de Solórzano García (FPU14/00970) funded by the Spanish Ministry of Education, Culture and Sports in the call of 2014.

We authorize and approve the presentation of this dissertation, in Zaragoza on 20th June 2019

Dr. Manuel Arruebo **Dr. Víctor Sebastián**

Los doctores Dr. **Manuel Arruebo Gordo** y Dr. **Víctor Sebastián Cabeza,** ambos Profesores Titulares pertenecientes al Departamento de Ingeniería Química y Tecnologías del Medio Ambiente de la Universidad de Zaragoza y miembros del Instituto Universitario de Nanociencia de Aragón,

CERTIFICAN

Que la presente memoria titulada:

"On the synthesis of polymeric, inorganic and hybrid nanoparticles for controlled drug delivery applications. From a molecular level to a whole-body distribution."

Se ha realizado bajo su dirección y supervisión por Dña. **Isabel Ortiz de Solórzano García**, en los laboratorios del Instituto Universitario de Nanociencia de Aragón y en el Centro de Investigación Biomédica de Aragón gracias a la ayuda del proyecto de investigación: NANOHEDONISM *"Photo-triggered On-demand Drug Delivery System for Chronic Pain"* (ERC-2013-CoG-614715) financiado por la Comisión Europea dentro de su programa IDEAS, ERC Consolidator Grant y gracias a la obtención por parte de Dña. Isabel Ortiz de Solórzano García de un contrato predoctoral FPU de código FPU14/00970 financiado por el Ministerio de Educación, Cultura y Deporte de España en su convocatoria del año 2014. Por lo que autorizamos su presentación.

Y para que así conste, firmamos este certificado en Zaragoza a 20 de Junio de 2019.

Fdo: Manuel Arruebo **Fdo: Víctor Sebastián**

Acknowledgments

Dear reader,

.

Acknowledgements

Summary and Thesis Outline

The present work has been performed in the Department of Chemical Engineering and Environmental Technologies at the University of Zaragoza (Spain), within the Nanostructured Films and Particles (NFP) group. The NFP is a member of the Nanoscience Institute of Aragon (INA). This research has been carried out in this Institute over a 4-year period (2015-2019) thanks to the FPU pre-doctoral contract (FPU14/00970) funded by the Spanish Ministry of Education, Culture and Sports in the call of 2014. Molecular Dynamics Simulation studies have been performed in the Chemical Engineering Department at Virginia Polytechnic Institute and State University (Virginia Tech, United States of America). This research was part of the research project NANOHEDONISM, which was funded by the European Research Council as an ERC-Consolidator Grant.

Here, we developed drug delivery vectors based on hybrid materials to demonstrate that an externally activated pulsatile drug release is possible making it potentially attractive for those pathologies which need with the release of a specific drug amount at a specific time point (i.e., pain, hormonal disorders, etc.). We started from well-known thermoresponsive polymers and we combined them with Near Infrared (NIR) sensitive plasmonic nanoparticles and a selected model drug (i.e., Bupivacaine), normally used for the treatment of chronic pain associated to sciatic nerve disease acting as a nerve blocker. Different steps were needed to follow; from the synthesis and characterization of those polymeric and plasmonic inorganic nanoparticles, to the development of drug-loaded hybrid nano- and micro- drug delivery vectors with reversible ability to release a drug on demand when externally activated with light. In order to achieve this aim, we took advantage of the combination of new synthesis methodologies such as the use of microfluidic platforms together with conventional batch approaches.

On the other hand, different points of view in the development of those drug delivery vectors were taken into account. Molecular dynamics simulations were carried out for the analysis of simple systems containing polymeric chains based on those thermoresponsive materials and the model drug to understand drug-polymer interactions at molecular level and achieve large drug loadings. *In vivo* biodistribution analysis brought some of these drug

delivery vectors close to their final purpose in order to evaluate their *in vivo* persistence and fate.

This thesis is structured in five chapters for the sake of an easy understanding:

- Chapter I provides a brief review of the recent literature and the state of the art about drug delivery vectors and the increasing influence of nanotechnology on the field. Moreover, some fundamental information about molecular dynamics simulations is explained focusing on their role in drug delivery and biomedical research.
- Chapter II describes a novel synthesis of biodegradable plasmonic copper sulfide nanoparticles based on microfluidics techniques. The complete set up of a microfluidic platform as well as the full produced materials characterization and degradation processes are depicted. Finally, subcytotoxic doses are analyzed together with their effect in cell membrane and cell cycle at this concentration to rank the materials. Those cell-based assays can mimic the *in vivo* physiologic environment, addressing biological activity and toxicity issues.
- Chapter III is composed of three different parts providing protocols about the synthesis and characterization of three different hybrid thermoresponsive polymer-inorganic vectors for triggered on-demand drug delivery applications. 1) Cleavable hybrid copper sulfide nanoparticles surface functionalized with a thermoresponsive coating based on ethylenglycol oligomers; 2) Temperature-responsive Poly(N-isopropylacrylamide) (PNIPAm) nanogels decorated with Hollow Gold Nanoparticles (HGNPs); and 3) Customized hybrid PNIPAm microparticles loaded with HGNPs obtained through one-step LED photopolymerization process using a novel microfluidic technique. In all cases drug loading and release studies have been carried out together with cytotoxicity analyses in at least two different cell lines.
- Chapter IV moves into an *in vivo* biodistribution analysis of some of the polymeric nanoparticles developed after local intramuscular and subcutaneous injection in order to evaluate the persistence of the materials and the potential foreign body reaction after administration. For this purpose, the IR820 dye was selected as fluorescent dye for labeling the materials developed and to follow their biodistribution using optical

imaging techniques on BALB mice which were monitored over 7 days after intramuscular administration and for 14 days after subcutaneous administration.

- Finally, Chapter V describes Molecular Dynamics studies of the thermoresponsive polymers of interest used in the experimental studies and their molecular behavior under different environmental conditions in order to maximize drug loadings in the developed drug carriers. Moreover, simulations and experimental studies of bupivacaine-polymer systems are validated.

Resumen y Esquema de tesis

El trabajo desarrollado en esta tesis doctoral ha sido llevado a cabo en el Departamento de Ingeniería Química y Tecnologías del Medio Ambiente de la Universidad de Zaragoza (España), dentro del grupo de Películas y Partículas Nanoporosas (NFP) miembro del Instituto Universitario de Nanociencia de Aragón (INA). Este trabajo de investigación se ha llevado a cabo en este Instituto durante un periodo de 4 años (2015-2019) gracias a la obtención de la beca predoctoral de Formación de Personal Universitario (FPU) financiada por el Ministerio de Educación, Cultura y Deporte de España en su convocatoria de 2014 (FPU14/00970). Los estudios de simulación basada en Dinámica Molecular se han desarrollado en el Departamento de Ingeniería Química de la Universidad de Virginia (Virginia Polytechnic Institute and State University, Virginia Tech) en Estados Unidos. Todo el trabajo de investigación ha sido parte del proyecto europeo NANOHEDONISM, financiado por el European Research Council como parte de ERC-Consolidator Grant.

En esta tesis doctoral, se han desarrollado vectores de liberación de fármacos basados en materiales híbridos para demostrar que la liberación pulsada de fármaco mediante activación externa es posible haciéndolas potencialmente atractivas para aquellas patologías que necesitan la liberación de una cantidad determinada de fármaco en momentos concretos (como por ejemplo tratamientos contra el dolor, desajustes hormonales…). El punto de partida fueron polímeros termosensibles ya conocidos y bien estudiados combinándolos con nanopartículas plasmónicas sensibles a la radiación en el rango del infrarrojo cercano (NIR) y tomando la Bupivacaina como fármaco modelo debido a su uso habitual para el tratamiento del dolor crónico asociado a enfermedades del nervio ciático actuando como bloqueo del nervio. Se han seguido numerosos pasos, desde la síntesis y la caracterización de las nanopartículas plasmónicas y poliméricas hasta el desarrollo de nano y micropartículas híbridas cargadas de fármaco con la habilidad de liberar el fármaco a demanda de manera reversible cuando son activadas externamente con luz. Para conseguir este objetivo, se ha aprovechado la combinación de nuevos métodos de síntesis como el uso de plataformas de microfluídica junto con métodos convencionales de síntesis en discontinuo.

Por otro lado, se han tenido en cuenta diferentes puntos de vista en el desarrollo de estos vectores de liberación de fármacos. Simulaciones basadas en dinámica molecular es

han llevado a cabo para el análisis de sistemas sencillos formados por cadenas poliméricas basadas en los polímeros termosensibles usados experimentalmente y la bupivacaina como fármaco modelo para entender las interacciones fármaco-polímero a escala molecular y con ello conseguir mejores y optimizadas cargas de fármaco. Finalmente, el análisis de la biodistribución *in vivo* de algunos de estos vectores de liberación de fármacos han acercado el estudio de los mismos a su aplicación final para evaluar su persistencia y destino final en modelos animales.

Esta tesis está estructuradas en cinco capítulos para su mejor comprensión:

- El capítulo I proporciona una breve revisión de literatura reciente y el estado del arte acerca de vectores de liberación de fármacos y la creciente influencia de la nanotecnología en el mismo. Además, se explican conceptos fundamentales acerca de simulación basada en dinámica molecular centrándose en su papel en desarrollo de vectores de liberación de fármacos y biomedicina.
- El capítulo II describe un novedoso método de síntesis de nanopartículas plasmónicas de sulfuro de cobre basada en técnicas de microfluídica. Se presenta la instalación completa de la plataforma microfluídica así como la completa caracterización y proceso de degradación de los materiales obtenidos. Finalmente, se analiza la dosis subcitotóxica y el efecto en la membrana y el ciclo celular a esta concentración para clasificar el material. Estos ensayos basados en células pueden reproducir el entorno fisiológico real proporcionando información sobre la actividad biológica y toxicidad de los materiales.
- El capítulo III está dividido en tres partes diferenciadas proporcionando información sobre la síntesis y la caracterización de tres vectores híbridos compuestos por políemros ermosensibles y nanopartículas inorgánicas para la liberación asistida a demanda en aplicaciones de liberación de fármacos. 1) Nanopartículas híbridas escindibles de sulfuro de cobre con la superficie funcionalizada con un polímero termosensible basado en oligómeros de etilenglicol; 2) Nanogeles sensibles a la temperatura con base de Poly(N-isopropilacrilamida) (PNIPAm) decorados con nanopartículas plasmónicas huecas de oro (HGNPs); y 3) Micropartículas de PNIPAm personalizadas cargadas con nanopartículas plasmónicas de oro (HGNPs) obtenidas mediante un proceso único de fotopolimerización con luz LED usando una técnica novedosa de microfluídica. En todos los casos, se han

llevado a cabo estudios de carga y liberación del fármaco modelo junto a análisis de citotoxicidad en al menos dos líneas celulares.

- El capítulo IV cambia su perspectiva al análisis in vivo de la biodistribución de seis nano y micropartículas poliméricas tras su inyección local intramuscular y subcutánea para evaluar la persistencia de dichas partículas y la potencial reacción del cuerpo frente a un cuerpo extraño tras su administración. Para este propósito, se seleccionó el fluoróforo IR820 para marcar los materiales a estudio y poder hacer su seguimiento usando técnicas de imagen óptica en ratones inmunodeprimidos (BALB) que fueron monitorizados durante 7 días tras una inyección intramuscular y durante 14 días en el caso de administración subcutánea.
- Finalmente, el capítulo V describe estudios basados en dinámica molecular de los polímeros termosensibles de interés usados experimentalmente y su comportamiento molecular bajo diferentes condiciones ambientales para conseguir maximizar la carga de fármaco en los vectores desarrollados. Además, las simulaciones de los sistemas fármaco-polímero han sido validados experimentalmente.

Abbreviations

- Å: Angstrom
- Aam: Acrylamide
- BVP: Bupivacaine
- CuS: Copper Sulfide
- CV: Coefficient of variance
- DLS: Dynamic light scattering
- EPR: Enhanced permeability and retention
- FDA: Food and Drug Administration
- FTIR: Fourier Transformed Infrared Spectroscopy
- GC-MS: Gas chromatography Mass spectrum
- GPC: Gel Permeation Chromatography
- HGNPs: Hollow Gold Nanoparticles
- HPLC: High Performance Liquid Chromatography
- IM: Intramuscular
- LCST: Low Critical Solution Temperature
- LED: Light emitting diode
- LJ: Lenard Jones
- MD: Molecular Dynamics
- mMSCs: murine Mesenchymal stem cells
- MPs: Microparticles
- NIPAm: N-isopropylacrylamide
- NIPMAm: N-isopropylmethacrylamide
- NIR: Near Infrared
- NMR: Nuclear Magnetic Resonance
- NPs: Nanoparticles
- PAAm: Polyacrylamide
- PEG: Polyethylene glicol
- p.i.: Post injection
- PNIPAm: Poly(N-isopropylacrylamide)

- PNIPMAm: Poly(N-isopropylmethacrylamide)
- $P_{res}(t)$: Residence time probability
- PTT: Photothermal therapy
- RDF: Radial distribution Function
- Rg: Radius of gyration
- ROS: Reactive Oxygen Species
- SC: Subcutaneous
- SEM: Scanning electron microscopy
- SPR: Surface plasmon resonance
- TEM: Transmission Electron microscopy
- UPLC: Ultra Performance Liquid Chromatography
- UV: Ultraviolet
- vdW: van der Waals
- XRD: X-Ray Diffraction

To you, my love…

CONTENTS

CHAPTER I

INTRODUCTION

"Research is what I'm doing when I don't know what I'm doing"

Wernher von Braun, Aerospace engineer (1957)

Chapter I

INTRODUCTION

Summary

In this chapter, a general analysis of the impact of nanotechnology on drug delivery is going to be reviewed as the common thread between all the chapters presented in this thesis dissertation. The importance of nanocarriers design in their drug loading ability and their drug release patterns together with the different methodologies to synthesize them will be discussed. In addition, nanoparticle persistence in preclinical models and its influence on drug delivery will be presented. Finally, a brief overview on the role of molecular dynamics simulations in drug delivery will be described.

1 Introduction

1.1 Drug delivery

Drug administration for diagnosis and treatment of human diseases has become one of the main challenges of modern medicine. Off-target effects can lead to toxic and side reactions to healthy tissues commonly suffered by patients. This has encouraged researches to pursue new routes of targeted and controlled drug dispensation avoiding collateral effects [1]. To achieve this goal, scientists from areas such as chemistry, materials science, biomedicine or nanotechnology work together to improve and design novel drug delivery systems capable to release the drug only where and when is needed, specifically targeting the required area of the body minimizing side effects.

In order to accomplish this goal, these systems need to overcome different barriers directly linked to their administration route: oral delivery systems have to resist extreme changes in pH; local delivery systems must prevent damage to the surrounding tissue; and systemic delivery requires the avoidance of a rapid drug clearance allowing to enter the drug into the pathological tissue [2]. Therefore, their design requires the proper protection of the drug, biocompatibility, stability and specificity as well as a good knowledge of their pharmacokinetic and pharmacodynamics principles.

The interest on the field of drug delivery systems has increased significantly the last decades and it has been reflected in the number of scientific articles published over the last years (Figure 1.1).

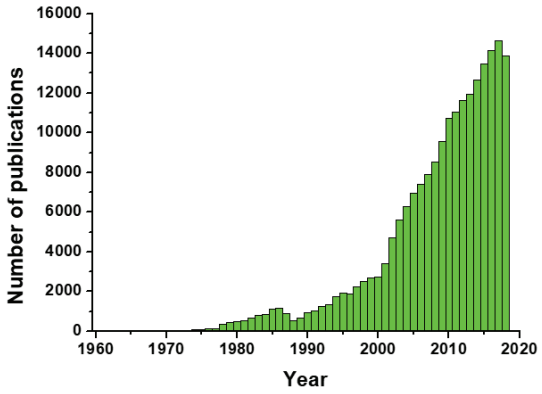

Figure 1.1: Number of scientific articles published each year (1960-2018). Source SCOPUS search criteria "drug delivery systems". *February 24, 2019.*

However, the concept of controlled drug delivery was already introduced by Judah Folkman in the early 1960's [3]. In his work, Folkman implanted macroscopic silicon rubber tubing loaded with drug, acting the tubing as a semipermeable membrane achieving a constant drug delivery rate. Afterwards, in the 1970's and 1980's another macroscopic devices were patented as drug delivery systems such as skin patches as drug reservoirs [4]. In these macroscopic devices, drug administration followed a zero-order release based on the diffusion of the drug through the pores of the semipermeable non-biodegradable materials used as membranes.

Improved sustained drug delivery systems were achieved when biodegradable microparticles were brought into the field of medicine. In the 1970's Du Pont researchers combined peptide drugs with biodegradable poly (lactic acid) (PLA) in microscopic particles for sustained drug release [5] and poly (lactic-co-glycolic) (PLGA) microparticles were loaded with luteinizing hormone-releasing hormone (LHRH) and patented as long-acting (1-month) sustained release reservoirs by Syntex [6]. Nevertheless, the lack of drug guidance of these macro- and microscopic systems leaded to unspecific treatments with possible side effects.

In this sense, nanotechnology provides an immense variety of opportunities and alternatives of targeted and site-controlled drug delivery [7]. The unique properties of materials at the nanoscale have shown promising potential to improve therapeutic efficacy [8]: improving the delivery of poorly water-soluble drugs, assisting the penetration of drugs in tissues and through cell barriers; targeting tissues or cells in a specific manner; providing on-demand drug delivery; or supporting real-time *in vivo* imaging. These nanocarriers combine advanced materials with therapeutic drugs to achieve targeted and *smart* drug delivery approaches [9].

Among these materials, polymer-based micelles and nanoparticles present the most spread, customized and successful drug delivery vectors. They provide a stable and biocompatible environment for active compounds due to their noticeable bio-imitative characteristics enhanced by their controllable surface features and tunable particle sizes [7]. Two major types of polymeric vectors may be differentiated: nanocapsules which contain the drug in the core inside a polymeric shell; while nanospheres refer to solid porous polymer

matrixes where drug molecules may be trapped within the sphere center or adsorbed on the matrix pores or on the surface [10].

Polymeric nanocarriers can be formulated from pre-polymerized polymers or by direct monomer polymerization [11]. Pre-formed polymeric nanoparticles are prepared by dissolving the polymer in an appropriate solvent adding an anti-solvent in which precipitation is achieved through the emulsification and solvent evaporation technique, nanoprecipitation or simply by expansion when using the supercritical fluid technology. Hydrophobic drugs can be loaded in oil in water emulsions (o/w) where the core of the emulsion is hydrophobic due to the non-polar contribution of the amphiphilic molecule (i.e. surfactant) used in the synthesis. However, when hydrophilic drugs are to be encapsulated, the double water in oil in water (w/o/w) emulsion is used keeping the hydrophilic drug molecules in the hydrophilic core of the two-layered micelles formed. On the other hand, polymeric nanoparticles can be directly formed by *in-situ* polymerization from monomers mainly using emulsification techniques to control the particle size distribution [12]. Microfluidics technique is a useful tool in this field due to the precise fluids manipulation, control on the polymerization rate and kinetics, as well as a fast response in terms of size tuning or components encapsulation variability [13].

An interesting approach to sustain drug delivery has been achieved by using biodegradable or bioerodible polymeric materials capable to release their payload while their erosion process. PLGA is the most common biodegradable polymer used so far with successful results mainly in antimicrobial therapy and cancer [14]. The first report of tumor specific systemic targeting of a nanoparticle- aptamer bioconjugate system was shown by Cheng et al. [15]. They studied *in vivo* prostate tumor specificity and effectiveness of PLGA-Polyethylene glycol (PEG) nanoparticles functionalized with A10 RNA Aptamer (Apt; that binds to specific prostate membrane antigen) and loaded with docetaxel having after systemic administration excellent results.

Other commonly used materials are lipid-based nanoparticles: liposomes [16]. These systems consist of submicron bilayer spherical nanostructuresof phospholipid-based agents that may include drugs, genes or antibodies inside or in between the constitutive bilayers. Their resemblance to biological membranes makes them perfect models for encapsulation

and delivery of bioactive agents together with their immediate interaction with membrane cells. Extrusion, sonication or microfluidics are the main methods for liposome synthesis. Liposomal nanoparticles are already present in dairy industry such as cheese [17]. Moreover, various anticancer drugs have been encapsulated in liposomes (e.g., Doxil®, liposomal doxorubicin) showing improved outcome and enhanced selectivity in targeting the pathological tissue than the corresponding free drugs [18][19].

Inorganic nanoparticles such as ceramic, metal or carbon nanotubes have expanded their traditional applications (i.e., optics, electronics, composites, sensing, etc.) into the biomedical field. Plasmonic, magnetic or fluorescent properties are exceptional physical properties that have attracted the interest of scientists of this biomedical field [20]. These features have allowed the creation of sophisticated drug delivery systems by merging them with active compounds for direct drug delivery or with polymeric structures as active elements to induce drug release. Metallic gold nanoparticles (AuNPs) are the most used nanoparticles, they can be functionalized with genes, antibodies or enzymes and act as active elements for drug delivery; they can also be functionalized with polymers or be part of larges polymer-based structures; and they can be the active part in supramolecular recognition (e.g., in SERS). Surface plasmon resonance (SPR) makes AuNPs and another plasmonic nanoparticles, such as semiconductor copper sulfide nanoparticles (CuS), present unique characteristics such as Surface plasmon resonance (SPR). This property is related to the vibration of conduction electrons at the surface of these materials under light irradiation, which provokes an increase of their environmental temperature what makes them ideal candidates for laser triggered on-site on-demand drug delivery. On their part, magnetic nanoparticles such as superparamagnetic iron oxide have been used as drug carriers and complement for MR imaging together with anticancer treatment [21].

Functionalized carbon nanotubes (CNTs) have a potential application in drug delivery due to their excellent mechanical, electric and surface properties [22]. Bioactive agents can be conjugated to CNTs acting as carriers for drugs [23] and also cross cell membranes making them ideal as penetrating drug delivery vectors [24]. On the other hand, mesoporous silica materials have received intensive attention because of their stability, high surface-volume ratio and well-defined pore structure making them perfect for drug delivery applications. The

outstanding advantages of porous materials rely on the ability of their pore size and surface modification capable to bear drugs from different sizes and reach selectively the target thanks to their easy surface functionalization with molecular recognition [25]. For example, functionalized MCM-41 or SBA-15 nanoparticles have been used for the controlled delivery of aspirin [26] and ibuprofen [27], respectively. On the other hand cancer therapeutic drugs such as paclitaxel (PTX) has been delivered from biodegradable porous silicon nanoparticles under controllable release [28].

Solid inorganic matrixes and reservoirs allow diffusion-controlled drug release over different time windows depending on their composition, size and active agent to release. Modified mesoporous materials such as functionalized MCM41 nanoparticles have been successfully demonstrated to have different drug release patterns depending on their surface modification. Vyskocilová et al. [29] loaded acetylsalicylic acid in amino, chloro and oxo functionalized MCM 41 nanoparticles showing how amino and chloro modified systems released the drug faster than the oxo-functionalized.

The most traditional method for metallic inorganic particle synthesis is chemical reduction, where particle growth is controlled through temperature or pH from a system composed of an inorganic precursor solution, an stabilizer and the reducing agent [30][31]. The control over this growth can be improved by using microfluidic platforms where diffusion and temperature profiles are well defined by flow rates and microchannel dimension [32].

The combination of all of these materials have led to *intelligent* nanovectors for drug delivery capable to achieve different release kinetics adjusted to each particular case. The tendency in controlled drug release is directed to intelligent drug administration by stimulus responsive drug delivery systems. pH, temperature or protein interaction may modify the carrier structure or its interaction with the drug, triggering its release. Hydrogel-based micro- and nanoparticles are widely used for this kind of release pattern due to their network reversibility under environment fluctuations [33].

Moreover, the therapeutic effect of an encapsulated drug increases compared to free drug administration. For instance, it has been demonstrated an enhanced *in vivo* effect of doxorubicin when incorporated in liposomal-based carriers as Doxil® reducing CT26 tumor

growth in immunocompetent mice because of a better internalization of the drug [19]. This was also proved in human patients suffering metastatic breast carcinoma (MBC). Lyass et al. [34] demonstrated the enhanced performance of Doxil® to induce durable response in MBC patients studying its pharmacokinetic and toxicity profiles.

In summary, the active payload of those nanocarriers described before can be released in a controlled way through different strategies resulting in particular release profiles strongly related to the nature of the previously described materials. All of them seek to limit off-target side effects and decrease the number of required doses. Controlled drug delivery is clearly the future of medicine and lots of efforts are being put together to achieve safe and effective drug administration from all areas of research. In this PhD work, we try to contribute to this end using nanotechnological-based approaches with inorganic and polymeric vectors obtained by efficient and scalable synthesis processes.

1.2 Biodistribution & Persistence

Understanding the biological distribution and persistence when micro- and nanocarriers are introduced in the human body is essential to test the effectiveness and safety of the treatment. The interaction between materials and biological systems is of paramount importance to follow the progression of the treatment when using nanoparticulated therapeutic carriers. As previously described, the migration of micro- and nanoparticles all over the human body is determined by their route of administration as well as by their physicochemical characteristics including shape, size, structure and surface chemistry, which determine their *in vivo* behavior and fate [2].

When drug delivery vectors are incorporated by parenteral administration, nanoparticles must obey certain size and toxicity restrictions because they are exposed to renal and hepatic clearance and to the immune response during blood circulation. On its part, oral administrated drug carriers have access to the gastrointestinal system and may interact with mucosal or epithelial barriers.[2] On the other hand, local injected micro- and nanoparticles have to cross anatomical barriers to distribute all over the body, and in some applications a local drug depot placed in the proximity of its point of action is needed and any displacement from the injection point should be avoided. After local injection, the immune system detects a foreign object (i.e., any nanoparticle) and reacts protecting the rest

of the body from it. The mononuclear phagocytic system recognizes the foreign material, leading to the innate reaction of cellular processes expressed as inflammation, formation of giant macrophages and fibrosis that might damage the surrounding tissue [35]. On the other hand, the presence of nano- and microparticles in the body can result to an adaptive immune response where regulatory macrophages dampen the immune response avoiding the inflammation through antibodies generation [36]. Anyhow, the immune system recognizes and tries to degrade the foreign body to restore homeostasis.

All these aspects have to be fully understood to accomplish a successful treatment and enable predictions of the beneficial or adverse effects of drug carriers. Nano- and microscale carriers composition, size, surface functionality, charge and active targeting functionalization determine their final location and time persistence in the body [37].

The origin of drug nanocarriers and their nature play a key role in how the human body handles their distribution and bioaccumulation. Metallic nanoparticles such as gold nanoparticles (AuNPs) or magnetic iron nanoparticles (FeNPs) tend to accumulate in tumors because of their small size and the leaky tumor vasculature, what is denominated ‘enhanced permeability and retention’ process (EPR). This characteristic is used as a passive targeting and takes advantage of the enhanced permeability which irrigate tumors [38]. However, the poor delivery efficacy and specificity and low successful results of this approach limits their use in clinical trials [39].

Previous studies have demonstrated how AuNPs accumulation after intravenous administration depends on their size. Sonavane et al. [40] observed that 15 nm AuNPs stayed longer and all over the body while 200 nm particles showed short time presence in blood, brain, stomach and 8rimethy. Superparamagnetic iron oxide nanoparticles (SPIONs) with sizes lower than 25 nm were tested in healthy nude-mice by Pham et al. [41] with similar results than gold nanoparticles: larger (25 nm) nanoparticles cleared faster than 10 nm particles after intraperitoneal administration but macrophages increase was observed in tissues such as liver and spleen probably involved in nanoparticle clearance.

Another inorganic nanoparticles have shown biodegradation properties enhancing the biocompatibility and decreasing their persistence and bioaccumulation. In this sense, copper sulfide nanoparticles (CuS) used for photothermal therapy have demonstrated better in vivo

performance than gold nanoparticles for the same use. Guo et al. [42] compared PEG-Au NPs and PEG-CuS NPs biodistribution after intravenous administration. The latter were eliminated by hepatobiliary and renal excretion (90%) thanks to their biodegradability condition, while for AuNPs only 3.98% of the injected dose was excreted by the liver and the kidneys within one month after injection.

On the other hand, polymeric nanoparticles have been widely studied. From biodegradable PLGA-based nanoparticles to innocuous PEGylated nanoparticles biodistribution have been studied via different administration routes. These long-lasting systems are required when the drug administration needs to be sustained over a long period of time and several factors affect to their biodistribution. Their composition determine their circulation half-time in the body, targeting and therapeutic efficacy. In this sense, poly(ethylene glycol) (PEG) has showed excellent results thanks to their physicochemical properties, low toxicity and no immunogenicity [37]. Size is another key factor in polymeric nanoparticles behavior in the body. Fang et at. demonstrated how larger pegylated poly(cyanoacrylate-co-n-hexadecyl) cyanoacrylate (PHDCA) cleared 2-fold faster than smaller ones (243 nm vs. 80 nm) delivering into the tumor half of drug loaded after 24 hours [43].

Finally, functional groups, charge and protein functionalization for active targeting of any nanoparticle affect their uptake by the cells of the phagocytic system. Several works have shown how positively charged nanoparticles have a higher rate of cell uptake compared to negative or neutral nanoparticles leading to shorter blood circulation life-times [44]. On its part, active targeting involves antibodies, aptamers, peptide, etc. usage and highly specific interactions and recognition to promote the accumulation of nanoparticles. Tumors are the main target of these vectors in targeted therapies and immunotherapies and successful results have been obtained with many nanoparticles including carbon quantum dots [45] to PEGylated liposomes [46].

The final purpose of the treatment determines the administration route and thus the possibilities of nanoparticle distribution. Protein-modified or specific targeted vectors may interact to cells into the blood stream and eventually reach the final target. Nevertheless, local

treatments involving local intramuscular or subcutaneous injection are meant to stay in their injection area acting as drug depots.

Briefly, the purpose, material and administration route of the drug carrier may influence also its final biodistribution and persistence in the human body. This is a key aspect to be taken into account when drug delivery systems are designed and it has paramount importance in the final efficiency and safety of the carriers; this is the reason why persistence and biodistribution have been included in this PhD dissertation.

1.3 Molecular dynamics simulations

In addition to experimental trials, computer simulations can be used as complementary tools to give a new insight into the structural and dynamic properties of the systems of interest at the atomistic and molecular level. In general, computer simulations describe the physics of a particular system with model equations and require a group of algorithms to solve these equations and generate data that can lead to conclusions about the behavior of the studied system at the macroscopic level.

Molecular dynamics in particular do not consider explicitly the electrons around atoms: each atom is represented as a single bead with mass, radius and charge (Figure 1.2). These characteristics allow them to interact through Coulomb and Van der Waals interactions, while bonds, angles and dihedrals present in molecules are described by harmonic terms.

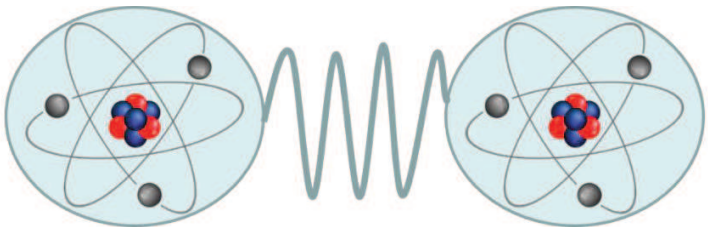

Figure 1.2: Schematic representation of atoms in molecular dynamics simulations

All these terms together build an equation denominated *Force Field*. The Force field is particular for each molecule of a system and is used to calculate its energy and geometry in each moment of the simulation. This equation relates the potential energy of a system and the coordinates of its composing particles and it must be simply enough to be evaluated quickly during the simulation and sufficiently detailed to reproduce the properties of interest.

The general analytical form is shown in Eq. 1.1 [47], which includes some parameters (Force constants:$k_b, k_\theta, k_\omega, k_\varphi$; Equilibrium values: b_0, θ_0, ω_0,; Multiplicity: n ; Phase: δ ; Lennard-Jones parameters: $\epsilon_{ij}, \sigma_{ij}$; Partial charges: q_i, q_j; and Dielectric constant: D) that vary depending on the atoms, molecule, environment and sometimes even on simulation conditions.

Eq. 1.1:General Force Field analytical form

$$U = \sum k_b(b_0 - b)^2 + \sum k_\theta(\theta_0 - \theta)^2 + \sum k_\omega(\omega_0 - \omega)^2 + \sum k_\varphi(1 + \cos(n\varphi - \delta)) + \sum 4\epsilon_{ij}\left[\left(\frac{\sigma_{ij}}{r_{ij}}\right)^{12} - \left(\frac{\sigma_{ij}}{r_{ij}}\right)^{6}\right] + \sum \frac{q_i q_j}{4\pi D r_{ij}}$$

The first four terms of Eq. 1.1. represent the bonded interactions of the molecule: bonds, angles, improper angles and dihedrals respectively, commonly described by harmonic movements in respect to an equilibrium point. The last two terms of Eq. 1.1 describe the non-bonded interactions of each atom of the molecule with the rest of the atoms of the system: Van-der-Waals interactions and electrostatic Coulomb interactions, respectively.

When these equations are available for all components present in a particular system of study and starting positions and velocities are set, the different molecular dynamics (MD) commercial packages such as GROMACS, CHARMM or NAMD solve them using statistical mechanics. Thanks to these statistical models, the movement of the composing molecules over time can be described concluding in macroscopic thermodynamic properties. This tool has the advantages of inherent speed and low computational cost when drug molecules are pricey and experimental trials become unaffordable and impractical, however, computational time is very high and computational studies can only be carried out under limited time and size scales.

Even though size and time scales are a handicap for MD simulations, thousands of studies have been carried out using this tool in drug delivery applications. Drug receptor binding and docking studies are the most studied issues because of the lack of definition in real experiments to understand the mechanism involved during these processes. Moreover, understanding the molecular basis of those processes allows to design specific ligands for a target receptor and thus obtain a good efficacy in the design of drug delivery systems [48].

For instance, the study of the interaction of chemokines (SDF-1α) with their specific receptors (CXCR4) involved in regulation of HIV-1 and metastasis of breast cancer [49] elucidated key information about bioactive conformation of the complex formed after docking and binding helping to understand the process and proposing new routes of treatment [50]. In search of specific inhibitors against tuberculosis, the study of binding characteristics into the active site of epoxide hydrolase gave some light into different possibilities [51]. Moreover, computer simulations also are helpful to test new biomolecules for specific targeting of treatments such as prostate cancer [52] among others [53].

Otherwise, computer simulations are useful as well to study drug loading mechanisms, capacity and rate; self-assembly of micelles; drug distribution/localization in the nanoparticles; dominant drug-system interactions and the effect of environmental conditions such as temperature or concentration in drug loading and release. In addition, it shows a new window to the drug interaction with its carrier and the environment on an atomistic basis and has a significant role to achieve better design and administration of controlled release systems with patient specific treatment regimens. Drug uptake by polymers is related to their capacity and absorption properties and can be an indirect and useful approach to drug loading and release studies. This was studied by Subashini et al. [54] in six polymer with different functional groups and three drugs with different water affinity: from doxorubicin (water soluble molecule) to glicazine (water insoluble molecule). After numerous combinations, they determined that hydrophobic interactions play a key role in the uptake of the drug by the polymer and an inverse relationship between polymer-water affinity and drug uptake, concluding that MD approach can save considerable time during the selection of the best polymer as carrier for a particular drug encapsulation. On the other hand, release studies of different drugs are also presented in several works [55][56]. Luo et al. [57] studied the anticancer drug camptothecin (CPT) loading and 12rimeth from a pH sensitive amphiphilic polymer showing the micelle formation of the polymer-drug system and the 12rimeth process under pH variation of the environment.

Furthermore, as we stated before, in drug delivery systems the development of novel biocompatible, biodegradable and stimulus-responsive polymers as drug carriers is one of the most active areas of biomedical research. MD can assess a necessary insight into detailed

interactions such as hydrogen-bonding, polymer-solvent and specific conformational effects. Moreover, the structure and key properties of the carrier such as stability, behavior under different environmental conditions and binding between molecules can be studied using MD computer simulations. Examples of these studies involve biodegradable polymers formulation and their degradation process under different physical chemical conditions [58], thermoresponsive polymers and their conformational changes under different environmental variations [59]; or carbon nanotubes and their functionalization with different drug molecules or proteins [60] for drug delivery applications.

In summary, computational simulations are a bridge between chemistry, nanoscience and medical applications and the unprecedented improvement in computational speed and computers' features have moved MD closer to experimentalist enriching laboratory results.

CHAPTER II

MICROFLUIDICS SYNTHESIS OF CUS NPs

"All of science is nothing more than the refinement of everyday thinking"

Albert Einstein, Physicist (1936)

Chapter II

MICROFLUIDICS SYNTHESIS

Summary

In this chapter, the continuous synthesis of biodegradable photo-thermally responsive copper sulfide nanoparticles with the aid of a microfluidic platform is described. A complete physicochemical characterization of the resulting products is presented and they are compared to the products obtained in conventional batch reactor. The nanoparticles biodegradation is demonstrated under simulated physiological conditions, identifying the obtained subproducts. Furthermore, a complete cytotoxicological analysis on different cell lines is performed and their photothermal effect and capability to generate reactive oxygen species is demonstrated.

The contents of this chapter were adapted from the following published manuscript:

Ortiz de Solorzano, I., Prieto, M., Mendoza, G., Alejo, T., Irusta, S., Sebastian, V., Arruebo, M.

"Microfluidic synthesis and biological evaluation of photothermal biodegradable copper sulfide nanoparticles"

ACS Appl. Mater. Interfaces, **2016**, 8: p. 21545−21554

2 Microfluidics synthesis: Copper sulphide nanoparticles

2.1 Introduction

Plasmonic materials absorb near-infrared (NIR) light, converting it into heat due to the excitation of direct (band-to-band) and indirect transitions and plasmonic photoexcitation [61]. Within this group of materials, copper (II) sulfide nanoparticles are semiconductor chalcogenides with unique electronic and optical properties. Depending of its atomic composition, the bandgap of copper sulfide crystalline structures varies between 1.2 eV for Cu_2S to 2.0 eV for CuS, which allows it to absorb a large fraction of the solar spectrum [62]. A wide variety of biomedical applications take advantage of those electro-optical properties including electrochemical sensing [63], diagnosis [64], theragnosis [65][66], photothermal [67][68] and NIR activation for drug delivery applications [69][70].

The most common application of these materials is focused on photothermal therapy (PTT) for cancer treatment. This approach uses light in the visible or near-infrared wavelength as an energy source to excite the electron bands of nanoparticles (NPs) materials and then release this energy as heat killing the targeted cells [71]. In the biomedical field, only materials based on plasmonic gold nanoparticles have reached clinical trials for photothermal therapy in cancer treatment [72][73]. However, tissue light penetration and scattering of the light passing through regions having different refractive indexes (i.e. cell membranes, vessel walls, etc.) have become a handicap for real applications. Therefore, the design of nanoparticles with enhanced NIR absorption and with response at wavelengths with reduced photon scattering [74] can potentially overcome this limitation.

Biodegradability and superior photothermal conversion efficiencies (~22-60%) [61], potentially enhanced by combining them with other plasmonic metal nanoparticles[75], are some of the main advantages of CuS nanoparticles (NPs) when used *in vivo* compared to gold-based plasmonic nanoparticles, upconversion nanoparticles [76][77] and other carbon-based nanoparticles such as carbon nanotubes or graphene oxide [78][79]. Guo et al. [80] demonstrated that using similar injected doses, plasmonic gold nanoparticles remained in the body one month after the injection in BALB/c mice at high levels (>96% of injected dose), while during the same period only 10% of the injected dose remained in animals treated with CuS NPs being mostly excreted following the hepatobiliary route. The same authors

demonstrated that the polycrystalline CuS NPs disintegrate from CuS shells into single CuS crystals after laser treatment, but those authors did not evaluate the biodegradation subproducts [81]. Other carbon-based nanoparticles used in photothermal therapy such as carbon nanotubes or graphene oxide have shown large physiological persistence [78] [79] despite the identification of some biodegradation cellular routes [82]. Upconversion nanoparticles have also been used in photothermal therapy [76], but again, biopersistence in the mononuclear phagocyte system is the major hurdle for their clinical translation unless they are produced in reduced sizes allowing renal excretion [77]. In addition, after describing hollow gold plasmonic instability and fragmentation *in vivo*, Goodman et al. [83] concluded that new biocompatible plasmonic nanoparticles appropriate for nanomedicine are required.

The batch synthesis used for the synthesis of the nanoparticles described in the previous paragraph has serious shortcomings such as polydispersity, low yield, and batch to batch inconsistencies, which can be overcome by using continuous-flow microfluidic reactors. Thanks to the use of confined growth in the microchannels driven by molecular diffusion under reduced concentration and temperature gradients, comparative syntheses of polymers, metals and oxides in microreactors have demonstrated a superior performance over conventional batch reactors.

Although, the high surface area-to-volume ratios of microfluidic reactors present a great potential for multiphase reactions, clogging of microchannels represents a big concern when using microreactors [84]. Moreover, their cost, complexity of fabrication and suitability for certain reactions makes them appropriate and practical only for specific applications over conventional techniques [85]. Also, an obvious limitation when using microreactors is the production volume capability due to the small amounts of reagents involved in the process. However, this can be solved thanks to the potential scale-out of microfluidic systems [86], increasing the number of microreactors in order to produce a parallel network [87].

Combinatorial synthesis [88], multistep microfluidic platforms [89], and on-line monitoring with feedback control to render a product with specific properties [90] are possible using microfluidics. Passive and active mixers are widely used to obtain nanoparticles without any chemical reaction, just achieved with the control of the self-assembly of precursors under the presence of surfactants or stabilizers to form polymeric

nanoemulsions [91], nanoprecipitated particles [92], liposomal formulations [93], solid-lipid nanoparticles [94], and so on.

Microfluidic reactors have been already used to synthetize photothermally responsive nanoparticles. Hollow gold nanoparticles have been produced following a redox reaction using sacrificial templates in a galvanic replacement reaction [95]. Gold nanoshells can also be prepared using sequential microfluidic platforms with significant time savings and with an improved control over the product properties compared to a conventional batch processing operation [96]. Recently, some studies of biodegradable CuS NPs synthesis in a millifluidic platform have been carried out by Cheung et al. [97] using organic solvents and surfactants to control the geometry and crystalline phase of the resulted NPs. However, the the removal of these organic solvents is a handicap for later biomedical use that can be overcome using water as synthesis medium.

2.2 Objectives

This chapter gathers all the studies driven towards the consecution of a novel microreactor platform for the synthesis of biodegradable copper sulfide nanoparticles. A double stage microfluidic reactor was selected to mimic the already well known conventional CuS batch production, but in a continuous fashion. Different synthesis conditions are discussed and the morphological characteristics and photothermal properties of resulted nanoparticles are compared to show the advantages of the new synthesis approach. Further, biodegradation processes at two different temperatures are tested under simulated physiological conditions, giving a new insight on resulted subproducts, scarcely known so far. Due to future biomedical applications, cell viability, apoptosis and cell cycle effects of copper sulfide nanoparticles are studied on four different cell lines. Finally, *in vitro* photothermal effects and reactive oxygen species (ROS) generation are evaluated corroborating their potential use in photothermal or photodynamic therapies.

2.3 Experimental

2.3.1 CuS nanoparticles synthesis

The synthesis of CuS NPs using a batch-type reactor was performed following the work of Ramadan et al. [98]. Briefly, the synthesis at 60 ºC was carried out in an open flask by mixing 240 mg of PVP K30 dissolved in 25 mL of water with 100 µL of a 0.5 M solution

of $CuCl_2$ and 25 mL of DDI water with its pH adjusted to 9. Next, 6.4 µL of hydrazine solution (N_2H_4) was added under stirring, with the consequent formation of Cu_2O seeds. Finally, 200 µL of Na_2S (320 mg/mL) was added to the previous dispersion while keeping it under heating at 60 ºC for 2 h (Figure 2.1) On the other hand, synthesis at 120-150 ºC were carried out following the same procedure but heating the final colloidal dispersion in a PTFE-lined sealed autoclave placed in a rotating oven. After synthesis, the resulting CuS NPs were thoroughly washed in DDI water by successive centrifugation cycles.

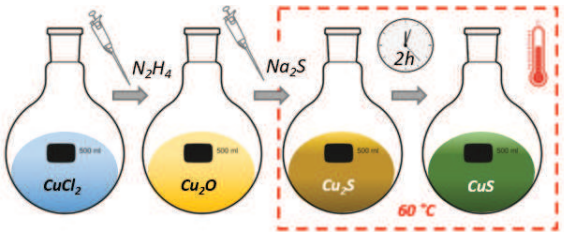

Figure 2.1: Scheme of CuS NPs batch synthesis

Continuous microfluidics synthesis was carried out using two consecutive Y-shaped PEEK micromixers (500 µm inner diameter) differentiating two separated stages in the reaction process. In the first stage, solution A and B interfaced in the first micromixer to form Cu_2O seeds. Solution A was prepared by mixing 480 mg of PVP K30 dissolved in 30 mL of DDI water with 200 µL of a 0.5 M solution of $CuCl_2$ adjusted at pH 9; while solution B was composed of 12.8 µL of hydrazine in 30 mL of DDI water and 25 mL of DDI water with its pH adjusted to 9. Both solutions were injected with the aid of a syringe pump with an equal flow rate (4.625 mL/h). The resulting Cu_2O colloid was then interfaced in a second Y-shaped micromixer with a solution fed at flow rate of 9.25 mL/h and prepared by diluting 400 µL of Na_2S solution (320 mg/mL) in 60 mL of DDI water (Figure 2.2). PTFE tubing (0.8 mm ID) was used in the first stage with the appropriate length to reach a residence time (t_r) of 30 s. In the second stage, 1.5 mm ID PTFE tubing was used with different lengths to reach different residence times (5 to 30 min). A back pressure regulator (Zaiput Flow Technologies) was used for synthesis at temperatures above 100 ºC. Reaction temperature was maintained by immersing the tubing reactor in a temperature-controlled oil bath.

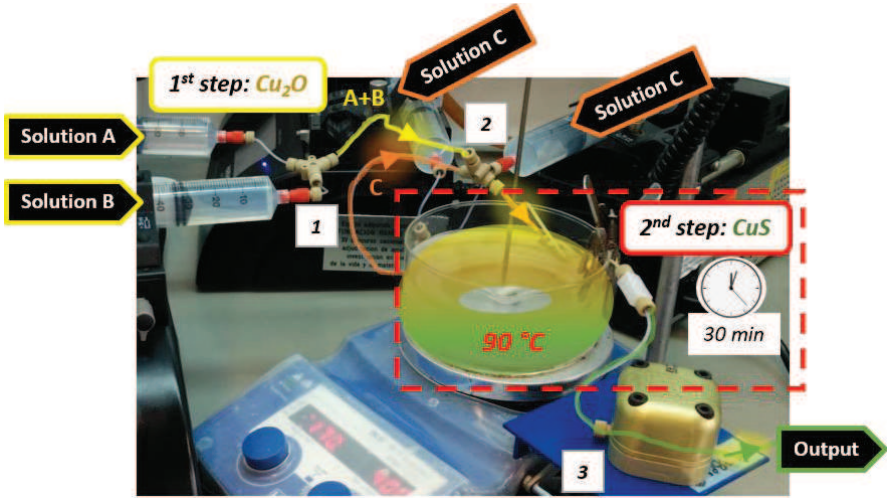

Figure 2.2: Microfluidic platform used for CuS NPs synthesis. Labels 1 and 2 represent the two Y-shaped micromixers connecting the initial point of the first and second synthesis stages. Label 3 shows the back pressure regulator (Zaiput Flow Technologies) used for synthesis at temperatures above 100 ºC.

2.3.2 *In vitro* studies

Cell culture, cytotoxicity assays and study of cell cycle have been carried out in the same way all along this PhD. For this reason, common details are described in Appendix I: I-Methods: Biological studies.

2.4 Results and discussion

2.4.1 CuS nanoparticles synthesis and characterization

As it was aforementioned, the optoelectronic properties of copper sulfide depend on the stoichiometry of its crystalline structure. Covellite (CuS) reaches the maximum excitation spectrum in the NIR region at 1050 nm, while the other crystalline phases like chalcocite (Cu_2S), djurleite ($Cu_{1.97}S$), digenite ($Cu_{1.8}S$) and anilite ($Cu_{1.4}S$) show minimal absorption at those wavelengths. Previous studies have shown how the maximum plasmon resonance, attributed to an in-plane dipolar-localized surface plasmon resonant mode [99], decreases with increasing *x* in $Cu_{2-x}S$ formula [100].

In photothermal therapy, NIR absorbing materials are selected to take advantage of the reduced absorption and scattering of biological chromophores, hemoglobin, and water in that region (Figure 2.3) and a deeper NIR light penetration in human tissues [101].

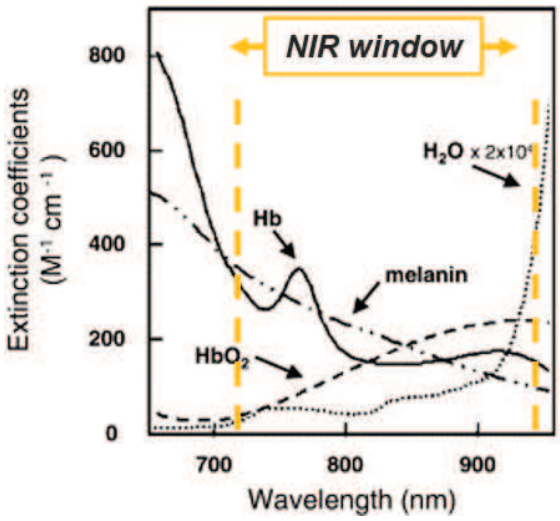

Figure 2.3: Visible and NIR absorption spectra of deoxyhemoglobin (Hb), hemoglobin (HbO_2), melanin and water (H_2O). Figure adapted from reference [102].

Initially, the morphology and absorption spectra of the resulting nanoparticles prepared in both microfluidic and batch reactors at different temperatures were analyzed to compare their optical properties. X-Ray diffraction (XRD) spectra of CuS nanoparticles synthesized with conventional batch reactor at medium (60 ºC) and high (120 ºC) temperatures are compared with the ones obtained using microfluidic reactors at 90 ºC and 30 minutes of residence time. In Figure 2.4 a), it is observed how the materials synthetized at 60 ºC show the characteristic diffraction planes of covellite phase, but the full width at half-maximum of the diffraction peaks decreased at 120 ºC indicative of an increased crystallinity. This sharp peak morphology is also achieved when CuS NPs were prepared in the microreactor platform, which suggests a higher covellite phase. This fact is confirmed looking at the absorption spectrum at the same concentration for both batch- and microreactor- produced samples. Figure 2.4 b) shows how the absorption peak of CuS NPs obtained in the microfluidic reactor at 90 ºC in only 30 min of residence time is similar to that of the materials synthetized in the conventional batch reactor at 120 ºC during 2 hours. However, CuS NPs synthetized during 30 min in the batch reactor at 90 ºC showed a 52% decrease in their maximum absorption.

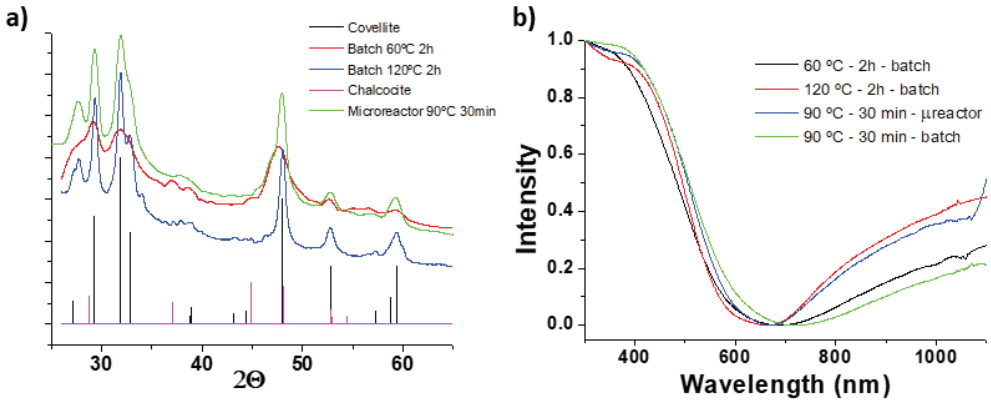

Figure 2.4: a) X-ray diffractograms of the materials obtained at different temperatures and the characteristic covellite and chalcocite Joint Committee on Powder Diffraction Standards (JCPDS) patterns; b) UV-vis absorption spectra of the materials obtained in both batch and microfluidic reactors

The formation of covellite is sensitive to a wide variety of synthesis variables such as pH, temperature, and solvents used. Depending of those variables it is feasible to obtain different non-crystalline Cu_xS_y phases [103]. Therefore, rapid mixing in microfluidic reactors allows to achieve a good control on fast-kinetic redox reactions, and crystallization processes; obtaining high crystalline phases in reduced times compared of those used required in conventional batch type reactors. EDS analysis for the CuS NPs produced in the microfluidic reactor rendered a Cu/S atomic ratio close to 1 (1.1 ± 0.1), similar to the one obtained after the synthesis at 120 ºC in a conventional batch reactor (Cu/S= 0.97 ± 0.1), but closer to 1 than that obtained in the batch synthesis at 60 ºC (1.27 ± 0.1). This fact also confirms that covellite was obtained during both microreactor and batch syntheses but it was achieved in the microfluidic system with a high purity and crystallinity as the synthesis temperature increased. XPS analysis also revealed that the oxidation state of the CuS was +1 in agreement with the previous literature [104].

As it as aforementioned in the experimental section, in this work, the selected CuS NPs reaction is based on hard-template-assisted technique using Cu_2O nanoparticles as a sacrificial template. Figure 2.5 a) and b) show the morphology of the sacrificial Cu_2O NPs with sponge-like morphology and homogeneous Cu distribution across the nanoparticle (Figure 2.5c)). After this sacrificed copper oxide NPs formation, the addition of sulfur produced hollow CuS NPs based on the Kirkendall effect. Sulfur diffuses into the Cu_2O

template particles at the same time that copper diffuses outward but at a slower rate than the sulfur. Thereby, the non-reciprocal diffusion between Cu and S ultimately renders the formation of an interior cavity. Figure 2.5 d) and e) depict CuS NPs produced after sulfur addition evidencing the formation of hollow nanostructures with a thin shell (~40 nm). The hollow structure was confirmed by the EDS analysis across a particle showing higher Cu concentrations in the external area (corresponding to the particle walls) and lower Cu concentration in the central area (Figure 2.5 f)).

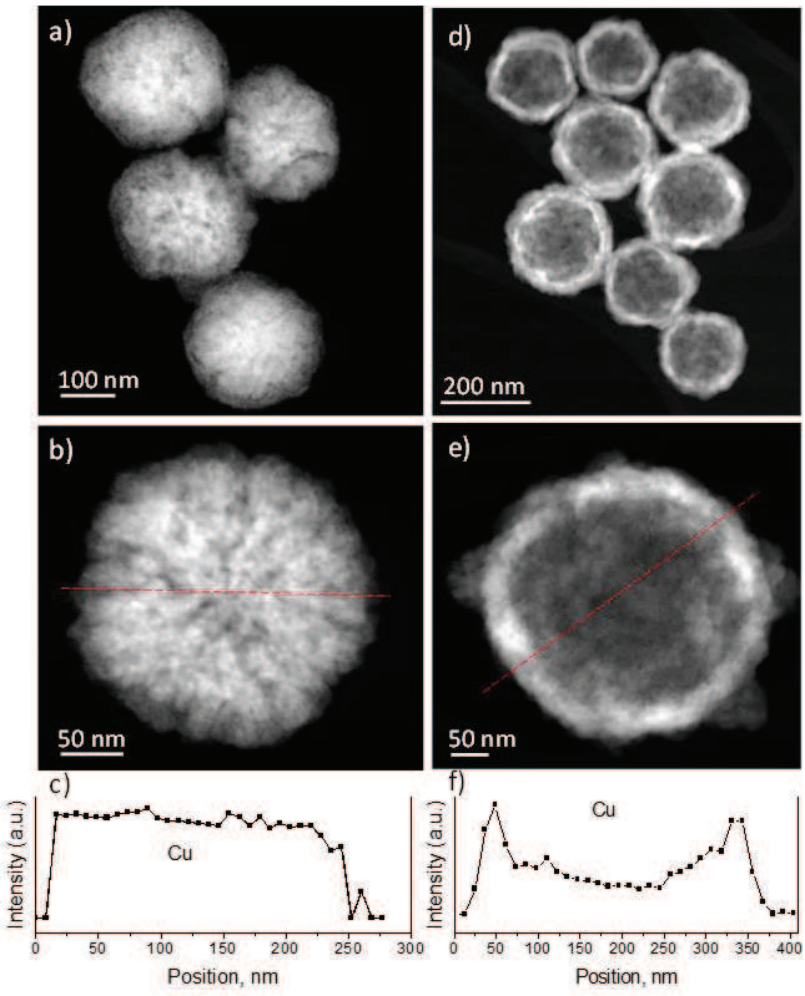

Figure 2.5: Morphological characterization of batch reactor produced CuS NPs at 60 ºC and 2 hours. STEM-HAADF images of a) and b) sacrificial Cu_2O NPs; d) and e) CuS NPs produced by Kirkendall diffusion. c) Cu EDS profile of the particle in b). f) Cu EDS profile of the NPs in e). Red dashed line depicts the location of the EDS profile.

Usually diffusion processes are slow (several to tens of hours under hydrothermal or annealing conditions) [105], and herein we demonstrate that microfluidics can overcome

those limitations. In agreement with the previous literature [106], an overall size increase was observed due to the Kirkendall effect varying the initial size of the Cu_2O NPs from 198 ± 37 nm to the final 208 ± 34 nm obtained for the resulting CuS NPs collected in the batch reactor at 60 ºC during 2 h. The hydrodynamic size of those CuS NPs (measured by DLS) was 164.1 ± 26 nm. Figure 2.6 shows how the morphology of the nanoparticles produced in both microfluidic and batch reactors is very similar but with the great advantage of the former of producing nanomaterials in a continuous manner and with 4-fold reduction in the crystallization time.

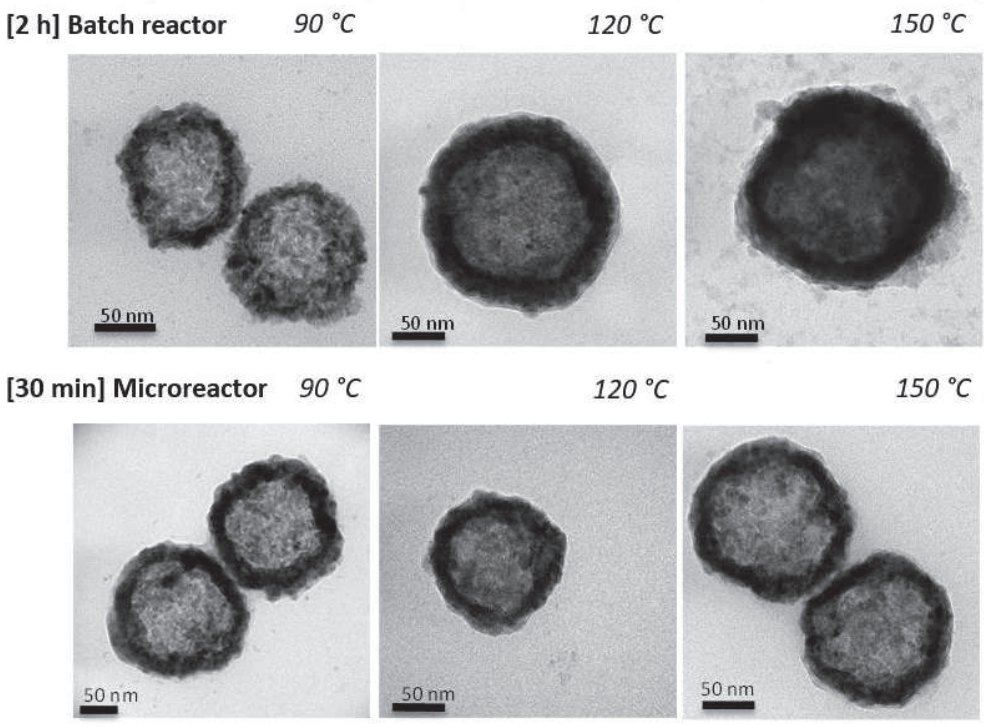

Figure 2.6: TEM images of the nanoparticles produced in both microfluidic and batch reactors under different temperatures.

To validate the potential applications in photothermal therapy, the heating efficiency of CuS NPs obtained by microfluidics synthesis was also evaluated. A colloidal CuS NPs suspension in water (0.05 mg/mL; 1 mL) was exposed to several irradiation cycles with a NIR laser (808 nm; 200 mW/cm^2) showing an increase of temperature close to 7 ºC after 10 minutes of irradiation. Figure 2.7 presents a fast temperature rise only slightly decreased after 20 successive cycles of irradiation (~2 ºC) probably caused by some degradation events.

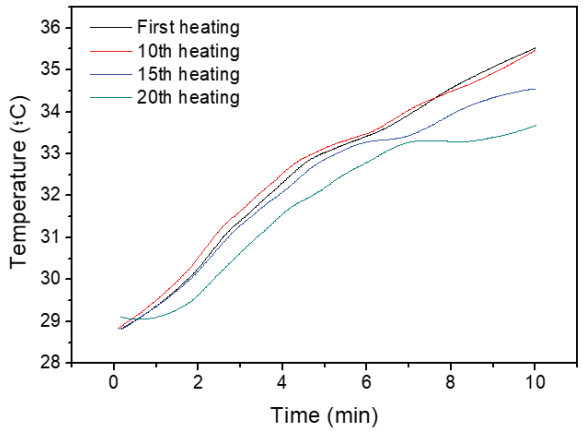

Figure 2.7: Photothermal heating rise of CuS NPs suspension (0.05 mg/mL; 1 mL) after successive laser irradiation cycles (200 mW/cm^2)

As it is depicted in Figure 2.8, most of the NPs after those 20 cycles kept their original morphology, although some fragmentation was observed in some areas of the sample. This effect was already observed by Guo et al. [42] who showed how polycrystalline CuS NPs disintegrate into single CuS crystals after laser treatment which can be directly related to the decrease of their photothermal efficiency.

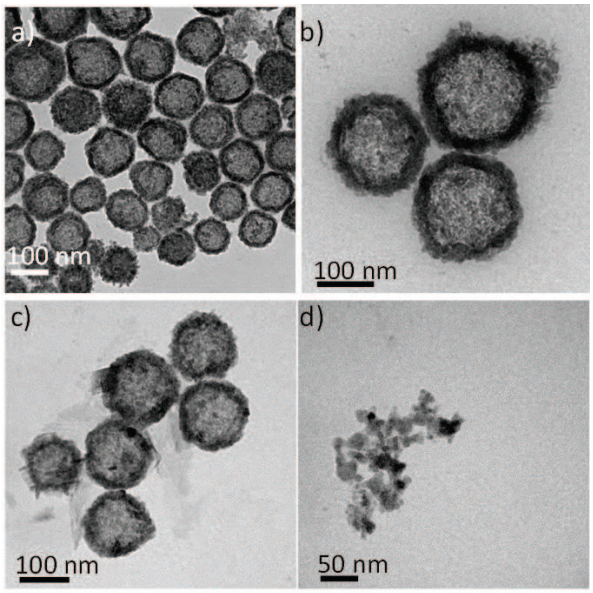

Figure 2.8: TEM images of CuS NPs obtained in the microfluidic reactor with t_r=30 min before (a and b) and after (c and d) 20 successive irradiation cycles.

For any biomedical application, a complete physiological biodegradation of the nanomaterial after use is advisable. Biopersistence is a concern when plasmonic nanoparticles are used for biomedical applications, and, as we mentioned before, CuS NPs in animal models have been demonstrated to degrade up to 90% of the injected dose, being mostly excreted following the hepatobiliary route [80]. In this sense, we characterized the degradation effects and subproducts after immersing CuS NPs in phosphate buffered saline (PBS) and other culture media including RPMI and DMEM (Figure 2.9).

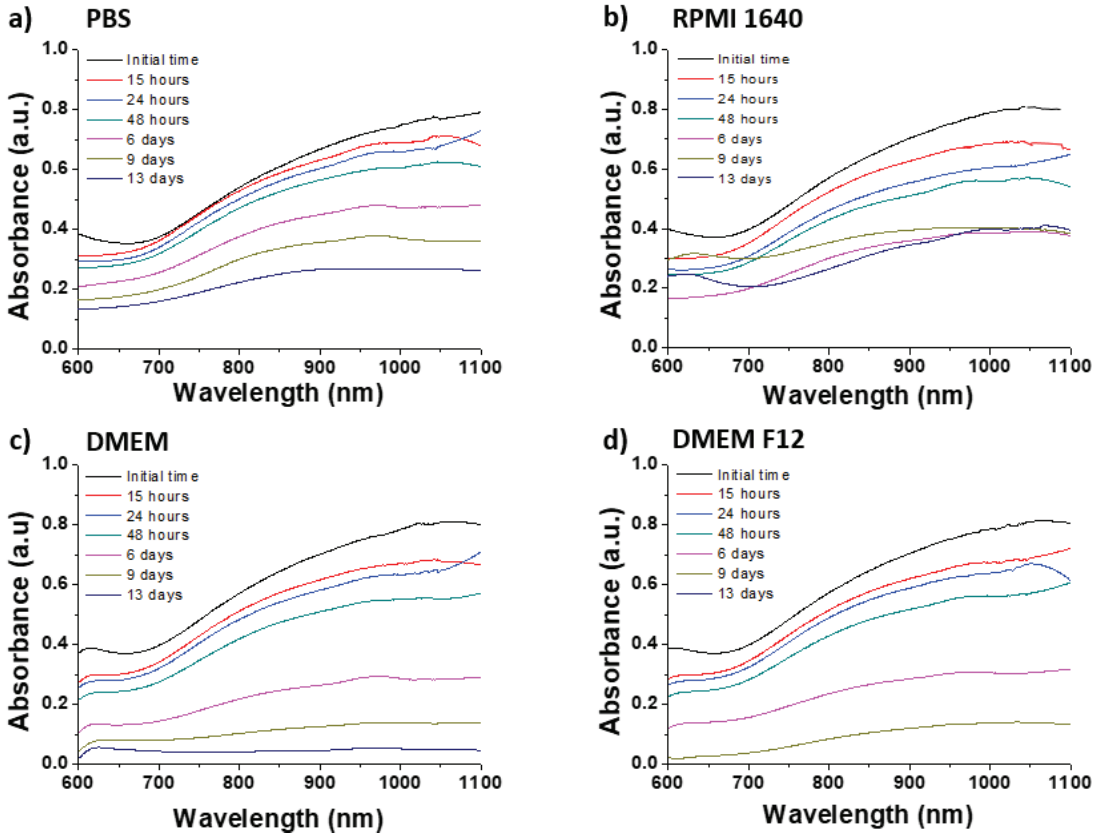

Figure 2.9: Absorbance evolution under simulated physiological conditions in four different cell culture media. A) Phosphate buffer saline (PBS); b) RPMI 1640; c) DMEM; d) DMEM F12.

In all cases, the plasmonic response of CuS NPs decreased over time, and this degradation was kinetically accelerated at higher temperatures, as shown in (Figure 2.10).

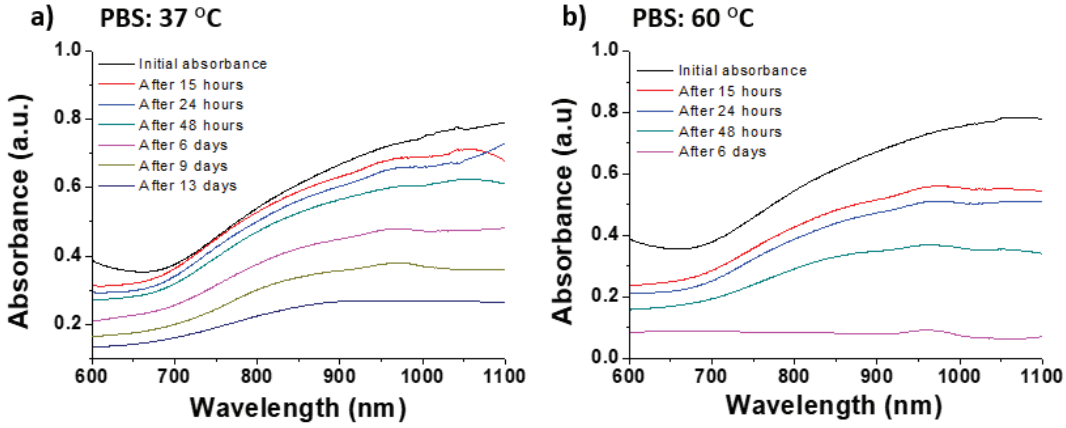

Figure 2.10: Temperature effect in degradation velocity of CuS NPs in PBS media at a) 37 ºC and b) 60 ºC.

The degradation process also has an influence in the color of the colloidal suspension of CuS NPs, directly related to their absorbance spectrum, and in their morphology. Figure 2.11 shows the color degradation of CuS NP samples before and after keeping them at 60 ºC for 6 days. The morphological changes after different aging conditions are presented in Figure 2.12.

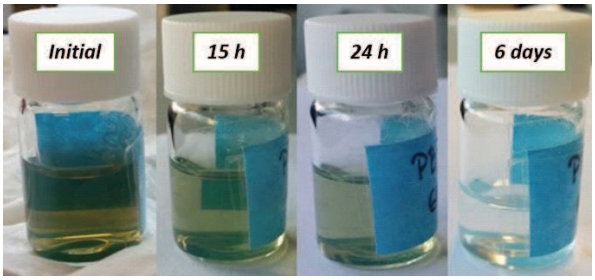

Figure 2.11: Images of the degradation process of colloid CuS after 6 days of aging at 60 ºC.

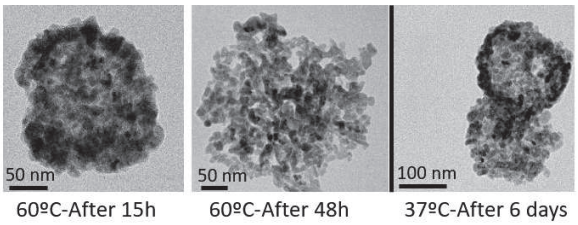

Figure 2.12: TEM images showing the morphology of the nanoparticles under different storage conditions.

Under those simulated conditions, CuS NPs are expected to degrade to form a mixture of water soluble sulfates such as chalcantite ($CuSO_4 \cdot 5H_2O$) and brochantite ($Cu_4SO_4(OH)_6$).

This analytical determination was qualitatively analyzed using precipitation techniques with barium chloride including sodium sulfate as control. Soluble sulfates (SO_4^{2-}) precipitate in presence of barium chloride because of barium sulfate formation, which is not soluble in water (Figure 2.13 a). On the other hand, when copper (II) ions are in an alkaline medium the formation of copper hydroxide generates a blue-green precipitate, observed in (Figure 2.13 b)) confirming the Cu^{2+} presence in the sample.

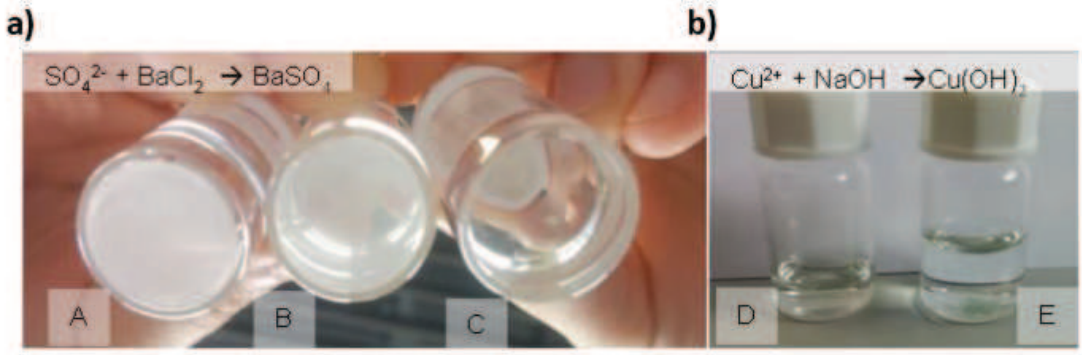

Figure 2.13: a) Sulfates precipitation in presence of barium sulfate using (A) Na_2SO_4 as control; (B) degraded byproducts from the CuS NPs under the presence of barium sulfate; (C) without barium sulfate; b) Precipitation of copper (II) ions with sodium hydroxide: degraded byproducts from the CuS NPs (D) without NaOH; I with NaOH.

XRD spectra of materials resulting from the degradation at 60ºC after 7 days in SBF (Figure 2.14 a)) corroborated the crystalline structure of copper sulfates, what was also observed under HRTEM electron diffraction (Figure 2.14 b) and c)).We can speculate that under physiological conditions CuS NPs would decompose and biodegrade to form water soluble copper sulfates.

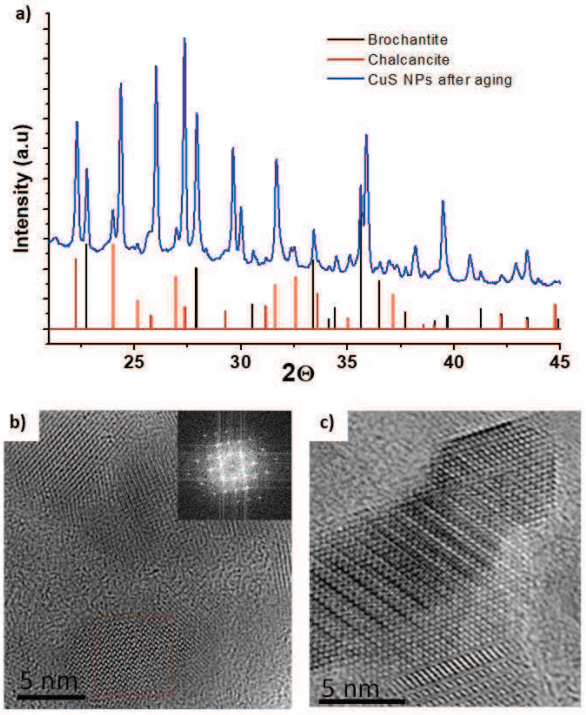

Figure 2.14: a) XRD spectra of resulting materials from degradation at 60 ºC after 7 days in SBF; b) HRTEM image showing polycrystalline nature of byproducts (inset DFT image); c) HRTEM image at higher magnification of the previous sample.

Copper ions are essential trace elements for the body involved in many metabolic functions. The liver is in charge of removing the excess of these ions via bile, and if that route were impaired, then some metabolites carry those ions and remove them via urine and bile [107].

2.4.2 Effect on cell viability, apoptosis and cell cycle

Four different cell lines (murine Mesenchymal stem cells (mMSCs); THP1 monocytes, THP1 macrophages and human fibroblasts) were tested in order to study the biocompatibility of CuS NPs obtained using microfluidic reactors (90 ºC, t_r = 30 min) at different levels. Figure 2.15 shows viability results obtained by the Alamar Blue assay at different CuS NPs concentrations (0.01 – 0.1 mg/mL). No significant viability decrease was observed at any of the concentrations tested, showing percentages over 73% in all cell lines studied.

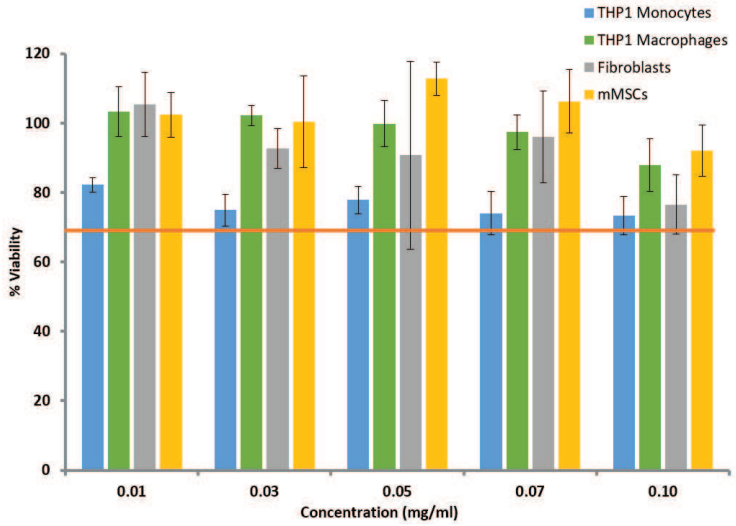

Figure 2.15: Cytotoxicity results of CuS NPs synthetized by microfluidic reactor evaluated by the Alamar blue assay after 24 h incubation. Mean and standard deviation of at least three experiments. The orange line represents the subcytotoxic concentration recommended by the ISO 10993-5 standard, which states a viability of 70 % as the threshold for considering non-cytotoxic concentrations.

For further studies, 0.1 mg/mL was considered as the subcytotoxic concentration following the recommendations given by the ISO 10993-5 standard in which viabilities higher than 70% are not considered cytotoxic. Cell apoptosis evaluation by flow cytometry showed the effects of CuS NPs on cell membrane and its results are depicted in Table 2.1. The addition of CuS NPs at subcytotoxic concentration (0.1 mg/mL) did not exert a significant harmful effect. Necrosis showed a maximum increase of 1.6% while apoptosis displayed an increase lower than 3.5% in fibroblasts and mMSCs and slightly higher percentage (< 12.6%) for phagocytic lines (macrophages and monocytes).

Table 2.1: Cell apoptosis evaluation by flow cytometry after 24 h of incubation with CuS NPs. Control samples (not treated cells) were established as background apoptosis level

	Fibroblasts		**Monocytes**		**Macrophages**		**mMSCs**	
	Control	CuS NPs	Control	CuS NPs	Control	CuS NPs	Control	CuS NPs
Necrosis	1.5%	1.6%	0.3%	0.8%	1.4%	3.0%	1.4%	0.9%
Late apoptosis	4.7%	4.7%	6.3%	17.6%	5.7%	9.0%	14.1%	17.6%
Early apoptosis	5.6%	7.1%	9.1%	10.4%	9.2%	16.4%	11.0%	10.9%
Viability	88.2%	86.6%	84.3%	71.3%	83.7%	71.6%	73.5%	70.7%

On the other hand, cell cycle distribution shown in Figure 2.16 did not show a significant change after CuS NPs incubation except for human dermal fibroblasts. All cell lines showed a slight decrease in G1 phase being more accentuated in fibroblasts, which also registered a considerable increase in G2 phase being almost the double of that obtained for control cells. However, as G1 and G2 percentages were very similar, it is not considered that CuS NPs have induced the arrest of the cell cycle or a damage in their DNA.

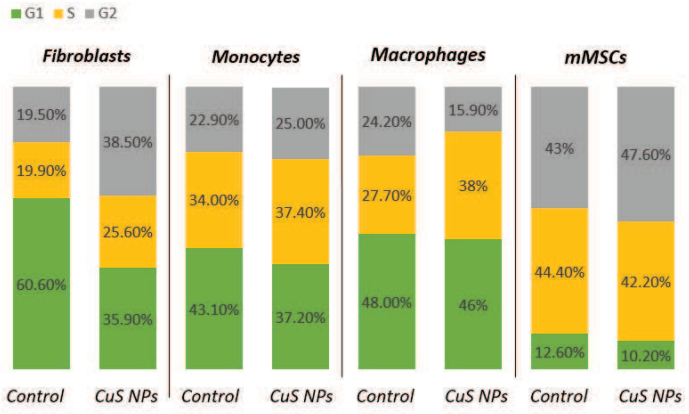

Figure 2.16: Cell cycle phase distribution for the four cell lines assayed after 24 h incubation with CuS NPs. Not treated samples (control) were also analyzed as basal cellular state.

Previous studies have shown similar effects in murine macrophages after treatment with hexagonal CuS nanoplates with an average edge length of 59.4 nm [108]. For the lowest concentration tested in this work (0.01 mg/mL), viabilities were reported close to the control sample for tumoral cells and for murine macrophages and a decrease around 10% was observed at 0.1 mg/mL, showing a more accentuated effect on human endothelial cells. These results agree with our studies where human macrophages displayed viability percentages higher than 87%.

Other studies corroborated high viability values (> 70%) at concentrations up to 0.4 mg/mL when CuS NPs were coated with bovine serum albumin-folic acid (BSA-FA) complex [109] or with DSPE-PEG2000 [110] in HeLa cells after 24 h, values which significantly decreased after NIR laser irradiation due to the photothermal effect. On the other hand, non-aqueous copper sulfide nanocrystals obtained from a continuous-flow millifluidic platform [97]exerted higher cytotoxic effects, decreasing the viability to 50% at lower concentrations (<0.003 mg/mL) in RAW264.7 mouse macrophages probably due to their

smaller size (< 30 nm) and the presence of L-glutathione (GSH) ligand on their surface. They also presented how this effect was enhanced after NIR laser irradiation due to the photothermal effect of CuS nanocrystals.

2.4.3 *In vitro* photothermal applications and ROS generation

The photothermal effect of CuS NPs at subcytotoxic doses (0.1 mg/mL) was studied in murine mesenchymal stem cells (mMSCs). After 24 h of incubation, samples were irradiated with a NIR diode laser (808 nm; 200 mW/cm^2) under the skin tolerance threshold 330 mW/cm^2 at 808 nm[111] for 20 min. Cell viability was observed by fluorescence microscopy through the double-staining procedure mediated by the LIVE/DEAD Viability/Cytotoxicity test. No cell viability reduction was depicted when NPs were not present in the sample (Figure 2.17 c) and g)). However, a reduced viability was observed when cells were irradiated in the presence of CuS NPs (Figure 2.17 d) and h)).

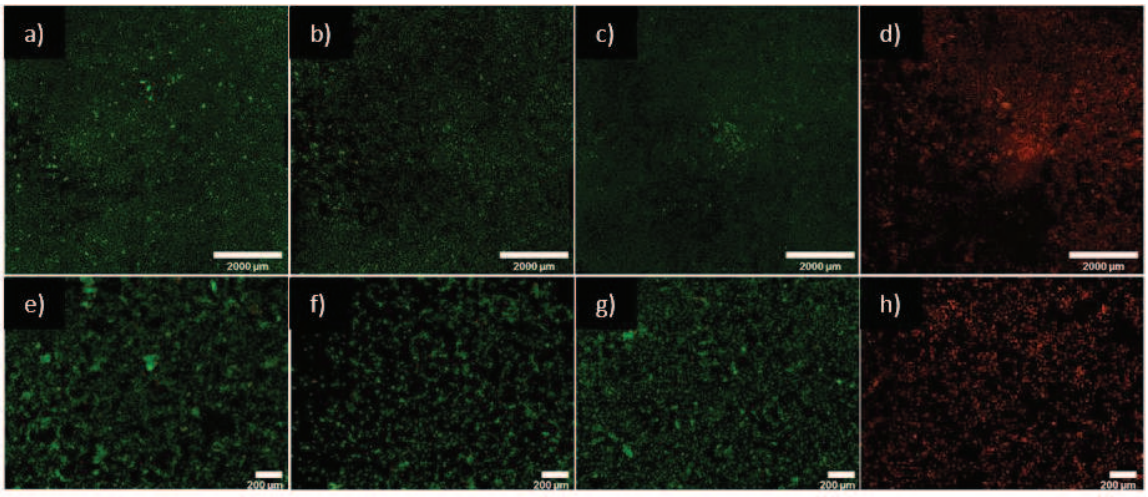

Figure 2.17: Photothermal effect on mMSCs. Upper row presents the complete cell culture well (4X magnification), while lower row focus on individual fields of each sample (4X magnification). A,e) mMSCs without CuS NPs treatment or laser irradiation; b,f) mMSCs treated with CuS NPs but no laser irradiation; c,g) mMSCs without CuS NPs incubation and irradiated; d,h) mMSCs incubated with CuS NPs and laser irradiated. Laser irradiation conditions: 808 nm, 200 mW/cm^2 for 20 min. Live cells are represented in green and dead cells are stained in red.

Finally, dihydrorhodamine 123 (DHR123) was selected as model component in order to decouple the photothermal effect from the photodynamic effect of the resulted CuS NPs. DHR123 is a non-fluorescent probe that does not degrade under heating conditions but it is easily oxidized to Rhodamine 123 in presence of reactive oxygen species (ROS). Due to the

fluorescence properties of Rhodamine 123 (Excitation wavelength: 485 nm; Emission wavelength: 530 nm), its degradation can be easily measured using fluorescence spectroscopy. Four different samples were selected in order to test the photodynamic effect of CuS NPs by measuring the fluorescence intensity of the resulted samples: DHR123; DHR123+CuS NPs; DHR123+CuS NPs heated; and DHR123+CuS NPs irradiated. With the aim to reproduce the heating conditions of irradiated samples: 1 mL of CuS NPs dispersion (0.05 mg/mL) in ethanol was irradiated (808 nm; 200 mW/cm^2). A temperature rise of 37 to 68 ºC in 4 minutes (7.75 ºC/min) was obtained and further used for non irradiated but heated samples. Figure 2.18 a) shows the fluorescence spectra for DHR123 (250 µL; 6.6 µM) ethanol solution combined with CuS NPs (0.05 mg/mL) at initial time and after 5 minutes. A clear increase in fluorescence was observed which was enhanced when the temperature increased and when the solution was irradiated with the NIR laser. Figure 2.18 b) presents the 530 nm absorbance peak intensity of a heated DHR123 solution; and the CuS-DHR123 solution heated and irradiated. Here, it can be observed how the presence of CuS NPs induced DHR123 oxidation to Rhodamine 123 depicted in the presence of the absorbance peak at 530 nm. Moreover, the intensity of this effect was more than 2-fold (x 2.02) enhanced when laser irradiation was applied due to higher ROS generation.

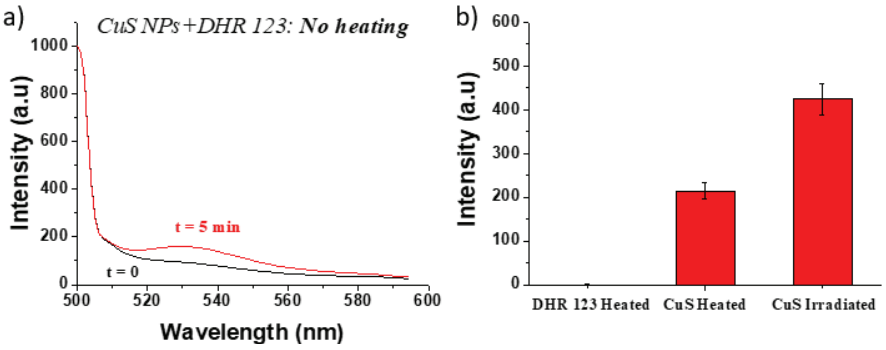

Figure 2.18: a) Fluorescence spectra of DHR123 chromophore incubated with CuS NPs. Black line represents the initial fluorescence intensity of the sample, while red line presents the measurement of the fluorescence intensity after 5 minutes of incubation at room temperature without laser irradiation. B) Intensity fluorescence at 530 nm of three different samples of DHR123 probe with and without CuS NPs.

All these results point to the biocompatibility of CuS NPs obtained by microfluidics and highlight their potential in clinical applications as components of therapeutic carriers, as

well as both as photothermal and photodynamic nanoparticulated photosensitizers in the treatment of malignant cells.

2.5 Conclusions

The possibility to synthesize CuS nanoparticles in continuous flow by using a simple microfluidic reactor was demonstrated. Operating in a continuous manner, CuS nanoparticles were obtained with a 4-fold reduction in the synthesis time compared to the one required when using conventional batch reactors having the resulting nanoparticles similar physicochemical characteristics. Under simulated physiological conditions, the degradation of CuS nanoparticles into soluble copper sulfates was confirmed, highlighting the great advantage of those materials compared to other conventional non-degradable plasmonic nanomaterials such as gold nanostructures or carbon-based nanoparticles. Subcytotoxic doses were established using the Alamar blue assay. Cell apoptosis and cell cycle were tested using flow cytometry showing no significant changes at subcytotoxic concentrations compared to the basal levels of untreated cells. Furthermore, *in vitro* photothermal effects and ROS generation were verified showing a potential use of those nanomaterials in the biomedical field.

Those biodegradable copper sulfide nanoparticles having excellent plasmonic properties were used to develop some of the hybrid polymer-inorganic drug delivery vectors described in the following chapter.

CHAPTER III

HYBRID NANOPARTICLES

"You never change things by fighting against the existing reality. To change something, build a new model that makes the old model obsolete"

Richard Buckminster Fuller, Architect and Systems theorist (1982)

Chapter III

HYBRID NANOPARTICLES FOR TRIGGERED DRUG DELIVERY

Summary

In this chapter, three different approaches to obtain hybrid drug delivery vectors for triggered on demand drug delivery were studied:1) Inorganic biodegradable CuS nanoparticles surface functionalized with a cleavable thermoresponsive polymer; 2) thermoresponsive PNIPAm nanogels decorated with hollow gold nanoparticles (HGNPs); and 3) customized PNIPAm nanoparticles synthetized in a microfluidic platform encapsulating HGNPs and a drug of interest. Bupivacaine has been used as a model drug and the synthesis, full physicochemical characterization and cytotoxicity analysis have been carried out for each approach.

3 Hybrid nanoparticles

Active drug delivery vectors are the future approach to smart drug administration to minimize undesired side effects. These novel devices are capable of regulating the supply of their payload depending on the biological needs of the patients[112]. In this sense, injectable hybrid biomaterials have become an interesting alternative for *in situ* delivery of therapeutic compounds through diffusion or degradation processes[113]. In some pathologies such as hormone disorders or chronic pain, a time- and site-specific drug administration is preferred over a sustained therapeutic dosage. These conditions demand a rapid and transient release of a certain amount of drug molecules after a programmed off-release period[114]. Controlled drug release systems release their entire payloads passively, or alter their release patterns in response to stimuli such as temperature, pH, ionic strength, or the presence of a specific protein or enzyme. These systems have enabled drug delivery with constant release profiles, and, in some cases, a release that is localized to a specific anatomic or physiologic location; such advances have improved drug effectiveness and reduced systemic toxicity. Some drug delivery systems are triggered by externally-applied stimuli such as light, ultrasound and electric or magnetic fields. These systems could be particularly useful for (a) achieving complex drug release profiles, (b) modulating release rates and timing according to patient needs, or (c) localizing release to a specific site, although on-demand systemic delivery can also be achieved, depending on the implementation.

An ideal device for long-term on-demand drug delivery should safely contain a large quantity of drug, release little or no drug in the “off” state, be repeatedly switchable to the “on” state without exhibiting degradation of performance, and be triggered non-invasively to accurately release the drug dosage demanded by a patient (e.g. local pain relief) or prescribed by a doctor (e.g. localized chemotherapy). Despite the clinical need, few such drug delivery devices have been developed and none are available for clinical use. The goal of this thesis is to develop hybrid nanoparticles that could provide tuneable on-demand drug release with an appropriate external trigger.

Here, we present three different hybrid thermoresponsive polymer-inorganic vectors capable to be triggered under NIR laser radiation in order to accomplish these pulsatile drug delivery needs.1) Completely cleavable hybrid nanoparticles composed by a cleavable

polymer and biodegradable CuS NPs developed in previous works of this thesis are described including their synthesis, characterization, drug release profiles and cytocompatibility. 2) Electrostatically stable hybrid HGNPs@PNIPAm nanogels loaded with bupivacaine as a model drug are presented as well, as novel approach for laser-activated and controlled drug delivery and their *in vitro* characterization. 3) Finally, a novel microfluidics platform for continuous production of customized hybrid drug-loaded PNIPAm@HGNPs microparticles by photopolymerization is described together with their full characterization, laser-activated response, drug delivery profiles and *in vitro* cytocompatibility.

3.1 Cleavable hybrid nanoparticles[1]

3.1.1 Introduction

External stimuli activation of drug delivery vectors has become the focus of attention for many researchers interested in biomedical nanotechnological applications. Magnetic fields[115][116], ultrasounds[117][118] and near infrared (NIR) radiation[119][120] are the main externally applied physical triggers used to timely activate drug release from nanoparticulated carriers in a specific target. These vectors can be selectively directed towards a specific area in the body and upon physical excitation they can transduce the incident electromagnetic wave into heat, which provokes a change or breakup of the vector releasing the transported drug. Those vectors are composed of a hybrid material, which is able to generate heat upon absorption of a specific electromagnetic radiation and also shows thermal responsiveness and hosts the transported drug.

Poly(N-isopropylacrylamide) (PNIPAm) is one of the most commonly used 43rimeth-responsive polymer due to its tuneable and stable lower critical solution temperature (LCST)[119][121][122][123][124]. Recent studies have demonstrated its

[1] The contents of this section were adapted from the following published work:

Ortiz de Solorzano, I.*, Alejo, T., Abad, M., Bueno-Alejo, C., Mendoza, M., Andreu, V., Irusta, S., Sebastian, V., Arruebo, M.

"Cleavable and thermo-responsive hybrid nanoparticles for on-demand drug delivery"

Journal of Colloid and Interface Science, 533 (**2019**): p. 171−181

application in drug delivery including intracellular cancer treatment[125][126] thanks to its temperature-dependent reversible switchable nature. For instance, Sheng et al.[127] corroborated the *in vivo* enhancement of the antitumoral effect of doxorubicin loaded in hybrid magnetic Fe_3O_4@PNIPAm nanoparticles compared to the effect of the free drug. Moreover, adjusting the polymer transition temperature below the body temperature, a jellification effect can be achieved in order to address different biomedical needs such as *in situ* bone repair[128] or the isolation of post-operative wounds from cellular adhesion[129]. In addition, another thermosensitive copolymer based on macromonomers of oligo (ethylene glycol) of different chain-lengths (i.e., poly(ethylene glycol) methyl ether methacrylate, POEGMA) shows very interesting advantages compared to PNIPAm. On the one hand, the transition temperature of this polymer can be varied and adjusted depending on the ratio of the monomers used, its hydrophobic content, and on the final molecular weight of the polymer[130]. This 44rimeth-responsive polymer is mainly composed of biocompatible oligo(ethylene glycol) segments that share the biocompatibility of poly(ethylene glycol) (PEG): non-toxicity and anti-immunogenicity[131][132]. PEG is not accumulated in the body because depending on its molecular weight it is eliminated unaltered via urine or faeces[133]. Furthermore, OEGMA-based copolymers can be degraded into short oligomers by hydrolysis, reaction that can be catalyzed by enzymatic activity[134]. On the other hand, PNIPAm nanogels can be synthetized with biodegradable crosslinkers for promoting their fragmentation in drug delivery applications[135], but its backbone chains, instead, do not degrade under physiological conditions[136] and monomer leftovers from their synthesis or generated by depolymerisation reactions can be potentially toxic[137][138].

Until now, several classes of nanoparticles have been attached or grafted with a 44rimeth-sensitive layer of PNIPAm: ranging from organic nanoparticles such as liposomes[139][140] to inorganic magnetic[141][142] or plasmonic[119][143] nanoparticles being the later sensitive to an external physical stimuli, acting as transducers. Among them, plasmonic nanoparticles such as hollow gold nanoparticles or gold nanorods have been widely used in photothermal therapy because of their reduced size, NIR-responsiveness and their biologically inert ability.

Polymer biodegradable nanomaterials for biomedical applications have been widely studied. They have incredible advantages in drug delivery applications[144], intracellular cancer treatment[145] and tissue engineering[146][147]. Nevertheless, the inorganic part of many drug delivery vectors usually do not biodegrade and they may bio-accumulate in the body[148][149]. In order to overcome this limitation, copper sulphide nanoparticles (CuS) appear as promising substitutes thanks to their enhanced biodegradation under physiological conditions and consequent lack of bioaccumulation[42] as it has been shown in Chapter II of this thesis dissertation. Copper sulphide nanocrystals have excellent plasmonic absorption properties in a wide NIR region because of their semiconductor properties[62] which have been applied in different biomedical scenarios[150]. Besides, they show a comparably easy synthesis, high colloidal stability, high photothermal efficiency (up to 22-60%)[71] and assured biodegradation. In this regard, Guo et al.[151], observed that CuS polycrystalline nanoparticles disintegrated into CuS crystals before completely disappear because of their degradation process. In Chapter II, we identified the biodegradation subproducts (i.e., water soluble copper sulphates) generated after several days under simulated physiological conditions. The functionalization of this kind of semiconductor nanoparticles with a PNIPAm-based thermosensitive coating has been previously carried out by Huang et al.[152] and their encapsulation in OEGMA based nanogels was recently developed by Meng et al.[153]; however, in these cases, the polymers did not present any cleavable bonds.

Moreover, in our case the long-acting local anaesthetic bupivacaine was selected as a model drug for carrying out light-triggered release studies. Side effects associated to the use of pain killers after surgery are very common[154] and in order to minimize them there is an increased interest associated to the use of controlled release systems[155]. To name just a few, poly(lactic-co-glycolic) acid (PLGA) biodegradable nanoparticles[156][13], liposomes[157], hydrogels[158], inorganic microparticles[159] and organic nanoparticles based on proteins, lipids and sugars[160] have been used as carriers in order to achieve a controlled and local release of bupivacaine. Only a few works describe the use of photo-triggered release systems of this anaesthetic drug[161] and, to the best of our knowledge, none of them describe a cleavable carrier with on-demand release ability which fragmentation by-products could potentially be eliminated unaltered from the body. Degradation or elimination is needed to avoid materials bioaccumulation and to further

progress in this area of research. Different poly oligo(ethylene glycol) copolymers have been combined previously with non-biodegradable inorganic nanoparticles like plasmonic gold NPs[162], fluorescent quantum dots[163], magnetic iron oxide NPs[164] or silica nanocomposites[165].

3.1.2 Objectives

In this section of chapter 3 it is described the synthesis of a novel amine terminated P(MEO_2MA-co-OEGMA) and its grafting on the surface of plasmonic copper sulphide nanoparticles leading to a cleavable 46rimeth-responsive nanocomposite able to host an anesthetic drug which release can be activated on-demand after light excitation.

3.1.3 Experimental

3.1.3.1 Synthesis of amine-terminated initiator

An amine initiator was prepared according to a previously reported protocol[166]. Diaminoethane (4 g, 0.066 mol) was dissolved in 20 mL of 1,4-dioxane under stirring, after that, a solution of di-*tert*-butyl dicarbonate (1.94 g, 9 $x10^{-3}$ mol) in 20 mL of 1,4-dioxane was added at room temperature to the former solution using a syringe pump at a flow rate of 1 mL/min. The reaction was kept under stirring during 48 h; afterwards a white precipitate was obtained. This precipitate was filtered off and the excess of solvents removed by evaporation. The water-insoluble byproduct, having both amines protected by the tert-butyloxycarbonyl protecting group (BOC group), was removed from the crude by filtration. Dichloromethane was used to extract the product from the aqueous phase, which was saturated with sodium chloride. Dichloromethane was dried using sodium sulfate and removed by evaporation using a rotary evaporator to obtain tert-butyl-N-(2-amino-ethyl) carbonate. 2-Bromoisobutyryl bromide (1.15 g, 5 mmol), was added drop by drop to a solution of tert-butyl-N-(2-amino-ethyl) carbonate (0.8 g, 5 mmol) and 46rimethylamine (0.51g, 5 mmol) in 8.2 mL of dry dichloromethane under stirring in an ice/water bath. The reaction was left to complete during 48 h at room temperature. After that, the precipitate obtained was filtered off, and the solvent was removed under vacuum. The product dissolved in methanol was precipitated with water saturated with Na_2CO_3 to obtain the amine initiator.

Characterization was carried out by Proton Nuclear Magnetic Resonance (^{1}H-NMR) spectroscopy carried out on a Bruker AV-400 spectrometer operating at 400 MHz using $CDCl_3$ as solvent.

H^1-NMR spectral data used were ((D_6) DMSO): d= 1.38 ppm ((C**H**$_3$)$_3$C-), 1.86 ppm ((C**H**$_3$)$_2$C-), 3.2 ppm (-C**H**$_2$-NH-COO-), 3.12 ppm (-C**H**$_2$-NH-CO-), 6.8 ppm (-CH$_2$-N**H**-COO-), 8.0 ppm (-CH$_2$-N**H**-CO-).

3.1.3.2 Synthesis of amine-terminated P(MEO2MA-co-OEGMA500) thermosensitive polymer

The thermosensitive polymer here reported was synthesized through a procedure previously developed by our group[167]. Briefly, 1.65 g MeO_2MA and 0.6 g $OEGMA_{500}$ (88/12 molar ratio) were mixed with 0.16 mg of $Ir(ppy)_3$ in 5.8 mL of anhydrous ethanol. The solution was introduced in a Schlenk tube together with 30 mg of the as-prepared amine initiator previously degassed with argon. Photopolymerization was carried out with a LED (UV: 365 nm; radiant flux 4.6 W 47rimeth.) during 8 h under vigorous stirring. After the reaction was completed, ethanol was separated through evaporation and the polymer obtained was dispersed in water, purified by dialysis and lyophilized. In order to unprotect the amine group of the polymer, 800 mg of the dried product were dissolved in 3 mL of dichloromethane. 3 mL of trifluoroacetic acid and dichloromethane (1:1) were added dropwise to the polymer solution and mixed during 4 h under stirring. The solution was neutralized by adding triethlylamine and concentrated by evaporation. The final product was precipitated with hexane, dissolved in water and purified by dialysis (14 kDa cut-off).

Characterization was carried out by Fourier Transformed Infrared Spectroscopy (FTIR) with a Vertex 70 (Bruker) having an ATR Golden Gate accessory and by Proton Nuclear Magnetic Resonance (^{1}H-NMR) spectroscopy carried out on a Bruker AV-400 spectrometer operating at 400 MHz using $CDCl_3$ as solvent. The cloud points of DI water polymer solutions (3 mg/mL) were obtained from the optical transmittance measurements at 670 nm varying the temperature using a Varian Cary® 50 UV-Visible spectrometer (Agilent Technologies, USA) equipped with a fiber optic dip probe. The temperature at which 50% of the transmittance was reached[168] was selected as the lower critical solution temperature (LCST) of the resulting polymer.

A simulated accelerated degradation was used to evaluate the cleavage of the polymeric side chains of the P(MEO2MA-co-OEGMA500). In this regard the polymer was dispersed in water and heated at 40ºC during 7 days using H^1 NMR to evaluate its evolution.

3.1.3.3 Synthesis of copper sulphide nanoparticles

The synthesis and characterization of CuS NPs was carried out as described in Chapter II Section 2.3.1 (page 20) of this thesis.

3.1.3.4 Synthesis of hybrid CuS-P(MEO2MA-co-OEGMA500) nanoparticles

Hybrid polymer-inorganic nanoparticles were obtained by mixing CuS NPs and P(MEO_2MA-co-$OEGMA_{500}$) amine polymer at 1:1 wt. ratio in a water solution during 3 h under vigorous stirring and purified by several centrifugation steps.

The final nanoparticles obtained were again characterized by UV-Vis spectroscopy, DLS, Z-potential, TGA, FTIR, TEM and STEM-HAADF in the equipment mentioned above. Diluted phosphotungstic acid solution was used as contrast agent for allowing polymeric coating electronic visualization in all CuS-P(MEO_2MA-co-$OEGMA_{500}$) nanocomposite samples. Gel Permeation Chromatography (GPC) studies were carried out using a Waters Alliance 2695 HPLC with an evaporative light scattering detector (Waters 2420) and Plgel 5µm MIXED-C Aglilent columns (7.5 mm x 300 mm), using THF (HPLC grade) as eluent (flow 1 mL/min). Calibration was made with poly(methyl methacrylate)-based standards. Samples were prepared by dissolving 2 mg of product in 2 mL of THF (HPLC) and filtering them using a 0.2 micron PTFE filter.

Thermogravimetric analysis (Mettler Toledo TGA/STDA 851e) on the resulting nanoparticles was used to evaluate the polymeric content in the hybrid nanoparticles. Samples were analyzed in a N_2 atmosphere (gas flow 50 mL/min) between 30 and 800 °C with a heating rate of 20 °C/min. Also, their photothermal properties were measured after laser irradiation. A dispersion of CuS-P(MEO_2MA-co-$OEGMA_{500}$) NPs (1.8 mg/mL in 1 mL) kept at 37 ºC in an incubator was irradiated with an 808 nm laser at 1.89 W/cm^2 in a 24-well cell culture plate. Once the dispersion reached 45 ºC, the laser was shut down and the sample was cooled without external convective cooling until reaching 37 ºC. The temperature

was measured with a thermocouple during all the process in a representative point far enough from the laser spot reach.

3.1.3.5 Bupivacaine loading and release

Bupivacaine was loaded by incubating the nanoparticles previously described at a concentration of 1.6 mg/mL in an aqueous bupivacaine solution (320 ppm) for 4 h. The resulting nanoparticles were washed twice before carrying out the release studies in order to eliminate the non-bound drug. Controlled release studies were developed in 1mL of DI water containing 1.6 mg/mL of the bupivacaine-loaded nanocomposites stirred at 37 ºC or 45 ºC, respectively. At selected times the samples were washed through centrifugation, the supernatants were lyophilized and dissolved again in ethanol before measuring the bupivacaine content through Ultra Performance Liquid Chromatography (UPLC; ACQUITY UPLC H-Class system with a PDA detector, Waters). This process was followed in order to concentrate bupivacaine content in the samples and improve drug detection in the UPLC equipment. Dexamethasone was used as internal standard.

Photothermally-triggering experiments were conducted using the same conditions that previous drug-release experiments. However, at selected times an irradiation with an 808 nm laser at 1.89 W/cm^2 was carried out producing a rapid temperature rise from 37 ºC to 45 ºC in 2 minutes. The amount of released bupivacaine under those conditions was again measured by UPLC.

Cumulative data obtained from the drug release analysis were fitted to mathematical models to explain the mechanism controlling drug delivery. Correlation coefficients I were determined from the linear regressions to fit zero order and Higuchi models.

3.1.3.6 *In vitro* studies

Cell culture, cytotoxicity assays and study of cell cycle have been carried out in the same way all along this PhD. For this reason, common details are described in Appendix I: I-Methods: Biological studies.

3.1.4 Results and discussion

3.1.4.1 Amine-terminated P(MEO_2MA-co-$OEGMA_{500}$) polymerization

The copolymer of oligo (ethylene glycol) methyl ether methacrylate (OEGMA) and di (ethylene glycol) methyl ether methacrylate (MEO_2MA) was synthetized by following a photochemical polymerization previously reported by our group [167]. However, some interesting modifications were introduced in order to obtain amine-functionalized polymeric chains. The methyl 2-bromopropionate (MBP) initiator was substituted for a synthetic amine-terminated initiator produced following the work of Brett et al.[166].

FTIR measurements confirmed the chemical structure of the polymer. Figure 3.1 a) shows the most important infrared absorption bands of the polymer: the band at 2880 cm^{-1} is ascribed to the C-H stretching vibrations; the sharp peak at 1720 cm^{-1} is attributed to the stretching of C=O groups present in the polymeric chains; and the intense peak at 1109 cm^{-1} is related to C-O-C stretching vibrations [169].

Moreover, ^{1}H-NMR studies demonstrated the presence of amino end groups in the polymeric chains. Figure 3.1 c), shows the principal resonance peaks of the obtained amine-terminated polymer. Several peaks represent the amino end group of the polymeric chain. The ones labeled as h and I present at 3.56 ppm and 3.38 ppm, respectively correspond to protons of (N-CH_2-C-) groups; the peak attributed to the protons of the amine end group j (C-NH_2) was assigned at 1.25 ppm together with the peak f, which represents the CH_3 groups. Finally, we observed that the amide proton (R-CO-NH-R) dissolved in a protic deuterated solvent, exchanged with the deuterium hydrogen leading to a complete disappearance of the peaks, which is in agreement with previous literature[170]. The peaks at 4.1, 3.5-3.7 and 3.4 ppm correspond to the principal chain protons of the chemical groups labeled as c (CH_2-CH_2-O), d (-CH_2-O-) and e (-OCH_3), respectively and peaks labeled as a, 1.81-1.78 ppm, and b, 1.05-0.89 ppm were assigned to the first and second protons of (-$CH_2C(CH_3)$), respectively.

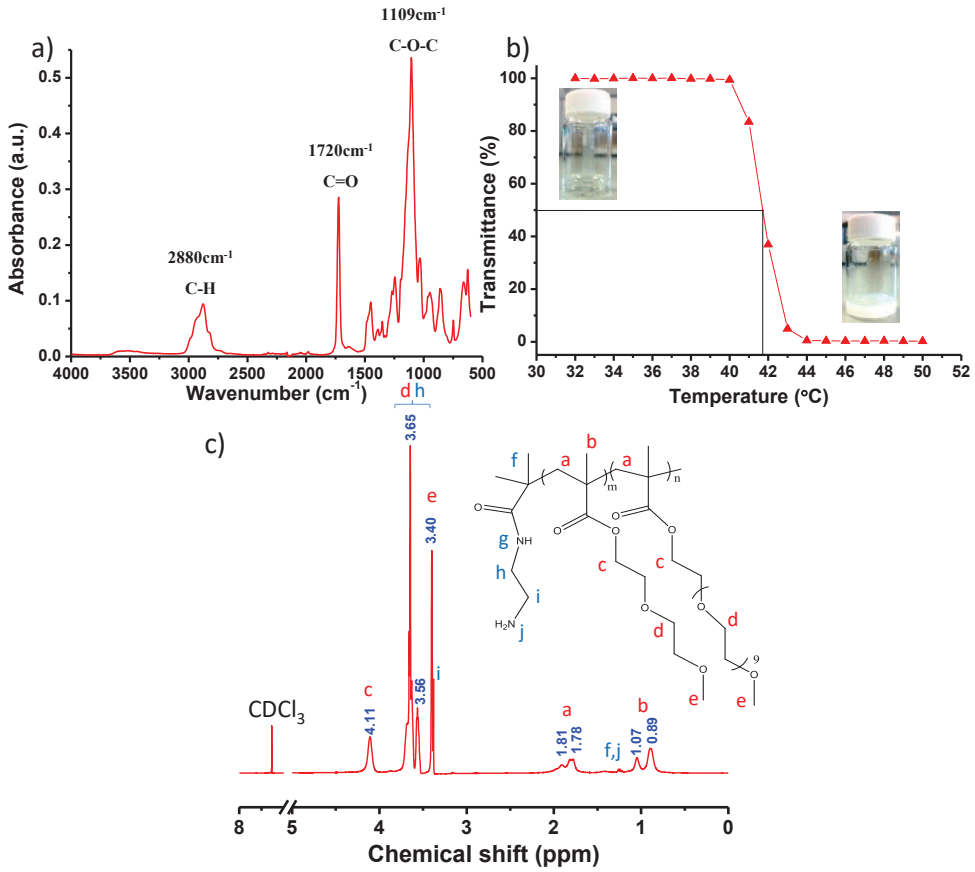

Figure 3.1: P(MEO_2MA-co-$OEGMA_{500}$) amine characterization: a) FTIR spectra; b) Cloud-point measurement by the transmittance curve (3mg/mL); c) ^{1}H-NMR spectrum in deuterated chloroform ($CDCl_3$).

Temperature dependence with the optical transmittance measured at the wavelength of 670 nm showed a polymer lower critical solution temperature (LCST) of 42 ºC having a sharp slope. Figure 3.1 b), shows the transmittance curve of a polymeric dispersion of 3 mg/mL in water.

3.1.4.2 Nanocomposite synthesis

Hollow CuS NPs covellite-based crystalline structure facilitates a large light absorption in the NIR region and its efficient transduction into heat. These nanoparticles were characterized by TEM and FTIR (Figure 3.2).

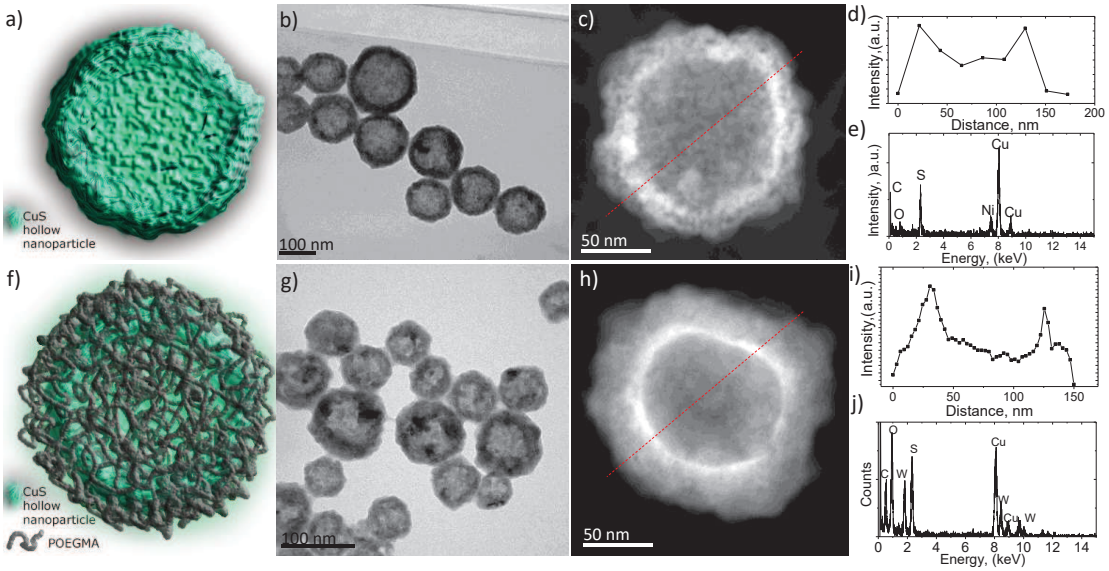

Figure 3.2: CuS-P(MEO_2MA-co-$OEGMA_{500}$) nanoparticles characterization. A) and f) show an scheme of the nanoparticles without and with the P(MEO_2MA-co-$OEGMA_{500}$) polymer, respectively. B) and g) are TEM images of CuS nanoparticles without and with the polymer coating respectively. C), d) and e) represent STEM-HAADF images, profile and spectra of CuS nanoparticles. Comparatively, h), i) and j) are the STEM image, profile and spectra of CuS-P(MEO_2MA-co-$OEGMA_{500}$) nanocomposites.

The amine-terminated 52rimeth-responsive polymeric chain was coupled to the copper sulphide hollow nanoparticles separately prepared following the mechanism proposed below. The polymeric content in the final hybrid nanoparticles was 40 wt. % (as determined by TGA analysis). An initial 10 wt.% weigh loss was attributed to the water content having the polymer a decomposition temperature in the range between 150 and 400ºC. In aqueous dispersion, the amine group of the polymer is likely to be bound with the copper ions of the crystalline nanostructure forming Cu complexes such as $[Cu(NH_3)_2]^+$ and $[Cu(NH_3)_2]^{++}$[171]. This phenomenon has been previously reported for studies of nanolayers on interfaces of Cu and Si, in which amine-terminated molecules bind on those solid interfaces following this route[172]. We postulated that copper sulphide nanoparticles oxidize in water releasing ionic copper, which can be subsequently chemisorbed on the surface of the CuS nanoparticles[173] and can be strongly bound to amino containing groups (e.g., as in the transport of metalloproteins [174]).

This efficient coupling can be observed in Figure 3.2 a)-j) where TEM and STEM-HAADF images show the different structure of the CuS NPs with and without P(MEO_2MA-

co-OEGMA$_{500}$)amine surface functionalization. Their atomic composition and copper to 53rimeth ratio correspond to the covellite structure according to the EDS analysis shown in Figure 3.2. The hollow structure of the NPs can be observed in Figure 3.2 d) where an EDS longitudinal profile of the hollow particles having high atomic density on the shell is clearly shown. Nevertheless, when the thermosensitive polymer was present on the surface of the NPs their roughness increased showing a fluffy surface having longitudinal irregularities as it was clearly observed in the NPs cross section. (Figure 3.2 i)

FTIR studies were performed in order to confirm the presence of P(MEO$_2$MA-co-OEGMA$_{500}$)amine on the surface of the CuS NPs. FTIR spectra of the compounds are presented in Figure 3.3 a) where the characteristic absorption peaks, representative of the PVP K30 polymer used during the synthesis for the stabilization of the CuS NPs, are present in both plain CuS NPs (blue) and P(MEO$_2$MA-co-OEGMA$_{500}$)-functionalized NPs (green). Moreover, the most important peaks of P(MEO$_2$MA-co-OEGMA$_{500}$)amine (red) [169] are present in P(MEO2MA-co-OEGMA500) functionalized CuS NPs (green) but they do not appear in the CuS NP spectrum. These results together with the Z-Potential studies (Figure 3.3 b)) verifying the change on the charge of the CuS NPs when the polymer is bound to them, corroborated the successful grafting of the polymer on the surface of the CuS NPs. In this case, the electrokinetic potential of the colloidal nanocomposites was more negative than the one obtained for the CuS NPs alone which can be attributed to a higher anion affinity of the P(MEO$_2$MA-co-OEGMA$_{500}$) ethylene glycol groups at neutral pH due to the interaction between the amino functionalized polymer and the metal nanoparticles. DLS measurements for three independent nanoparticle batches revealed hydrodynamic sizes of 158 ± 57 nm (0.125 PDI) without showing statistically significant variations after P(MEO$_2$MA-co-OEGMA$_{500}$) grafting. This result correlates with the TEM images as can be seen in Figure 3.2, where P(MEO$_2$MA-co-OEGMA$_{500}$) represents an extremely thin covering around the CuS NPs without a significant change in their size and morphology. This DLS analysis guaranteed colloidal stability.

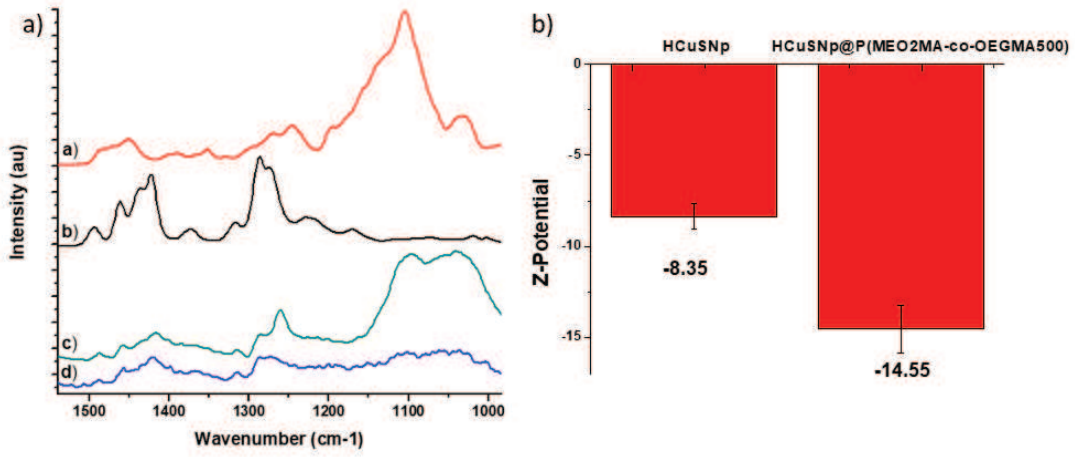

Figure 3.3: a) FTIR spectra of the different compounds present in the CuS-P(MEO_2MA-co-$OEGMA_{500}$) nanocomposites. A) (red) P(MEO_2MA-co-$OEGMA_{500}$) amine polymer; b) (black) PVP K30; c) (green) CuS-P(MEO_2MA-co-$OEGMA_{500}$) nanoparticles; d) (blue) CuS nanoparticles; b) Z-potential results measured at pH=6.

The photothermal properties of the resulting CuS NPs were tested in order to confirm that the thermosensitive coating did not affect the original characteristics of the CuS crystalline structure. Figure 3.4 a) shows the very similar UV-Vis absorbance spectra of CuS NPs with and without the polymer coating, both compared at the same metal concentration. Their photothermal properties were also evaluated after laser irradiation (808 nm; 1.89 W/cm^2) Figure 3.4 b). Under those conditions, a dispersion of CuS-P(MEO_2MA-co-$OEGMA_{500}$) NPs (1.8 mg/mL in 1 mL) increased the temperature from physiological temperature, 37 ºC, to 45 ºC after 2.5 minutes of irradiation. The suspension cooled down to body temperature in only 4 minutes after stopping the laser irradiation, which makes these NPs potentially interesting for pulsatile photo-thermosensitive applications as drug delivery vectors.

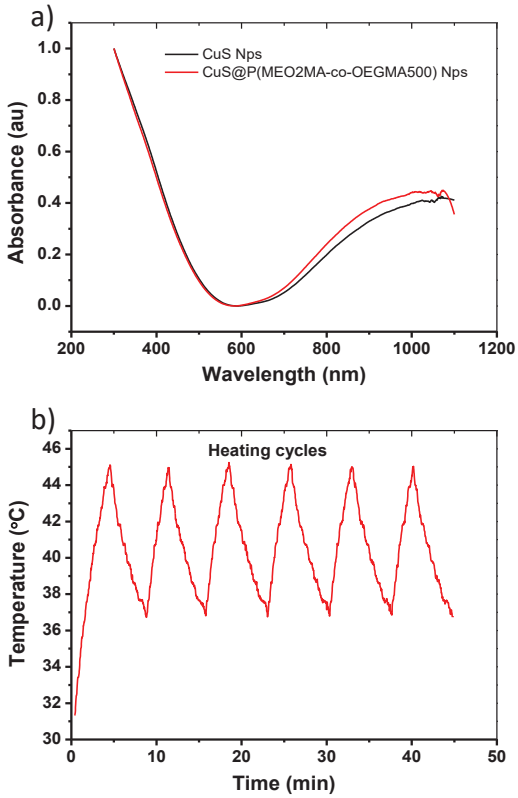

Figure 3.4: a) Comparative UV-Vis spectra of CuS and CuS-P(MEO_2MA-co-$OEGMA_{500}$) nanoparticles; b) Heating efficiency of CuS-P(MEO_2MA-co-$OEGMA_{500}$) nanoparticles under laser irradiation (808 nm; 1.89 W/cm^2; Volume: 1mL and concentration: 1.8 mg/mL)

3.1.4.3 Drug loading and release

The process of drug loading was carried out by incubating bupivacaine hydrochloride monohydrate, the hydrophilic form of the drug, with the resulting with the CuS-P(MEO_2MA-co-$OEGMA_{500}$) NPs during 4 h to allow its diffusion into the polymeric structure. After incubation and purification, bupivacaine drug loading (Eq 3.1) and encapsulation efficiency (Eq 3.2) reached 2.1 ± 0.3 wt.% and 10.46 ± 1.44 wt.%, respectively.

Eq 3.1: Drug loading

$$D.L.(wt.\%) = \frac{[BVP]_f}{[NPs]}\ x\ 100$$

$$[BVP]_f = \textit{Final bupivacaine weight in the loaded Nanoparticles } (mg)$$

$$[NPs] = Total\ Nanoparticles\ weight\ (mg)$$

Eq 3.2: Encapsulation efficiency

$$E.E\ (wt.\%) = \frac{[BVP]_f}{[BVP]_i}\ x\ 100$$

$$[BVP]_i = \ Initial\ bupivacaine\ weight\ added\ in\ the\ system\ (mg)$$

$$[BVP]_f = \ Final\ bupivacaine\ weight\ in\ the\ loaded\ Nanoparticles\ (mg)$$

After that, drug release patterns were analyzed at temperatures above and below the LCST of the polymer (37 and 45 ºC) using a temperature-controlled bath. The results are shown in Figure 3.5 , where it was demonstrated that a higher temperature leaded to a faster and extended drug release. Desorption is favored at higher temperatures and also upon heating, the 56rimeth-responsive polymer experiences a transition from coil (at 37 ºC) to globule (at 45 ºC) state, shrinking the polymeric layer and squeezing the drug out from the nanoparticle. The reversible phase transition of the polymer is then used to act as a drug reservoir that can be activated on-demand releasing the drug after reversing its conformation to its globular shrunken dehydrated state. Under physiological conditions (37 ºC) Higuchi release kinetics were observed which was attributed to the coil conformation of the hydrophilic polymer at that temperature. The release profile at 37ºC showed r-values of 0.970 and 0.998 after fitting the data to zero order (Figure 3.5 a)) and Higuchi (Figure 3.5 b)) kinetic models, respectively.

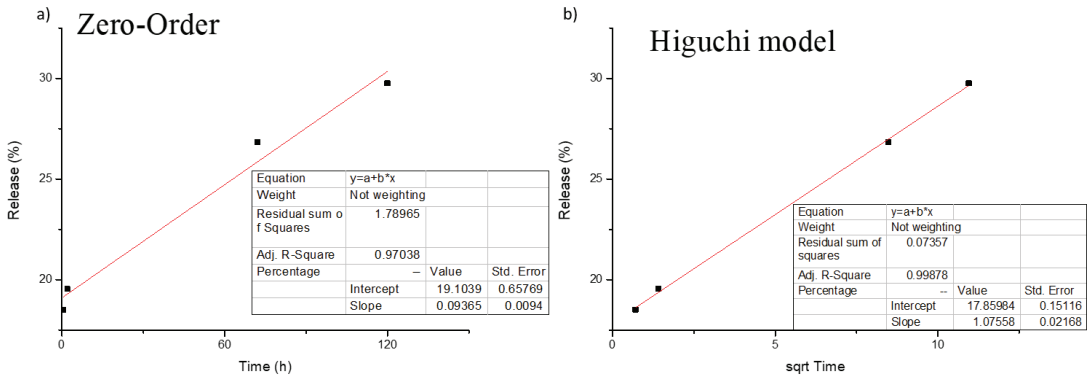

Figure 3.5: Data and graphics corresponding to a) Zero-Order and b) Higuchi model mathematical equation used to fit Bupivacaine release profile data

Taking advantage of the photothermal properties of copper sulphide crystals, light activated triggered release was demonstrated. After 6 and 24 h of drug release at constant temperature (37 ºC) the sample was stepwise irradiated with an 808 nm laser (1.89 W/cm^2) in order to raise the temperature to 45 ºC. This instant heating induced a pulsatile release in independent samples as shown in Figure 3.6 with drug release values above the 50 wt.% of the bupivacaine released: 53.5 and 52.7 wt.% for the pulsatile light triggered heating at 6 and 24h, respectively. This enhancement of the amount of drug released upon light triggering can be attributed to the increased desorption caused by a local heating considering that the temperature near the surface of the metallic nanoparticle can be very high. Moreover, when a double pulse was performed on independent samples, at 6 h and 24 h, similar results were obtained, with a 54.23 wt.% release.

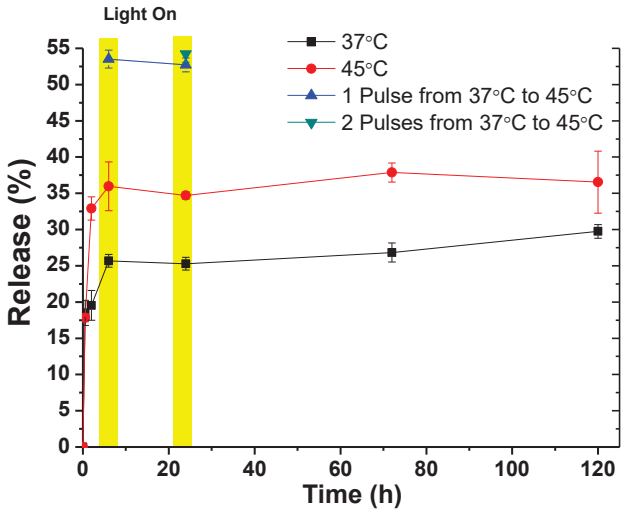

Figure 3.6: Bupivacaine release curve after 7 days at 37 ºC and 45 ºC, under and above LCST temperature respectively. Two specific time points 6 h and 24 h (highlighted in yellow) where selected to irradiate (808 nm, 1.89W/cm2) the sample (1mL, 1.8 mg/mL) in order to rise the temperature from 37 ºC to 45 ºC and enhance the total amount of drug released due to the swelling/collapse effect of the polymer. Average and error bars obtained from 3 different samples for each time point.

Thanks to these pulses we were able to enhance the cumulative drug release up to a 20 wt.% at specific time points. Therefore, P(MEO_2MA-co-$OEGMA_{500}$) functionalized CuS NPs allow an on-demand drug release externally activated by using NIR light. This ability has been previously demonstrated with other nanoparticulated photo-triggered systems. For instance, Huang et al.[152] in their work with $Cu_{1.75}S$ nanocapsules grafted with PNIPAm reached a 2 wt.% drug (doxorubicin) release increase after 10 minute pulses during a continuous release in an aqueous solution at a pH of 7.4. A light triggered increase in the release of more than 12 wt.% was reached by Rwei et al.[175] in their study with tetrodotoxin-loaded liposomes thanks to the use of the $PdPC(Obu)_8$ (1,4,8,11,15,18,22,25-octabutoxyphthalocyaninato-palladium(II))NIR-absorbing compound and two NIR light irradiation cycles.

3.1.4.4 Biodegradation

The biodegradation under *in vitro* conditions of the resulting CuS-P(MEO_2MA-co-$OEGMA_{500}$) nanocomposites was morphologically evaluated by TEM and UV-Vis spectroscopy. The CuS NPs biodegradation was previously studied in Chapter II of this thesis under different conditions including varied temperatures and culture media. In addition, the

copolymer of oligo (ethylene glycol) methyl ether methacrylate (OEGMA) and di (ethylene glycol) methyl ether methacrylate (MEO_2MA) has been previously demonstrated to be cleavable at physiological temperature producing oligomers that are not harmful for the human body and are excreted without any signs of bioaccumulation[132][134].

Gel Permeation Chromatography (GPC) studies were carried out before and after an accelerated simulated degradation process (i.e., dispersing the polymer in water at 40 ºC during one week). Results can be observed in Figure 3.7 and they show an increase in the short chains of the polymer with an average molecular number ($\overline{Mn}$) of 1166 Da probably attributed to oligomers generated due to the accelerated degradation process. Moreover, a shoulder in the main peak-tail was observed which also corroborates polymer degradation. Molecular numbers showed a slight decrease from 27.3 kDa to 25.9 kDa and an increase in the polydispersity (1.14 to 1.56), which confirms as well the change in the side chains of the initial polymer. It has been demonstrated in previous studies[133], that poly(ethylene glycol) (PEG) can be excreted *in vivo* via urine and feces. Therefore, the PEG-based fragments obtained after fragmentation of the polymer would not constitute a toxicological concern. In addition, another *in vitro* and *in vivo* study of acrylate derivate of PEG hydrogels[176] support our results demonstrating their fragmentation into smaller oligomers.Consequently, the degradation mechanism proposed involves ester group cleavage via hydrolysis, and the release of side ethylene oxide units [176].

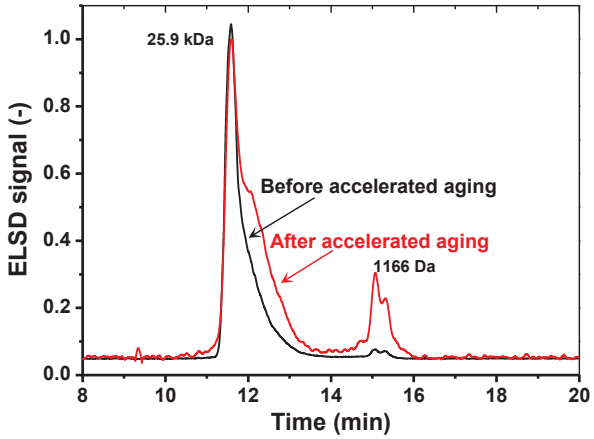

Figure 3.7: Normalized Gel Permeation Chromatography spectra of P(MEO_2MA-co-$OEGMA_{500}$) amine polymer before and after 7 days in water at 40 ºC.

Figure 3.8 shows the temperature effect on the cleavage of the resulting nanocomposites. The characteristic nanocomposite absorbance peaks (Figure 3.8 a and b) decreased faster at 45 ºC ($k = -0.2296\ day^{-1}$) than at 37 ºC ($k = -0.1477\ day^{-1}$), which indicated that the first order degradation observed was accelerated with temperature. TEM images shown in Figure 3.8 from c) to j) corroborated the erosion of the nanocomposites over time, including not only the crystalline structure of the copper sulphide core but also its polymeric thermosensitive coating. An increased turbidity in the aqueous suspension was observed for aged samples, which can be attributed to the fragmentation of the polymer and the generation of polymeric oligomers since the degradation of CuS nanoparticles rendered colorless products. As mentioned before, under simulated physiological conditions the degradation byproducts of the original copper sulphide consisted of a mixture of water soluble salts based on copper sulphate[173].

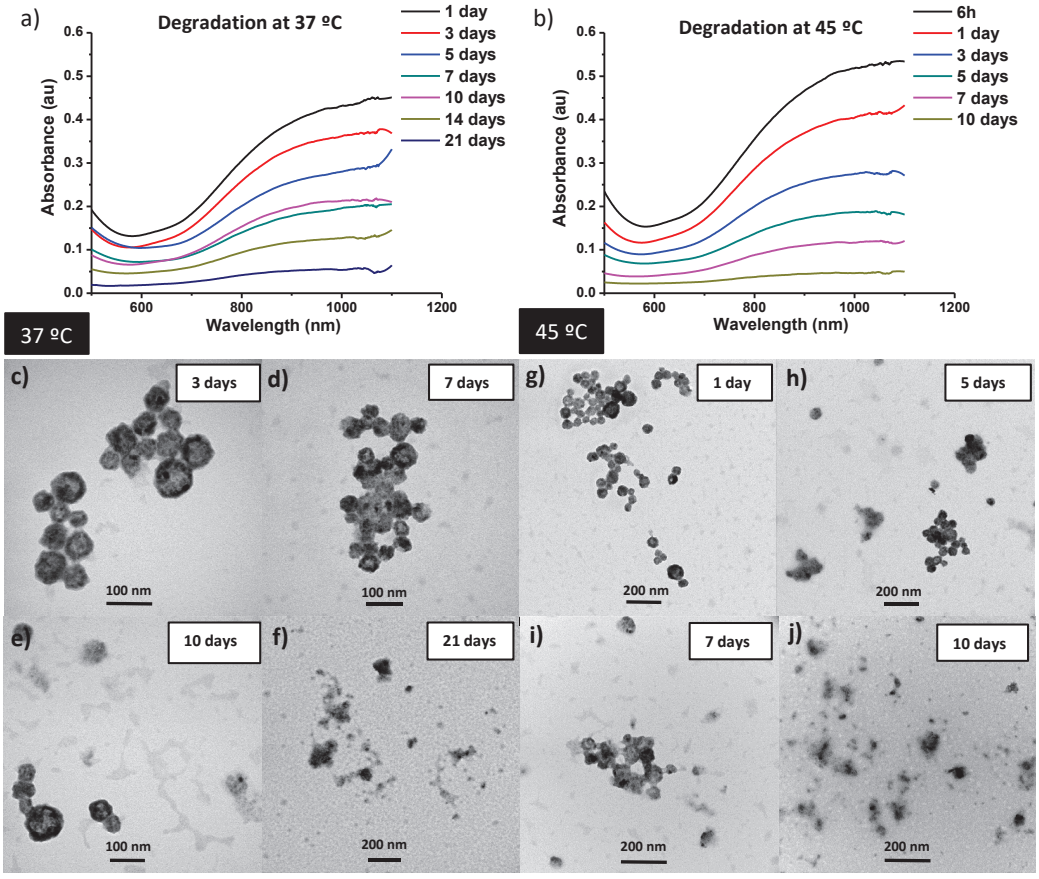

Figure 3.8: Degradation studies of CuS-P(MEO_2MA-co-$OEGMA_{500}$) nanocomposites at different ambient conditions. a) and b) UV-Vis spectra showing the decrease in the

absorption peaks in water depending on the ambient temperature, 37 ºC and 45 ºC, respectively; c)-f) TEM images of CuS-P(MEO_2MA-co-$OEGMA_{500}$) nanoparticles at 3,7,10 and 21 days kept at 37 ºC as colloidal suspensions in water. In the same way, g) – j) TEM images show the CuS-P(MEO_2MA-co-$OEGMA_{500}$) nanoparticles at 1, 5,7 and 10 days kept at 45 ºC.

3.1.4.5 Cell viability, apoptosis and cell cycle evaluation

The cytocompatibility of synthetized nanocomposites was studied on four different cell lines. In this analysis, four different samples were taken into account: CuS NPs, CuS-P(MEO_2MA-co-$OEGMA_{500}$) NPs, CuS-P(MEO_2MA-co-$OEGMA_{500}$) NPs loaded with bupivacaine (BVP), both from 0.01 to 1 mg/mL; and the corresponding concentration of free bupivacaine (0.248 to 24.8 µg/mL). Cell viability estimated by the cell metabolism assay (Figure 3.9) was high (>70%) for doses up to 0.1 mg/mL decreasing at higher concentrations for both empty and drug loaded CuS-P(MEO_2MA-co-$OEGMA_{500}$) nanocomposites. However, no cellular viability reduction was observed for the free bupivacaine in any of the cell lines studied at the concentrations assayed.

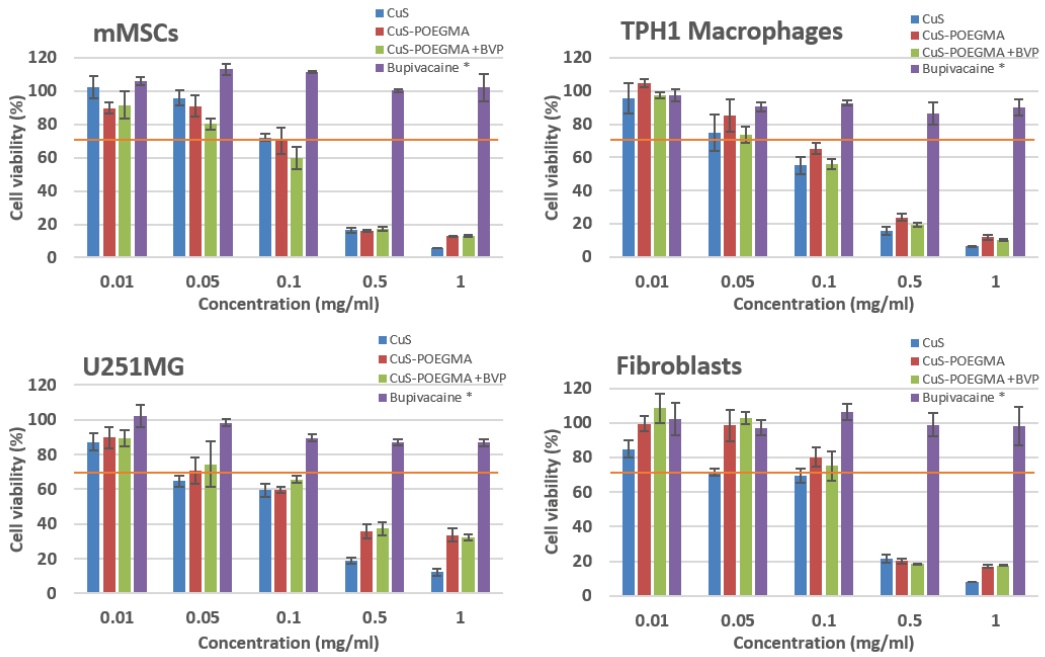

Figure 3.9: Cell metabolism studies of CuS NPs, CuS-P(MEO_2MA-co-$OEGMA_{500}$) NPs, CuS-P(MEO_2MA-co-$OEGMA_{500}$) NPs loaded with bupivacaine and free bupivacaine. *Bupivacaine

concentrations are 0.248, 1.24, 2.48, 12.4 and 24.8 µg/mL, respectively, which corresponds with the amount of bupivacaine loaded in the CuS-P(MEO_2MA-co-$OEGMA_{500}$) nanocomposites. The orange line represents the subcytotoxic concentration recommended by the ISO 10993-5 standard, which states a viability of 70% as the threshold for considering non-cytotoxic concentrations. Data are presented as the mean ± SD of at least three experiments.

Following studies were developed at a nanocomposite concentration of 0.1 mg/mL as it was considered as subcytotoxic for all the cell lines tested. The potential cell membrane effect caused by the NPs was analyzed through cell apoptosis studies using flow cytometry. The incubation of the four different cell lines (mMSCs, TPH1 Macrophages, U251MG and Human Fibroblasts) at the subcytotoxic concentration (0.1 mg/mL) with plain CuS NPs, with the two different combined nanoparticles (CuS-P(MEO_2MA-co-$OEGMA_{500}$) and with CuS-P(MEO_2MA-co-$OEGMA_{500}$) loaded with bupivacaine and with free bupivacaine (2.48 µg/mL) did not show remarkable changes compared to the control samples (non treated cells) (Table 3.1).

Table 3.1: Apoptosis results obtained by flow cytometry

	Control	BVP 2.48 µg/mL	CuS NPs 0.1 mg/mL	CuS- P(MEO_2MA-co-$OEGMA_{500}$) 0.1 mg/mL	CuS- P(MEO_2MA-co-$OEGMA_{500}$) +BVP 0.1 mg/mL
	MACROPHAGES (%)				
Necrosis	0.1	1.0	0.5	1.0	0.1
Late apoptosis	11.4	10.3	5.3	7.8	9.3
Early apoptosis	4.1	14.2	25.7	3.8	2.5
Viability	84.4	74.4	68.5	87.3	88.1
	mMSCs (%)				
Necrosis	1.1	3.4	2.4	0.5	9.5
Late apoptosis	1.9	7.8	3.0	2.8	2.7
Early apoptosis	6.2	5.1	4.1	8.5	19.9
Viability	90.8	83.7	90.4	88.2	67.9
	U251MG (%)				
Necrosis	0.5	4.8	0.2	7.2	3.8
Late apoptosis	16.0	12.6	18.8	3.2	9.5
Early apoptosis	9.3	7.0	7.0	9.7	21.9
Viability	74.2	75.5	74.0	80.0	64.8
	FIBROBLASTS (%)				
Necrosis	6.0	6.1	2.9	7.2	5.2
Late apoptosis	2.9	11.1	0.7	1.9	5.1
Early apoptosis	4.8	7.2	4.3	4.8	14.3
Viability	86.3	75.6	92.2	86.1	75.4

Compared to the controls, only mMSCs showed a slight increase of 13.7% and 8.4% in early apoptosis and necrosis, respectively when bupivacaine was loaded in the NPs. Furthermore, a slight rise in the levels of early apoptosis was also observed for fibroblasts and U251MG cells when testing NPs loaded with bupivacaine (≤ 12.6%), while macrophages displayed a higher increase in early apoptosis levels (21%) when cells were treated with CuS NPs.

Cell cycle studies are depicted in Figure 3.10. Cell treatment for 24 h with P(MEO_2MA-co-$OEGMA_{500}$) functionalized CuS nanocomposites with and without bupivacaine did not display accentuated effects on the cell cycle phases obtaining changes in the percentages up to 20% though a higher effect was detected on the S phase of macrophages, in which the addition of free bupivacaine involved an increase of 40% together with a countervailing decrease in the G2 phase. However, the addition of encapsulated bupivacaine showed a very slight increase in the S phase (< 5%), pointing to a lower detrimental effect on cell cycle when the drug was administered encapsulated in the nanomaterials here reported. Thus, cell nuclei were not affected and cell cycle was not halted either by the NP treatment.

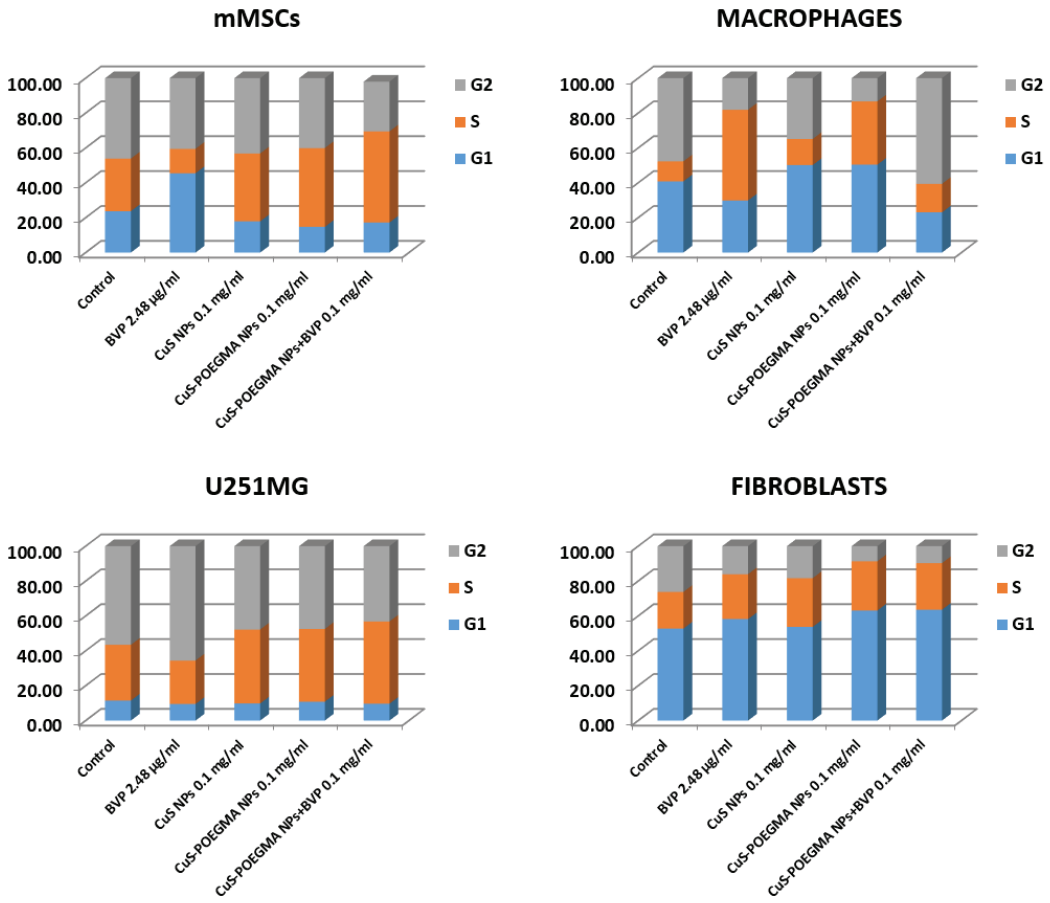

Figure 3.10: Cell cycle results obtained by flow cytometry after 24 h of incubation with the different samples.

Similar results were obtained in Chapter II for bare CuS nanoparticles, in which 0.1 mg/mL was also established as the subcytotoxic concentration. In addition, only phagocytic cell lines (i.e., macrophages) suffered an increase lower than 12.6% and 1.6% in apoptosis and necrosis, respectively. Furthermore, cell cycle and DNA were not damaged in any of the cell lines studied, highlighting the cytocompatibility of the nanomaterial assayed at the subcytotoxic dose. In addition, the cytotoxic effect of bupivacaine has been previously studied on different cell lines showing comparable results to ours[177][178][179]. In this work we tested a bupivacaine concentration of 43 µM during 24h. Similar results were obtained, for cytotoxicity studies of bupivacaine loaded lipid-polymer hybrid nanoparticles on 3T3 murine fibroblasts at concentrations from 1 to 20 µM during 8 h with a viability decrease lower than 30% for the free bupivacaine[177]. Cell membrane influence of free

bupivacaine in mouse C2C12 myoblasts was also tested in a previous study[178] where, after treatment for 24 h, cells incubated with 0.77 mM of free bupivacaine showed apoptosis and necrosis percentages up to 30% and 45%, respectively, much higher than that obtained for the control sample or for other anesthetic drugs such as lidocaine. 3T3 fibroblasts incubated during 24h showed viability percentages up to 60% for concentrations higher than 8μM with a notable decrease above it which agrees with our results[179].

3.1.5 Conclusions

In brief, in this thesis it was developed a cleavable and cytocompatible nanocomposite capable to release an adsorbed drug on demand upon externally applied NIR light stimulation. The nanocomposite fragmentation has been corroborated at different temperatures *in vitro*, being this degradation promoted with the increased temperature. The metallic cores can be degraded whereas the polymeric ethylene oxide side chains can also be cleaved from the polymeric central backbone rendering a fragmentable hybrid thermosensitive nanocomposite capable of release a drug on demand upon light stimulation. A bupivacaine loading up to 2 wt.% has been achieved in the nanocomposite material and the resulting nanoparticles showed a Higuchi kinetic-type release that can be modified at specific time points by using externally applied light activating the release of additional encapsulated drug. Furthermore, *in vitro* cytotoxicity, metabolism and cell cycle studies have been carried out concluding that those hybrid nanoparticles are not cytotoxic at doses below 0.1 mg/mL.

3.2 Thermoresponsive hybrid hydrogels[2]

3.2.1 Introduction

The reversible temperature-driven phase transition of Poly-N-isopropylacrylamide (PNIPAm) in water from its expanded coil conformation to its globular shrunken dehydrated state has been used in a growing number of research fields including biomedicine (e.g., in drug delivery, biosensing, biomolecule immobilization, etc.) [180][181][182], catalysis (e.g., to recover the catalyst in heterogeneous catalysis) [183], water purification (e.g., in forward osmosis for seawater desalinization) [184]; optics (e.g., as responsive photonic crystals, optical switching devices, etc.) [185], or electronics (e.g., as conductive polymers, printed electronics, etc.) [186].

In the drug-delivery field, the reversible phase transition of PNIPAm has been used to trigger the release of an encapsulated drug or bioactive molecule on-demand in response to a temperature increase above the lower critical solution temperature (LCST) of the polymer. Brushes based on PNIPAm on inorganic host matrices [187] or on porous membranes [188] have been synthetized as molecular gates to control the delivery of an encapsulated cargo. Micro- and nanoparticles based on PNIPAm are also commonly used to take advantage of their volume phase transition to control the temperature-driven release of the drug. Also, by introducing another monomers during the copolymerization, the LCST can be tuned (i.e., hydrophobic co-monomers decrease the LCST) and even those added co-monomers can induce the response not only to temperature but also to other chemical stimuli (i.e., pH or ionic strength) in the resulting PNIPAm-based micro- [189] and nanoparticles [190]. Not only temperature and pH have been used to trigger the release, but also, diblock copolymer brushes based on PNIPAm and polystyrene-b-poly(4,5-dimethoxy-2-nitrobenzyl methacrylate) have been synthetized to include light as a third stimuli to induce the

[2] The contents of this section were adapted from the following submitted work:

Ortiz de Solorzano, I.*, Prieto, M., Mendoza, M., Sebastian, V., Arruebo, M.

"Triggered drug release from hybrid thermoresponsive nanoparticles using near infrared light"

Journal of Materials Chemistry B

responsiveness of the resulting copolymers by means of photocleavable bonds [191]. Two-dimensional and 3D hydrogels have also been widely prepared for the triggered delivery of different active principles by crosslinking neighbouring PNIPAm nanoparticles as building blocks where the transition temperature and the crosslinking degree can be tuned to control release profiles [192]. Injectable PNIPAm sols have also been prepared to form gels *in situ* when reaching body temperature acting as drug depots. They have been applied in active tissue regeneration including interpenetrating networks of those materials containing different bioactive molecules (i.e., growth factors, drugs) that speed up the healing and prevent infection during the regenerative processes [193][194].

PNIPAm polymeric chains, micro- and nanoparticles and hydrogels based on this polymer have also been grafted-from or grafted-to metal nanoparticles to form hybrid nanoparticles able to act as sinks of specific external physical stimuli (i.e., magnetic, optical, ultrasonic, etc.) undergoing phase transition of the polymer releasing the contained drug. In hydrogels, metal nanoparticles have been formulated as fillers in the resulting nanocomposite materials acting as actuators to control the drug release as remote valves. For instance, near infrared (NIR) absorbing nanoparticles (i.e., gold, graphene oxide, etc.) have been included as fillers on PNIPAm-based membranes to absorb the NIR radiation externally applied converting it into heat through non-radiative decay processes to trigger the PNIPAm shrinkage and release a contained drug on-demand upon light stimulation [195][196].

Alternating magnetic fields have also been used to trigger drug release upon heating magnetic nanoparticles (due to Brownian and Néel relaxation mechanisms and hysteresis loses) grafted with PNIPAm brushes containing chemotherapeutic drugs [197]. Plasmonic [198] and semiconductor [199] nanoparticles have also been grafted to PNIPAm and loaded with different drugs to be activated via photothermal heating. Gold nanorods, core/shell silica/gold nanoparticles and hollow gold nanoparticles (HGNPs) have been commonly used as transductors of the NIR radiation into heat to apply them as photoinducible switches or in the photothermal ablation of malignant tissues. The reduced size of the HGNPs compared to core/shell silica/gold nanoparticles gives them prolonged blood circulation half-life. Compared to gold nanorods, HGNPs show reduced cytotoxicity due to the scarcity of cytolytic capping agents (i.e., CTABr, cetyltrimethylammonium bromide) commonly used

during the synthesis of gold nanorods. In addition, not only the external surface of HGNPs can be used to adsorb therapeutic molecules but also their hollow interior represents an additional reservoir to carry the therapeutic load [200]. Furthermore, Bartczak et al. [201] demonstrated that even though HGNPs showed reduced internalization in human umbilical vein endothelial cells compared to core/shell silica/gold and to gold nanorods, at subcytotoxic doses, they were equally efficient in promoting cell death under laser hyperthermia. This highlights their high efficiency in transducing light into heat. In addition, pegylated HGNPs have shown reduced toxicity *in vivo* when used as 68rimethylamin contrast agents for imaging the brain vasculature of mice [202]. Those authors showed that the nanoparticles presented an elimination half-life of 72 ± 30 h and no signs of inflammatory reactions or acute toxicity to the liver, spleen, or kidneys. HGNPs have also been used as radiosensitizers in the treatment of mice bearing triple negative breast cancer xenografts with no signs of adverse effects [203]. In our research group, it has been demonstrated tha those nanoparticles used as fillers within fibrin based scaffolds can be used to control the spatiotemporal patterning of transgene expression mediated by NIR irradiation with no signs of acute toxicity in mice after implantation [204].

3.2.2 Objectives

Herein, we show that those HGNPs can be electrostatically bound to PNIPAm-based nanogels prepared with selected monomer ratios in order to tune the volume phase transition temperature to a few degrees above body temperature. The hybrid nanogels were loaded with bupivacaine as a model drug and its *in vitro* release was reversibly triggered with the aid of externally applied NIR light. Comparative cytotoxicity studies were conducted to elucidate future biomedical applications.

3.2.3 Experimental

3.2.3.1 Synthesis of hollow gold nanoparticles (HGNPs)

Hollow gold nanoparticles (HGNPs) were synthetized following previous protocols developed in our group [95]. In brief, 400 mL of deionized (DI) water, 400µL of 0.35 M cobalt chloride hexahydrate and 1.6 mL of 0.1 M sodium citrate trihydrate were deoxygenated in a two-necked round-bottom flask by bubbling argon for 45 min. 2 mL of 1

wt. % of PVP and 400 μL of 1.0 M sodium borohydride were added to the previous solution under magnetic stirring to form cobalt nanoparticles. Argon flux and stirring were kept for 15 min. After that, 380 mL of this nanoparticle dispersion was transferred to a beaker containing 120 mL of DI water and 180 μL of 0.1 M gold (III) chloride hydrate and kept under stirring for 30 min to assure a complete oxidation and depletion of the sacrificial cobalt nanoparticles. The final color suspension changed to green, which is indicative of the formation of HGNPs. The final nanoparticles were thoroughly washed by centrifugation and re-suspended in DDI water for further use.

The electrokinetic potential of the HGNP-based colloids was carried out by Z-Potential measurements at pH=6 in a Zeta Plus (Brookhaven Instruments Corporation, NY, USA). Ultraviolet-visible (UV-Vis) absorption spectra were collected using a Varian Cary® 50 UV-Visible spectrophotometer (Agilent Technologies, USA). In addition, Transmission Electron Microscopy (TEM) analysis was performed in a FEI Tecnai T20, operating at 200 kV. A drop of the corresponding suspension was placed on a Holey carbon film-copper grid before TEM observation.

3.2.3.2 Preparation of PNIPAm nanogels

PNIPAm nanogels were synthetized following a previously reported protocol [195]. Briefly, N-isopropylacrylamide (0.6 g), N-isopropylacrylmethylamine (0.8 g), acrylamide (50 mg) and N,N'-methylenebisacrylamide (80 mg) were dissolved in 150 mL distilled deionized water (DDI) previously degassed with argon for at least 15 min. The solution was degassed again through two vacuum-argon cycles and heated to 70 ºC. Ammonium persulfate (APS) as initiator (5 mL of 20 mg/mL solution in DDI water) was then added to the solution under high stirring. After 6 h under argon atmosphere, the reaction was stopped and the particles were dialyzed against DDI water to remove unreacted monomers. Finally the collected polymer was lyophilized and stored in the freezer for further use.

The polymer characterization was carried out by Fourier Transformed Infrared Spectroscopy (FTIR) with a Vertex 70 (Bruker) with an ATR Golden Gate accessory and Proton Nuclear Magnetic Resonance (^{1}H-NMR) spectroscopy was carried out on a Bruker AV-400 spectrometer operating at 400 MHz using $CDCl_3$ as solvent. The cloud point of aqueous polymeric solution (3 mg/mL) was obtained from the optical transmittance

measurements at 670 nm by varying the suspension temperature using a Varian Cary® 50 UV-Visible spectrometer (Agilent Technologies, USA) equipped with a fiber optic dip probe. The temperature at which 50% of the transmittance was reached [168] was selected as the LCST of the polymer. Scanning Electron Microscopy (SEM) analyses were performed in a FEI Inspect 50, operating at 1-30 kV.

3.2.3.3 Synthesis of hybrid HGNPs-PNIPAm nanogels

The coupling of HGNPs with PNIPAm nanogels was carried out following the work previously reported by Karg et al. [205] with slight modifications. Briefly, HGNPs were coated with poly(allylamine hydrochloride) (PAH), to obtain a positive surface charge. 5 mL of HGNPs (1.0 mg/mL) were added to 5 mL of DDI water containing 2 mg/mL PAH and kept under magnetic stirring for 3h. To eliminate the PAH in excess, HGNPs were washed by several centrifugation cycles. Coated HGNPs were characterized by Z-Potential measurements at pH=6, by UV-Vis spectrophotometry and by TEM as mentioned above. Diluted phosphotungstic acid solution was used as negative contrast agent for allowing polymer coating visualization during the TEM observation. Samples stabilized at 45 ºC were kept at this temperature for 30 minutes before and during the addition of the contrast agent. They were also kept in an oven at 45 ºC during the drying period in the carbon film-copper grid.

Total amount of gold derived from HGNPs was determined by MP-AES using Plasma-Atomic Emission Spectrometer (4100 MP-AES, Agilent Technologies, USA). Calibrations were carried out using Au standards from 0 to 10 ppm in 10 % Aqua regia.

3.2.3.4 Bupivacaine loading and release

A dispersion of hybrid HGNPs-PNIPAm nanogels (5 mg/mL) was incubated with a bupivacaine solution at different concentrations (from 5 to 30 mg/mL). The resulted loaded dispersions were washed three times by centrifugation until non-loaded bupivacaine was removed. Samples were lyophilized before drug release studies.

Controlled release studies were carried out with the drug-loaded hybrid HGNPs-PNIPAm nanogels (1 mg/mL) at body temperature (37ºC) monitoring the amount of bupivacaine released over time to the supernatants. In order to verify their photo-responsive behavior, photothermally-triggered samples were also studied. At selected times, laser pulses

(808nm, 1.89 W/cm^2) were used to increase the initial dispersion temperatures from the physiological (37ºC) to 45ºC after 2 minutes of irradiance. Bupivacaine contents in the supernatants were measured by Gas Chromatography-Mass Spectrometry (GC-MS-QP2010 SE, Shimadzu). Limonene was used as internal standard.

3.2.3.5 *In vitro* studies

Cell culture, cytotoxicity assays and study of cell cycle have been carried out in the same way all along this PhD. For this reason, common details are described in Appendix I: I-Methods: Biological studies.

3.2.4 Results and discussion

3.2.4.1 Hybrid HGNPs-PNIPAm nanogels characterization

Thermoresponsive PNIPAm-based nanogels (Figure 3.12 a)) were synthetized following the protocol previously reported by Timko et al.[195]. A complete chemical characterization using Fourier-transform Infrared Spectroscopy (FTIR) and Nuclear Magnetic Resonance (NMR) Spectroscopy was carried out in order to confirm that the nanogels were successfully obtained (Figure 3.11).

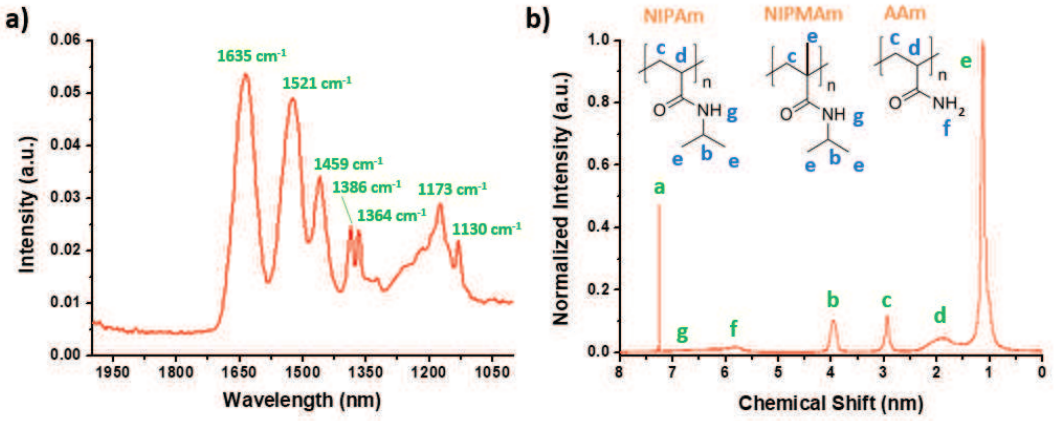

Figure 3.11: PNIPAm-based nanogels chemical characterization: a) Fourier Transform Infrared Spectroscopy (FTIR) spectrum; and b) Nuclear Magnetic Resonance Spectroscopy (NMR) spectrum

FTIR spectrum presents the characteristic peaks for PNIPAm polymer (Figure 3.11 a)): 1635 cm^{-1} and 1536 cm^{-1} represent the characteristic absorption peaks for amide I C=O stretching and amide II C-N stretching, respectively. Besides, the N-H vibration defined as amide III peak is present at 1173 cm^{-1} [206]. Methyl groups of the isopropyl groups present

were detected including the CH_3 bending peak at 1459 cm^{-1}; symmetric and asymmetric deformations at 1386 cm^{-1} and 1354 cm^{-1}; and also CH_3 out of plane rock at 1130 cm^{-1} [207].

The structure of the resulted polymer was further confirmed by ^{1}H-NMR spectroscopy. Figure 3.11 b) shows the representative peaks for the three monomers present in the hydrogels: N(isopropylacrylamide) (NIPAm); N(isoprpopylmethacrylamide) (NIPMAm); and Acrylamide (Aam) with their corresponding molecular structures. [206] [208]

The average diameter of the resulting PNIPAm-based nanogels was determined by Dynamic Light Scattering (DLS) (828 ± 45 nm) and their low critical solution temperature (LCST) was established as the mid-point of the transmittance results achieved during reversible heating cycles. Figure 3.12 c) represents the transmittance change with temperature for linear PNIPAm-based polymer (black) and nanogels (red). While linear polymer showed a sharp decay of transmittance with mid-point at 42 ºC, 72rimethy-based dispersions presented a linear transition. This may be attributed to polydispersity in the polymer chain lengths and crosslinking degree [209][210] being in good agreement with previous results [195]. On the other hand, hollow gold nanoparticles (HGNPs) (Figure 3.12 b) with an average diameter of 40.8 ± 6.4 nm were used as the light-sensitive moiety in the final hybrid nanocomponents. In order to attach these HGNPs to PNIPAm-based nanogels an electrostatic surface modification was used by adsorbing a positively charged polyelectrolyte (PAH) on the surface of the HGNPs to reverse their charge.

Table 3.2: Z-Potential measurements at pH=6; Mean diameter size of PNIPAm-based nanogels obtained from DL spectrometry and initial and PAH modified HGNPs by TEM image analysis

Sample	**ζ-Potential (mV)**	**Size (nm)**
PNIPAm-based nanogels	-5.77 ± 0.50	828 ± 45
HGNPs	-8.85 ± 1.22	40.8 ± 6.4
HGNPs@PAH	9.87 ± 1.23	42.7 ± 10.3

No significant size change was observed after this surface modification (42.7 ± 10.3 nm). However, whereas the original HGNPs showed a zeta potential of -8.85 ± 1.22 mV, their electrokinetic charge turned to 9.87 ± 1.23 mV after their chemical modification with PAH (Table 3.2). The as-synthesized PNIPAm nanogels presented an electrokinetic potential

of -5.77 ± 0.5 mV (Table 3.2) attributed to the strong acid group introduced by the APS. In this way, positively charged HGNPs@PAH and negative PNIPAm-based nanogels were electrostatically bound and formed the hybrid component.

The HGNPs showed their characteristic maximum in the surface plasmon resonance (SPR) absorbance peak centered at 772 nm. This SPR induces a strong absorption of the incident NIR light. A reduced scattering at lower wavelengths and a relatively small full width at half maximum shown in Figure 3.12 d) are characteristic of the homogenous nanoparticle sizes obtained. It has been previously demonstrated that total light extinction (i.e., absorption and scattering) of HGNPs with SPR around 800 nm is dominated by absorption and therefore they constitute very efficient transducers of photons into heat [211]. After surface modification, HGNPs@PAH also showed a notable change in their SPR peak (Figure 3.12 d)). The maximum absorbance intensity blue shifted to 647 nm having a broader peak than uncoated HGNPs. Similar phenomenon has been previously observed after surface modification of gold nanoparticles with dopamine dithiocarbamate ligand [212][213], which suggests an interaction between the plasmonic resonance and the component attached to HGNPs surface as well as to changes in the dielectric constant of the media. Moreover, a broader standard deviation (10.6 vs 6.4 nm) suggested the possibility of a wider absorbance peak. Previous studies showed how the SPR peak shifts to higher wavelengths after the addition of a capping agent that induced the aggregation of Au nanoparticles [214]. In this case, after PAH addition HGNPs have a positive charge inducing repulsive forces among them. This can lead to separation of the possible nanoparticle aggregates and thus shifting the SPR maximum to lower wavelengths. However, HGNPs@PAH still presented high absorbance at 800 nm making them suitable for NIR-irradiation response.

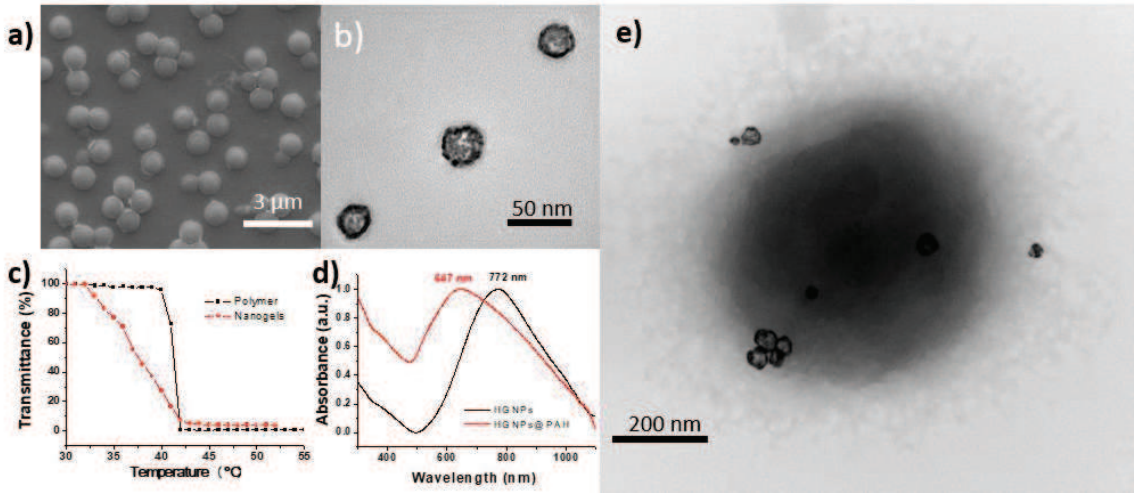

Figure 3.12: a) Scanning Electron Microscopy (SEM) image of PNIPAm-based nanogels; b) Transmission Electron Microscopy (TEM) image showing Hollow Gold Nanoparticles (HGNPs); c) PNIPAm-based polymer and Nanogels transition temperature measured by transmittance; d) Normalized absorbance peak for plasmonic HGNPs and modified HGNPs@PAH; e) Hybrid nanogels high resolution TEM image.

The morphology of the hybrid HGNPs-PNIPAm nanogels is depicted in Figure 3.13 a). As it can be observed the polymeric nanogels were surface decorated with HGNPs. An image in detail of a hybrid nanostructure shows that the PNIPAm nanogels exhibited a brush structure (Figure 3.12 e)) grafted on the PAH functionalized HGNPs. A competitive adsorption experiment using a high ionic strength media was carried out in order to corroborate the stability of the supramolecular interaction. Figure 3.13 b) shows that after electrostatic competition in saline media (0.15 M NaCl) the HGNPs remained strongly bound to the surface of the PNIPAm nanogels.

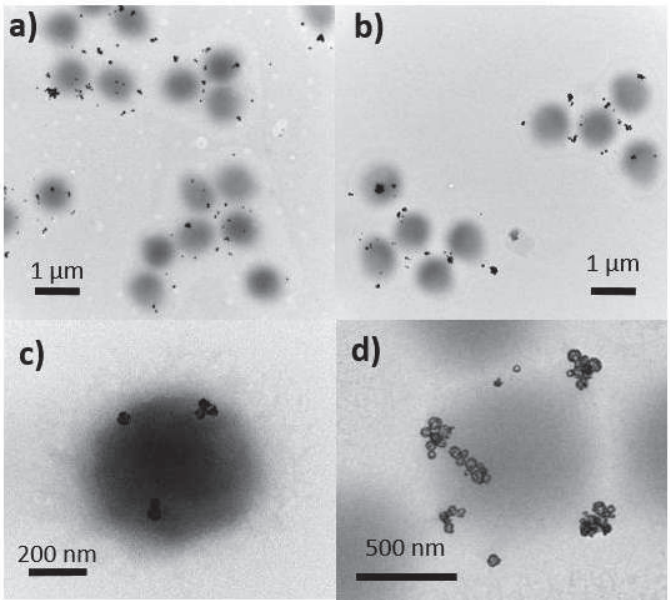

Figure 3.13: TEM images of hybrid PNIPAm-based decorated with HGNPs a), c) before and b), d) after saline competition with NaCl 0.1 M. Samples were negatively stained to properly differentiate the organic counterpart of the hybrid nanostructure.

Gold content (111 ± 9 µg Au/mg hybrid gels) in the hybrid HGNPs-PNIPAm nanogels was evaluated by MP-AES. With this HGNPs load a fast photothermal response was achieved. As shown in Figure 3.14 a), after 10 min of irradiation at different laser intensities, a colloidal water suspension of the hybrid HGNPs-PNIPAm nanogels (0.1 and 5 mg/mL) was rapidly heated, which is indicative of the efficient transduction of the electromagnetic radiation by those hybrid nanocomposites. This heating could be modulated not only by changing the laser irradiation power but also by varying the hybrid 75rimethy concentration (Figure 3.14 b) and c)).An increase of NPs concentration in the sample leads to faster temperature rise with more notable changes at low temperatures (0.1 to 0.5 mg/mL) where a 5-fold increase of concentration represents an increase of temperature of 10 ºC. This effect is reduced at high NPs concentrations (1 to 5 mg/mL) where the same proportional increase of NPs concentration only increase the temperature 6 ºC. (Figure 3.14 b)). On the other hand, laser irradiation power effect (1 and 1.5 W/cm^2) is more representative at 5 mg/mL NPs concentration than at 0.1 mg/mL increasing 6 ºC and 2 ºC respectively.

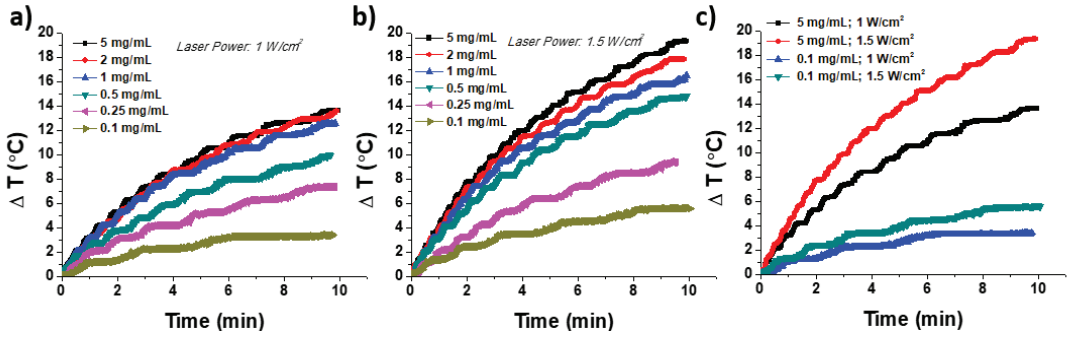

Figure 3.14: Heating efficiency analysis under 808 nm wavelength laser irradiation. Graphs a) and b) show the increase of the temperature at constant laser power, 1 W/cm^2 and 1.5 W/cm^2, respectively at different hybrid hydrogels concentrations varying from 0.1 to 5 mg/mL. Figure c) compares the heating efficiency of two selected concentrations at different laser output power.

3.2.4.2 Thermoresponsive properties

This heat produced by the HGNPs attached to the 76rimethy surfaces was used as the driving force for their volume change.

In Figure 3.15 the morphological study of the hybrid nanogels below and above their transition temperature can be observed. Expanded nanogels at room temperature kept the same size measured before HGNPs grafting (828 ± 45 nm) estimated by Dynamic Light Scattering (DLS) (Figure 3.15 a). However, when temperature increased above the LCST hybrid nanogels shrunk reducing 93.5 % of their volume. This volume reduction of polymeric nanogels from the expanded coil conformation to the globular-collapsed structure accompanied by dehydration is in agreement with the previous literature where volume reductions of 95.2 % as determined by DLS have been previously reported for PNIPAm-based nanogels [215]. TEM images of both samples (Figure 3.15 d and e) and their diameter distribution at 22 ºC and 45 ºC (Figure 3.15 b and c)) showed how the external shell of hybrid nanogels has an expanded brush structure at temperatures below the 76rimethy LCST, but a collapsed compact structure was observed when the temperature increased to 45 ºC. To allow this observation, hybrid nanogels were kept at selected temperatures before, during and after phosphotungstic acid staining and dried at 22 ºC and 45 ºC, respectively. As can be observed in Figure 3.15e the hydrogel does not show the complete diameter reduction of the core of hybrid nanogels retrieved from DLS results (632 ± 42 nm vs ~500 ± 80 nm) most likely because the electronic observation takes place at room temperature. However, we preserved

the collapsed polymeric chains located on the shell of the hybrid nanogels by staining the structure using phosphotungstic acid (Figure 3.15e). The TEM analysis of stained samples rendered a 44.5% of volume reduction. HGNPs were still located at the shrunk structure, which highlights the successful grafting of the metal nanoparticles to the polymeric nanogels.

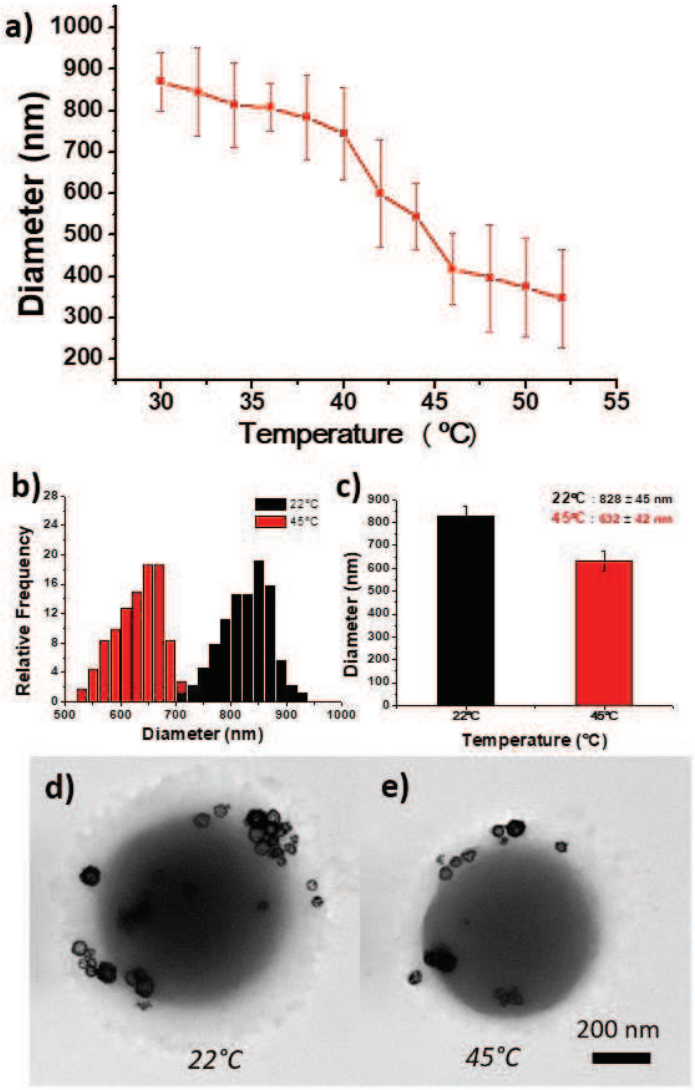

Figure 3.15: a) Dynamic Light Scattering results for PNIPAm-based nanogels at different temperatures; b) Diameter size distribution of Hybrid nanogels at 22 ºC and 45 ºC; c) Mean diameter and Standard deviation below and above gels transition temperature; d) and e) TEM images of hybrid nanogels at 22ºC and 45ºC, respectively

3.2.4.3 Drug loading and release

GC-MS analysis revealed a drug-loading dependence to the initial bupivacaine (BVP) loading concentration. BVP was loaded by diffusion into the hybrid nanogels by placing them into 5, 15 and 30 mg/mL BVP aqueous solutions. It can be inferred from Figure 3.16 a) that the higher the concentration of BVP in the loading media, the higher the drug loading achieved due to a typical Fickian diffusion controlled process. While samples immersed in 5 mg/mL BVP solutions showed drug loadings of 10.5 ± 2.7 wt. %, increasing this initial concentration to 30 mg/mL lead to loadings up to 86.6 ± 43 wt.%. The temperature of the *in vitro* release media was set at 37 ºC and 45 ºC to investigate the temperature-responsive release of the here produced nanohybrid materials.

The accumulative release profiles of BVP at physiological temperature (37 °C) and at 45 °C are shown in Figure 3.16 b), together with those releases collected after triggered drug release induced by laser irradiation. It can be highlighted that an initial burst drug release was observed regardless of the delivery temperature. However, a more pronounced release (fast diffusion rate) was exhibited when the *in vitro* release temperature was increased from 37ºC to 45ºC, obtaining almost 90% of bupivacaine released after 1 hour.

At selected times, laser pulses (808nm, 1.89 W/cm^2) were used to increase the initial dispersion temperature from the physiological (37ºC) to 45ºC. An abrupt increase of the release rate was observed as the temperature exceeded 45 ºC due to the two laser pulses conducted at the release times of 24h and 48h, respectively. The relative BVP released at first pulse (24h) was of 12 wt.%, decreasing to a 6 wt.% after the second pulse at 48 h. These results show an obvious temperature-modulated on–off switch, demonstrating their ability for NIR-induced on demand drug delivery. Bupivacaine hydrochloride presents a pK of 8.1 [216], which means that at pH above 8.1 it will be negatively charged whereas at pH below 8.1 its charge will be positive. Therefore, we evaluated the potential electrostatic interaction and consequent potential HGNPs detachment from the PNIPAm nanogels after drug loading. Figure 3.16 c) shows that even after drug-loading (at neutral pH) HGNPs remained strongly bound to the surface of the PNIPAm-based nanogels.

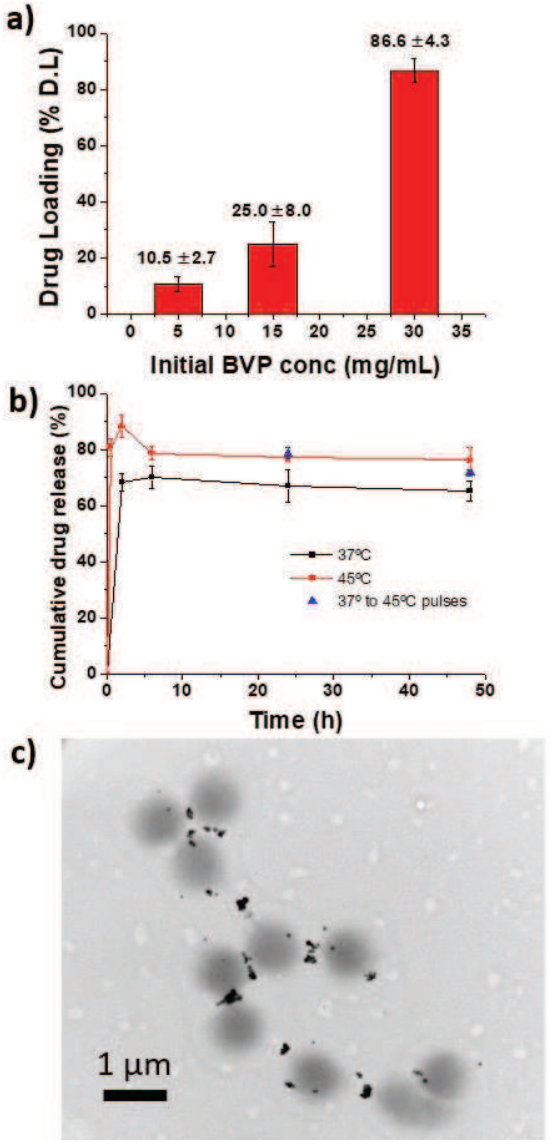

Figure 3.16: a) Drug loading data of Bupivacaine molecules into hybrid nanogels incubated with 5, 15 and 30 mg/mL BVP water solutions; b) Bupivacaine release profile at 37ºC, 45ºC and under two laser pulses (2 minutes; 1.89 W/cm^2) after 24 and 48h of release studies at 37ºC; c) TEM image of BVP loaded hybrid nanogels after loading and release steps.

3.2.4.4 Cell viability, apoptosis and cell cycle evaluation

The cytotoxicity of hybrid nanoparticles was evaluated on four different cell lines: Human fibroblasts, mouse mesenchymal stem cells (mMSCs), human glioblastoma U-251 MG cells and macrophages as phagocytic line. In this analysis, four samples were considered: PNIPAm-based nanogels, HGNPs decorated PNIPAm-based nanogels, HGNPs decorated

PNIPAm-based nanogels loaded with bupivacaine and free bupivacaine (BVP). The samples from 0,01 to 1 mg/mL were incubated for 24 hours and then cell viability was studied using the Blue Cell Viability test. Figure 3.17 shows the results for the different cell lines demonstrating a significant decrease of viability when HGNPs are incorporated in PNIPAm-based nanogels.

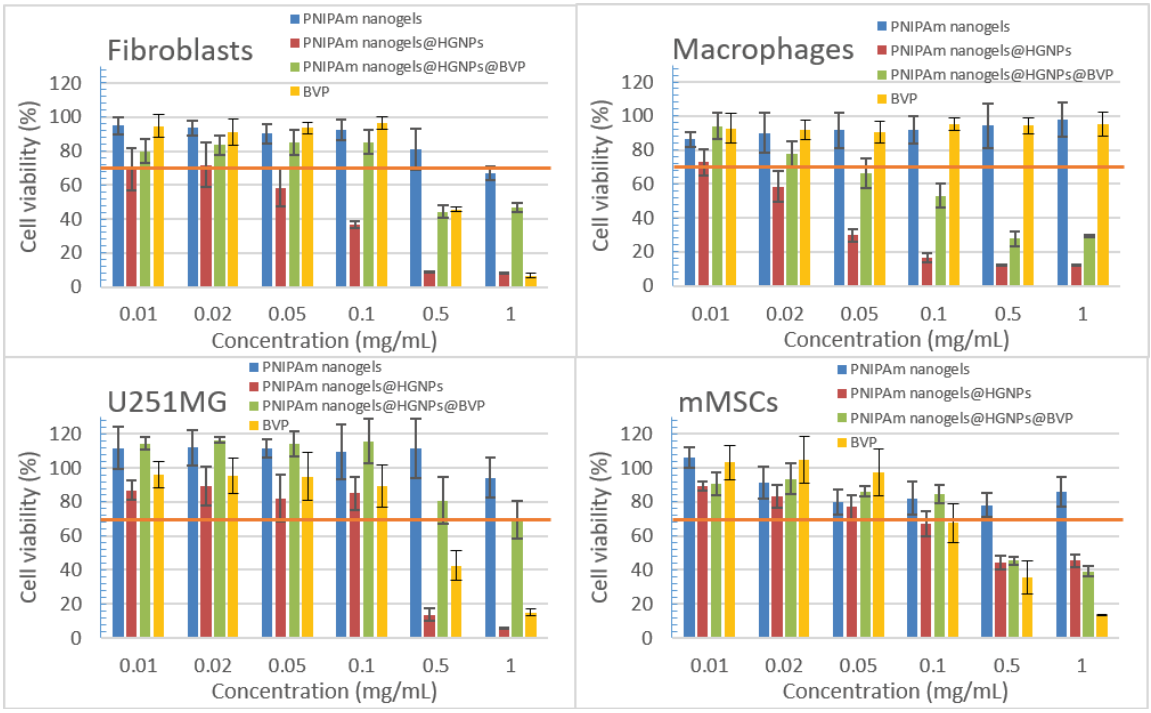

Figure 3.17: Cell metabolism studies in the four different cell lines studies for non-loaded PNIPAm-based nanogels, PNIPAm-based@HGNPs nanogels, bupivacaine loaded PNIPAm-based@HGNPs nanogels and correspondent free bupivacaine. Recommended subcytotoxic limit by ISO 10993-5 standard (viability > 70 %) is represented with an orange line. At least five experiments were considered to represent the mean and SD data shown.

This effect has been observed before in similar systems [217][218] and can be attributed to a high HGNPs concentration and their associated cytotoxicity [219]. However, this influence is not so notable when bupivacaine is also present in the sample, in agreement with a decrease of HGNPs when BVP is also present in the sample. For these two samples, high viability above 70% was observed up to 0.1 mg/mL decreasing at higher concentrations. In case of free BVP the reduced viability was observed at lower concentrations than those obtained for loaded NPs except for macrophages. On the other hand, for plain PNIPAm-

based nanogels no cell viability reduction below 70% was observed in any of the concentrations assayed and cell lines studied.

Based on recommended subcytotoxic limit by ISO 10993-5 standard (viability > 70 %), we selected 1 mg /mL as subcytotoxic concentration for PNIPAm-based nanogels and 0.1 mg/mL for the rest of the samples to evaluate cell membrane and cell cycle effects by flow cytometry. Cell apoptosis studies were used to analyze the potential cell membrane effect caused by the different samples. Table 3.3 summarizes all data collected from the four cell lines analyzed (Macrophages, mMSCs, U251MG and Fibroblasts) showing no remarkable differences compared to control samples. Only mMSCs showed a slight increase of late apoptosis (<10%) compared to control cells and minor viability decrease when treated with bupivacaine loaded HGNPs decorated PNIPAm-based nanogels.

Table 3.3: Apoptosis results obtained by flow cytometry

	Control	PNIPAm nanogels 1 mg/mL	HGNPs PNIPAm nanogels 0.1 mg/mL	BVP-HGNPs PNIPAm nanogels 0.1 mg/mL	BVP 0.1 mg/mL	Control	PNIPAm nanogels 1 mg/mL	HGNPs PNIPAm nanogels 0.1 mg/mL	BVP-HGNPs PNIPAm nanogels 0.1 mg/mL	BVP 0.1 mg/mL
	MACROPHAGES (%)					U251MG (%)				
Necrosis	4.0	4.0	3.8	5.5	2.2	1.8	1.5	2.4	3.0	0.2
Late apoptosis	10.3	6.3	5.4	5.0	11.9	2.3	6.3	9.1	4.5	18.7
Early apoptosis	1.5	1.1	1.5	0.6	2.0	1.6	1.7	2.1	1.4	11.9
Viability	84.2	88.6	89.3	88.9	83.9	94.4	90.5	86.5	91.1	69.2
	mMSCs (%)					FIBROBLASTS (%)				
Necrosis	0.1	0.6	0.3	2.2	0.1	0.4	0.4	0.4	0.5	0.5
Late apoptosis	10.3	11.5	6.2	20.0	5.3	2.6	1.8	2.7	2.7	3.0
Early apoptosis	4.9	3.8	2.4	3.4	4.4	3.1	1.7	2.8	2.1	3.5
Viability	84.7	84.1	91.1	74.4	90.2	93.8	96.2	94.1	94.7	93.0

Similar results were discussed by Marsich et al. [220] when gold nanoparticles were combined with chitosan polymer and incubated in MG63 cells for 24 h. They observed a slight increase in late apoptosis and necrosis from 2.8% to 10.8% suggesting no remarkable damage. On the other hand, U251MG tumor cells showed a significant increase of apoptosis

(early + late) when cells were treated with free bupivacaine (30.58%) related to that observed in control cells (3.83%). This effect was not observed when bupivacaine was loaded into nanogels (increase lower than 3% compared to the control sample), diminishing its apoptotic effects. These results are in agreement with previous studies that highlighted the induction of apoptotic death in different types of tumor cells (i.e. human thyroid, ovarian, prostatic or breast cancer), even at clinically relevant doses [221][222][223].

Table 3.4: Cell cycle results obtained by flow cytometry after 24 h of incubation with the different samples

	Control	PNIPAm ngels 1 mg/mL	HGNPs@PNIPAm ngels 0.1 mg/mL	HGNPs@PNIPAm-BVP ngels 0.1 mg/mL	BVP 0.1 mg/mL
			MACROPHAGES (%)		
G1	56.10	56.54	55.95	55.02	54.12
S	13.47	13.62	15.24	16.62	12.26
G2	30.43	29.84	28.80	28.35	33.62
			mMSCS (%)		
G1	23.20	51.47	32.06	36.94	18.25
S	53.63	31.29	41.77	35.89	51.59
G2	23.17	17.24	26.17	27.16	30.17
			U251MG (%)		
G1	28.93	52.00	41.92	43.13	37.51
S	41.28	19.66	22.51	22.77	29.71
G2	29.80	28.34	35.57	34.11	32.77
			FIBROBLASTS (%)		
G1	48.31	66.13	43.61	47.10	61.78
S	34.04	19.58	26.97	26.29	27.69
G2	17.65	14.30	29.42	26.60	10.53

The effects of the samples at subcytotoxic concentration on cell cycle after 24 h of incubation are depicted in Table 3.4. Here, PNIPAm nanogels and free bupivacaine showed an increase in G1 phase and a decrease in S phase, also observed in mMSCs when any sample of PNIPAm-base nanogels with or without modification was present in the sample (<20%). No remarkable differences were detected in phagocytic cell lines (macrophages) but a general G1 phase increase with a countervailing S phase decrease were noticed in U251MG cells for all samples. Thus, no accentuated changes in cell cycle were observed suggesting cell nuclei and DNA were not affected by the presence of any sample at subcytotoxic doses. Similar results have been observed previously when PNIPAm has been tested on different cell lines.

For instance, Guo et al. [224] showed similar behavior of PNIPAm at 1 mg/mL than PBS treated cells in four different cell lines.

Our results demonstrate the cytocompatibility of the synthesized materials and their potential for their biomedical application, due to the temperature-modulated on–off switch, facilitating the controlled and on demand drug delivery.

3.2.5 Conclusions

In this study, electrostatic interactions have been used to synthetize hybrid HGNPs-PNIPAm based nanogels. Surface ligand modification of HGNPs was successfully used to decorate PNIPAm-based nanogels and their stability under ionic competition was corroborated. In order to confirm their suitability for triggered drug delivery, their photothermal properties were studied under different NIR laser irradiation powers and concentrations. Despite the absorbance shift after coating HGNPs with PAH, heating efficiency of hybrid nanogels was good enough to be used under different laser-power irradiations and concentrations to control drug release using bupivacaine as model drug. Further, *in vitro* viability, metabolism and cell cycle on four different cell lines showed no remarkable effects at subcytotoxic doses: 1 mg/mL for plain PNIPAm nanogels and 0.1 mg/mL for the rest of the samples studied.

3.3 Customized hybrid microparticles using microfluidics technique[3]

3.3.1 Introduction

Engineered polymeric microparticles (MPs) have become very interesting multifunctional platforms in biomedicine[225]. Biosensing[226], drug delivery[13] or tissue engineering[227] are some of the biomedical areas in which MPs standout as advanced materials at the cutting edge of functional polymers. However, their biological suitability depends on their properties, which have a direct relationship with their size, composition, structure and configuration. Thus, controlling them has turned into the key challenge for researchers of the field[228][12].

Conventional discontinuous polymerization methods such as emulsion[12][229], dispersion[230] or spraying[231] do not allow a good control over the final MPs properties leading to polydispersity and low reproducibility[232][233][234] even at a small production scale due to the heterogeneous distribution of reactants and temperatures and to an insufficient mixing. In the last years, the production of monodisperse particles for biomedical use has stimulated great interest in a myriad of scientific and engineering fields to take advantage of their benefits in controlling drug release rates and obtaining reliable results. Continuous microfluidic devices have introduced different approaches to overcome these limitations.[235][236] Micro-sized channels permit to handle fluid flows at the microscale very precisely leading to highly reproducible synthesis and narrow size distributions in the resulting MPs due to an efficient mixing driven by molecular diffusion.[237][238] Microfluidic systems offer also some advantages against classical systems[239]: homogenous reaction conditions, portability/easy wear, high sensitivity, low energy consumption, highly integrated multifunction and easy scalability.

[3] The contents of this section were adapted from the following submitted work:

Ortiz de Solorzano, I.*; Mendoza, G; Arruebo, M; Sebastian, V.

"Customized hybrid and thermoresponsive drug delivery microparticles synthetized by photopolymerization in a one-step flow focusing continuous microreactor"

ACS Applied Materials and Interfaces

Droplet microfluidics has been demonstrated to be one of the most efficient microfluidic approaches due to the facile control of the reaction conditions and MP formation[240]. Two types of flow focusing devices have been considered in the droplet based microfluidics approach to produce spherical MP[241]: 1) a chip-based flow focusing device with a T or Ψ shaped microchannel integrated on a chip), and 2) a capillary-based flow focusing device (coaxially aligned microcapillaries). Glass-made microchips and capillaries are very expensive, as well as fragile materials.[242][243] Glass manufacturing has the limitations of a complicated welding and gas tight sealing, a difficult integration into a macro-system (connecting to the macro scale) and also any posterior modification is not economically viable. On the other hand, the design and fabrication of microfluidic silicon-based chips can be expensive, labour-intensive and more specifically, it requires clean room facilities. Furthermore, polymerization reactions can easily promote the chip blockage, precluding a stable flow. Consequently, while some problems can be overcome by careful choice of reaction conditions, there is a need for low-cost, modular components that can be easily assembled into flow-focusing devices by users lacking proficiency or access to microfabrication facilities[244]. In this sense, polymeric PTFE coaxially aligned capillaries provide a real alternative thanks to their ease of fabrication and modification, flexibility, re-usability and excellent chemical and mechanical properties and optical transparency.[245][246]

Microparticle precipitation can be provoked by ionic crosslinking[247], temperature induced gelation[248] or by polymerization[249]. Polymerization can be carried out upon heat assisted radical generation or by UV irradiated photopolymerization among other techniques.[250] In this sense, photopolymerization represents a fast process having a precise control over the characteristics of the final polymer after the induction by a UV-light lamp exposure[242] avoiding the potential problems that high temperature may provoke in biomolecules used during the synthesis. The use of light emitting diodes (LEDs) holds great promise in the field of photopolymerization due the following advantages[251]: 1) low energy consumption, 2) no ozone release, 3) low heat generation, 4) low operating costs and maintenance, 5) high lifetimes, 6) easy and safe handling, 7) 100% output immediately obtained after turn-on, and 8) easily controlled intensity. Then, the assembly of LED devices and microfluidics to control the polymerization process is an interesting alternative to deal

with the controlled production of polymer MPs. Polymerization of droplets can be accomplished upon incorporating a curing agent directly into the droplet, or in the continuous phase. The photoinitiator solubility in disperse or continuous phases will be the key value to select the polymerization approach. The droplet polymerization can be accomplished during the droplet formation, inside the microreactor chip[252][253], or in a totally separated step off-chip[254][255][256]. Time, intensity of light, and reaction components determine the composition, size and properties of the synthetized MPs.[257][258]

MPs prevail as drug delivery vehicles, considering that a large number of products based on polymer MPs have already been commercialized. To name a few: 1) Trelstar® injectable microspheres loaded with triptorelin pamoate and Enantone LP® loaded with Leuprorelin and Lupron® depot loaded with leuprolide acetate for prostate cancer treatment; 2) Sandostatin LAR® depot loaded with octreotide acetate and Somatulin L loaded with lanreotide for acromegaly treatment; 3) Risperdal Consta® depot loaded with risperidone for the treatment of schizophrenia as well as for the longer-term treatment of Bipolar I disorder; 4) Nutropin® depot loaded with recombinant human growth hormone as growth hormone regulator; and 5) Vivitrol® depot loaded with naltrexone for treating alcohol dependence and preventing relapse to opioid dependence.

One of the most promising MPs so far for biomedical applications are gel structures.[259] Their capability to respond to several external stimuli such as temperature[260] or pH[261] make them extremely interesting in biomedicine. Among them, microgels based on thermoresponsive polymers are widely studied. One of them, PNIPAm presents a broad variety of opportunities in order to customize the final product according to the desired application[262][263][264]. Crosslinking, monomer and initiator concentration as well as flow ratio, irradiation time and intensity of the UV-light source, lead to MPs with completely different properties[265]. Mechanical and thermoresponsive properties of resulted MPs are determined by the fine-tuning of synthesis variables. Synthesis of hybrid PNIPAm MPs has been conducted in conventional batch type reactors, showing the possibility to combine the function of both thermoresponsive polymers and stimuli sensitive inorganic NPs. For example, Ekici et al.[266] incorporated magnetic iron NPs in hyaluronic acid-PNIPAm nanogels obtaining a double magnetic-temperature responsive system.

Moreover, microfluidics allows the precise and controlled encapsulation of different components ranging from fluorescent dyes[267] to live cells[268][269] that can be useful in drug delivery studies or biosensing[270].

In general, the loading of cargos capable to respond to external stimuli such as light, ultrasound or magnetic fields is very interesting to explore the versatility of hybrid MPs. Superparamagnetic Fe_3O_4 NPs (SPIONs) have been used as triggers for achieving a burst release of oil cores for encapsulating lipophilic substances in core-shell PNIPAm microparticles induced by alternating magnetic fields[271]. Also, gold nanostructures have been widely used for light-triggered drug release from PNIPAm microcapsules[264]. Wang et al.[272] recently showed the possibility to activate shape transition of Au nanorods-PNIPAm hybrid MPs using high power NIR laser irradiation. Those hybrid MPs were produced in several stages, resulting in a semi-continuous process: 1) Drop formation in continuous flow, 2) Drop sedimentation in stagnant conditions for 5 minutes after collection in order to fine tune the shape and 3) Drop photopolymerization in stagnant conditions under 365 nm UV light during 5 min. Kim et al.[273] also used the same microfluidic approach to generate hollow PNIPAm microcapsules containing gold nanorods. But in this last case the double-emulsion droplets were incubated in a glass vial for 12 hours at room temperature to complete the polymerization, turning it also as a semi-continuous process, which represents a drawback to increase the productivity. Although a high control over the size and thermoresponsive properties of the MPs were achieved by the reported methods[272][273], the production of Hollow gold nanoparticles (HGNPs) and drug-loaded PNIPAm hybrid MPs in a single flow device and in continuous fashion by photopolymerization is still lacking. The development of a new flow synthesis approach that enables to address previous drawbacks would accelerate the translation of hybrid MPs towards a biomedical use.

3.3.2 Objectives

In this chapter, we describe a facile, low-cost, and efficient method of producing drug loaded HGNPs-PNIPAm hybrid MPs, capable to tune the structure of the MPs in order to achieve different pharmacokinetics in drug delivery applications. A capillary-based flow-focusing device with coaxially aligned micro capillaries was coupled to a UV-LED to facilitate the controlled droplet formation and fast polymerization at different synthesis

conditions obtaining customized MPs for purpose-specific drug delivery applications. Flow dynamics, reagent ratios and UV exposure times were studied to obtain two types of MPs that behave in a different way, accordingly to the type of drug delivery targeted. The efficient simultaneous loading of a drug and HGNPs is also described. Hollow gold nanoparticles (HGNPs) were selected as trigger NPs for on-demand light-responsive drug delivery. Bupivacaine was used as a model drug in order to test the pharmacokinetic response of MPs with different shell thicknesses together with the reversible temperature-dependence of hybrid MPs sizes. HGNPs immobilized in the hydrogel network enable the localized heating of the MPs by NIR light illumination, providing the remote control of permeability of the shell and the triggered release of bupivacaine used as a model drug. Cytotoxicity analyses were carried out with the materials developed in two different cell lines studying their subcytotoxic concentration and their effect in cell membrane and cell cycle.

3.3.3 Experimental

3.3.3.1 Synthesis of hollow gold nanoparticles (HGNPs)

Hollow gold nanoparticles (HGNPs) were synthetized following the same procedure described in section 3.2.3.1 (page 68) developed previously in our group.[95]

3.3.3.2 Microreactor characteristics

To produce HGNPs-PNIPAm hybrid microparticles, a coaxial capillary microfluidic device was assembled (Figure 3.18). The dimensions of the inner and outer capillaries were modified to tune the microparticle size. The inner and outer capillaries were made of PEEK (hydrophilic) and PTFE (hydrophobic), respectively. The inner capillary diameter was varied from 150 μm to 25 μm, whereas outer capillary diameter was altered from 560 μm to 790 μm. The dispersed phase (aqueous) was injected at low rates of flow (2.5-30 μL/min) in order to avoid co-laminar flows and unsteady microparticle formation. The inner capillary was coaxially localized under an optical microscope in order get an axisymmetric flow-focusing device where the dispersed phase is surrounded symmetrically by the continuous phase. The coaxial capillary reactor was supported in a polymer housing fabricated by 3D-printing to avoid capillaries misalignment and to favor fluid dynamic reproducibility. In the downstream flow after droplet formation, a UV irradiation provided by a 4.6 W LED (365 nm wavelength) was used to activate the photoinitiator and promote the formation of radicals to polymerize

the monomers inside the resulted droplets. LED intensity was modulated in order to obtain the optimum polymerization rate.

Two different syringe pumps (Harvard Apparatus PHD ULTRA™) at selected flow rates were used to control the drop residence time. Finally, microparticles were collected in a water recipient in order to avoid the blockage of the outer tubing.

3.3.3.3 Preparation of PNIPAm Microparticles

PNIPAm microparticles (MPs) were based on the protocol published by Choi et al.[274]. However, in this work we move to a facile-fabrication PTFE coaxial microreactor commercially available without clean-room fabrication needs. This platform is combined with a low-cost and environmentally friendly UV-LED source not used in the work described by Choi et al.[274]. Moreover, chemical composition and reaction conditions were tuned to achieve different pharmacokinetic patterns for specific drug delivery applications. In brief, two immiscible phases were coaxially injected to create a coaxial flow in a dripping mode to form w/o monodisperse droplets at the tip of the inner capillary. The disperse aqueous phase was injected through the inner capillary and was composed of the monomer NIPAM (N-isopropylacrylamide) with concentrations between 150 and 250 mg/mL (aqueous solution), and the crosslinker N,N-methylenebisacrylamide (BIS) with a monomer/crosslinker ratio ranging from 25 to 75. On the other hand, the continuous phase was injected through the outer capillary and was composed by hexadecane, Span 80 as surfactant at a constant concentration (0.043 mg/mL) and 2, 2-diethoxyacetophenone (DEAP) as photoinitiator, ranging its concentrations between 4–50 µL/mL. Flow ratio between both phases was tuned to generate MPs with different chemical and physical properties.

Hybrid HGNPs-PNIPAm MPs were obtained under the same procedure aforementioned but adding different concentrations of HGNPs in the disperse phase stream. Once the hybrid HGNPs-PNIPAm MPs were successfully produced and characterized, the production of the therapeutic vector with the ability of remotely control drug release was attempted. The production of the drug loaded hybrid HGNPs-PNIPAm MPs was addressed by a modification of previous HGNPs-PNIPAm MPs protocol, but adding diverse concentrations of bupivacaine hydrochloride monohydrate together with NIPAM monomers, crosslinker and HGNPs in the disperse phase stream of the microfluidic system.

3.3.3.4 Characterization techniques

The characterization of the resulted HGNPs was carried out by Z-Potential measurements at pH=6 in a Zeta Plus, Brookhaven Instruments Corporation, NY, USA. Ultraviolet-visible (UV-Vis) absorption spectra was retrieved via a Varian Cary® 50 UV-Visible spectrometer (Agilent Technologies, USA). In addition, Transmission Electron Microscopy (TEM) analyses were developed in a T20-FEI Tecnai thermoionic microscope operated at an acceleration voltage of 200 kV. TEM samples were prepared by dropping 20 µL of sample on a Holey carbon coated nickel grid (200 mesh), and let them dry it at room temperature.

Characterization of the chemical structure of resulted MPs was carried out by Fourier Transformed Infrared Spectroscopy (FTIR) with a Vertex 70, Bruker with an ATR Golden Gate accessory and by Proton Nuclear Magnetic Resonance (^{1}H-NMR) spectroscopy carried out on a Bruker AV-400 spectrometer operating at 400 MHz using $CDCl_3$ as solvent. In order to demonstrate the proper behavior and reversibility of conformational changes due to temperature variations, the swelling ratio, images and videos were obtained in a multidimensional real time microscope Leica AF6000 LX. The inner presence and distribution of HGNPs inside the polymeric MPs was confirmed by electronic imaging with a Cryogenic Dual Beam Nova 200 (Electron Voltage 200V-30kV; Ion voltage 2kV-30kV). Encapsulation efficiency of gold derived from HGNPs was determined by MP-AES (4100 MP-AES, Agilent Technologies, USA). Calibrations were carried out using Au standards from 0 to 10 ppm in 10 % *Aqua regia*.

Scanning Electron Microscopy (SEM) images were taken for morphology characterization. Gel Permeation Chromatography (GPC) studies were carried out in order to study the molecular weight of the resulted samples using a Waters Alliance 2695 HPLC with an evaporative light scattering detector (Waters 2420) and Plgel 5 µm MIXED-C Aglilent columns (7.5 mm x 300 mm), using THF (HPLC grade) as eluent (flow 1 mL/min). Calibration was made with poly(methyl methacrylate) standards. Samples were analyzed at 1 mg/mL after filtration using a 0.2 µm PTFE filter.

3.3.3.5 Bupivacaine release studies

Drug release experiments were carried out in 1 mL of distilled water with 1 mg/mL of loaded hybrid MPs. The samples were kept at 37ºC under stirring and at predefined times they were collected, centrifuged and the content of bupivacaine measured using Gas Chromatography (GC-MS QP2010 SE, Shimadzu). Limonene was used as internal standard.

3.3.3.6 *In vitro* cell culture studies

The cytocompatibility of solid and hollow MPs loaded with HGNPs and bupivacaine was tested in two different cell types, human dermal fibroblasts and macrophages, through the evaluation of their effects in cell metabolism, apoptosis and cell cycle. Regarding the micrometric size of the synthesized materials, which implies the unfeasibility to be phagocytized by cells, *in vitro* cell cultures were treated with the exudates released from the MPs for 24h in cell culture medium.

Cell culture, cytotoxicity assays and study of cell cycle have been carried out in the same way all along this PhD. For this reason, common details are described in Appendix I: I-Methods: Biological studies.

3.3.4 Results and discussion

3.3.4.1 Production of PNIPAm MPs in a capillary-based flow focusing device

The study of single step photopolymerization of PNIPAm MPs was carried out using the capillary-based flow-focusing device depicted in Figure 3.18. As it was described in the materials and methods section, the capillary-based flow-focusing device was coupled with a UV LED lamp in order to continuously produce thermoresponsive MPs. Both systems were assembled in a 3-D printed housing to assure a good alignment of the capillaries and an axisymmetric flow-focusing production of MPs. The UV-LED lamp was also assembled in the same housing to preserve the same light distance and thus the same light depth in the capillary in all case studies (Figure 3.18-b). Capillaries alignment and UV-light distance will be key factors to ensure an excellent MPs production reproducibility. In addition, this production strategy exerts the advantage that each MP is loaded with a similar amount of cargo and that either the polymerization rate or the grade of crosslinking can be easily controlled.

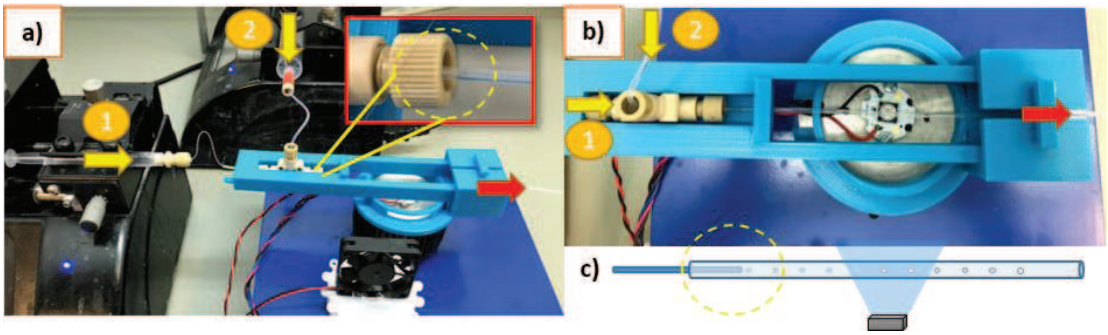

Figure 3.18: Microfluidic device. A) Complete platform used to synthesize all MPs. Upper right corner shows a detail image of the coaxial capillary microfluidic system; b) UV-LED photopolymerization stage coupled to the microfluidic device; c) Scheme of coaxial droplet formation and MPs formation after LED irradiation. (Yellow arrows represent the inlet precursor flows and red arrows guide the already formed MPs outlet flow.

As shown in Figure 3.18, the capillary-based flow-focusing device depended on the use of two immiscible streams. The hydrophilic stream (arrow 1) is injected in the inner capillary (disperse phase) and contains the monomer, crosslinker and the cargo to load inside the thermoresponsive MPs such as hollow gold nanoparticles (HGNPs) and bupivacaine. On the other hand, the hydrophobic stream (arrow 2) is the continuous phase injected in the outer capillary. The disperse phase is driven into a UV light transparent capillary and encounters the immiscible carrier stream, which is driven independently. The geometry of the junction where both immiscible phases meet, together with the phases flow rates and physical properties of fluids will determine the local flow field and the interface deformation that promote the droplet breakup in co-flowing streams. The continuous phase stream consists of hexadecane as organic solvent, Span 80® as surfactant and DEAP as photoinitiator of the polymerization process. In co-flowing streams, the dripping regime occurs at low flow rates of inner and outer fluids and is characterized by the periodic formation of individual droplets that pinch off from the inner capitally tip (Figure 3.18-c). Once the injected aqueous droplets co-flow with the continuous phase containing the photoinitiator and are introduced in the UV-irradiated region, the photoinitiator is activated and radicals enable the droplet gel formation and further polymerization.

Considering previous limitations[272][273] that unable PNIPAm MPs polymerization in continuous flow, we selected dripping regime conditions instead of jetting conditions to promote a fast polymerization during the drop flow in the microfluidic system.

The residence time of formed droplets is usually larger in dripping mode because low flow rates (inner and outer phases) are required. In addition, droplets produced under dripping mode are pinched off near the inner capillary tip, whereas in jetting regime, droplets are pinched off from an extended thread generated downstream of the inner capillary tip. Droplet formation in co-flowing microfluidic systems is sensitive to the viscous shear stress of the external flow and the capillary pressure resisting deformation of the internal phase.[242] The dimensionless capillary number (Ca) compares the relative importance between the friction force and the surface tension. Then, we considered previous studies of droplet formation in dripping mode using similar fluids[274], to select the fluid dynamic conditions to get stable droplet formation. Several factors such as stream composition or capillary dimensions were tuned in order to control the morphology and the polymerization efficiency of the system. The effect of those parameters will be discussed in the following sections

3.3.4.2 Microparticles morphology and dimensions

It is well accepted that the size of droplet formation in a co-flowing microfluidic device depends on the capillaries dimensions, and inner and outer flow rates. These parameters are highly important because then can modulate the competition between viscous shear stress of the external stream and capillary pressure resisting deformation of the internal stream. In this work, we have selected two different inner and outer capillaries to tune the size of MPs under a stable droplet formation in the dripping regime.

Figure 3.19 shows the averaged MPs diameter obtained under different capillary dimensions and flow rates. In general the most important effect is observed when the external PTFE capillary was modified.

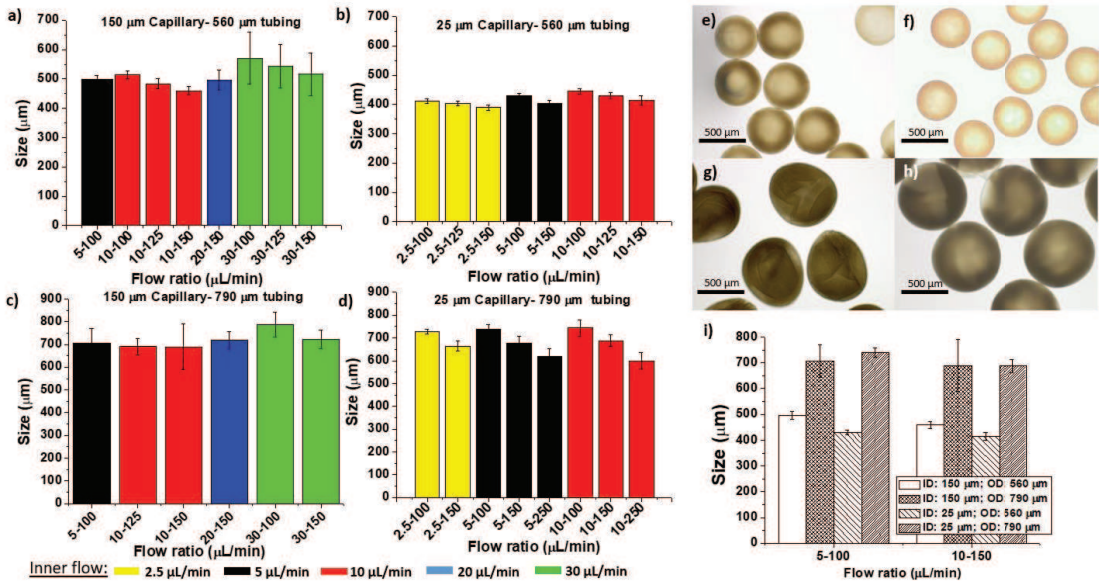

Figure 3.19: Average MPs size depending on flow ratio and inner diameter of the microreator channels. A) and b) show the results for the smallest external PTFE tubing (560 µm) and large (150 µm) and small (25 µm) internal capillary, respectively. C) and d) present the results for the larger PTFE tubing (790 µm) and large (150 µm) and small (25 µm) internal capillary, respectively. Same colors represent the same inner flow. For each of them, from left to right continuous flow increases. Inverted microscope images of MPs synthesized with flow ratio of 5-100 L/min are shown in: e) ID: 150 µm and OD 560 µm; f) ID: 25 µm and OD 560 µm; g) ID: 150 µm and OD 790 µm; h) ID: 25 µm and OD 790 µm. i) Summary and comparison of MPs diameter synthesized with two different flow ratios and all combinations of internal and external tubing diameters.

Smaller outer capillary yielded to microparticles between 400 and 500 µm (Figure 3.19 b) and a)); while a larger outer capillary diameter generated MPs over 700 µm in diameter (Figure 3.19 c) and d)). These results can be rationalized by the droplet formation mechanism. The junction close to the inner capillary tip is obstructed by the inner fluid protrusion. The continuous flow close to the protrusion is restricted when the protrusion is enlarged, establishing a pressure gradient across the protrusion. The droplet is pinched off once the pressure gradient in the continuous flow is sufficiently high to overcome the capillary pressure inside the dispersed drop. Viscous shear forces are usually sufficiently large to pinch off the droplet before it grows to block the outer capillary[275]. Then, the droplet diameter is usually smaller than the outer channel diameter. In addition, the droplet diameter is inversely proportional to the average velocity of the carrier flow because the drag force increases as the continuous phase velocity does[276]. This fact confirms that the MPs diameter increases as the flow rate of the outer stream is decreased when the inner flow rate

is kept constant (the drag force is small). On the other hand, the inner capillary size mainly affects to MPs polydispersity. A most confined droplet formation benefited from a smaller capillary, generated narrower diameter deviation. This is reflected in the different coefficient of variance (CV) of MPs size obtained with the four systems studied. While MPs CV's obtained with larger inner capillary (790 µm) have values between 15 nm (when inner flow rate is 10 µL/min) to 100 nm (when continuous phase gets to 30 µL/min), a maximum variance of 30 nm is achieved in experiments using 25 µm inner capillary diameters. Similar results were previously observed with analogous platforms.[277] Dripping frequency production (*f*) for all samples ranged between 7.5 Hz to 0.2 Hz depending on the inner flow rate and final size of MPs. Slow flow rate (2.5 µL/min) and large final MPs (~700 µm) lead to slow droplet formation and frequencies around 0.2 Hz. However, increasing the inner flow rate up to 30 µL/min and confining the size of the outer capillary, and thus the final MPs size (~400 µm), provoked a faster droplet formation and frequencies over 7.5 Hz. It is of paramount importance to highlight that this low dripping frequency was required in order to get a complete polymerization reaction in continuous fashion, a fact that is novel in this work.

According to the aforementioned polymerization requirements, it is essential to achieve certain level of polymerization rate in order to obtain stable MPs with a competent functionality for a potential biomedical use. This fact, together with the fluid dynamic restrictions to achieve a stable droplet generation, limits the available phase flow rates. It has been demonstrated that droplet size in coaxial flow platforms with flow ratios within our working limits do not change significantly[243]. However, it can still have small effects in the final MPs sizes. Statistical analysis of our results (Figure 3.20) showed some significant differences in almost all flow ratio combinations suggesting that as mentioned before keeping the same inner flow, the increase in the continuous flow rate for all samples led to a slight decrease in the final size of MPs. In all cases, monodisperse MPs were obtained with variations less than 15 % of their size in worst-case scenario (150 µm inner capillary) but with an average CV of 2.5 % in the most stable cases (25 µm inner capillary).

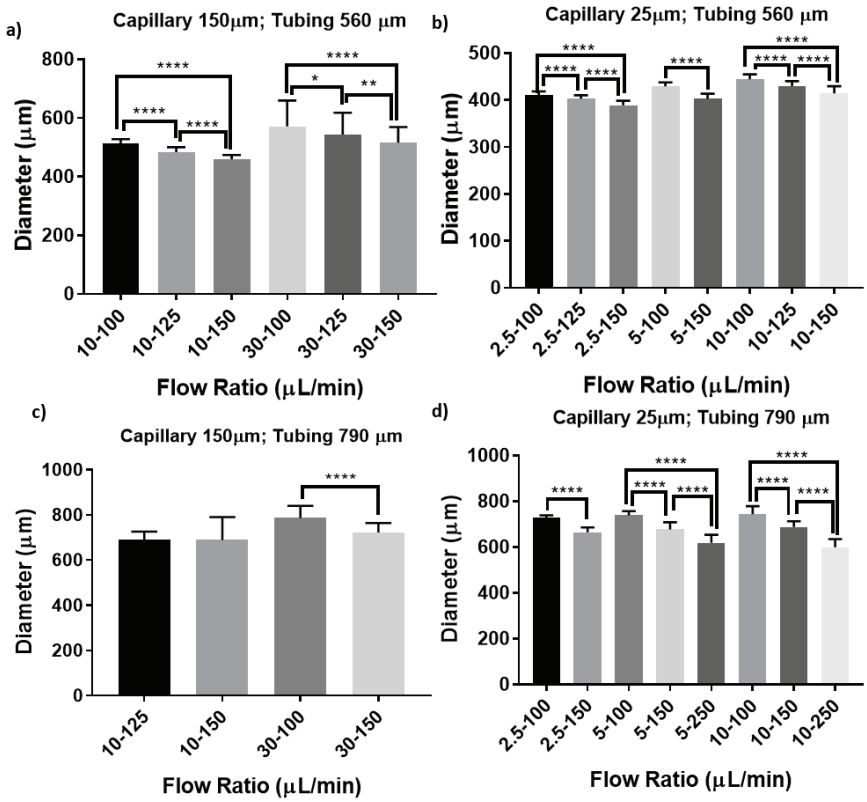

Figure 3.20: Statistical analysis for flow ratio influence in the final MPs diameter.

3.3.4.3 Polymerization efficiency and thermoresponsive properties

Photopolymerization reactions depend on a set of different variables (monomer, photoinitiator and crosslinker concentration, LED intensity and time of irradiation) and some of them were studied using this co-flowing microfluidic device. Considering that the main goal of this research is to produce MPs with on-demand light-responsive drug delivery ability and remote control of the polymeric shell permeability, we have attempted the analysis of volume ratio reduction in the resulted MPs. This parameter was also selected as a key factor to analyze the polymerization efficiency and 96rimeth-responsive properties. It must be highlighted that either an unsuccessful or limited polymerization yield can induce MP collapse, aggregation or scarce volume shrinkage upon a temperature variation in the lower critical solution temperature (LCST) range.

On the other hand, the crosslinking agent entails a key role in the shrinkage behavior of any hydrogel. Higher concentration of crosslinking molecules among formed polymeric

chains leads to more steric difficulties to achieve a complete shrinkage of the hydrogel from its swollen hydrated state to its shrunken dehydrated state.

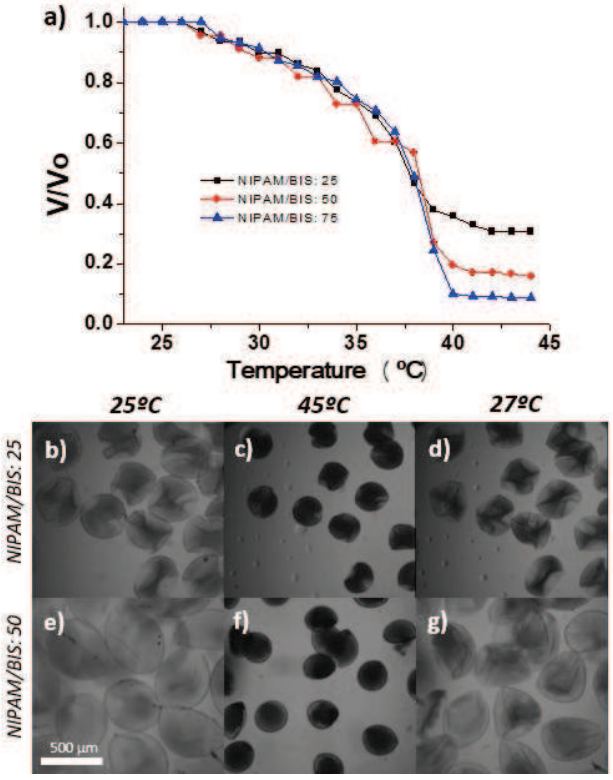

Figure 3.21: Volume change with temperature for a) MPs synthetized with 250 mg/mL monomer concentration and 40 µL DEAP and different crosslinker concentrations; b) to g) Time lap microscopy images of MPs synthetized with the same conditions at different temperatures. All samples were synthetized under flow ratio of 5/100 µL/min, inner capillary diameter: 25 µm and outer capillary: 560 µm.

Figure 3.21 a) represents the volume ratio variation with temperature obtained for three different samples containing 25, 50 and 75 monomer-crosslinker NIPAM-BIS ratio, respectively. The results confirm that all MPs produced show a fast response to environmental temperature. It is relevant that dramatic changes occur between 32- 39ºC (LCST of PNIPAm is 32ºC). This may be attributed to polydispersity in the polymer chain lengths and crosslinking degree[209][210]. It was also confirmed that the highest the NIPAM-BIS ratio, the largest the rate of volume change of the photo-polymerized MPs is. The volume change in PNIPAm MPs is rationalized because MPs are in a swollen and hydrophilic state below the LCST that is switched to a shrunken and hydrophobic state above

LCST. The state transition was studied in a time laps inverted microscope at different temperatures. Figure 3.21 b) to g) depicts representative optical images at different environmental temperatures, where the dramatic reduction of MPs size above the LCST is clearly observed and the reversibility of this process once the temperature decreases. Similar behavior was also observed when monomer concentration and monomer/crosslinker ratio (NIPAM/BIS) were modified (Figure 3.22) confirming the thermoresponsive behavior of the final polymer conforming MPs.

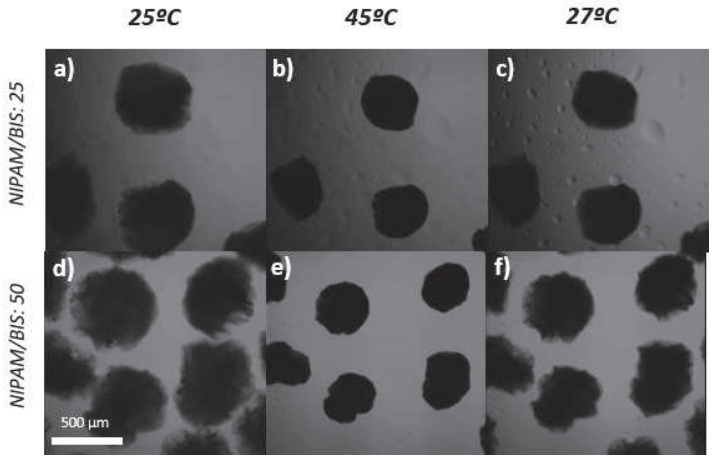

Figure 3.22: Inverted microscope images of MPs synthetized with 250 mg/mL monomer concentration and 500 µL of DEAP as photoinitiator at different crosslinking ratios and temperatures.

Polymerization efficiency is related to the polymerization rate and it has direct influence in the length of the polymeric chains formed and the possibility to collapse and reduce their volume and size under high temperatures. Figure 3.23 shows the effect of monomer (NIPAM) and photoinitiator (DEAP) concentration on the final molecular weight of resulted MPs and their ability to reduce their volume under temperature variations.

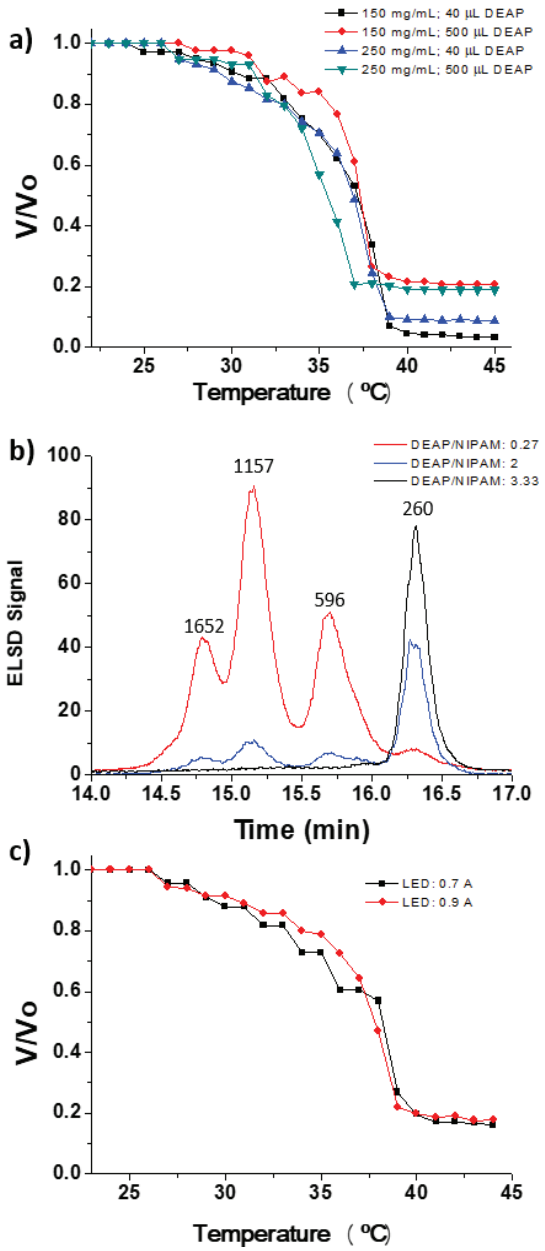

Figure 3.23: a) Volume ratio observed in samples synthesized with different monomer and photoinitiator concentrations; b) GPC results for three different samples with different DEAP/monomer ratio; c) Volume ratio shown for two samples polymerized with two different LED light irradiation intensities.

Figure 3.23 a) demonstrates that the photoinitiator (DEAP) concentration is crucial to achieve a desired grade of polymerization that is high enough to endow MPs formation with the appropriate rate of volume change and thermosensitive behavior. A high DEAP concentration leads to a high concentration of radical species that initiate polymerization.

However, the fastest the polymerization is, the shorter the polymer chains formed are and then, the less is the volume change when the environmental temperature increases. This observation was also confirmed by Gel Permeation Chromatography (GPC) (Figure 3.23 b). The GPC chromatogram provides the molecular weight distribution of the resulting species, labeling the main molecular weight peaks (Figure 3.23-b). According to GPC analysis, the molecular weight of the resulted polymer was smaller as the photoinitiator concentration was increased because a high density of monomer building blocks was activated by the radical species. This fact was also evidenced by inverted microscopy, where optical images taken at different environmental temperatures depicted a significant shrinkage as the photoinitiator content was decreased (Figure 3.24).

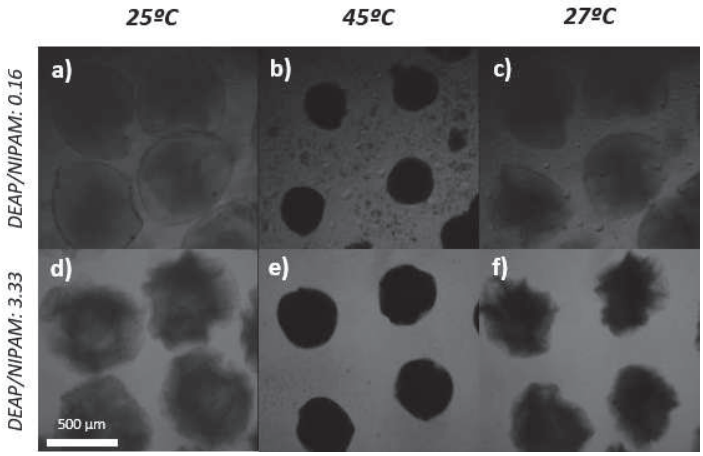

Figure 3.24: Inverted microscope images of MPs synthetized with 75 monomer-crosslinking ratio at different photoinitiator-monomer ratios and temperatures.

On the other hand, the activity of the photoinitiator molecules is determined by their stimulation source, the UV-LED light in our system. The irradiance of LED source determines the velocity of the polymerization process leading to different polymer chain lengths and thus to different photothermal properties. There is an intensity threshold that determines the minimum intensity necessary in order to obtain rigid and stable MPs and below that one no enough polymeric chains were formed and MPs did not keep their shape after exiting the microfluidic platform. Intensities from 0.2 to 0.9 A were used in our study finding the threshold described before at 0.7 A. At intensities of 0.2 and 0.4 A no MP formation took place and easily breakable MPs were obtained, respectively. However, above 0.7 A no significant changes were observed when UV-LED light intensity was increased to 0.9 A (Figure 3.23 c) in our system.

As the polymerization is initiated at the interface of the aqueous/organic phase of detached droplets, the diffusion of radical species that conduct the polymerization reaction might have a relevant role in the MPs structure. In these terms, hollow or solid MPs could be produced depending on the radical species droplet internalization. Kim et al.[253] corroborated the relationship of a high polymerization ratio with the improved mechanical strength of the resulted MPs. Long irradiation times, high DEAP concentration and high irradiation intensity produced a solid structure and mechanically resistant MPs. However, the solid MPs obtained under these conditions resulted in low shrinkage ratios (~24 v/v%).

The 101rimethylami glycol diacrylate (PEGDA) photopolymerization reaction from a droplet microfluidic device emulsification process was also studied by Filatov et al.[258] showing the importance of the photoinitiator concentration and the reaction time in the final core-shell structure and MPs resistance. However, a plateau in the reaction time exists at very high photoinitiator concentration and increasing photoinitiator concentration does not lead to a faster polymerization. On the other hand, when the monomer concentration increases, more monomer molecules are available at the droplet surface leading to thicker MP shells and thus more mechanically resistant MPs. This is explained due to a faster polymerization process with the same reaction time.

Considering our previous remarks, it was devised the formation of two types of MPs with a different internal structure and good mechanical properties, where the density of polymeric chains was tuned in order to modulate the void fraction and the rate of volume shrinkage. Figure 3.25 shows some of the most representative MPs produced by tuning the polymerization rate, either by modifying the flow rate of the continuous outer phase or the photoinitiator concentration. MPs produced at the opposite conditions were discarded because they unfeasible applicability. That is, MPs produced with the smallest flow rate and photoinitiator concentration (Figure 3.25-a), because they were not mechanically stable. On the other hand, MPs produced at the highest flow rate and photoinitiator concentration (Figure 3.25-b), because the high density of polymeric chains and rigidity would seriously affect the rate of volume shrinkage. As a result, intermediate conditions were selected as the proper ones in order to load the cargo and study the temperature assisted drug release (Figure 3.25 b-c).

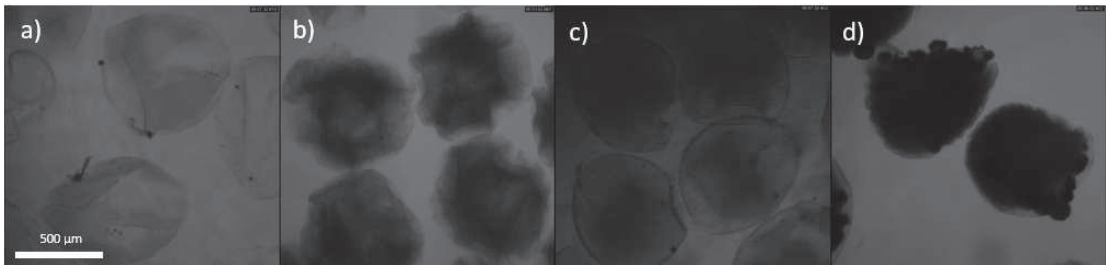

Figure 3.25: From left to right MPs synthesized with monomer concentration of 150 mg/mL (a) and b)) and 250 mg/mL (c) and d)). Images a) and c) were synthetized with 40 µL of photoinitiator (DEAP); while 500 µL of photoinitiator (DEAP) were used in images b) and d).

Transition temperature in drug delivery applications may lead to different drug release profiles, which could be appropriate for a broad variety of disease treatments. This tuning of LCST can be achieved by combining different monomers in the polymeric structure. It has been previously demonstrated that the presence of diverse functional groups at the side chains of the polymer chain results in variations of hydrophobicity and thus polymer-water interactions[278]. Acrylamide monomer has been widely used in order to increase transition temperature in PNIPAm-based polymers. The lack of isopropyl groups in its side chain increases water-polymer interactions making more energy necessary to fold the polymer chains[278].

In our proposed microfluidic platform, this varied monomer combinations driven to obtain customized thermoresponsive MPs with desired LCST is easy to carry out. We demonstrated that adding Acrylamide (Aam) as a co-monomer the LCST of the resulting MPs, this transition temperature could be easily modified (See Figure 3.26). LCSTs for MPs with different acrylamide percentages are summarized in Table 3.5.

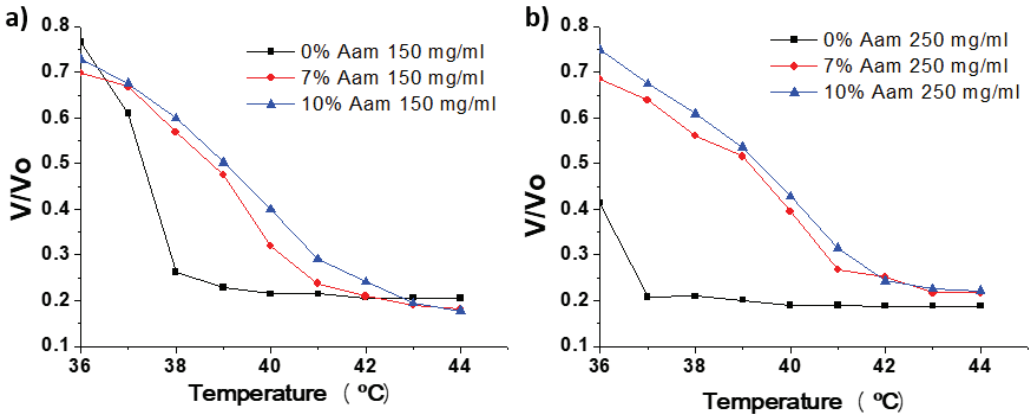

Figure 3.26: Volume ratio change with temperature for NIPAM-co-Aam polymer showing LCST shift. A) 150 mg/mL total monomer concentration; a) 250 mg/mL total monomer concentration

Table 3.5: LCST summary for P(NIPAM-co-Aam) MPs. LCST were selected as the 50% of volume change during temperature increase

Sample	**150 mg/mL**	**250 mg/mL**
PNIPAm	37.32 °C	35.50 °C
P(NIPAM-co-Aam) 7 %	38.69 °C	39.12 °C
P(NIPAM-co-Aam) 10 %	39.06°C	39.45 °C

In all cases, the addition of extra Aam monomers leads to higher LCST over body temperature making them ideal for triggered on-demand drug delivery applications. Therefore, the proposed microfluidic platform allows modifying the particle size, its LCST and composition easily depending on the needs.

3.3.4.4 HGNPs encapsulation and NIR triggered drug delivery

It is well known that hollow gold nanoparticles (HGNPs) present excellent plasmonic properties based on their Surface Plasmon Resonance (SPR) band with a maximum at ~808 nm. As it was mentioned previously, this property has been widely used in biomedical applications because of the coincidence with the absorption water window. Thus, we took advantage of the optical properties of HGNPs in order to obtain hybrid thermoresponsive MPs for triggered drug delivery.

For this, we added the prepared HGNPs in the disperse phase of the coaxial flow microfluidic device to translate the synthesis conditions optimized in the previous section. Based on previous works where nanoparticles with photothermal properties[279][272] were

encapsulated, the concentration of HGNPs was set at 10 mg/mL. Further, we confirmed their NIR responsive effect under laser irradiation (2.2 W/cm^2; λ= 808 nm). (Figure 3.27)

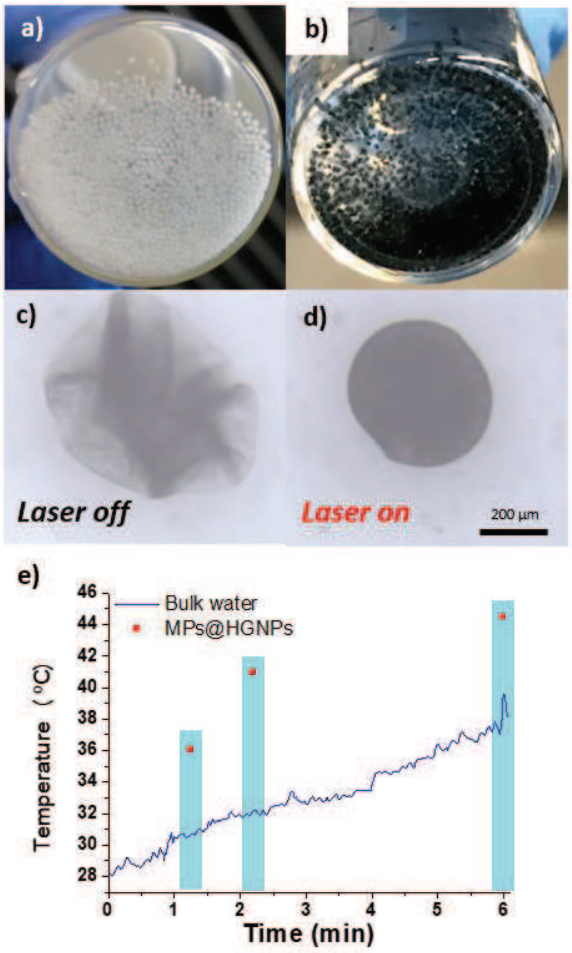

Figure 3.27: a) and b) PNIPAm MPs without and with HGNPs; c) and d) Optical microscopy images without and with laser irradiation (2.2 W/cm^2); e) Time heating evolution of bulk water in presence of MPs@HGNPs. Red dots represent selected times where MPs@HGNPs cluster (i.e., agglomerated MPs) temperature was measured.

Figure 3.27 a) and b) show the notable color differences when HGNPs were loaded inside PNIPAm MPs (66% HGNPs encapsulation efficiency obtained by MP-AES analysis). It must be highlighted than the proposed production approach enables a selective loading of HGNPs, where the dose of HGNPs can be easily modified by tuning their concentration in the disperse phase stream. No size and shape modifications were observed after adding HGNPs to the disperse phase together with the monomer molecules. The continuous phase wraps the droplet and inhibits the diffusion of HGNPs during the polymerization process. It was selected an IR laser with a wavelength of 808 nm (2.2 W/cm^2) to heat the MPs@HGNPs

owing to its longer penetration depth compared to visible light. MPs@HGNPs were illuminated at 25ºC with the laser to study the rate of volume shrinkage. As it is depicted in Figure 3.27 d), upon laser illumination, MPs@HGNPs shrunk due to a local temperature increase caused by the light-to-heat transduction generated by the HGNPs. This result confirms the new functionality of the proposed hybrid MPs, where the MP collapse can be triggered by externally applied NIR illumination. It is also interesting to remark that the optical properties of HGNPs were not modified during the loading and polymerization processes under the presence of highly oxidant radical species. The shape transition during the MPs@HGNPs collapse upon laser heating and the reversibility of the process once the laser was switched off were also recorded in a single MP using time-lapse microscopy, obtaining that the collapse occurs instantaneously at the selected laser intensity.

Temperature rise under NIR laser irradiation is plotted in Figure 3.27 e). Due to the size of MPs studied, MPs@HGNPs settle in the bottom part of the vial and temperature of bulk water around them and the one of the MPs@HGNPs themselves were tested separately. It was observed that the bulk water temperature rose slowly under the presence of MPs@HGNPs, however, it was the MPs@HGNPs cluster itself the one which suffered an abrupt temperature rise. Temperature was monitored with a thermocouple located in the middle of MPs@HGNPs cluster at selected times. It increased clearly above the aqueous medium temperature almost 10 ºC reaching 45 ºC after 6 minutes of irradiation. This suggested a local heating effect in the surroundings of the HNPs loaded MPs, what together with the shrunk behavior observed under optical microscopy confirm their suitability for triggered on demand drug delivery applications.

As it was described in the previous section, two different polymeric MPs were selected for drug loading and release studies obtained under distinct synthesis conditions. The porosity of drug delivery vectors determines not only their drug loading capacity but also drug release profiles once they are under physiological conditions. In our case, two kinds of MPs determined as hollow (*NIPAM: 250 mg/mL and DEAP: 40 µL*) and solid (*NIPAM: 150 mg/mL and DEAP: 500 µL*) were studied. Even with the same size, the structure of the MPs studied was different: hollow MPs were more fragile and with a thinner polymeric shell while solid MPs had a polymeric dense structure even in their core, reducing their porosity

but increasing their mechanical strength. Bupivacaine was selected as model drug due to its common applications in peripheral nerve blockage in pain management and due to its inert behavior under UV-LED light irradiation. Figure 3.28 a) shows the lack of light absorption at UV-LED light irradiation and the stability of two sample concentration was corroborated by GC-MS measurements before and after 4 hours of LED irradiation showing no significant changes.(Figure 3.28 b))

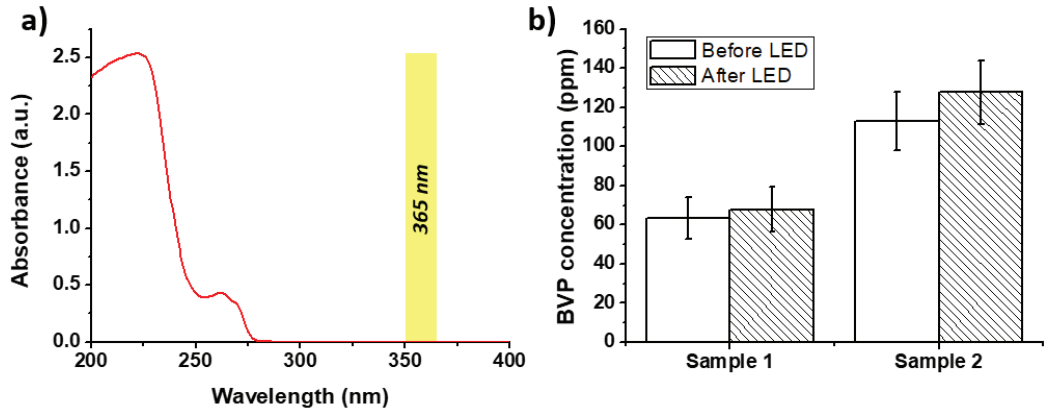

Figure 3.28: a) Absorbance spectrum of Bupivacaine; b) Two bupivacaine solutions: GC-MS results before and after 4 hours of UV-LED irradiation.

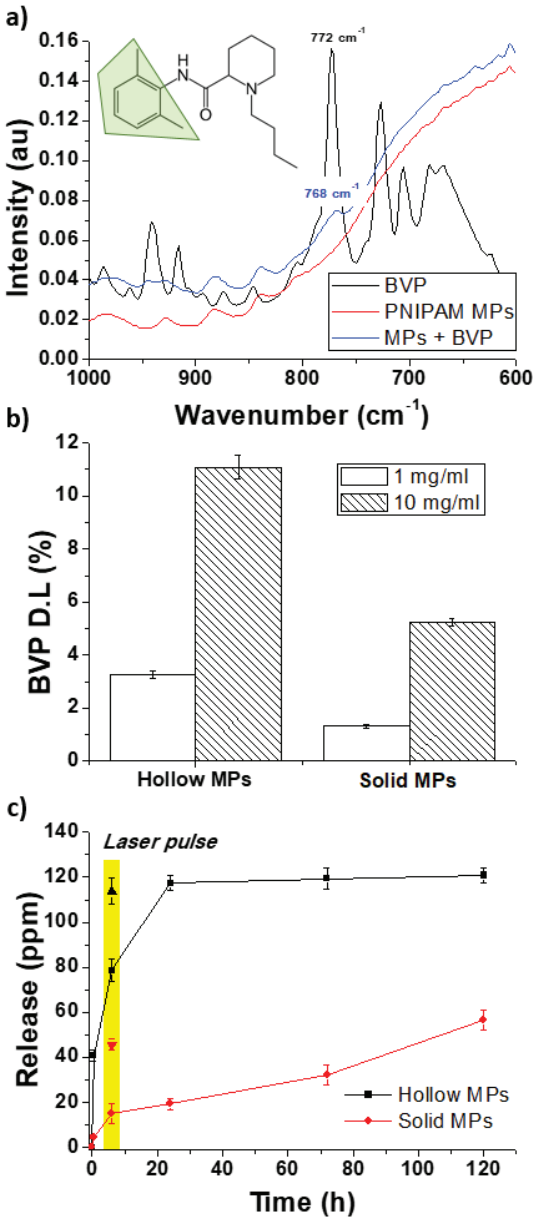

Figure 3.29: a) FTIR spectra of Bupivacaine (BVP), PNIPAm-based MPs and BVP loaded MPs; b) Drug loading of hollow and solid MPs after adding two different BVP concentrations in the disperse phase; c) Cumulative release profile for both solid and hollow MPs. Yellow band shows a burst release under a single laser pulse irradiation.

Figure 3.29 a) shows the FTIR spectra for empty and BVP loaded MPs together with free BVP. Here, we can observe the existence of a shift in the peak (772 to 768 nm^{-1}) associated to the aromatic ring of BVP molecule suggesting an interaction between the polymer and bupivacaine molecules present in the sample. In Figure 3.29 b) drug loadings

of BVP for hollow and solid MPs are compared. The higher the BVP content is, the higher the final BVP content in the sample. However, notable differences are present when comparing hollow and solid MPs. While solid MPs are composed by an inner entangled core composed of polymeric chains, hollow MPs have a central empty space available to adsorb the drug inside. Also, the thickness of the MPs wall has an important effect in the release profile as is depicted in Figure 3.29 c). The drug release at body temperature for hollow MPs is faster than the one obtained for solid ones. Bupivacaine molecules interact more with a larger amount of polymeric chains inside solid MPs probably due to hydrogen bonding and hydrophobic Van der Waals interactions leading to a sustained drug release. These two drug delivery vectors can be used for different purposes. Khan et al.[277] have already observed a similar behavior in the simultaneous release of two drugs (i.e., ketoprofen and ranitidine HCl) from MPs with different polymer density. A faster release was achieved when crosslinker and monomer concentrations decreased.

3.3.4.5 Cell viability, apoptosis and cycle evaluation

Due to the MPs sub-millimetric size and inability to be internalized by cells, the cytocompatibility studies were carried out in two different cell lines (phagocytic macrophages and human dermal fibroblasts) analyzing the exudates released (i.e., leaching liquour) by the MPs during 24h as described in the materials and methods section. Figure 3.30 presents cell viability results for concentrations ranging from 0.1 to 0.5 mg/mL and the corresponding bupivacaine concentration. High cell viability (> 70%) was observed for all MPs concentrations tested for both solid and hollow MPs exudates showing more compatibility than free BVP in human fibroblast. Following studies were developed at a MPs concentration of 0.5 mg/mL as it was considered as subcytotoxic dose following the ISO 10993-5 standard, which states a viability of 70% as the threshold for considering non-cytotoxic concentrations.[280]

Cell apoptosis studies by flow cytometry were selected to show the potential cell membrane effect caused by the MPs exudes (Table 3.6). The incubation of the two cell lines (TPH1 macrophages and human dermal fibroblasts) at the subcytotoxic concentration (0.5 mg/mL) with MPs exudates loaded with HGNPs and BVP did not show remarkable changes compared to non-treated samples. Only macrophages showed a slight increase in necrosis

and late apoptosis for hollow and solid loaded MPs, respectively (<3%) and a consequent decrease in viability (<4%).

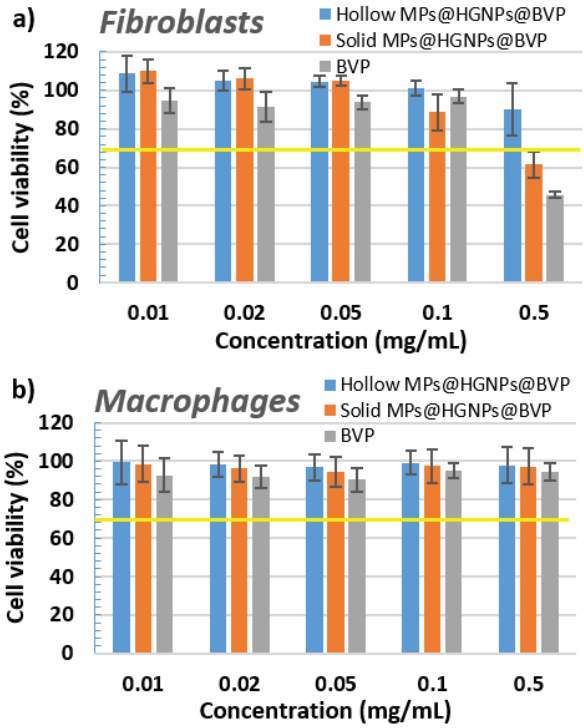

Figure 3.30: Cytotoxicity results for two cell lines: a) Human fibroblasts and b) macrophages for two different shell thickness MPs denominated solid and hollow MPs loaded with HGNPs and Bupivacaine; and free bupivacaine. Mean values and SD obtained from at least three independent samples.

Table 3.6: Apoptosis results obtained by flow cytometry (%)

	Control (%)	Exude solid MPs (%)	Exude hollow MPs (%)
	Macrophages		
Necrosis	4.43	2.09	7.41
Late apoptosis	1.72	5.74	2.58
Early apoptosis	0.59	1.44	1.14
Viability	93.26	90.74	88.87
	Fibroblasts		
Necrosis	0.51	0.33	0.38
Late apoptosis	1.99	2.47	2.01
Early apoptosis	3.05	3.18	2.76
Viability	94.44	94.02	94.85

Cell cycle studies are depicted in Table 3.7. Cell treatment for 24 h with HGNPs-BVP loaded PNIPAm MPs exudates at subcytotoxic doses (0.5 mg/mL) did not display

accentuated effects on cell cycle. A slight increase in G2 phase in macrophages (<2%) and in S phase in fibroblasts (<4%) are the only changes observed after treatment compared to control samples. Therefore, at the doses tested the exudates released by the MPs here prepared did not show cytotoxicity, cell-cycle arrest or apoptotic induction.

Table 3.7: Cell cycle results obtained by flow cytometry (%)

	Control (%)	Exudates of solid MPs (%)	Exudates of hollow MPs (%)
	Macrophages		
G1	55.72	53.44	54.11
S	13.32	13.49	13.41
G2	30.96	33.08	32.48
	Fibroblasts		
G1	45.72	43.83	44.19
S	31.34	35.99	35.17
G2	22.94	20.18	20.64

3.3.5 Conclusions

Summing up, in this section we obtained thermosensitive light-responsive hybrid MPs loaded with an anesthetic drug using an innovative one-step continuous synthesis method. A simple, versatile and high productive microfluidic synthesis was developed for this purpose and the reaction conditions influence in the final MPs characteristics was also analyzed. The presence of plasmonic HGNPs in the MPs was demonstrated as potential trigger for drug delivery applications in biomedicine. In order to test drug loading and release behavior, bupivacaine was selected as a drug of interest and the interaction, loading capacity and release studies confirmed the suitability of the MPs obtained for obtaining tunable drug delivery profiles. Finally, cytotoxicity assays showed a subcytotoxic dose of 0.5 mg/mL further used to study the cell metabolism and cell cycle showing no remarkable influence on any of the cell lines studied.

3.4 General conclusions

In conclusion, this chapter collect three different approaches of hybrid nano- and microparticles for triggered on demand local drug delivery. Complete cleavable structures have been corroborated as excellent approach to overcome bioaccumulation problems of

common drug delivery vectors showing excellent photothermal and drug release properties together with good cytocompatibility. Stable electrostatically combined PNIPAm-HGNPs nanogels have been proved to be a simple and easy-synthetized approach for power laser controlled local drug delivery applications suitable for biomedicine applications at subcytotoxic concentrations. Finally, continuous production of customized hybrid microparticles have been evidenced to be a novel approach for the synthesis of reversible laser-activated drug-delivery vectors for local drug administration.

CHAPTER IV

BIODISTRIBUTION ANALYSIS

"Your theory is crazy, but it's not crazy enough to be true"

Niels Bohr, Physicist (1958)

Chapter IV

BIODISTRIBUTION ANALYSIS

Summary

In this chapter, the in vivo optical tracking of polymeric micro- and nanomaterials based on poly(lactic-co-glycolic) acid and thermoresponsive poly(N-isopropylacrylamide) tagged with the fluorescent probe IR-820 is described. This dye was chemically modified to allow its covalent coupling to these materials, which could be potentially used as drug depots of different therapeutic molecules. The resulting labelled products were completely characterized. In vitro biological studies were carried out to evaluate the subcytotoxic doses of those materials and a spatiotemporal in vivo tracking evaluated their local persistence and confirmed high biocompatibility after pathological studies.

4 Biodistribution analysis

4.1 Introduction

As mentioned in previous chapters, the use of micro- and nanomaterials as carriers of therapeutic molecules can enhance the efficiency of treatments while avoiding side effects thanks to the development of controlled drug delivery systems.[281] Some of them have been discussed in Chapter III, where different hybrid platforms have been studied for site-specific treatment of local pain. The development of this kind of targeted therapies is closely linked to the profound knowledge of drug biodistribution in order to increase selectivity and decrease undesired side effects.

In order to deepen the understanding of *in vivo* drug biodistribution, the tracking of drug carriers has been widely studied by using radiotracers, obtaining the distribution of the drug carrier by liquid scintillation counting[282] of by scintillation proximity assays based on immune recognition[283]. However, the synthesis and manipulation of radiolabeled materials imply some occupational risks and the required resources are not always affordable; therefore, the search for safe and equally effective technologies represents an ongoing scientific task.

Medical imaging encompasses techniques based on different physical or chemical approaches such as ultrasonography, elastography, molecular imaging or chemical shift imaging[284]. Imaging techniques are widely used in the diagnosis, progression and treatment of different diseases in the medical field due to their outstanding role in the deeper understanding of *in vivo* molecular events[285]. These techniques are classified into morphological (e.g. magnetic resonance imaging (MRI) and computed tomography (CT)) and functional (e.g., modern CT and functional magnetic resonance imaging, fMRI) and molecular techniques (e.g., optical imaging, , positron emission tomography (PET) and single photon emission computerized tomography (SPECT))[286][287].

Optical imaging allows the non-invasive real-time imaging of physiological events in living organisms using non-ionizing radiation. It is based on the light emission by bioluminescence, in which the enzyme luciferase and the substrate luciferin take part, or by fluorescence, which involves the absorption of light at specific wavelength to emit light at

higher wavelength[286][288]. Bioluminescence relies on the conversion of chemical energy into light and the detection of photons emitted by living cells or tissues, though with the requirement of the expression of the enzyme luciferase, whereas fluorescence is supported by light absorption without the involvement of an endogenous molecule[288]. Optical imaging techniques present advantages compared to other diagnostic techniques, such as safer manipulation, reduced costs and a faster and more reliable response, as they are not restricted to anatomical or physiological processes[285][289][290]. Considering these advantages, an optical imaging technique called IVIS® (*in vivo* imaging system) has emerged as a useful preclinical equipment for facilitating the diagnosis in different biomedical fields such as pharmacology, oncology or immunology[289]. It is widely used in research to visualize multiple events simultaneously and to extract the maximum information from each subject leading to a greater biological understanding.

In this regard, the development of safe and novel fluorescent organic dyes has yielded interesting derivatives which combine in the same molecule water solubility (e.g. mediated by functionalization), high quantum yield, reduced photobleaching and stability to enhance the molecule lifetime and to guarantee near infrared (NIR) emission with an elevated signal-to-noise ratio[291][292]. NIR dyes appear as useful tools for fluorescence detection and imaging due to their reduced light scattering and almost no interference regarding tissue autofluorescence [293][294][295]. Among them, only methylene blue and indocyanine green (ICG), are approved dyes by the Food and Drug Administration (FDA) as extrinsic fluorescent contrast agents [296]. The medical uses of methylene blue are much more restricted than those of ICG, which has been widely used in the evaluation of hepatic and cardiac function and in ophthalmic angiography[294][296][297]. However, its low stability, slight *in vitro* toxicity (10 μM after 72 h of incubation with murine endothelial cells (SVEC4-10) and macrophages (J774)) and quick liver clearance have been reported [298], pointing to the outstanding necessity of developing novel or even superior NIR dyes for biomedical imaging.

IR-820 is a NIR dye with and improved *in vitro* and *in vivo* stability compared to ICG and the same optical properties [299]. Furthermore, its chemical modification to be anchored to polymers has been shown to be a more effective approach than the use of a free fluorophore

[300], highlighting its potential to allow an efficient tracking of the *in vivo* drug carrier biodistribution.

The biodegradable and biocompatible properties of polymeric micro- and nanomaterials make them very attractive for tuning their lifetime and play an important role in the sustained or triggered release of drugs [297] or even in the photodynamic treatment of cancer [301][302][303]. Poly(lactic-co-glycolic) acid (PLGA), a building polymer in many FDA-approved biomedical products, has been widely described as a 118rimethylami protecting NIR dyes from degradation [304][305][306]. This fact, together with the well-known biocompatibility of PLGA for therapeutic approaches, points to the suitability of these systems for *in vivo* biomedical imaging. In fact, the successful loading of drugs and NIR dyes in PLGA nanosystems has been widely evaluated in *in vivo* tumor models [307][308]. The thermoresponsive polymer poly(N-isopropylacrylamide) (PNIPAm) shows the possibility to trigger the delivery of an adsorbed or encapsulated drug in response to temperature changes. The increase on temperature above its lower critical solution temperature (LCST) produces the collapse of the polymer domains and the shrinkage of the forming particles [195]. Furthermore, the need for long-term therapies in pathologies as diverse as cancer, cardiovascular affections or chronic pain has produced the compelling development of sustained or triggerable release carriers. In order to obtain the required drug release avoiding multiple administrations, these novel carriers based on PLGA and/or PNIPAm have shown *in vivo* release times up to 28 days after local administration, much longer than systemic administrations and preventing the non-specific delivery of drugs and the subsequent side effects [309][310][311].

4.2 Objectives

This chapter studies the development of novel polymeric micro- and nanomaterials of different sizes, which were dye-labelled with the NIR dye IR-820 to track their *in vivo* biodistribution and persistence after intramuscular (IM) and subcutaneous (SC) administration in nude mice. The main objective is the evaluation of the local persistence of micro- and nanoparticles based on the well-known and widely used polymers PNIPAm and PLGA. In order to achieve this goal, the chemical modification of the dye has been carried out to enable its covalent attachment to the polymers as terminal groups and to obtain stable

and biocompatible materials for potential traceable drug delivery applications. The dye-labelled materials are physico-chemically characterized and *in vitro* tested for their cytotoxicity on different cell lines. Further, *in vivo* studies after IM and SC injection are shown to test their persistence and biodistribution and finally, pathological studies are evaluated to test tissue response after administration.

4.3 Experimental

4.3.1 Synthesis of PLGA and PNIPAm tagged materials

Synthesis of IR820-COOH

A round bottom flask containing 150 mg of IR-820 (80% dye, 0.141 mmol, 1 eq.) and 63 mg of 6-aminocaproic acid (0.480 mmol, 3.4 eq) was purged with argon prior to the addition of 5 mL of dry DMF and 0.1 mL of 119rimethylamine. The green solution was stirred and heated in a pre-warmed oil bath at 85 °C for 3 h under argon atmosphere and protected from the light. The mixture upon reaction turned into a deep blue color and after completing the reaction time the stirring was stopped, the reaction was cooled down and the solvent evaporated under vacuum to dryness. The crude was purified by column chromatography using a polarity gradient (ethyl acetate-methanol 7:3 to 3:2) and dried under vacuum obtaining 105 mg of IR820-COOH.

Synthesis of IR820-NH_2

A round bottom flask containing 150 mg of IR-820 (80% dye, 0.142 mmol, 1 eq.) and 20.52 mg of 1,6-hexanediamine (0.142 mmol, 1 eq) was purged with argon. 25 mL of dry DMF and 0.1 mL of 119rimethylamine were added. The green solution, under argon atmosphere, was protected from the light, stirred and heated in a pre-warmed oil bath at 85 °C for 3 h. After completing the reaction time the stirring was stopped, the blue mixture was cooled down and the solvent evaporated under vacuum to dryness. The crude was purified by column chromatography using a polarity gradient (ethyl acetate-methanol 7:3 to pure methanol) and dried under vacuum obtaining 63 mg of IR820-NH_2.

Synthesis of PLGA-IR820

The carboxylic group of the polymer was first activated through reaction with EDC and NHS followed by the coupling reaction with IR820-NH_2. Then, 100 mg of PLGA (3.2

μmol, 1 eq) were stirred with 6.1 mg of EDC (32 μmol, 10 eq) and 3.7 mg of NHS (32 μmol, 10 eq) in 1 mL of dry DMF under argon atmosphere at room temperature. After 2 h of reaction, a solution of IR820-NH_2 was prepared under argon atmosphere in a round bottom flask, protected from the light with 3.6 mg of IR820-NH_2 (3.8 μmol, 1.2 eq) dissolved in 134 μL of 120rimethylamine-dry DMF (20 μL in 2 mL of DMF, 15.2 μmol, 4 eq) and 100 μL of dry DMF. The content of the vial was then added to the dye mixture and later washed with a total amount of 600 μL of dry DMF. The mixture was stirred at room temperature overnight protected from the light. After, the solvent was evaporated to dryness under vacuum and the solid obtained was purified dissolving it in acetone (3 mL) and precipitated with methanol (30 mL) for 3 times. 93 mg of polymer (90% efficiency were obtained.

Synthesis of PNIPAm-IR820

In this procedure, the carboxylic group of IR820-COOH was first activated through reaction with EDC and NHS followed by the coupling reaction with PNIPAm. In a round bottom flask protected from the light, 20.6 mg of IR820-COOH (21.8 μmol, 1.2 eq) were stirred with 16.8 mg of EDC (87.6 μmol, 4.8 eq) and 10 mg of NHS (86.9 μmol, 4.8 eq) in 1 mL of dry DMF under argon atmosphere at room temperature. After 2 h of reaction, a solution of PNIPAm was added under argon atmosphere over the activated IR820-COOH. PNIPAm (100 mg, 18.2 μmol, 1 eq) was dissolved in 800 μL of dry DMF and 6.8 μL of 120rimethylamine (92.5 μmol, 5 eq) added as a solution in DMF (40 μL TEA in 1 mL of DMF, 170 μL of the solution). The vial was washed with 500 μL of dry DMF and the solution added to the reaction mixture. The mixture was stirred at room temperature overnight and protected from the light. After, the solvent was evaporated to dryness under vacuum, methanol was added to remove the remaining DMF in the crude reaction and the solid obtained was purified by dialysis against water for 3 days. After lyophilisation, 86 mg of PNIPAm-IR820 were obtained (78% efficiency).

4.3.2 Preparation of fluorescently labelled polymeric nanoparticles

The tagged nanoparticles (NPs) were synthesized with the pre-labeled materials (PLGA IR820-NH_2 NPs and PNIPAm-IR820-COOH NPs) or were first synthesized and then labeled with the modified dye (PNIPAm-IR820-COOH post-synthesis NPs) or with the

commercial IR-820 (PLGA-IR820 encapsulated NPs, PNIPAm-IR820 microgels and PNIPAm-IR820 microparticles).

Preparation of PLGA nanoparticles

50 mg of the pre-synthetized PLGA-IR820-NH_2 polymer were dissolved with 150 mg of Pluronic-F68 in 5 mL of ethyl acetate. 10 mL of water were then added to the solution and the mixture was sonicated 25 sec in an ice bath with a sonicator probe at 40% of amplitude. The cloudy suspension was stirred for several hours until the complete evaporation of the organic solvent. The remaining aqueous suspension was centrifuged (10 min, 4500 rpm) to concentrate NPs, which were finally resuspended in water to a final volume of 10 mL.

The encapsulation of IR-820 in PLGA (PLGA-IR820 encapsulated NPs) was performed following also the procedure explained above but with slight modifications. Commercial PLGA-COOH was used and 625 µg of IR-820 were added to the initial ethyl acetate solution. The cleaning centrifugation step was performed twice in order to remove the not encapsulated dye.

Preparation of PNIPAm nanoparticles

25 mg of the corresponding PNIPAm polymer and 125 mg of Pluronic-F68 were dissolved in 5 mL of chloroform and subsequently 10 mL of water were added. The mixture was sonicated for 25 sec with a sonicator probe at 40% of amplitude in an ice bath. The cloudy suspension was stirred at 700 rpm for several hours to evaporate the chloroform. The remaining aqueous phase was centrifuged for 10 min at 4500 rpm to remove the supernatant containing the polymeric material not incorporated into the NPs. NPs were then resuspended in water to a final volume of 10 mL.

Procedure to functionalize pre-synthesized PNIPAm nanoparticles

The carboxylic acid group of IR820-COOH was activated prior to the reaction with PNIPAm. 4.5 mg of the dye (4.54 µmol, 1 equivalent) were stirred for 1 h at room temperature with 8.7 mg of EDC (45.4 µmol, 10 eq) and 5.23 mg of NHS (45.4 µmol, 10 eq) in 1 mL of water. The activated dye was then added to 10 mL of the PNIPAm nanoparticle suspension (25 mg of PNIPAm, 4.54 µmol, 1 equivalent) and the mixture was stirred at room

temperature overnight. NPs were finally centrifuged for 10 min at 4500 rpm, the supernatant was removed and the pellet containing the NPs was resuspended in 10 mL of water and centrifuged again to discard the excess of dye and EDC/NHS.

Preparation of PNIPAm Microgels

PNIPAm microgels were synthetized following the synthesis shown in Chapter III, section 693.2.3.2 (page 69) of this work.

Preparation of PNIPAm Microparticles

PNIPAm microparticles (MPs) were prepared following the protocol described in Chapter III, section 3.3.3.3 (page 89) using the microfluidic-LED continuous platform.

Loading of IR-820 commercial dye in PNIPAm microgels and microparticles

Microgels or MPs were dispersed in water with a final concentration of 5 mg/mL. A polymer/dye weight ratio of 1:10 was kept in contact with the commercial IR-820 dye for 3 days. Then, dye-labeled polymers were washed twice by centrifugation to discard the not encapsulated dye and re-suspended in water to a final concentration of 5 mg/mL.

4.3.3 *In vitro* studies

Cell culture, cytotoxicity assays, study of cell cycle and endotoxin analysis have been carried out in the same way all along this PhD. For this reason, common details are described in Appendix I: I-Methods: Biological studies.

4.3.4 *In vivo* studies

All procedures were carried out under Project License 02/16 approved by the Ethics Committee for Animal Experiments of the University of Zaragoza (Spain). The care and use of animals were performed accordingly with the Spanish Policy for Animal Protection RD53/2013, which meets the European Union Directive 2010/63 on the protection of animals used for experimental and other scientific purposes.

Five- to eight-week-old female BALB/c nu/nu mice were used for these studies. The mice were anesthetized with 5% isoflurane under an oxygen flow of 1 L/min and maintained with 2% isoflurane. All animals received subcutaneous (SC; 200 µL) or intramuscular (IM; 20 µL) injections of the materials described above (1 mg/mL) diluted in saline solution (or

just saline solution in the control animals) in order to evaluate the biodistribution and persistence of locally administrated injections (Figure 4.1). The animals were examined daily with special attention to the injection site.

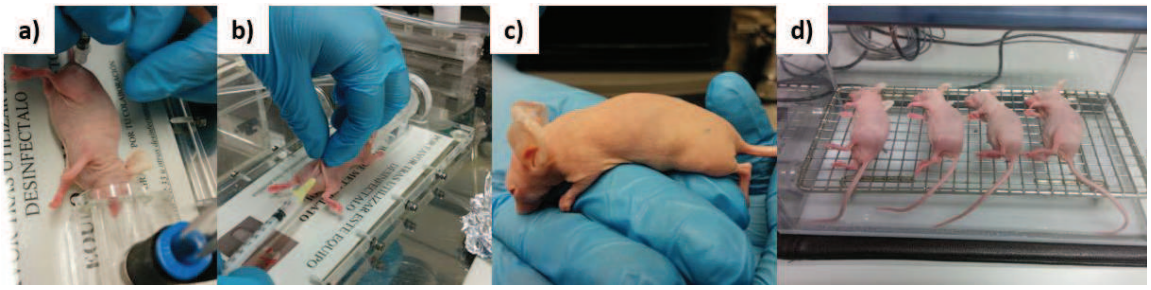

Figure 4.1: BALB/c nu/nu mice during a) intramuscular (IM) injection; b) subcutaneous injection; c) after PNIPAm-IR820-COOH SC injection; d) Under 2% isoflurane anesthesia.

The purpose of this study was to target the key tissue avoiding systemic administration and to further investigate the differences between both administrations taking into account the different volumes administered as well as the different metabolic rates of both tissues. The administration was located as closer as possible to sciatic nerve for future chronic pain treatments and to evaluate the persistence of different approach considered in our laboratory. Dye stability after micro- and nanoparticles labeling was confirmed, thus dye fluorescence intensity allowed their tracking after injection. Imaging analysis was developed at different time points up to 7 days when using IM administration and 14 days when using SC administration in an IVIS® Lumina Xenogen equipment and the Living Image® software (Caliper, USA).(Figure 4.2).

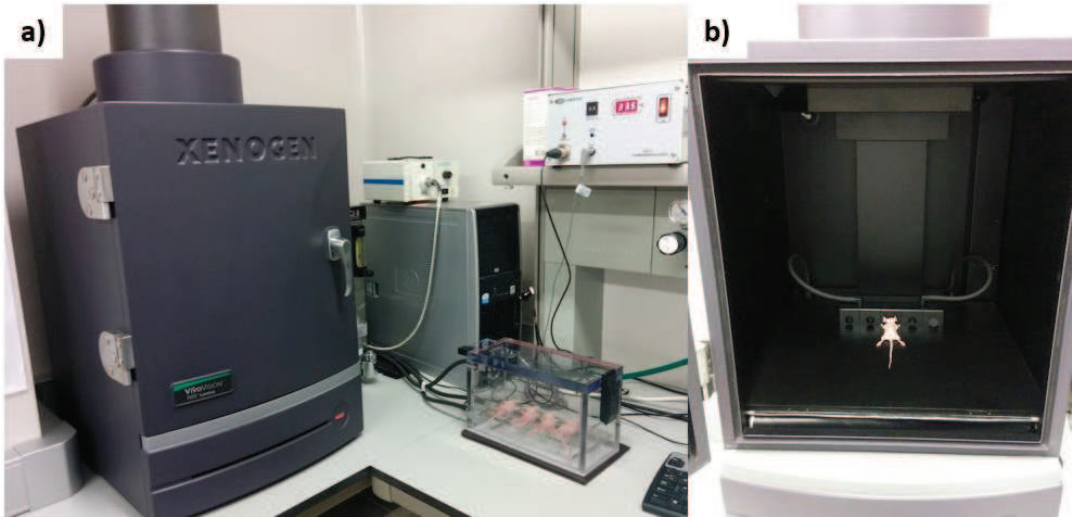

Figure 4.2: IVIS® Lumina Xenogen equipment with the camera of anesthesia; b) Inside IVIS® equipment with studied mouse under 2% isoflurane anesthesia.

In addition, the persistence of IM- and SC-administered not labelled PNIPAm MPs in tissues was also assayed in order to elucidate their long-term persistence and the possible damage to tissues after 30 and 60 days post-injection (p.i). and to decouple the potential influence of the dye. PLGA NPs were not included in this study as it is widely known that their tunable persistence depends on their monomeric composition and demonstrated safety *in vivo*[310][312]. As before, MPs were administered IM and SC under the same conditions as stated above and the animals were euthanized at 30 and 60 days post injection (p.i.).

4.3.5 Pathological studies

All animals were euthanized by cervical dislocation under 5% isoflurane anesthesia under an oxygen flow of 1L/min (unconscious condition). A full post mortem procedure was carried out with special attention to the injection site (subcutaneous tissue, muscular tissue, inguinal and popliteal lymph nodes). These studies were performed to assess the safety and biocompatibility of the synthetized materials at a local and whole body level, complementing the *in vitro* cell studies. Representative sections of the injection area and local lymph nodes, lung, heart, brain, liver spleen, kidney and gastrointestinal organs were systematically collected. The tissues were fixed in 4% buffered paraformaldehyde and embedded in paraffin. Five-micron-thick tissue sections were obtained and stained with hematoxylin and eosin (HE). Masson's trichrome staining was applied to the skin samples to better describe the connective tissue reaction to the materials at the injection area.

4.4 Results and discussion

4.4.1 Synthesis and characterization of dye-labelled materials

As it was aforementioned, PLGA and PNIPAm micro- and nanoparticles (MPs and NPs) were labelled with the IR820 dye through three different methodologies in order to obtain dye-labelled materials of different sizes for potential drug delivery approaches as depot devices. IR820 was chemically modified with amine and carboxyl groups to enable a proper labelling of PLGA and PNIPAm. Chemically modified IR820-NH_2 (Figure 4.4) and IR820-COOH (Figure 4.5) were studied by NMR spectroscopy of 13C and 1H, Fourier transform infrared spectroscopy (FTIR) and mass spectrometry in order to determine their purity and chemical and spectral stability.

Comparing the amino- and carboxyl-functionalized dyes with unmodified IR820 dissolved in methanol, it was observed that the IR820 derivatives exhibited a larger Stokes shift (difference between the excitation and emission wavelengths of the same electronic transition) compared to the unmodified IR820 (Figure 4.3). This effect has been already observed in similar components and attributed to an excited-state intramolecular charge transfer (ICT) between the donor and acceptor in the dyes when Cl atom of the commercial IR820 is replaced [313].

This ensures a better performance of the modified dyes since it reduces the chances of self-quenching. Thus the resulting dyes were more sensitive NIR fluorescent probes than the non-functionalized ones. When the solvent was changed to water, the fluorescence decreased for both IR820 and IR820-COOH, in agreement with the previous literature [314] as it is reported that cyanine dyes show lower quantum yield values when using water as solvent.

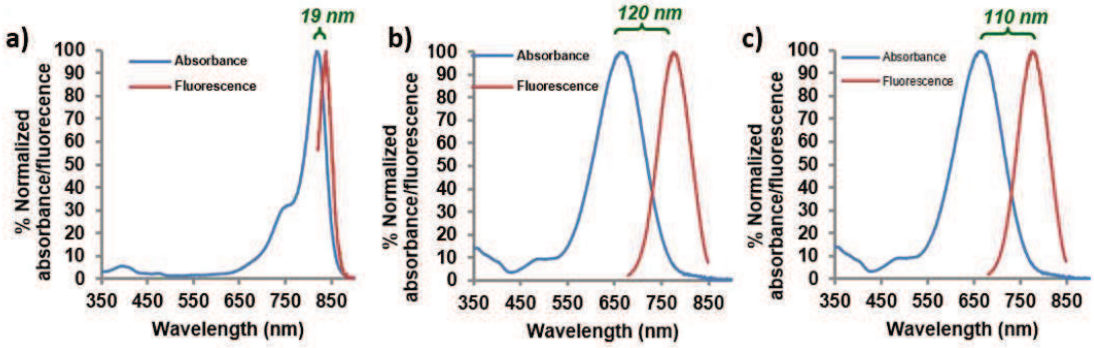

Figure 4.3: Normalized absorbance and fluorescence spectra in methanol: a) IR820; b) IR820-COOH; c) IR820-NH_2

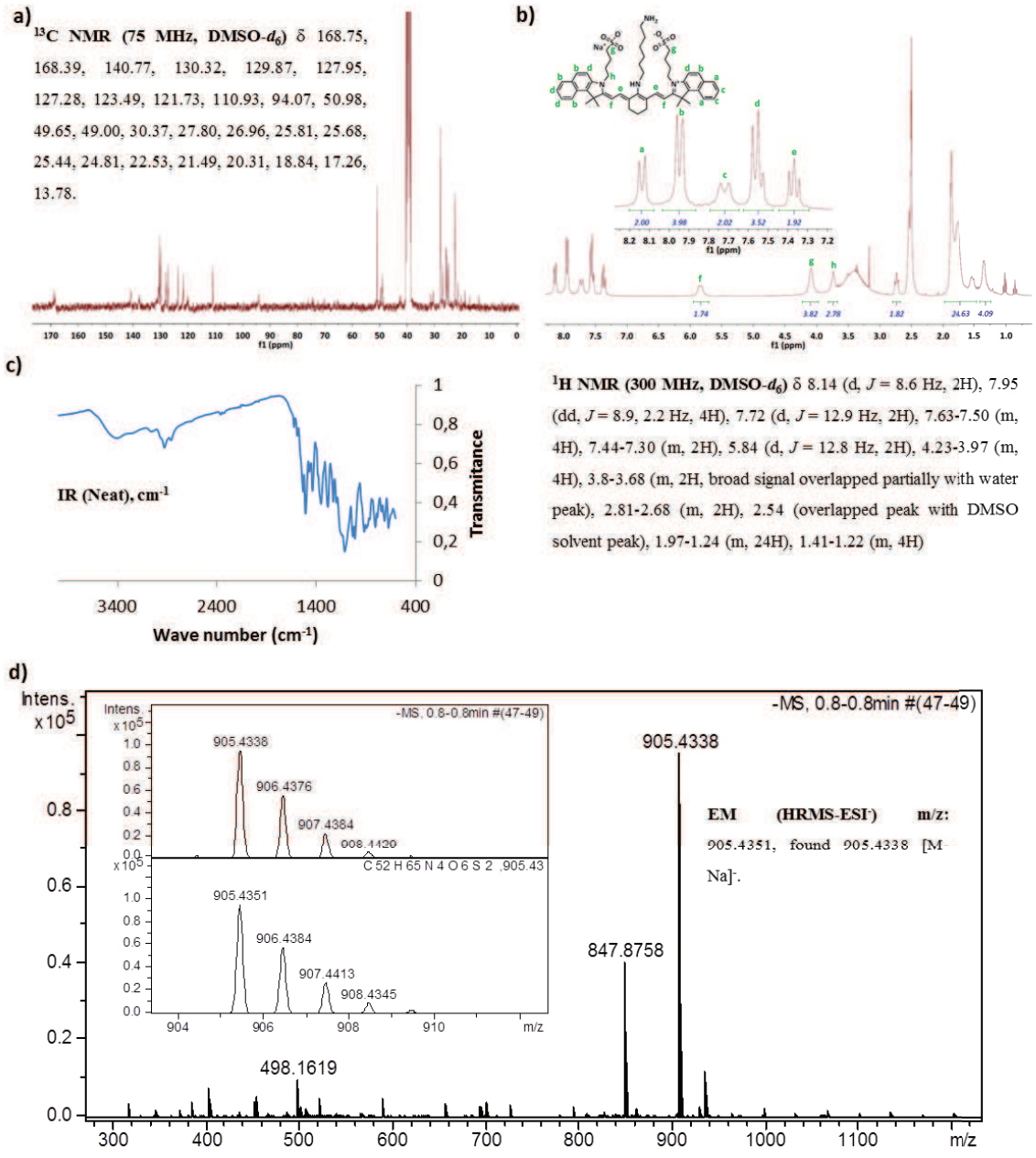

Figure 4.4: Characterization of modified IR820-NH_2: a) NMR spectroscopy of ^{13}C; b) NMR spectroscopy of ^{1}H; c) FTIR; d) Mass spectroscopy.

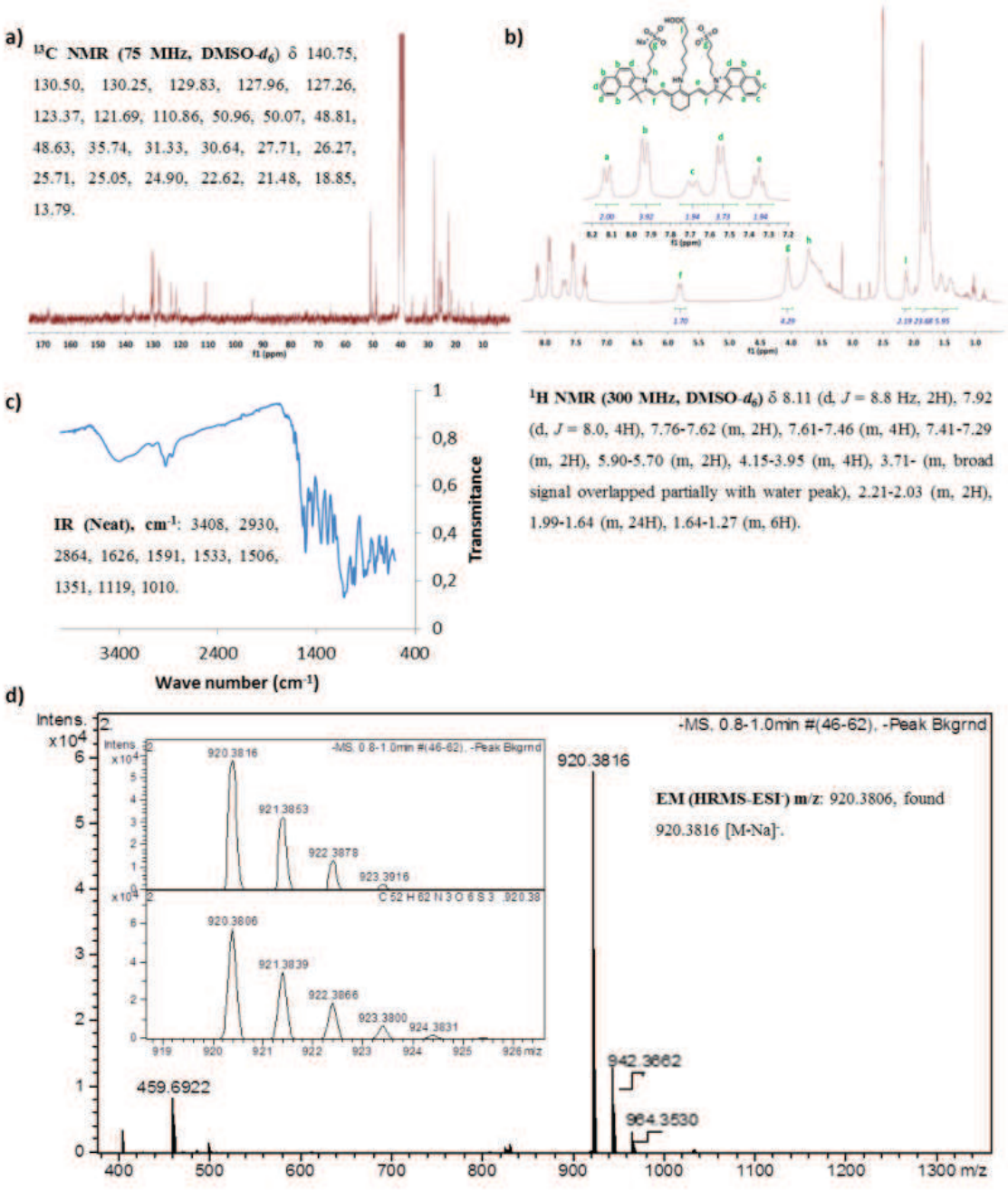

Figure 4.5: Characterization of modified IR820-COOH: a) NMR spectroscopy of ^{13}C; b) NMR spectroscopy of ^{1}H; c) FTIR; d) Mass spectroscopy

The characterization of modified polymers was carried out in order to evaluate their chemical and spectral properties as NIR fluorophores (Figure 4.6 and Figure 4.7).

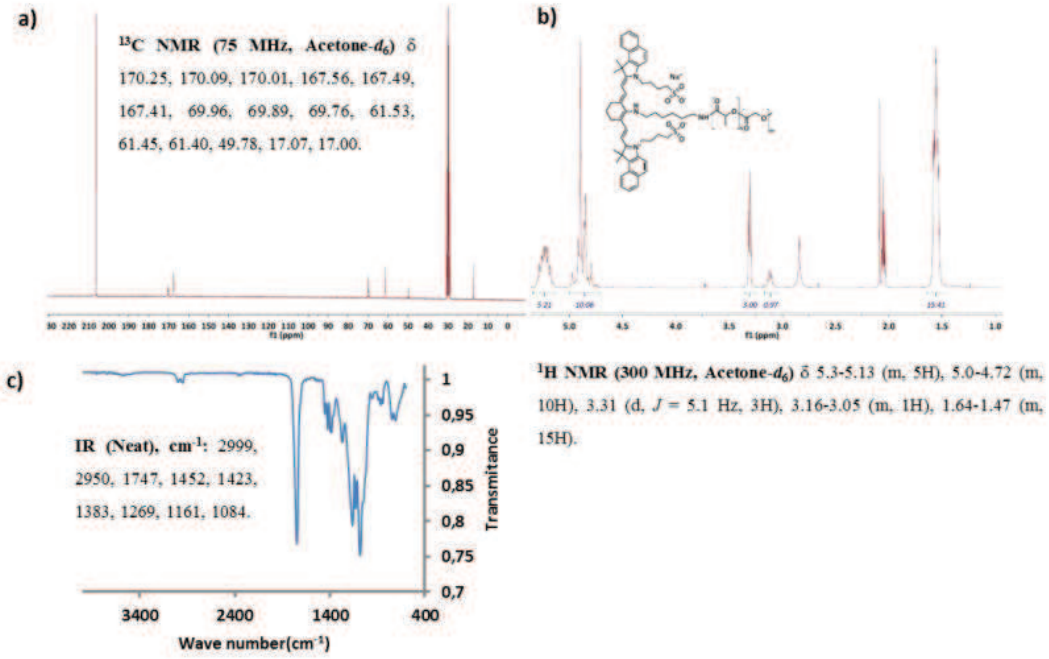

Figure 4.6: Characterization of PLGA-IR820-NH_2: a) NMR spectroscopy of ^{13}C; b) NMR spectroscopy of ^{1}H; c) FTIR.

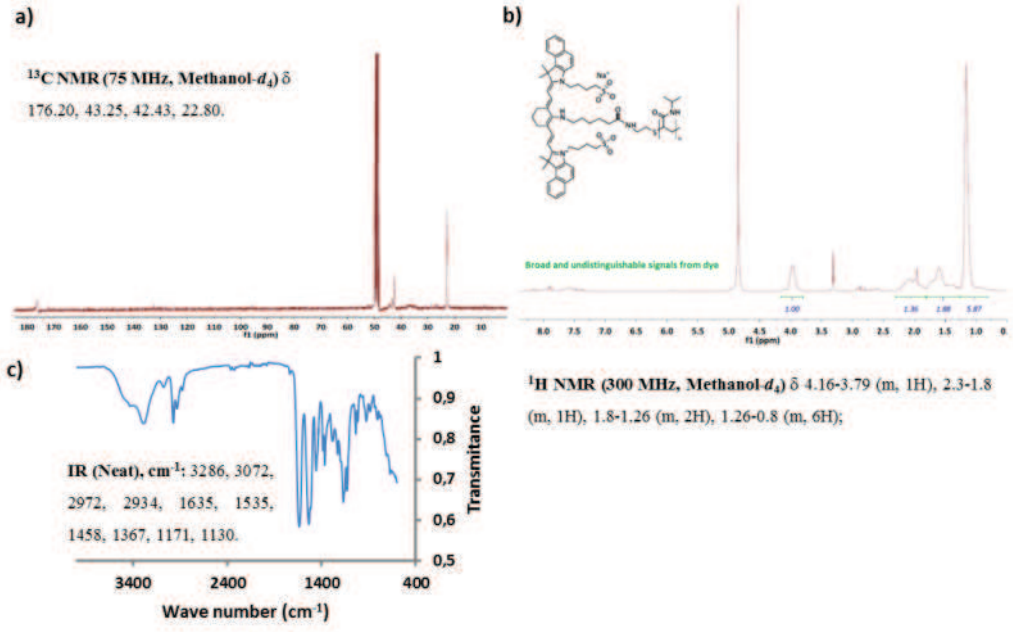

Figure 4.7: Characterization of PNIPAm-IR820-COOH: a) NMR spectroscopy of ^{13}C; b) NMR spectroscopy of ^{1}H; c) FTIR.

Moreover, in the case of PNIPAm, its thermoresponsive behavior should be preserved after chemical modification. To ensure this, a transmittance curve of the chemically modified polymer was measured observing insignificant variations compared to commercially acquired PNIPAm, which exhibits a transition temperature of around 36.5 ºC at 50% transmittance (Figure 4.8).

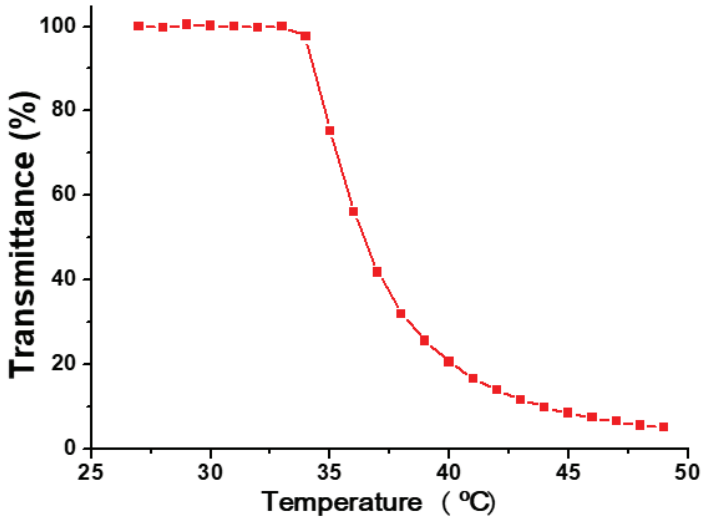

Figure 4.8: Transmittance measurement of Low critical transition temperature (LCST) measurement of thermoresponsive behavior of PNIPAm chemically bonded to IR820-COOH dye (0.25 mg/mL).

The study of the absorbance and fluorescence of the dye-functionalized polymers revealed similar optical performance compared to that of the unmodified dye in terms of Stokes shift and stability. Table 4.1 summarizes the maximum absorbance and emission values for these polymeric dispersions. PLGA-IR820-NH_2 could only be measured in acetone because it is not soluble in methanol or water. For that reason, no comparison between dyes could be conducted, as those dyes are insoluble in acetone. In the case of PNIPAm-IR820-COOH, the effect of the solvent is similar, increasing the Stokes shift in water, being the value for this polymer the highest of all measured samples. This fact indicates that the attachment of the dye to the polymer did not significantly alter the emission properties of the dye as its emission range still remained in the NIR region (750-950 nm)

Table 4.1: Stokes shift of the polymers in different solvents. The data are presented in nm

Sample	Solvent	λ_{max} abs	λ_{max} em	Stokes shift
IR820	Methanol	819	838	19
PLGA-IR820-NH₂	Acetone	623	767	144
PNIPAm-IR820-COOH	Methanol	664	780	116
PNIPAm-IR820-COOH	Water	642	792	150

Considering that the NPs size is an important factor for *in vivo* studies, six different particles were synthetized with a wide range of sizes in order to determine the differences in their behavior prior to carry out *in vivo* experimentation. IR820 was internalized in the polymeric vectors by two approaches: (1) tagging the polymer with the dye and (2) encapsulating the dye in the polymeric matrix.

The size, morphology and loading protocol of the different particles used in this study are summarized in Figure 4.9. NPs based on PLGA-IR820-NH_2, PLGA-IR820 encapsulated, PNIPAm-IR820-COOH and PNIPAm-IR820-COOH post synthesis were produced through a simple emulsion-evaporation method assisted by ultrasound radiation leading to NPs sizes between 119 and 560 nm (Figure 4.9 a) – d)). Nevertheless, in order to study the *in vivo* animal response to larger particles, PNIPAm microgels and MPs were loaded by diffusion with IR820 after three days of contact in a solution of the saturated fluorophore and subsequent purification as already described in the Experimental section. Their sizes were much larger than those displayed by the other materials synthetized, exhibiting diameters larger than 600 nm in the case of the microgels (Figure 4.9 e)) whereas MPs achieved a mean size up to 439 µm (Figure 4.9 f)). After synthesis, a potential detachment of the dye from the corresponding particles was discarded after evaluating the fluorescence of the supernatants collected by incubating the particles in saline media.

PNIPAm hydrogels tagged with IR820 have been previously developed [315] following the same labelling methodology as the one used in this PhD by submerging the hydrogels in a saturated IR820 solution. However, these authors used only one monomer (N-isopropylacrylamide), reporting a low cloud point (~32 ºC), that is, the temperature above

which an aqueous solution becomes turbid due to its change in solubility (i.e. coil to globule transition), and larger gel sizes (millimeter range), which preclude their potential biomedical application.

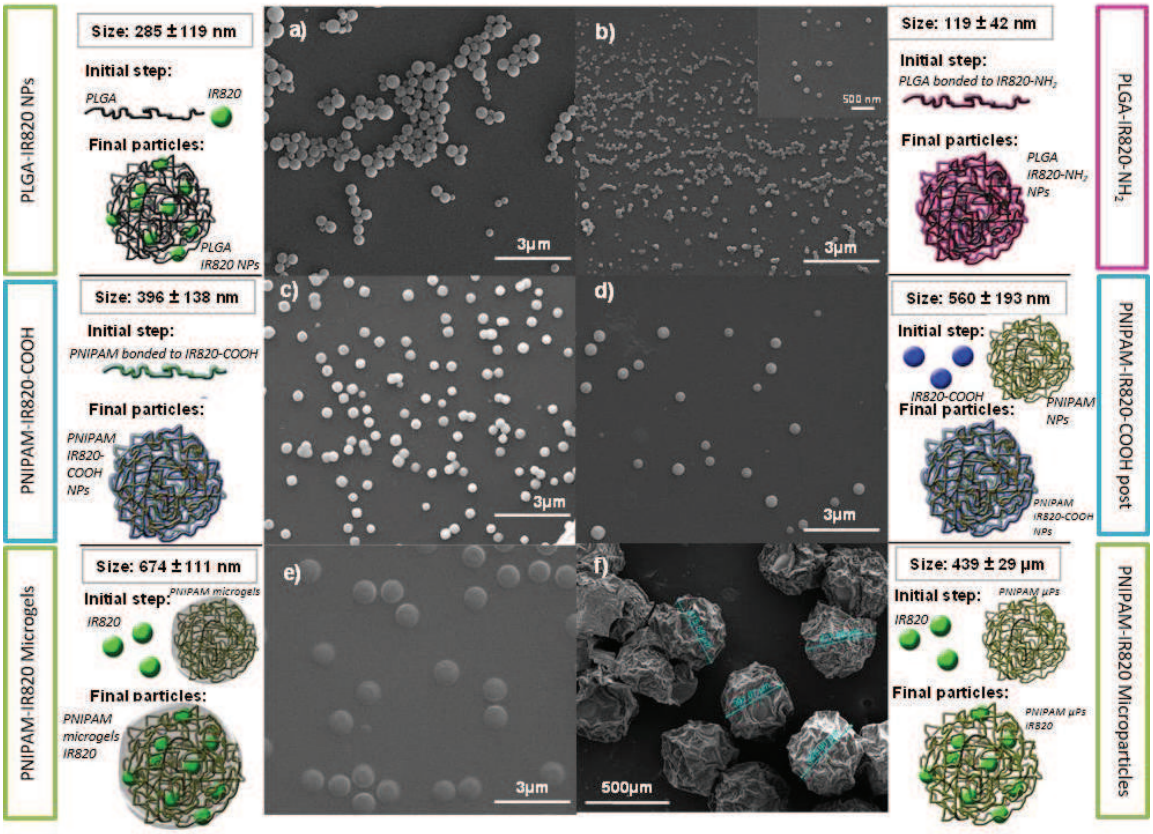

Figure 4.9: SEM images and loading scheme of the materials synthetized

Our results clearly show the broad spectrum of sizes of our labelled materials to fulfill different requirements for screening the biodistribution and persistence of different materials of different sizes widely used as drug delivery vectors. In order to complete the characterization of the different vectors, the IR820 concentration was also estimated on each carrier (Table 4.2) through its quantification with the Living Image® software (Caliper, USA). A clear correlation between these measured concentrations and the intensity of the *in vivo* signal retrieved was not observed, which is consistent with a higher efficiency related to their chemical modification to be anchored to the polymers and their interaction with the surrounding tissues.

Table 4.2: IR820 dye concentration in the final materials (Mean ± SD; n = 4)

	PLGA-IR820-NH_2	PLGA-IR820 Encapsulated	PNIPAm-IR820-COOH	PNIPAm-IR820-COOH Post-synthesis	PNIPAm-IR820 Microgels	PNIPAm-IR820 MPs
Dye concentration (µg/mL)	21.0 ± 0.5	32.2 ± 3.7	3.9 ± 0.3	12.0 ± 3.5	28.5 ± 6.4	48.6 ± 4.5

4.4.2 *In vitro* cytotoxicity studies

The cytotoxic effects of the materials described above were analyzed on human dermal fibroblasts, monocytes, macrophages, mouse mesenchymal stem cells (mMSCs) and human tumoral cells (U251MG) through the treatment of these cell lines with the different synthetized materials for 48 h. The effects on cell metabolism were assessed by using the blue cell viability assay while the cell cycle was analyzed by flow cytometry. In addition, the potential endotoxin content of the synthesized materials was also tested to assure their safety for *in vivo* administration. According to ISO 10993-5 (Biological evaluation of medical devices: Test for *in vitro* cytotoxicity) [280], a reduction in viability larger than 30% is considered a cytotoxic effect.

The treatment of cell lines assayed with increasing concentrations of PLGA and PNIPAm-IR820-COOH up to 2 mg/mL did not involve a substantial decrease in cell viability in all cases (Figure 4.10) showing viability percentages higher than 70% at a final concentration of 1 mg/mL. PNIPAm-IR820-COOH post synthesis (Figure 4.10 d)) produced slightly higher toxic effects in the cell types tested at 2 mg/mL. However, cell viability was higher than 70% at a concentration of 1 mg/mL for macrophages, monocytes and U251MG cells. The effects of cell treatment with PNIPAm-IR820 microgels (Figure 4.10 e)) were found to be more cytotoxic at the highest concentration studied (2 mg/mL) pointing to 1 mg/mL as the non-cytotoxic dose yielding viability percentages higher than 70% on fibroblasts and mMSCs. PNIPAm-IR820 MPs (Figure 4.10 f)) showed low cytotoxicity, exhibiting viability percentages higher than 66% at concentrations up to 1 mg/mL.

Furthermore, the viability of mMSCs treated with microgels and MPs was found to be higher than that obtained for the control samples (Figure 4.10 e) and f)). These results

might be attributed to the polymeric nature, mechanical features and viscosity of these dispersions, mimicking the extracellular matrix (ECM). This extra surface in the media assists the division of cells and benefits their anchorage dependency avoiding apoptosis process [316][317][318]. Moreover, higher viability and proliferation of mesenchymal stem cells seeded in PNIPAm gels compared to that obtained on 2D cultures had been already demonstrated [319]. Regarding this data, 1 mg/mL was considered as the subcytotoxic concentration used for further studies.

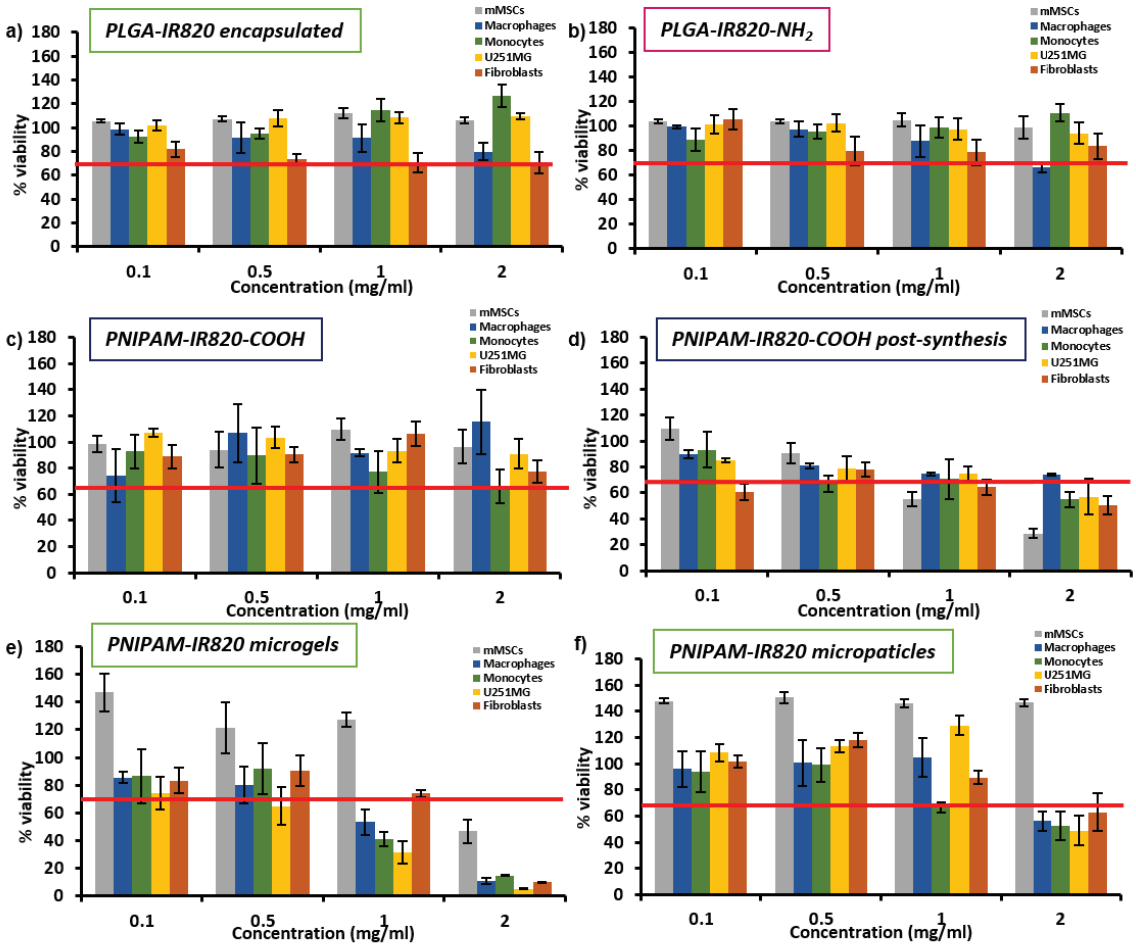

Figure 4.10: Cell viability of the dye-labelled materials on the five cell lines assayed after 48 h. The possible interferences of the labelled materials with the methodology or the reagent were evaluated and discarded. The red mark sets the biocompatibility threshold percentage (70% viability). Control group (not treated cells)=100% viability. The data are expressed as mean ± SD (n=5)

The effect of PLGA and PNIPAm at 1 mg/mL on cell cycle after 48 h of incubation is shown in Table 4.3. The addition of PLGA and PNIPAm at the subcytotoxic dose did not involve an accentuated effect on cell cycle phase distribution; hence DNA replication and cell division were not affected or halted by these treatments. The addition of PLGA to the cells barely displayed effects on cell cycle; only a slight decrease in the G2 phase in U251MG and fibroblasts and a reduced increase in the G1 phase in mMSCs were observed. PNIPAm produced mild changes in the cell-cycle phases, these being a little more accentuated for PNIPAm-IR820-COOH post-synthesis.

Table 4.3: Distribution of cell cycle phases for the different cell lines studied when treated with the dye-labelled materials synthetized (1 mg/mL)

	CELL CYCLE PHASES	CONTROL	PLGA-IR820-NH_2	PLGA-IR820 Encapsulated	PNIPAm-IR820-COOH	PNIPAm-IR820-COOH Post-synthesis	PNIPAm-IR820 Microgels	PNIPAm-IR820 MPs
mMSCs	**G1**	**42.04**	31.94	60.45	36.41	36.13	26.71	30.43
	S	**30.53**	40.35	21.11	35.94	44.53	30.80	37.80
	G2	**27.43**	27.71	18.44	27.65	19.34	42.49	31.77
Macrophages	**G1**	**25.37**	36.35	50.28	36.69	41.41	56.36	28.04
	S	**46.53**	31.61	29.88	33.69	21.62	22.33	48.30
	G2	**28.10**	32.04	19.85	29.62	36.98	21.31	23.66
Monocytes	**G1**	**50.82**	40.78	45.00	41.23	47.02	45.35	45.64
	S	**30.32**	39.65	35.65	43.45	23.49	34.18	32.22
	G2	**18.85**	19.57	19.35	15.32	29.49	20.48	22.04
U251MG	**G1**	**50.24**	62.88	63.86	61.94	71.05	42.64	44.40
	S	**34.21**	29.65	29.82	30.43	13.23	39.14	36.78
	G2	**15.56**	7.47	6.32	7.63	15.72	18.22	18.82
Fibroblasts	**G1**	**65.42**	62.91	74.85	54.34	34.15	64.95	59.49
	S	**4.92**	9.21	14.46	6.36	37.51	19.54	21.03
	G2	**29.66**	27.88	10.70	39.29	28.34	15.50	19.48

The determination of the endotoxin content with the end-point chromogenic LAL assay did not reveal the presence of significant endotoxin concentrations. The measured values were lower than 0.05 ng/mL (0.5 endotoxin unit (EU) per mL), the safe threshold established by the Food and Drug Administration (FDA). In addition, the materials and fluorophores assayed did not show any interference with the reagents or with the developed techniques.

In conclusion, labelled PLGA and PNIPAm materials did not significantly alter cell metabolism or cell cycle on the cell lines tested at concentrations up to 1 mg/mL, and did not display potentially harmful endotoxin levels for *in vivo* administration, showing their suitability for *in vivo* imaging and potential drug delivery applications.

4.4.3 *In vivo* imaging and biodistribution

IVIS® scanning was used to visualize the material biodistribution at different time points after IM and SC administration in nude mice. Figure 4.11 display the results obtained from IM administrated animals visualized until 7 days (p.i.), while Figure 4.12 shows SC administrated animals analyzed until 14 p.i.

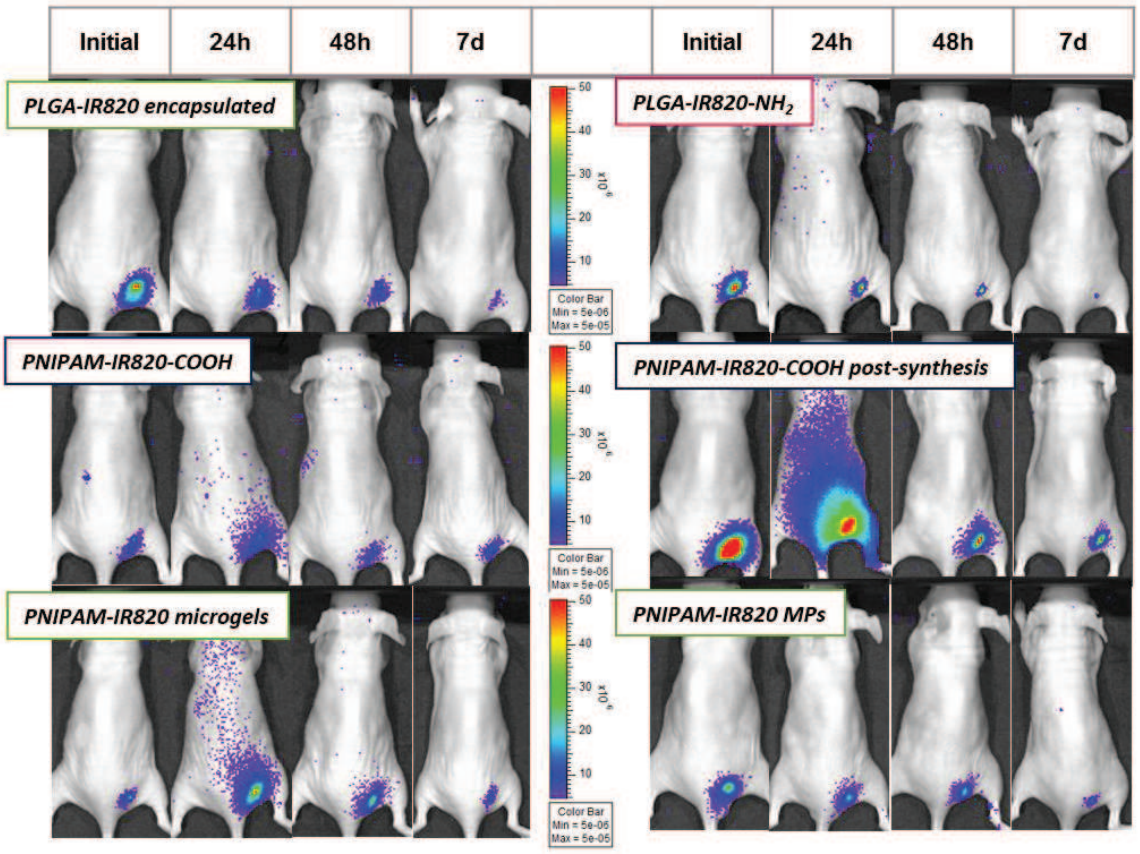

Figure 4.11: *In vivo* course fluorescence imaging of the labelled materials after intramuscular injection. All signals are presented according to the same color scale in order to be able to compare signal intensity among samples and times.

IM administration produced fluorescent signals until the end of the experiments (7 days p.i.), showing the highest intensity when PNIPAm-IR820-COOH post-synthesis was injected, while the lowest signals were recorded for dye-labelled PLGA samples at the end of the study. When the materials were SC administrated, the intensity of the signal after 14 days p.i. was noticeable in all mice, being superior in both PNIPAm-IR820-COOH samples while the lowest intensity was again displayed for the dye-laballed PLGA-treated experimental groups. This fact may be attributed to the lower number of carbonyl groups of PLGA susceptible to be labelled with IR820-NH_2 functional groups resulting in less dye molecules in the sample. Furthermore, the signals displayed an increase after 24 h p.i. in SC administrations and also for IM PNIPAm-IR820-COOH post-synthesis and PNIPAm-IR820 microgels due to the well-known binding between the dye and albumin in the serum present

in human tissue [320]. This effect probably was also displayed by the other experimental groups, though their lower signals hid this increase and subsequently did not correlate with the dye-concentration data described in Table 4.2.

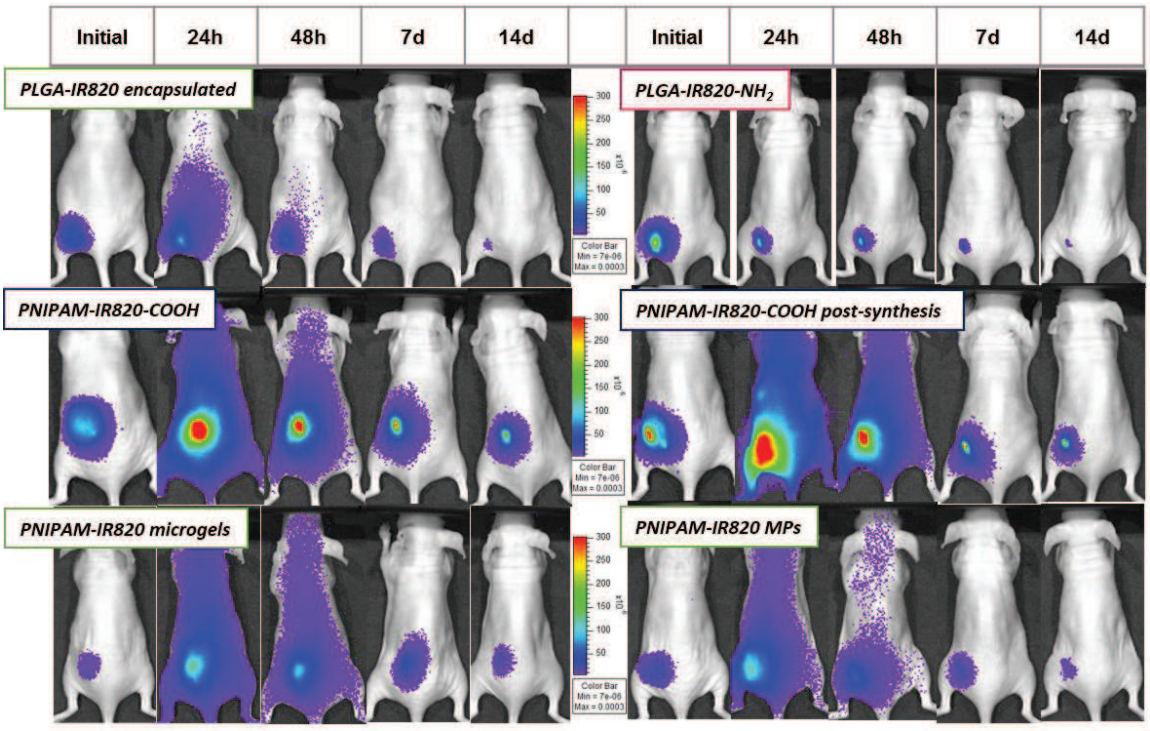

Figure 4.12: *In vivo* time course fluorescence imaging of labelled materials after subcutaneous injection. All signals are presented according to the same color scale in order to be able to compare signal intensity among samples and times.

In addition, at the end of the experiments and immediately after euthanasia, the main organs were *ex vivo* visualized by IVIS® scanning to track the possible accumulation of the materials though no trace was observed, highlighting the local biodistribution and persistence of the administrated materials. The high intensity of the signal in both types of administrations should also be noted, pointing to the potential of these labelled materials for the study of micro- and nanoparticle biodistribution as well as for drug delivery (using particles co-encapsulating both a drug and the dye) taking into account the high biocompatibility of the dye-labelled materials described above.

4.4.4 Pathological studies

After necropsy, no animal showed macroscopic lesions compatible with inflammation, infection or degeneration at the local or systemic levels. Microscopically, all animals injected with the different synthetized materials did not present any lesions at the epidermis, dermis, subcutaneous tissue, musculature or local lymph nodes for both SC and IM administrations. Some of these histological studies are shown in Figure 4.13.

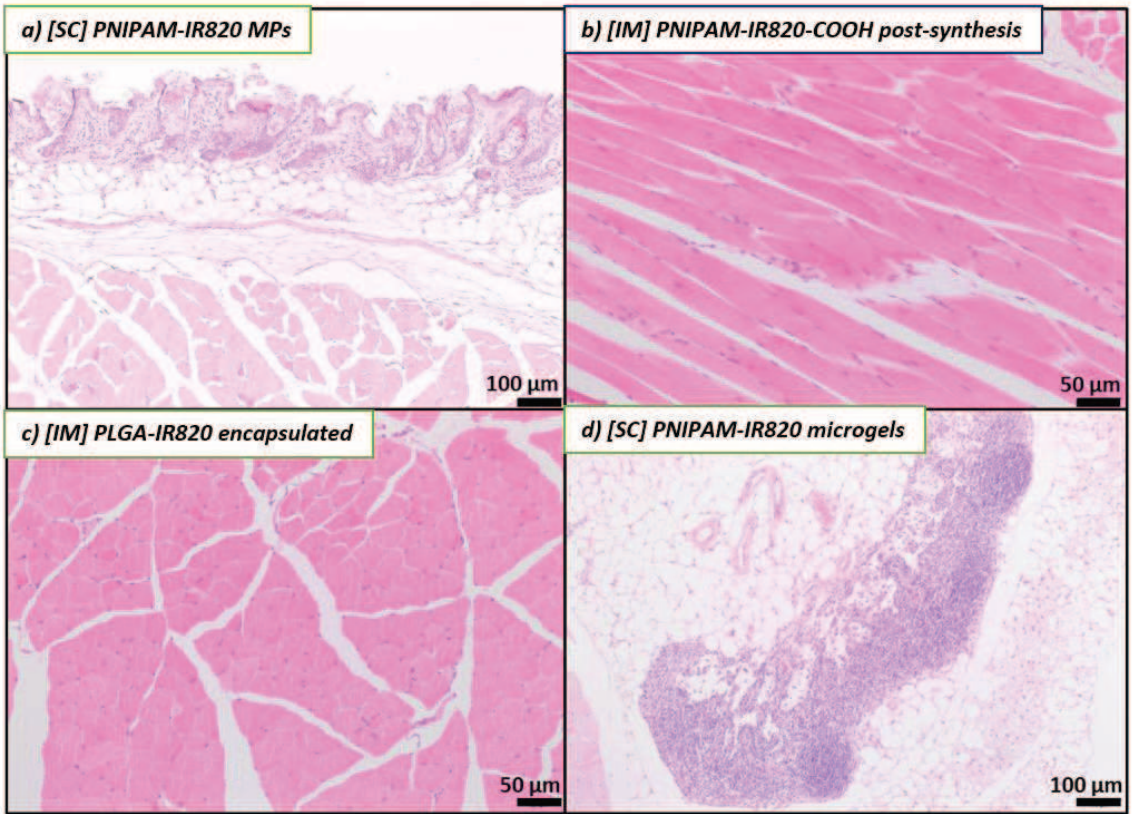

Figure 4.13: Histological analysis after 7 days (IM) and 14 days (SC) post injection. a) and d) have a magnification of HE 10x; while b) and c) have HE 20x magnification.

Figure 4.13 a) presents a histological microscopy image of mouse tissue treated with PNIPAm-IR820 MPs after SC injection. Here, it can be observed normal histological features at the epidermis, dermis and subcutaneous tissue and musculature. A sample from a longitudinal section of subcutaneous musculature of a treated mouse with PNIPAm-IR820-COOH post-synthesis after IM injection is displayed in Figure 4.13 b). Again, no inflammatory infiltrate is observed between the muscle fibers. Myocytes nuclei are well positioned and the fibers are aligned. The cross section of subcutaneous musculature of

mouse specimen retrieved from an animal IM administered with PLGA-IR820 encapsulated is presented in Figure 4.13 c), where no degradation or inflammatory lesions were observed at the muscle fibers. Finally, popliteal lymph node is shown in Figure 4.13 d) preserving its ratio of cortical/medullary thickness after PNIPAm-IR820 microgels SC injection.

In order test the persistence of PNIPAm MPs in tissues at longer times, one group was administered with non-labelled PNIPAm MPs (Figure 4.14), showing a foreign body reaction at the subcutaneous musculature at day 60.

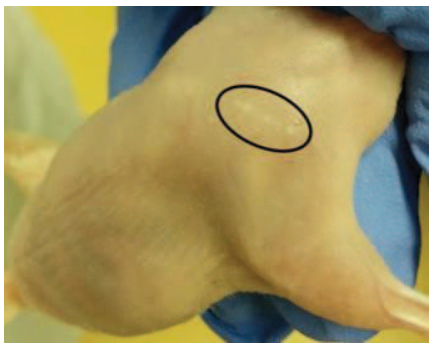

Figure 4.14: BALB/c nu/nu mouse after SC PNIPAm MPs injection (circle).

This reaction was well circumscribed, characterized by active fibroblasts forming a fibrous encapsulation of the eosinophilic amorphous material intermixed with moderate numbers of macrophages, foreign body giant cells and scarce neutrophils which is indicative of a mild reaction. (Figure 4.15)

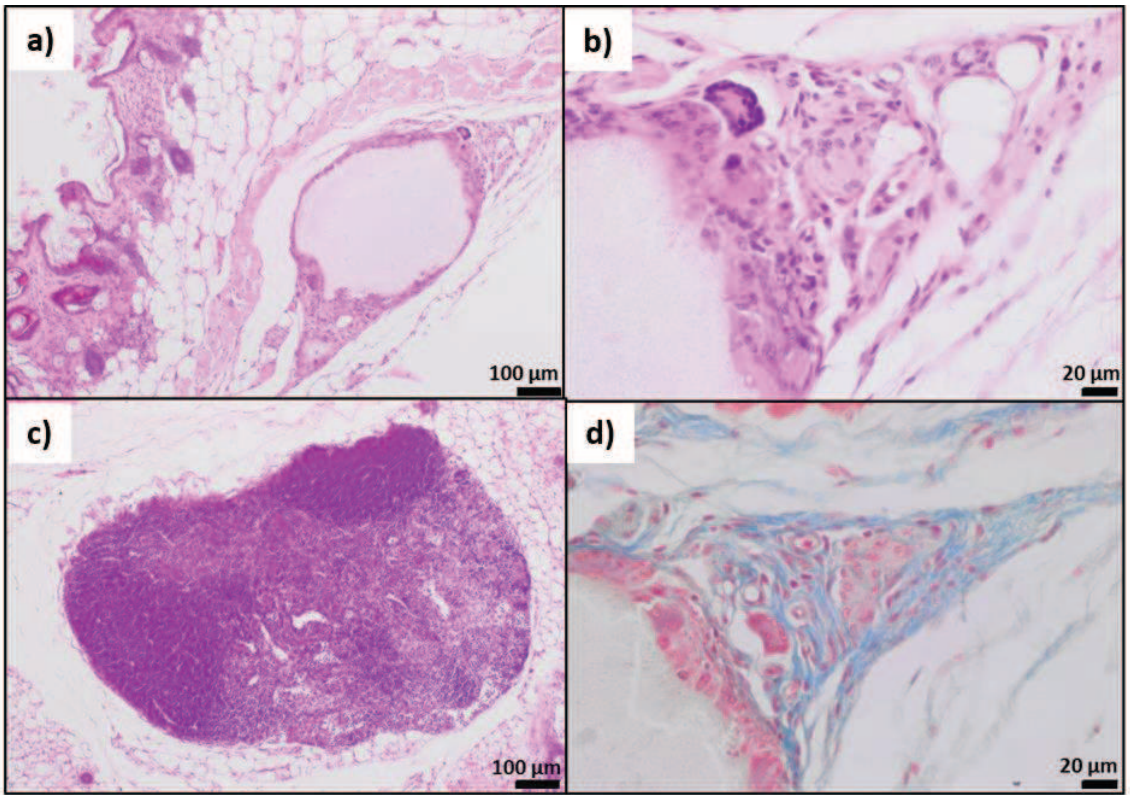

Figure 4.15: Histological study of the persistence of non-labelled PNIPAm MPs in the tissue after SC injection. a) Well-circumscribed fibrous encapsulation of foreign material at the subcutaneous musculature. Moderate amount of fibroblasts and macrophages surrounding the eosinophilic amorphous material, HE 10x; b) Foamy macrophages, giant cells and spindle-shaped active fibroblasts, HE 40x; c) The number of lymphocytes is increased expanding in the paracortical area, HE 10x; d) Blue staining indicating fibroplasia phenomena with the formation of collagen fibers surrounding the foreign material, Masson's trichrome stain, 40x.

The collagenous tissue and fibroblast encapsulation of the material was more evident using Masson's trichrome stain (Figure 4.15 d)). The popliteal lymph node showed a moderate paracortical lymphocyte hyperplasia identified by increased lymphocyte density accompanied by an increased paracortical area. No microscopic lesions were found in all the remaining organs studied (brain, heart, kidney, liver, lung, spleen and gastrointestinal organs), denoting the lack of systemic toxicity by the synthetized materials.

4.5 Conclusions

The study described in this chapter deals with the development and *in vivo* evaluation animal test of the labelled biocompatible micro- and nanomaterials for the study of their biodistribution and local persistence. The synthetized dye-labelled materials were optimized for biomedical applications for their potential use as drug depots in local affections. The

chemical modification of IR-820 to introduce a short linker chain with a terminal carboxylic group or with an amine groups was successfully carried out. These derivatives showed improved fluorescent properties compared to the unmodified free dye. The acid and amino derivatives of IR-820 prepared allowed the labelling of the amino and acid terminated polymers, respectively, used afterwards for NPs synthesis. IR-820-COOH also allowed the labelling of the already prepared PNIPAm NPs in a post-grafting reaction.

In vitro studies highlighted their biocompatibility at the doses tested after the evaluation of their effects on different cell lines regarding cell metabolism and cell cycle as well as their endotoxin-free nature. Fluorescent labelled PLGA and PNIPAm expressed local detectable signals up to the end of the studies after 7 days (IM) and 14 days (SC) of the administration exhibiting higher signals for PNIPAm derivatives due to their higher proportion of label susceptible amine functional groups, pointing to their suitability to study the biodistribution of novel materials intended for medical purposes.

Furthermore, the labelled materials did not show any inflammatory or degenerative process and no lymphadenopathies were observed either. These results clearly pinpoint to the potential use of our novel labelled micro- and nanomaterials for safe and localized drug delivery as well as to the suitability of PNIPAm as a long-term drug carrier. The determination of drugs in physiological fluids (blood, urine, etc.) or in tissues can be challenging and, for that reason, tracking the drug carrier without the need for drug radiolabeling or using time-consuming chromatographic methods could represent a clear advantage when clearly knowing the dye release kinetics from the carrier.

CHAPTER V

MOLECULAR DYNAMICS

"Atoms are very special: they like certain particular partners, certain particular directions, and so on. It is the job of physics to analyze why each one wants what it wants"

Richard P. Feynman, Theoretical physicist (1946)

Chapter V

MOLECULAR DYNAMICS

Summary

In this chapter, molecular dynamics simulations are used to assist the study of thermoresponsive polymeric vectors and to understand their interaction with water and bupivacaine as model drug in order to know how to obtain the maximum drug loadings from an atomistic insight. The effect of different functional groups in the polymeric structures on the organization of solvent molecules around them and their influence on their transition temperature is depicted. In addition, polymer-drug systems are studied comparing different drug and polymer concentrations and temperatures showing interesting differences that were further confirmed by the experimental results obtained in the laboratory.

5 Molecular dynamics

5.1 Introduction

Until now all along this work, the drug delivery vectors developed have been analyzed from a macroscopic level. In Chapters II and III synthesis processes of inorganic and hybrid nanovectors have been studied including their physico-chemical properties and their *in vitro* cell viability to guarantee their suitability in future biomedical applications. For its part, Chapter IV gathers *in vivo* biodistribution results of six different polymeric vectors and their pathological effects after intramuscular and subcutaneous injections. However, none of these experimental tests conducted during this PhD work shows what is really happening in the closest environment at the molecular level. This fact is due to the lack of resolution of conventional imaging and measurement instruments because most of those techniques evaluate a macroscopic property.

In this sense, techniques such as molecular dynamics (MD) simulations are powerful tools to capture drug delivery systems behavior at the molecular level. The knowledge at this level of both carrier-solvent and drug-carrier interactions can help in the design of advanced carriers, improving their drug loading and consequent efficiency for each specific application.

So far, MD simulations are not able to mimic full size and characteristics of real nanotechnological vectors due to time-scale and size limitations in computer processing. However, it has been demonstrated that the behavior of scaled versions or even fragments of these vectors match with the real macroscopic characteristics and, in addition, the growing development of computing processing allows to continuously study larger and more complex systems [321].

In particular, polymers have been widely studied by MD simulations as drug delivery agents. Their extraordinary versatile conformation and structure can be customized depending on their application. Their performance in presence of different solvents and drugs can be studied using MD simulations and extrapolated to future systems, saving experimental time and resources. Their physical properties determine their behavior under changing environments and computational MD simulations can aid to visualize and understand it.

The understanding of polymer chain behavior in solution has attracted the attention of scientists from the 1970's. Rapaport in 1979 [322] introduced the necessity to take into account explicit solvent molecules in polymer-solvent systems because of their influence to polymer chain mobility equilibrium. Dünweg and Kremer in 1993 [323] extended simulation times to reach complete polymer relaxation, where polymer chain releases the initial stress after being introduced in a new environment interacting with water molecules, with the computational resources of that moment. No explicit type of polymer was described in these early studies. However, the improvement in computational performance in the 1990's allowed more detailed studies of different types of polymers.

Self-assembled polymers like block co-polymers based on biocompatible polyethylene glycol (PEG) and polyethylene oxide (PEO) organize themselves in solution forming micelles and presenting an excellent potential as drug delivery vectors. MD simulations have been used to study this organization in water-air interfaces [324] and the behavior and micellar structure of hybrid block-co polymers in water [325]. The customization of these polymers may assist different micellation structures and characteristics what can result in different interaction with drug molecules [326].

PEG itself is also commonly used as drug carrier, thus several studies are focused on understanding its behavior in solution. The effect of molecular weight and chain length in solution and its correlation to solution polarity was studied by Oelmier et al. [327]. On the other hand, when PEG is used as inner spacer for peptide and protein display its size and peptide/protein interaction are really important for its final purpose. Thus, MD simulations has been used to study the dependency of PEG size and peptide interaction showing different behavior depending on the peptide to display helping to design more efficient systems [328].

Currently, there is notably interest in developing 'smart' materials capable to accomplish multiple tasks under an external stimuli [329]. In this scope, one of the most studied polymers so far is Poly (N-isopropylacrylamide) (PNIPAm) mainly due to its high biocompatibility and Low Critical Solution Temperature (LCST) tunable in the proximity of the physiological temperature [330]. As mentioned in Chapter III of this thesis dissertation, its adjustable structure can be combined to other acrylamide-based monomers to tune its thermo-responsive properties, what makes it very appealing for biomedical issues [331]. In

general, coupling monomers with different hydrophobicity leads to changes in inter- and intra-chain interactions that have a direct effect in the LCST of the resulting copolymer [278]. Acrylamide monomer has been commonly used for increasing from 32 ºC to up to 37 ºC the LCST of the copolymer chain [278][332] and also N-(isopropylmethacrylamide) is another monomer used for this purpose [333]. Contrary to acrylamide, the potential mechanism of this shifting has been attributed to an increase in the stiffness of the backbone of the polymeric chain due to the presence of an extra methyl group [334][335]. However, to the best of our knowledge there are not specific studies that have demonstrated it so far.

The coil-to-globule phenomenon is the result of a balance between chain-water interactions and inter-chain interactions, and their understanding can lead to a better knowledge of the polymer thermoresponsive properties. PNIPAm chain has been widely studied by MD simulations explaining its properties [336], however no report has been shown yet about its analogue Poly(N-isopropylmethacrylamide) (PNIPMAm) polymer. The additional methyl group in the backbone of the polymer is the only difference between PNIPMAm and PNIPAm chains but it has been demonstrated to have a remarkable difference in their corresponding LCST [337]. Some MD simulation studies describing the monomer hydration ability and comparing these two components were described in 2011 by Pang et al. [338] showing that steric effects affect to inter and intra interactions among the free monomers mixed together in a system using short oligomers (n=10) and only at one temperature. Nevertheless, these 10-oligomers do not show LCST phase transition experimentally so their behavior could not be extrapolated to real settings.

Another commonly studied aspect in the design of drug delivery vectors is drug-carrier interaction. This relationship determines drug uptake and release patterns from the carrier, which afterwards can be relevant for further applications. Moreover, the stability of the binding between molecules is also a key property for drug delivery vectors after their administration and can be understood and improved with the use of MD simulations.

As described in previous chapters, structures at the nanoscale used in drug delivery englobe from inorganic carbon and metal nanoparticles to polymeric macromolecules, hence drug-carrier interactions have been studied for a wide variety of systems.

Commercial Eudragit® (i.e., esters of acrylic and methacrylic acid) oligomers and drug interactions under physiological conditions were already investigated in 1998 [339]. Heun et al. selected four different drugs (furosemide, indometacin, nicotinamide and etilefrine) and studied the number of contacts of each molecule to two different Eudragit® resins. Afterwards, they confirmed their MD results with experimental data showing a reasonable match between them. Years later, Subashini et al. [54] corroborated the value of MD simulations for drug uptake forecast by combining six different polymers (alginic acid, sodium alginate, chitosan, Gantrez AN119 (methyl-vinyl– ether-co-malic acid based), Eudragit L100 and Eudragit RSPO (both acrylic acid based)) and three drugs (doxorubicin (water soluble), silymarin (sparingly water soluble) and gliclazide (water insoluble)). Diverse drug-water affinity and polymer functional groups present were selected to investigate the effect of these interactions on polymer-drug systems and thus on drug-uptake results.

Mahdavi et al. [340] studied the interaction of the anticancer drug Doxorubicin (DOX) with graphene oxide and pristine graphene structures showing the differences in drug loading and release patterns. Here, the authors showed the influence of pH and surface oxygen density on molecular mechanisms of DOX loading and release. On the other hand, Patel et al. studied the self-association of Poly(ethyleneoxide)PEO-b-poly(ε-caprolactone)PCL block copolymers and their interaction with water insoluble drugs. In this case, the orientation of hydrophobic and hydrophilic functional groups of fenofibrate and nimodipine and polymers during micelle formation showed consistent results with the experimental solubility of the drugs in the polymeric micelles [341]. The drug with more hydrophobic groups presented stronger interactions with hydrophobic polymer chains than the hydrophilic drug, corresponding to higher drug encapsulation in experimental trials. Afterwards, they widen their studies to hydrophobic drugs with different hydrogen bond donors and acceptors, demonstrating an stronger binding and encapsulation potential when increasing H-bond interactions between the drug and the polymer [342]. Therefore, by analyzing the supramolecular chemical interactions (i.e., non-covalent interactions such as electrostatic interactions, van der Waals forces, hydrogen bonds, metal–ligand bonds, and hydrophobic forces) between polymers and drugs it could be feasible to improve the design of drug delivery carriers, achieving both elevated drug loadings and drug encapsulation efficiencies.

5.2 Objectives

This chapter describes the study of solvent and drug interactions of the three different thermoresponsive polymeric chains previously used in the experimental drug delivery vectors synthesized in this work with the aim of deeply understand their performance from an atomistic insight.

Polyacrylamide (PAAm), Poly(N-isopropylacrylamide) (PNIPAm) and Poly(N-isopropylmethacrylamide) (PNIPMAm) atactic 30-mer oligomers will be compared at three different temperatures below and above their lower critical solution temperature taking notice of their structural analysis and solvation and considering the dynamic properties of water around them. The hydration network and extent around the polymeric chains together with hydrogen bond characteristics will be discussed and extrapolated to the experimental thermoresponsive properties of the different polymers.

After understanding water-polymer interactions, bupivacaine will be selected as a model drug to study the interactions of these polymeric chains with larger molecules, extrapolating the results to drug uptake and release processes. Polymer and drug concentrations as well as temperature will be the parameters tuned in this study giving an overall picture of what is happening during drug loading and release. Bupivacaine dynamics and strength of interactions will be discussed, drawing the most relevant conclusions from MD simulations, that on the other hand, will be validated with experimental studies.

5.3 Simulation methods and models

5.3.1 Potential model

To study the solvation dynamics of N- substituted acrylamide polymers below and above their lower critical solution temperatures, all-atom molecular dynamics simulations of atactic 30-mer polymers generated from Acrylamide, N-isopropylacrylamide (NIPAm) and N-isopropylmethacrylamide (NIPMAm) monomers solvated with water were performed. Selecting a suitable force-field (equation and parameters representing the potential energy of each molecule of the system) is relevant for the accuracy of the MD simulations. The Chemistry at Harvard Macromolecular Mechanics (CHARMM) general force-field is a widely used potential parameter set able to describe the majority of functional groups present

in biomolecules and drug-like molecules [47]. In this work the CHARMM General Force-Field described in **Eq. *5.1*** was used to describe the three studied polymers.

Eq. 5.1: CHARMM Force Field equation

$$E_{pot} = \sum_{bonds} k_b\,(b - b_0)^2 + \sum_{angles} k_\theta\,(\theta - \theta_0)^2 + \sum_{dihedrals} k_\varphi\,[1 + \cos(n\varphi - \delta)]$$

$$+ \sum_{impropers} k_\omega\,(\omega - \omega_0)^2 + \sum_{Ury-Bradley} k_{UB}\left(r_{1,3} - r_{1,3;0}\right)^2$$

$$+ \sum_{non-bonded} \frac{q_i q_j}{4\pi D r_{ij}} + \varepsilon_{ij}\left[\left(\frac{R_{min;ij}}{r_{ij}}\right)^{12} - 2\left(\frac{R_{min;ij}}{r_{ij}}\right)^{6}\right]$$

The first to the fifth terms of Eq. 5.1 represent the bonded interactions: bond stretching, angle bending, dihedral angles, improper dihedral angles and a Urey-Bradley 1,3 term respectively. Force constants are represented by the k's of each term. The bond, angle, improper and Urey-Bradley equilibrium terms are b_0, θ_0, ω_0 and $r_{1,3;0}$ respectively, and n and δ are the dihedral multiplicity and phase. The Coulombic electrostatic forces and Van der Waals (vdW) interactions are described in the last two terms. The partial atomic charges of atoms i and j are described as: q_i and q_j. In the Leonard-Jones (LJ) 6-12 term, ε_{ij} is the well depth; $R_{min;ij}$ is the threshold radius used to take into account vdW interactions; and r_{ij} is the instant distance between atoms i and j. Numerical values for various force fields parameters are available in reference [47]. The TIP3P water model with partial charge of -0.834 on oxygen atom was used in all simulations [343]. Figure 5.1 shows the monomer units for the three polymers studied.

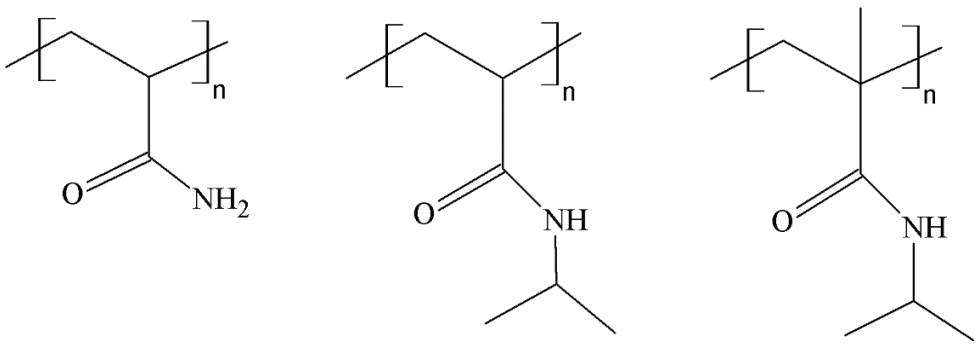

Figure 5.1: From left to right: PAAm, PNIPAm and PNIPMAm monomeric units, respectively.

Charges for some atoms of these monomers were taken from similar structures present in General CHARMM FF. However, some adjustments were needed in carbon atoms and water oxygen atoms and their non-bonded interactions in order to mimic the experimental transition temperature for both PNIPAm and PNIPMAm polymeric chains. An increase of a 15% in Van der Waals parameters value between these atoms was necessary to avoid early collapse of the chains at lower temperatures than expected. (*Appendix II: Table II.1*)

Bupivacaine model was optimized using Gaussian package. Geometry optimization was carried out under B3LYP/6-311G** algorithm; partial charges were obtained though B3LYP/6-311G** algorithm and Merz-Singh-Kollman (MK) scheme. Mulliken charges were selected as Bupivacaine charges (*Appendix II: Table II.2*). Parameters were obtained from CHARMM General FF from similar already tested molecules such as piperidine [47].

5.3.2 MD simulation details

The generation of 30-mer oligomeric chains for the three compounds studied in this work started from a monomeric unit of each of them. Here the structure generation process for PNIPMAm is described. A monomeric unit was generated and repeated to create the complete oligomeric chain. One end of the chain was closed with a methyl group (CH_3) and the other with a hydrogen atom. Monomers were connected and placed in a 90 Å side cubic simulation cell for equilibration during 100 ps. After the equilibration step, each polymer was solvated with 12000 water molecules in order to obtain a density of bulk water ~1 g/cm^3. Further minimization was carried out for 5000 steps to relax the complete system. The resulting systems were the initial point for all temperatures: 22 ºC (295 K), 37 ºC (310 K) and 47 ºC (320 K).

Bupivacaine–polymer systems were generated similarly to the previously described systems. 30-mer oligomers after the equilibration step were solvated with 18000 water molecules and different bupivacaine molecules to obtain a density of bulk water ~1 g/cm^3. Further, minimization was carried out for 10000 steps to relax the complete system. The resulting systems were the initial point for all temperatures: 22 ºC (295 K) and 42 ºC (315 K).

All Molecular dynamics (MD) simulations were carried out under *NPT* ensemble (moles (*N*), pressure (*P*), and temperature (*T*) are conserved) to study the dynamics and

structural evolution of the systems. Simulations were run at atmospheric pressure. Nosé-Hoover thermostat and barostat with 1 ps and 2 ps time constants, respectively were used to maintain temperature and pressure of the systems. The NAMD package was used to carry out the simulations [344] with periodic boundary conditions. Non-bonded interactions used a spherical cut-off of 1.4 nm and the long-range electrostatic interactions were calculated using Particle Mesh Ewald algorithms [345]. For each polymer-water system, simulations were run for 100 ns with a time step of 1 fs. However, the PNIPMAm and PNIPAm systems at 320 K needed 100 ns extra in their simulation period in order to show the coil to globule state transition. Typically, large systems like these ones equilibrate within few nanoseconds so we used the final 50 ns as the production run for all dynamical analysis. The frequency of accumulation of atomic trajectories (atom positions, temperature, pressure, velocities, etc.) was 1 ps and at least three different runs were carried out with different initial conditions finding no remarkable differences among them.

5.3.3 Trajectory analysis

Data obtained from NAMD trajectory files were analyzed using the post-processing AMBER tool Cpptraj [346]. Radial Distribution Functions (RDFs) were studied in order to analyze the differences among polymer-water/polymer-bupivacaine structural arranges in the three different oligomers below and above their LCST. The Radius of gyration (Rg) is a parameter that measures the size of a group of atoms and was used to study the structural evolution of the polymeric chains. Rg was calculated using **Eq. *5.2***:

Eq. 5.2: Radius of gyration

$$R_g^2 = \frac{1}{M}\sum_i m_i\,(r_i - r_{cm})^2$$

where r_{cm} is the center of mass of all the atoms of the chain, M is their atomic mass and m_i, r_i represent all the atoms in each polymer. The end-to-end distance of the chain, however, measures only the simple distance between the first and the last atom of the backbone and it was compared to R_g in order to understand the flexibility of the polymeric chains. Snapshots were rendered using the VMD visualization package [347].

Residence time probability of water ($P_{res}(t)$) present in the first hydration shell of the three polymeric chains was calculated at 295 K, 310 K and 320 K. This parameter defines

the probability of finding a water molecule in a certain region next to an specific atom at time t_0 and staying in the same region at a time $t + t_0$ without leaving that region in this specific time window [348][349]. $P_{res}(t)$ was averaged over 10 ns of simulation for water-polymer systems in intervals of 0.01 ps. For this analysis, water molecules were divided into three different regions:

1) Hydrophilic region: This region encompasses water molecules located in the region up to the first minimum of the RDF between oxygen atoms of water molecules and atoms of the side chain of hydrophilic groups of the different 30-mers studied. This means water molecules present in the first hydration shell around amide groups of polymer chains.
2) Hydrophobic region: In this case, this region covers water molecules located in the region of the RDF between oxygen atoms of water molecules and hydrophobic groups present in the side chain and backbone of the oligomers studied from r = 0 to the first minimum of the RDF. In this case, again water molecules of first hydration shell around hydrophobic groups of the backbone and side chain of 30-mers are taken into account.
3) Bulk water: water molecules located in the region that extends beyond the first minimum in the RDF of the water oxygen atoms and the hydrophilic/hydrophobic atoms of the oligomers.

For the three polymers, two hydrophilic groups are present in the side chain of the oligomers: the nitrogen and oxygen atoms of the amide group. However, hydrophobic groups change among the three systems: while PAAm only presents the hydrophobic CH- and CH_2-groups of the backbone, PNIPAm and PNIPMAm also have the isopropyl group as hydrophobic group in their chain. Moreover, PNIPMAm chain includes and extra methyl (CH_3-) group in the backbone, which is added to the total hydrophobic groups to take into account in the study.

Water-polymer interactions have been demonstrated to have a very important role in coil-to-globe state transition in PNIPAm [137][350] and hydrogen bonding is one of the most likely interactions between them. We studied these interactions for the three systems and

their change with temperature. The following geometric criterion was used to represent water-water hydrogen bonding:

$R_{OO} \leq 3.6$ Å

$R_{OH} \leq 2.45$ Å

$\theta \leq 30$

In the equations above, Roo represents distance between oxygen atoms from two different water molecules and R_{OH} the distance between oxygen-hydrogen that forms the hydrogen bond. The angle Θ is the angle formed by oxygen of the first water molecule and the hydrogen and oxygen atom of the other one. In this work, we have selected as minimum distance the first minimum of the corresponding RDFs of pure water. Two types of hydrogen bonds between water and oligomers are possible in our systems: (1) the carbonyl oxygen of the amide side group of any of the three oligomers and water hydrogen; and (2) hydrogen of amide group and water oxygen.

A time dependent correlation function was used in order to define the stability of these hydrogen bonds. We established a hydrogen bond occupation number which value is 1 when the hydrogen bond exists and 0 when there is not present a hydrogen bond between two atoms. The correlation function of this number describes the existence or not of hydrogen bonds over time. This can be studied in a continuous or intermittent way [351][352]. In the continuous analysis, the occupation number is allowed to vary from 1 to 0 only once. After the first breakage of the hydrogen bond between atoms i and j the occupation number cannot return to 1 anymore. However, in the intermittent analysis this tuning can be done as many times as needed until the bond is established.

Residence time probability $P_{res}(t)$ of bupivacaine molecules in the first hydration shell of the three polymeric chains was calculated at 295 K and 315 K. It defines the probability of finding a bupivacaine molecule in a certain region next to an specific atom of the polymer chain at time t_0 and staying in the same region at a time $t + t_0$ without leaving that region in this specific time window. In this case, $P_{res}(t)$ was averaged over 5 ns of simulation for bupivacaine-polymer systems in intervals of 0.01 ps.

For this analysis, polymers were divided into the same hydrophilic and hydrophobic regions described before and bupivacaine atoms were classified into these two regions as well. Atoms belonging to benzene ring and piperidine ring together with alkane chain were selected as hydrophobic regions of the molecule. On the other hand, amide nitrogen and oxygen atoms and nitrogen atom of amino cation of piperidine ring were classified as hydrophilic regions.

Once both components were divided into hydrophilic and hydrophobic regions, interactions among them were divided into:

1) Hydrophilic contacts: bupivacaine molecules located in the region that covers the inner part up to the first minimum of the RDF between hydrophilic atoms of bupivacaine molecules and hydrophilic groups of the different 30-mers studied.
2) Hydrophobic region: bupivacaine molecules located in the region of the RDF between hydrophobic atoms of bupivacaine molecules and hydrophobic groups present in the side chain and backbone of the oligomers studied from r = 0 to the first minimum of the RDF.

The same hydrophilic and hydrophobic classification was used for the calculation of minimum distance among bupivacaine molecules and 30-mer oligomers. In this case, the minimum distance between these two components was recorded and plotted all over the simulation run every time step.

5.3.4 Experimental

5.3.4.1 Microgels synthesis

PNIPAm and PNIPMAm microgels were synthetized following the protocol described in Chapter III Section 3.2.3.2 (page 69). using only NIPAM and NIPMAM monomers respectively.

5.3.4.2 Bupivacaine loading and release studies

Bupivacaine hydrochloride was load into polymeric nanogels through diffusion process. A dispersion of hybrid PNIPAm or PNIPMAm nanogels (5 mg/ml) was incubated with a bupivacaine solution (30 mg/mL). The resulted loaded dispersions were washed several times by centrifugation until non-loaded bupivacaine was removed. Samples were lyophilized before carrying drug release studies.

Controlled release studies were carried out with the drug-loaded nanogels (1 mg/mL) at room temperature (25ºC) monitoring the amount of bupivacaine released over time in the supernatants. Gas Chromatography-Mass Spectrometry (GC-MS-QP2010 SE, Shimadzu) was used to measure bupivacaine content in the supernatants. Limonene was used as internal standard.

5.4 Results and discussion

5.4.1 Structural analysis

a) Conformation Evolution. Figure 5.2 shows the conformation of (a) Polyacrylamide (PAAm), (b) Poly(N-isopropylacrylamide) (PNIPAm) and (c) Poly(N-isopropylmethacrylamide) (PNIPMAm) polymer chains after 100 ns simulation at 295 K and 310 K and 200 ns for PNIPAm and PNIPMAm simulations at 320 K. From experimental studies, the LCST of PNIPAm and PNIPMAm have been determined as 32 ºC (305 K) and 42 ºC (315 K), respectively [353] and is well known that polyacrylamide does not show any phase transition when temperature increases [354]. This behavior is observed in Figure 5.2 a), wherein PAAm 30-mer keeps its coil-like state at the three temperatures studied. However, PNIPAm and PNIPMAm (Figure 5.2 b) and c) respectively) clearly turn into a globule-like state at different temperatures. While PNIPAm folds itself at 310 K and is completely compact at 320 K, PNIPMAm 30-mer remains in its coil-like state at 310 K and undergoes to a globule configuration when the temperature rises to 320 K. Figure 5.2 suggests that coil-to-globule transition happens at different temperatures for PNIPAm and PNIPMAm chains: between 295 K and 310 K for the first one; and from 310 K to 320 K for the last one in good agreement with experimental observations.

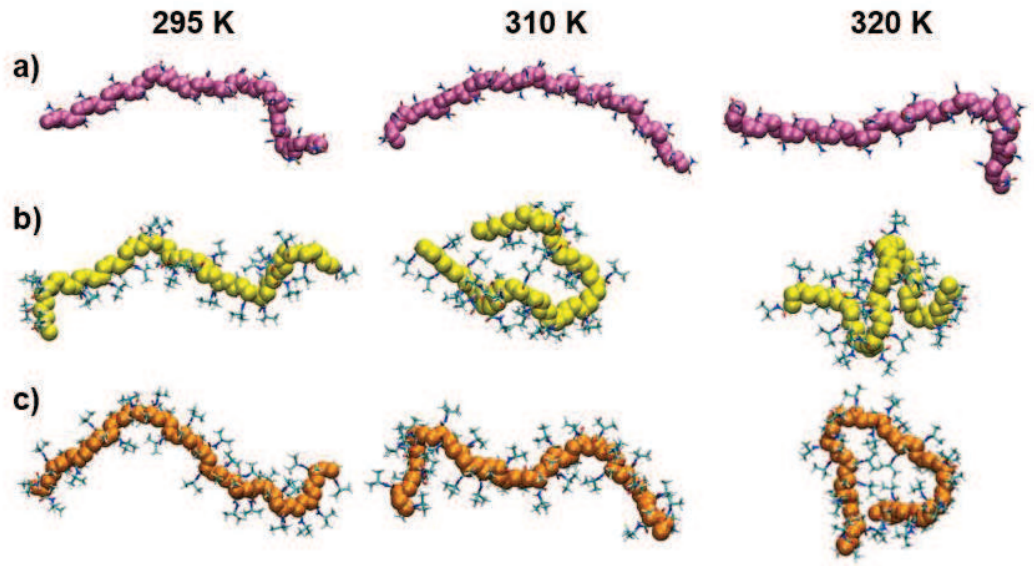

Figure 5.2: Snapshots of a) Polyacrylamide (purple backbone); b) Poly(N-isopropylacrylamide) (yellow backbone) after 100 ns of simulation; and c) Poly(N-isopropylmethacrylamide) (orange backbone) after 200 ns of simulation at the three simulation temperatures studied.

b) Radius of Gyration (R_g). The R_g distribution mean value and standard deviation of the three single polymeric chains over the 50 ns production run at 295 K , 310 K and 320 K are compared in Table 5.1.

Table 5.1: Radius of gyration (R_g) mean values and standard deviations obtained from MD production runs of all systems studied

	Temperature					
	295 K		**310 K**		**320 K**	
	Mean (Å)	*Std. Dev*	*Mean (Å)*	*Std. Dev*	*Mean (Å)*	*Std. Dev*
PAAm	15.72	1.39	15.83	1.83	17.06	1.46
PNIPAm	15.03	1.35	13.21	1.42	11.11	0.92
PNIPMAm	15.66	1.17	15.43	0.87	12.14	1.54

As seen at the first row of Table 5.1 PAAm polymer chain remains in coil-state no matter the temperature of simulation used. Mean values are over 15 Å at the three temperatures with an averaged standard deviation of ~1.5 Å. This suggests that the flexibility of the chain allows it to fluctuate, move and interact with water keeping its hydrophilic characteristics. On the other hand, it can observed in the second row of Table 5.1 a coil-to-globule transition for PNIPAm 30-mer. This transition already starts at 310 K where R_g mean

value changes from ~15 Å to 13 Å with a standard deviations of 1.35 Å and 1.42 Å respectively. However, at 310 K PNIPMAm chain keeps the same mean value and fluctuation than at 295 K suggesting a different behavior than the one of PNIPAm chain. In the case of 320 K systems, both PNIPAm and PNIPMAm undergo to globule state with a considerable decrease in R_g mean values to ~11 Å with a narrow standard deviation. In all cases fluctuations of polymer chains play an important role in R_g and therefore in their coil or globule-state. These fluctuations have a strong dependency on the tacticity, the relative stereochemistry of adjacent chiral centers within a macromolecule, of the chain [355] and time of simulation [356]. However, it is evident that PNIPAm and PNIPMAm chains have a different behavior consistent with experimental data.

End-to-end distance and radius of gyration (R_g) of both PNIPAm and PNIPMAm 30-mers at 310 K are compared in Figure 5.3. This temperature was chosen because of the conformation differences of the two polymeric chains. While R_g takes into account the center of mass of all atoms of the molecules, end-to-end distance is only a geometric measurement of the distance between the first and the last monomer of the chain.

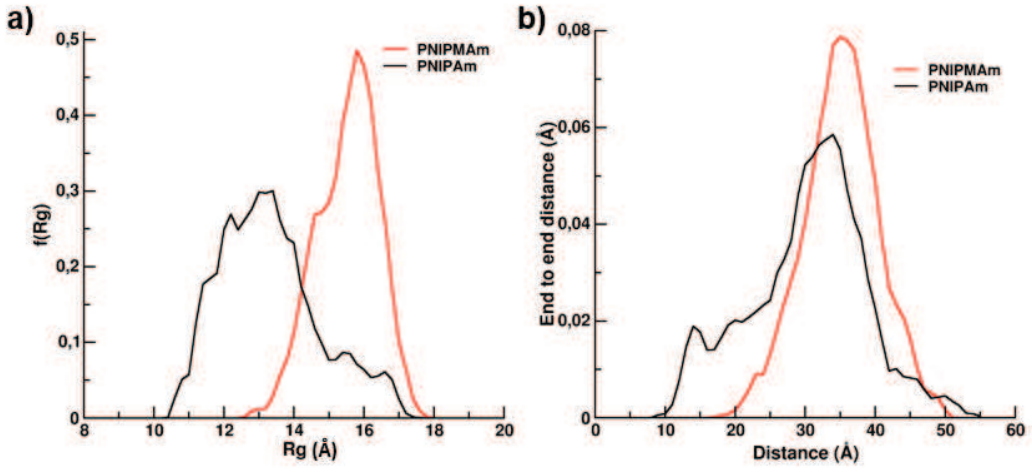

Figure 5.3: a) Radius of gyration (Å) distribution for PNIPAm and PNIPMAm polymeric chains simulation after 50 ns at 310 K; b) End-to-end distance distribution for PNIPAm and PNIPMAm single chains after 50 ns stabilized at 310 K.

In Figure 5.3 a) we can see a clear difference in the R_g of both polymers, wherein PNIPAm has a mean value of ~13 Å while PNIPMAm value is ~16 Å. However, in Figure

5.3 b) we observe how both polymers share the same end-to-end distance mean value (~35 Å). This suggests that PNIPAm chain backbone is more flexible than the PNIPMAm one, hence, PNIPAm polymer chain can collapse easier and with less energy than PNIPMAm polymeric chain.

Table 5.2 summarizes the distance distribution between the carbon of the backbone bonded to a side chain (C2) and the center of the isopropyl group (C7) of consecutive monomers for PNIPAm and PNIPMAm 30-mers at 310 K (Figure 5.4).

Table 5.2: Mean values and standard deviation of distribution of the distance between the center of isopropyl group in PNIPAm and PNIPMAm polymer chains (C7) with the previous backbone carbon (C2)

	Backbone-Isopropyl distance (Å)			
	PNIPAm		**PNIPMAm**	
	Mean	*Std. Dev*	*Mean*	*Std. Dev*
295 K	5.00	0.06	5.34	0.04
310 K	4.99	0.07	5.38	0.04
320 K	5.02	0.17	5.29	0.05

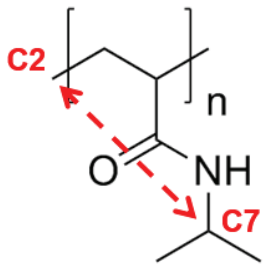

Figure 5.4: PNIPAm monomer scheme emphasizing the two atoms considered for backbone-isopropyl distance

The mean value for PNIPMAm polymeric chain is significantly above the one for PNIPAm: ~5.4 Å vs ~5 Å. These values suggest that side groups of PNIPMAm polymer are more separated from the backbone than PNIPAm ones. The main difference between them relies on the presence of a methyl group bonded to the backbone carbon (C2) in PNIPMAm polymer. Figure 5.5 shows five monomeric units of PNIPAm (a) and PNIPMAm (b) polymeric chains marking the backbone carbons (yellow and orange, respectively) and functional groups attached to C2 carbon of the backbone (dark blue).

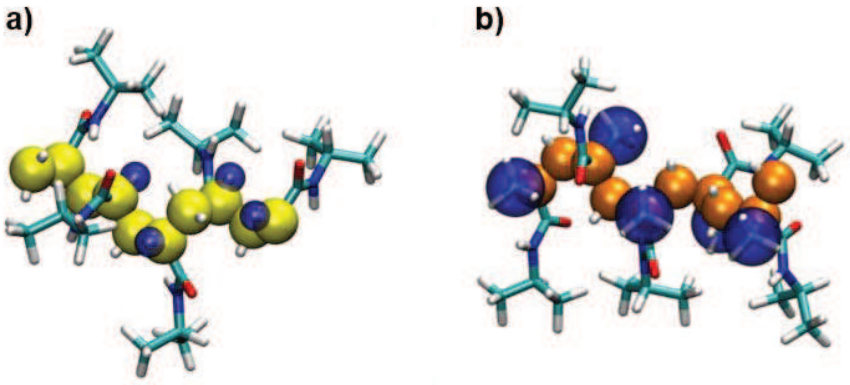

Figure 5.5: Snapshots of five monomer units of PNIPAm (a) and PNIPMAm (b) polymer chains. Backbone carbons are represented in yellow and orange, respectively. Hydrogen in a) and methyl group in b) are marked in dark blue.

In case of PNIPAm units, blue spheres represent hydrogen atoms, while in PNIPMAm chain these represent methyl groups. As methyl groups are more voluminous than hydrogen atoms, it is more difficult for PNIPMAm chain to bend itself. This fact hinders the interaction among side chains of the polymer and so it takes more energy and needs higher temperature to achieve a globular state. The steric conformation of these two polymers has been thought to be the reason of the shift of LCST between them by experimental researchers [334][335], however, in this dissertation we discuss another causes of this change in the thermoresponsive properties.

c) Radial Distribution Function. Radial distribution Function (RDF) can be used to study the structure of water molecules near polymeric chains and can be related to the thermo-responsive properties of our systems.

Figure 5.6 shows RDF for water oxygen and hydrophilic and hydrophobic groups of polymeric chains at 295 K and represents the most favorable atom pairs for hydrogen bond formation between water and polymers. The first peak for PAAm 30-mer in Figure 5.6 a) at ~2.6 Å is much more intense that the ones obtained for PNIPAm and PNIPMAm polymeric chains. The lack of isopropyl groups in PAAm chain permits water to have more accessibility to the amide group. Also, we can observe a shift in this peak for PNIPMAm polymer to ~3 Å. On the other hand, water accesses easily to carbonyl oxygen for the three polymer chains. Figure 5.6 b) demonstrates how the height of the first peak, and thus the number of water molecules next to selected atoms, shows the following tendency PAAm > PNIPAm >

PNIPMAm. This behavior is also observed for the second and third hydration shells (peaks at ~5.5 Å and ~7 Å, respectively). All these results suggest a different organization of water molecules around hydrophilic groups of PNIPAm and PNIPMAm chains. Extra methyl groups present in PNIPMAm backbone may hinder the accessibility of water molecules to its hydrophilic groups.

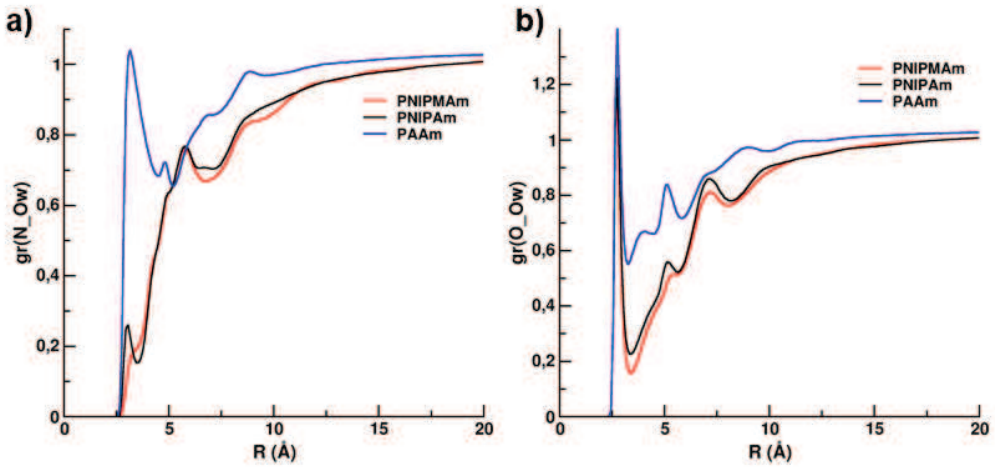

Figure 5.6: Radial distribution function (RDF) for a) water oxygen and amide nitrogen (Ow-N6) in water; b) water oxygen and carbonyl oxygen of polymers side chains both at 295 K.

In the case of water accessibility to the polymer backbone, we compared PNIPAm (black) and PNIPMAm (red) 30-mers in Figure 5.7. Dotted lines represent RDF for water oxygen and backbone carbon CH_2 (C3). We observe a shift in the first hydration shell from PNIPAm to PNIPMAm polymer chains, as well as a clear decrease of peak's height. However, second hydration shell remains with the same intensity and is slightly closer than PNIPAm one. On the other hand, straight lines represent the distance between water oxygen and backbone carbon attached to the side chain and methyl group in case of PNIPMAm (C2). Here, Figure 5.7 shows a wider first hydration peak for PNIPAm (from ~3.0 Å to ~5.1 Å) compared to PNIPMAm (from ~4.0 Å to ~5.1 Å) but a higher intensity in the peak. Second hydration shell peak for PNIPMAm is also lower than that for PNIPAm chain showing less presence of water around its backbone.

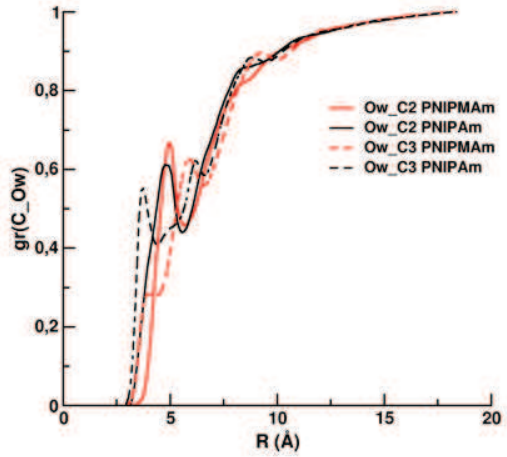

Figure 5.7: Radial distribution function (RDF) comparison of water oxygen and the two carbon present in the backbone: C substituted (C2) (straight line) and CH_2 (C3) (dotted line) at 295 K.

These results are in agreement with the steric effect of methyl group discussed previously. Methyl group has more volume than a hydrogen atom, which hiders the accessibility of water molecules to the backbone. Also, the rotation of consecutive monomers for PNIPMAm depends on this extra methyl group that needs more space to be located during the polymerization process. This organization of monomers affects to polymer-polymer and water-polymer interactions leading to a different structure of water around the polymeric chains and changing their coil-to-globule transition temperature.

Figure 5.8 shows the RDF for water oxygen and methyl groups of the isopropyl side chain for PNIPAm and PNIPMAm 30-mers. Contrary to the other RDF analysis, PNIPMAm first hydration peak is slightly higher than that of PNIPAm. However, the third hydration shell peak disappears for the PNIPMAm polymeric chain.

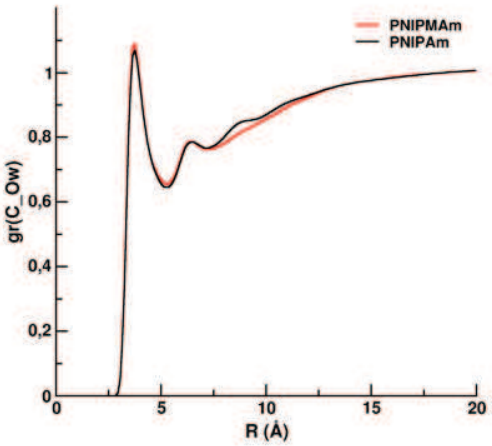

Figure 5.8: Radial distribution function (RDF) for water oxygen and methyl isopropyl groups at 295 K.

All results previously discussed are also observed at 310 K and 320 K. In Figure 5.9 a) and d) PAAm chain does not show a remarkable decrease of its RDF's peaks because of the lack of conformational change with temperature. However, it was observed a clear decrease in PNIPAm and PNIPMAm 30-mers (Figure 5.9 b) and c) respectively) of second and third hydration shells in case of water-hydrophilic groups interaction. Also a notable decrease of the peaks intensity from the first to the third hydration shell of water oxygen and backbone carbons interaction is depicted in PNIPAm and PNIPMAm chains. (Figure 5.9 e) and f) respectively). This suggests a change in the organization of water molecules when temperature increases, increasing the hydrophobicity of these two polymeric chains inducing their phase transition.

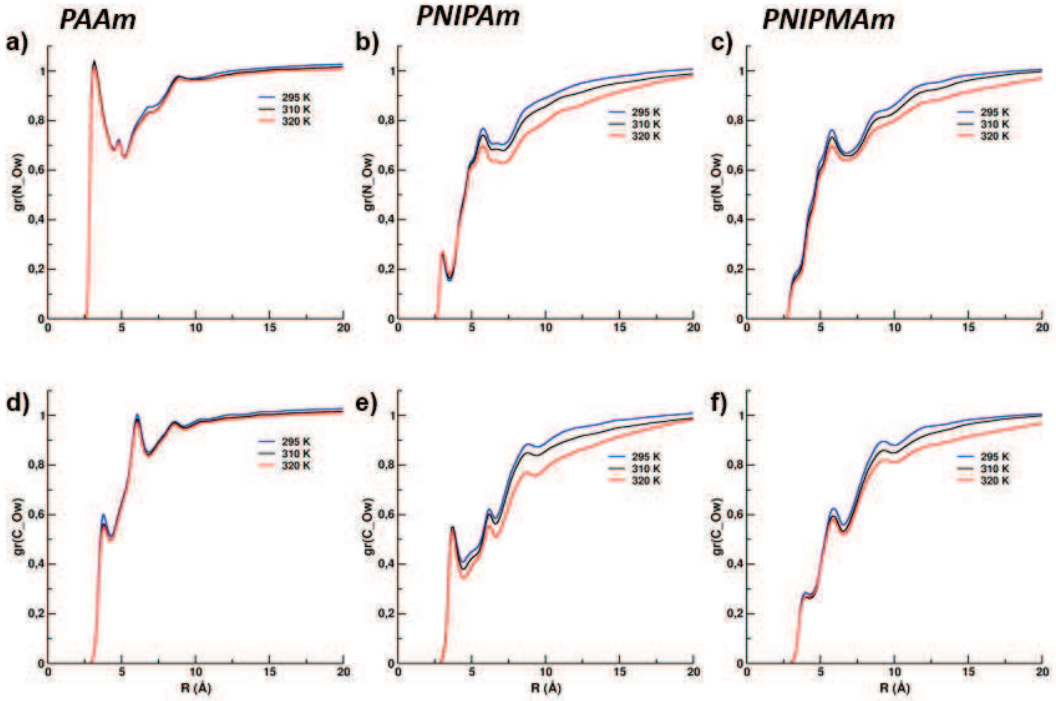

Figure 5.9: a)-c) Radial distribution function (RDF) for water oxygen and amide nitrogen (Ow-N6) of PAAm, PNIPAm and PNIPMAm respectively; d)-f) Radial distribution function (RDF) for water oxygen and backbone carbon (Ow-C3) of PAAm, PNIPAm and PNIPMAm, respectively. All results showed at three different temperatures above and below LCST: 295 K, 310 K, 320 K.

5.4.2 Solvation and dynamic properties of water

a) Hydration network between monomers. In RDF calculations, the area under the peaks represents the number of water molecules present in the hydration shells. The first peak corresponds to the first hydration shell, the second to the second hydration shell and so on. Also, how these water molecules are structured and how the network formed can give an atomistic insight into water conformation around the polymer explaining the LCST behavior.

Table 5.3 contains the coordination number of water molecules for first hydration shell for PAAm, PNIPAm and PNIPMAm 30-mers both below and above LCST. Results for hydrophilic groups ($N_{Ocarb\text{-}Ow}$ and $N_{Nam\text{-}Ow}$) indicated that there are not remarkable changes when temperature increases from 295 K to 320 K. However, values for isopropyl groups ($N_{iso\text{-}Ow}$) and for the backbone ($N_{back\text{-}Ow}$) decrease when the polymeric chains are above their LCST. At 295 K, PNIPMAm isopropyl groups are more solvated than PNIPAm ones (~13.1 Å vs ~12.88 Å). This may lead to a higher energy to dehydrate the polymeric chain and thus shifts PNIPMAm LCST to higher temperatures. Nevertheless, when the system reaches 320

K PNIPMAm is less solvated than PNIPAm. The change in the first hydration shell of the backbone follows the same behavior than the isopropyl groups but in this case PNIPMAm is less hydrated than PNIPAm at both temperatures. The change of water molecules for PNIPAm is ~1.21 and for PNIPMAm ~0.06, which suggests that water molecules next to PNIPMAm backbone have less mobility than that for PNIPAm so they cannot desorb even when the temperature rises. The main change was observed for isopropyl groups in the case of PNIPMAm 30-mer.

Table 5.3: Coordination number of water molecules in first hydration shell at both 295 and 320 K for PAAm, PNIPAm and PNIPMAm polymers during the 50 ns of production run. (Data obtained from integration of RDF peaks showed before)

	$N_{iso\text{-}Ow\ (C8\&C9)}$		$N_{back\text{-}Ow\ (C3)}$		$N_{Ocarb\text{-}Ow}$		$N_{Nam\text{-}Ow}$	
	295 K	320 K	295 K	320 K	295 K	320 K	295 K	320 K
PAAm	-	-	3.2	3.0	2.31	2.26	8.26	8.14
PNIPAm	12.88	11.88	3.52	2.31	1.92	1.93	0.64	0.69
PNIPMAm	13.10	11.80	1.52	1.46	1.68	1.67	0.49	0.41

b) Extent of hydration of polymeric chains. Figure 5.10 shows the continuous Residence time probability ($P_{res}(t)$) of water molecules next to hydrophobic and hydrophilic groups below and above the LCST following the criteria described in the "Simulation details" section 5.3.2 (page 154).

These results can be used to quantify how long on average, water molecules stay within a certain distance around the polymer. Here, we used the first minimum of RDF analysis to describe the first hydration shell for all systems studied. Figure 5.10 a) compares $P_{res}(t)$ of water molecules around the backbone of polymers at 295 K. PAAm and PNIPMAm 30-mers have a sharp decrease compared to that obtained for PNIPAm. This observation suggests that mobility of water next to the backbone for PNIPAm chain is more restricted than that retrieved for the other two polymers. This represents a slow dynamical behavior for water molecules next to the polymer that permits water-PNIPAm interactions being more stable and keeps the PNIPAm polymer chain hydrophilic below the LCST.

However, it is observed in Figure 5.10 b) that water $P_{res}(t)$ is next to hydrophilic groups. In this case, PNIPMAm has longer water residence time than PNIPAm. This suggests

that water cages around side chains of PNIPMAm polymer are more stable than those for PNIPAm. The extra methyl group of the backbone creates voids between monomeric units where water molecules are adsorbed and thus stay longer than in PNIPAm chains. This can be related to the necessity of high energy to remove these water molecules from the surroundings of the polymeric chain and and it also explains the higher LCST required for this polymer.

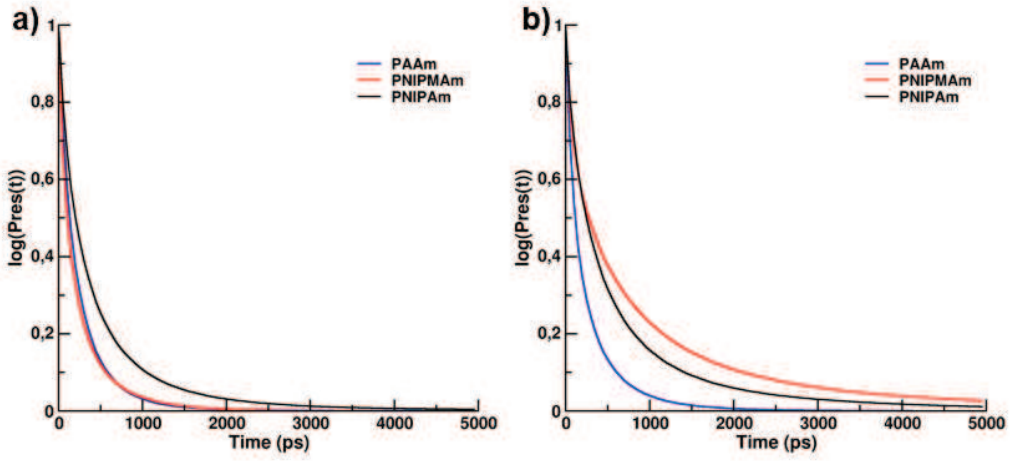

Figure 5.10: Continuous residence time probability of water molecules near a) backbone carbons and b) hydrophilic groups at 295 K.

As we discussed previously, the orientation of the methyl group in each monomer of the PNIPMAm chain is mainly oriented the same way than the amide nitrogen, hindering its interaction with the solvent and letting the oxygen to be more accessible to form hydrogen bonds to water molecules.

On the other hand, Figure 5.11 show $P_{res}(t)$ of water around isopropyl groups for PNIPAm and PNIPMAm 30-mers at 295 K and 320 K, respectively. They show a slightly faster decrease when temperature is above the LCST (320 K) than when temperature is below LCST for both polymers. However, water molecules stay slightly longer near PNIPMAm chain than by PNIPAm chain at 320 K and the opposite behavior is shown at 295 K. This may be explained because of the larger voids present in the PNIPMAm chain due to the extra methyl group in the backbone.

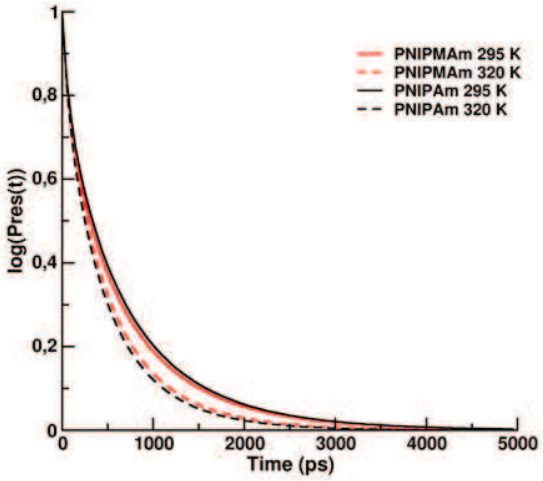

Figure 5.11: Continuous residence time probability of water molecules near methyl groups of isopropyl side chain groups at 295 K and 320 K.

c) Hydrogen-bond characteristics. Hydrogen bonds were studied following the geometric criteria described in the "Simulation methods" section. Table 5.4 contains the number of water-polymer hydrogen bonds (type 2 and type 3 respectively) taken over 1 ns of simulation for PNIPAm and PNIPMAm polymeric chains at 295 K, below their LCST.

It can be observed that, above their LCST, when the polymer acts as acceptor (type 3) and water molecules are the donors of hydrogen bonding, there are much more hydrogen bonds than when it is water the acceptor and the polymer the donor in both cases. However, the value for this type 3 hydrogen bonds for PNIPMAm chain is higher than that for PNIPAm chain what can be another reason of its higher LCST. The necessary energy to break these hydrogen bonds in PNIPMAm chain is higher than for PNIPAm one, what matches with the shift of the LCST of PNIPMAm 30-mer to higher temperatures.

Table 5.4: Number of type 2 and type 3 hydrogen bonds between water and PNIPAm and PNIPMAm polymeric chains at 295 K below their LCST

	Hydrogen Bonds	
	Type 2: **Ow-N6**	*Type 3:* **Hw-O5**
PNIPAm	1.8	9.8
PNIPMAm	0.3	13.1

On the contrary, at globule-like state, polymer-polymer (type 1) hydrogen bonds are the atomic interactions that play the main role. As a result, the surface area exposed to bulk water decreases and polymeric chains undergo to a globule-state. Figure 5.12 a) shows the continuous autocorrelation function for type 1 hydrogen bonds for the three polymers studied at 320 K. We observe how the hydrogen bond correlation decays faster for PAAm 30-mer due to its coil-like state at 320 K. However, PNIPMAm chain has a slower decay and the one for PNIPAm is even slower. This suggests that although both chains are in globule-state, the interactions among PNIPAm monomers are longer than that observed for PNIPMAm chain, which can explain its lower LCST. We find the same tendency for the intermittent correlation function.

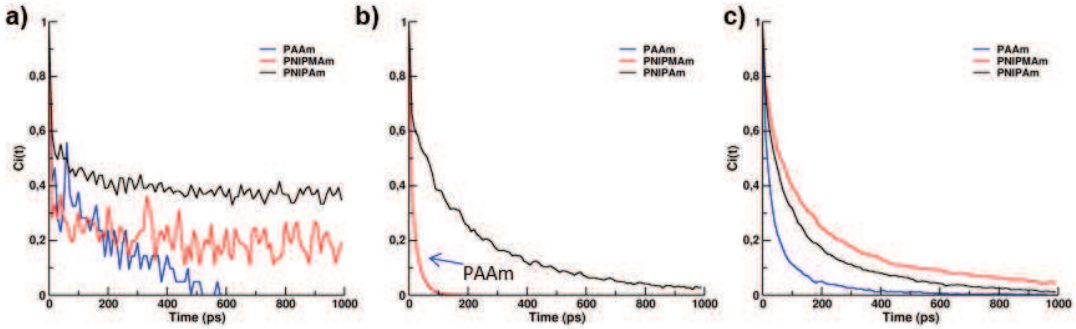

Figure 5.12: Hydrogen bond correlation for a) polymer-polymer hydrogen bonds (type 1)) at 320 K; b) type 2 hydrogen bonds where polymer act as donor; and c) type 3 hydrogen bond where polymer act as donor at 295 K, both at 295 K.

Figure 5.12 b) and c) presents the comparison of type 2 and type 3 hydrogen bonds continuous correlation functions at 295 K where polymers act as donor and acceptor, respectively. This hydrogen bond lifetime analysis below the transition temperature pretends to explain the reasons of the LCST shift between these polymers. Figure 5.12 b) shows how PNIPMAm and PAAm have a sharp decay of hydrogen bonding while PNIPAm chain's decay is smoother. Comparing these results with Figure 5.12 c) where type 3 hydrogen bond correlation functions are presented, we observed two different behaviors. While the decay is slower for PAAm and PNIPMAm chains in type 3 hydrogen bonding, PNIPAm chain has a sharper decay. This suggests that hydrogen bond between carbonyl oxygen and water hydrogen (type 3) is more stable than that for amide hydrogen and water oxygen in

PNIPMAm but not in PNIPAm. This fact, together with the higher number of type 3 hydrogen bonds in both cases, can explain the higher LCST for the PNIPMAm chain.

5.4.3 Bupivacaine interaction

a) Extent of bupivacaine interaction with polymer chains.

Simulations of single PAAm, PNIPAm and PNIPMAm polymeric chains in water showed a different behavior and interaction with their environment. Thus, we extended our study not only to water molecules, but also to drug macromolecules already experimentally studied in the laboratory such as Bupivacaine (BVP).

In order to cover several aspects in the study, different parameters were modified to simulate real experimental conditions. In the first place, polymer and drug concentrations are usually altered when drug delivery vectors synthesis is optimized. Thus, three different drug concentrations and two different polymer concentrations were analyzed.

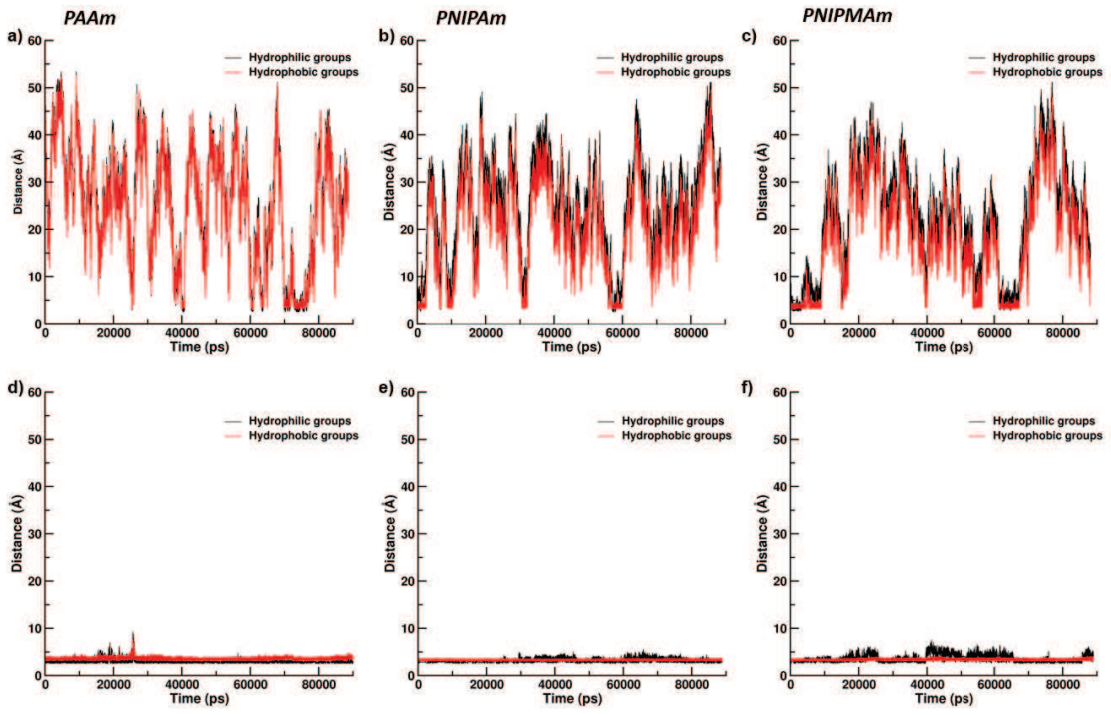

Figure 5.13: Minimum distance between bupivacaine molecules and polymer atoms of PAAm (a) and d)); PNIPAm (b) and e)); and PNIPMAm (c) and f)). Upper line represents 1 BVP molecule-1 polymer chain system. Lower line represents a system composed of 10 BVP molecules and 4 polymeric chains. All those systems are studied at 295 K.

Figure 5.13 shows the minimum distance among any polymer-drug molecule pair at 295 K. The higher both concentrations are, the longer they are stuck together. These results match perfectly with the probability to interact when the number of molecules in the environment increases in the same space. Both hydrophilic and hydrophobic groups were considered separated in order to elucidate any different behavior, showing no remarkable variations.

However, more specific information can be obtained when residence time probability of hydrophilic and hydrophobic groups of bupivacaine are close to the different polymeric chains. Figure 5.14 presents the results for the residence time probability of bupivacaine molecules to polymeric chains.

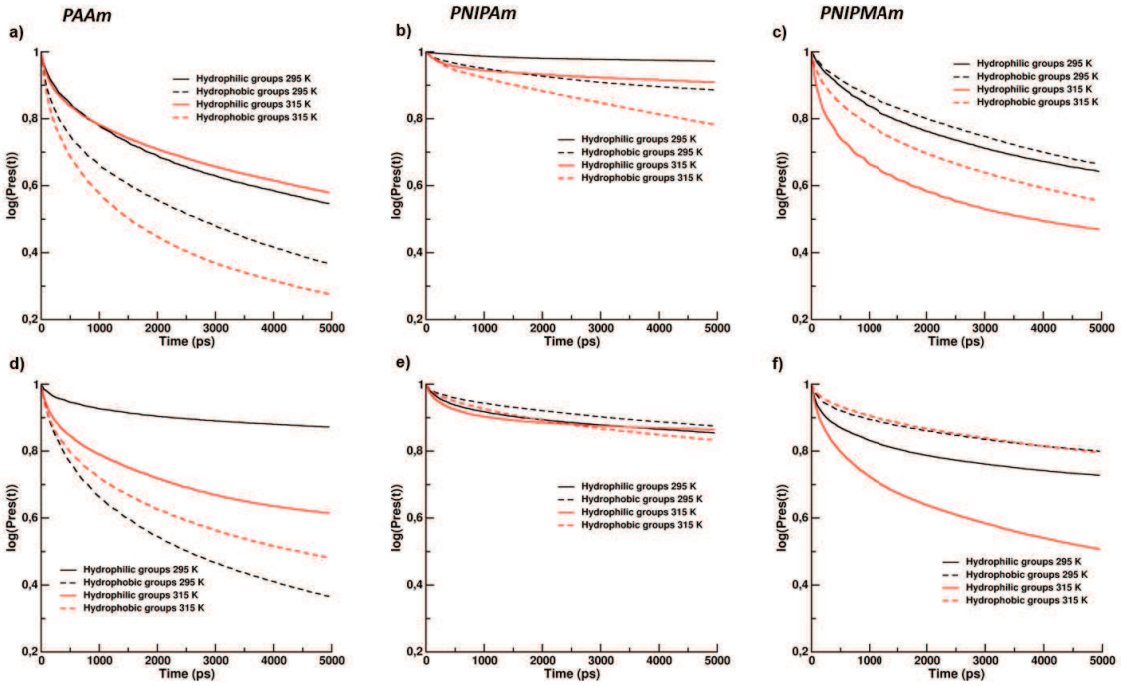

Figure 5.14: Residence time probability of bupivacaine molecule next to polymer chains: PAAm (a) and d)); PNIPAm (b) and e)) and PNIPMAm (c) and f)) at 295 K (black) and 315 K (red). Straight lines refer to hydrophilic contacts and dotted lines to hydrophobic interactions. The number of bupivacaine molecules in the system remains constant for all of them (4) but polymer concentration varies from 1 (Upper line) to 4 (Lower line). Simulation time: 5 ns.

Two different systems were considered: the upper row represents systems with 1 polymeric chain and 4 bupivacaine molecules, while the lower row shows the results for systems formed by 4 polymeric chains and 4 bupivacaine molecules. In both cases, the

general conclusions are similar. Comparing hydrophilic (straight lines) and hydrophobic (dotted lines) for each polymer, PAAm presents longer hydrophilic interactions; PNIPMAm interacts preferably with its hydrophobic groups and PNIPAm chain shows equal residence time for both hydrophilic and hydrophobic interactions. These results, suggest that the lack of accessibility of external molecules to hydrophilic amide groups in PNIPMAm chain already showed in solvent interaction analysis, also affects to drug-polymer interactions making hydrophobic interactions dominant for this chain. Meanwhile, PNIPAm chain has the possibility to connect equally with the hydrophilic and hydrophobic groups of BVP. This behavior is observed also when the polymer concentration increases in the system.

In terms of temperature, the results obtained do not depict clear conclusions about its effect in the residence time stability for drug-polymer interactions. It would be expected that drug-polymer interactions weaken when temperature increases due to the stronger polymer-polymer interactions for hydrophobic groups. Results for 295 K (black lines) and 315 K (red lines) below and above polymers LCST are presented in Figure 5.14. Moreover, Table 5.5 presents the summary of residence time probability of PAAm, PNIPAm and PNIPMAm bupivacaine systems after 5 ns of simulation run at two temperatures (295 K and 315 K).

Table 5.5: Residence time probability to find hydrophilic and hydrophobic contacts after 5 ns of simulation run. First column represent the number of polymeric chains in the systems (1 or 4); first row indicates the number of bupivacaine molecules in the systems (4 or 10)

		Hydrophilic				Hydrophobic					
		295 K		315 K		295 K		315 K		**Average**	
		4	*10*	*4*	*10*	*4*	*10*	*4*	*10*	*Philic*	*Phobic*
PAAm	*1*	0.55	0.71	0.58	0.28	0.38	0.58	0.28	<0.2	0.63	0.39
	4	0.88	0.81	0.61	0.49	0.38	0.51	0.49	0.28		
PNIPAM	*1*	0.98	0.49	0.91	0.91	0.89	0.4	0.79	0.88	0.81	0.80
	4	0.85	0.78	0.85	0.71	0.86	0.89	0.83	0.83		
PNIPMAM	*1*	0.63	<0.2	0.49	0.32	0.67	0.41	0.56	0.38	0.45	0.60
	4	0.71	0.25	0.5	0.51	0.8	0.48	0.8	0.69		

These data do not show a clear conclusion about the temperature effect on our systems because when temperature increases residence time probability doesn't show a clear increase or decrease tendency While predictions are accomplish by 1polymer-10 BVP PAAm system or 1 polymer-4 BVP system; there are discrepancies in 1 polymer-10 BVP systems for PNIPAm, 4polymer-10 BVP for PNIPMAm or 4 chains-4 BVP molecules for PAAm. More

studies and the effect of bupivacaine molecule orientation in each case would be necessary to determine a reliable conclusion about temperature effects on drug-polymer interactions.

On the other hand, the average values point that PNIPAm interactions for both hydrophilic and hydrophobic groups are longer than the ones for PAAm and PNIPMAm polymeric chains. While the probability to find hydrophilic or hydrophobic interactions between PNIPAm chains and bupivacaine after 5 ns of simulation is ~0.8; the most important interactions for PNIPMAm chain, in other words, hydrophobic groups interactions is only ~0.6 and the ones for PAAm, hydrophilic groups, is also around ~0.63. Moving this findings to real drug-polymer systems, it would be expected to observe a slower drug release for PNIPAm drug delivery carriers than for PNIPMAm or PAAm systems due to its longer residence time close to the polymeric chains.

b) Experimental release studies. The all-atom study of bupivacaine-polymer interactions suggested a different behavior at molecular level depending on the polymer chain present in a bupivacaine saturated environment. Thus, it encouraged us to try to prove it experimentally in the laboratory.

In order to get that, two polymers from pure NIPAm and NIPMAm monomers, respectively were synthetized and loaded with bupivacaine following the process already developed by out group (see Experimental section for more details). After bupivacaine loading, the samples were kept at room temperature, closer to 295 K as studied in MD simulations, and its release was monitored using GC-MS.

Figure 5.15 shows the release pattern from both samples treated under the same loading and release conditions.

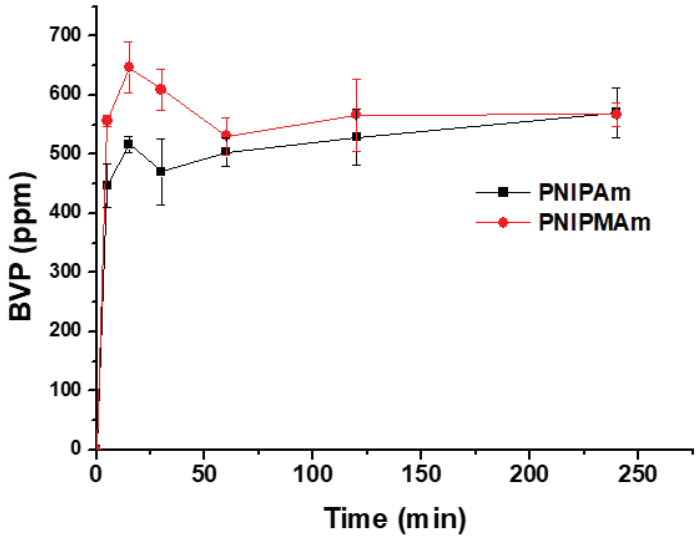

Figure 5.15: Bupivacaine release profile from PNIPAm and PNIPMAm microgels at 295 K.

It can be observed that PNIPMAm microgels released bupivacaine molecules in a more abrupt way while PNIPAm ones presented a more sustained release. This fact matches perfectly with MD results where bupivacaine molecules stay closer to PNIPAm oligomers for a longer time than when they are by the PNIPMAm ones. Hence, it suggests that the methyl group from the backbone of PNIPMAm oligomers does not allow a good interaction with the drug molecules producing a faster release despite their higher hydrophobic properties, what can be extrapolated to other polymeric chains and could be helpful for future design of drug delivery vectors.

5.5 Conclusions

After analyzing by atomistic simulations the solvation structure of water around three different thermo-responsive polymeric chains we can confirm that this structure has a notable effect on their thermoresponsive properties. The presence of an extra functional group in the backbone affects the hydration shell of the polymer modifying its LCST. The higher hydration, the higher temperature needed to remove water molecules from its surroundings. Comparing PNIPMAm and PNIPAm compounds, it was proved that the higher LCST obtained for the first one is caused by the fact that its isopropyl side groups in coil state is more hydrated that the ones in PNIPAm. The angle among monomers allows water molecules

to be closer to them making more difficult to desorb and thus increasing its LCST. Moreover, the extra methyl group of its backbone makes isopropyl-backbone distance larger than when only hydrogen atom is bonded to the backbone hindering the possibility of collapse (i.e., coil-to-globule transition).

The approach described in this work can be extended to the study of different functional groups substituted in the backbone of N-polyacrylamides in order to tune their LCST as homopolymers. Geometric organization during the polymerization and intramolecular interactions of this group in the backbone have been demonstrated to play a key role in the thermo-properties of those polymeric chains hindering the solvent access to the backbone, the distance among side chains of the polymer and the bending possibilities of the main chain.

This was also observed and certified when drug molecules interact with polymeric chains. Functional groups affect the strength of polymer-drug binding conditioning the drug uptake and release patterns as experimentally depicted in this work. This illuminates the understanding of drug delivery vectors behavior from an atomistic scale and may help to synthetize customized polymeric structures for desired drug release patterns according to personalized treatments.

CHAPTER VI

CONCLUSIONS/CONCLUSIONES

"Nothing in life is to be feared, it is only to be understood. Now is the time to understand more, so that we may fear less"

Marie Curie, Chemist and Physicist (1973)

Chapter VI

GENERAL CONCLUSIONS

6 General conclusions

The main focus of the work conducted in this thesis was placed on the synthesis of hybrid drug delivery vectors used as triggered on-demand drug carriers, which were externally activated to obtain a pulsatile drug release. The results reached and the experience gained brought us to draw the following conclusions:

- Microfluidic platforms can be used as continuous reactors for the synthesis of biodegradable plasmonic CuS nanoparticles having a 4-fold reduction in the synthesis time compared to traditional batch reactors. These nanoparticles are capable to fully biodegrade under simulated physiological conditions and show excellent photothermal and ROS generation effects under subcytotoxic doses in four different cell lines. This highlights the great advantage over other plasmonic nanoparticles including gold or carbon based nanoparticles which are not biodegradable and where bioaccumulation constitutes a concern.
- These biodegradable CuS nanoparticles can be combined with the cleavable thermosensitive copolymer P(MEO_2MA-co-$OEGMA_{500}$) obtaining a complete cleavable drug delivery vector having the ability to release a drug on demand with spatio-temporal control. Apart from this huge advantage over conventional hybrid vectors, the loading and on-demand triggered release of bupivacaine has been demonstrated and no cytotoxic effect has been observed at doses up to 0.1 mg/mL.
- This pulsatile drug release can also be achievable using PNIPAm hybrid nanogels decorated with HGNPs under different NIR laser irradiations. A strong electrostatic interaction between the plasmonic nanoparticles and the polymer guarantees their stability under physiological conditions. Moreover, it has been validated their *in vitro* loading and on-demand release properties and no remarkable cytotoxic effects have been observed at doses up to 0.1 mg/mL in four different cell lines.
- Customized hybrid and thermoresponsive drug delivery microparticles can be successfully synthetized by a simple LED-activated photopolymerization process in a one-step flow focusing continuous microreactor. A simple PTFE tubing microreactor interfaced with a UV LED device can be used to easily tune the resulting MPs properties by altering microreactor features and synthesis conditions. HGNPs

and bupivacaine can be co-introduced during the synthesis and their triggered thermoresponsive properties are demonstrated. For the resulting materials, no remarkable influence on the cell metabolism and cell cycle was corroborated under subcytotoxic doses (0.5 mg/mL).

- The successful chemical modification of IR820 as label dye and its attachment to six different polymeric nanoparticles has been demonstrated to be a useful approach for the study of biodistribution and local persistence. These results have corroborated their potential application as drug depots in local affections showing no inflammatory or degenerative reactions 7 days and 14 days after intramuscular and subcutaneous administration, respectively. It permits to overcome the disadvantages of using radiolabeling or time-consuming chromatography methods to track the local persistence of drug-loaded nanoparticles.
- Thanks to molecular dynamics simulations, it has been demonstrated that the presence of different functional groups in the polymer chain backbone can tune the LCST of the resulted polymers and thus can modulate their behavior as drug delivery vectors. Also, pharmacokinetics of bupivacaine release have been validated over MD simulations and confirmed in experimental tests to suffer remarkable changes when different functional groups are present in the system. It has been proved that drug-polymer interactions determine the drug loading and release pattern opening a broad variety of opportunities for customized medical treatments.

Capítulo VI

CONCLUSIONES GENERALES

6. Conclusiones generales

El objetivo principal del trabajo llevado a cabo en esta tesis doctoral ha recaído en la síntesis de vectores híbridos de liberación de fármaco para su uso como portadores de fármaco activados a demanda externamente activados mediante luz infrarroja para obtener una liberación pulsada de fármaco. Los resultados alcanzados y la experiencia adquirida nos han llevado a discernir las siguientes conclusiones:

- Plataformas microfluídicas pueden ser utilizadas como reactores continuos para la síntesis de nanopartículas plasmónicas biodegradables reduciendo 4 veces el tiempo de síntesis comparado con reacciones discontinuos convencionales. Estas nanopartículas son capaces de degradarse completamente bajo condiciones fisiológicas simuladas y muestran excelentes propiedades fototérmicas y generación de especies reactivas de oxígeno (ROS) a concentraciones subcitotóxicas en cuatro líneas celulares. Esto recalca la gran ventaja respecto a otras nanopartículas plasmónicas como nanopartículas de oro o carbón no biodegradables y donde la bioacumulación presenta un gran problema.
- Estas nanopartículas de sulfuro de cobre biodegradables pueden combinarse con co-polímeros termosensibles como el P(MEO_2MA-co-$OEGMA_{500}$) obteniendo un vector de liberación de fármaco completamente fragmentable con la habilidad de liberar el fármaco a demanda con control espacio-temporal. Además de esta gran ventaja sobre vectores híbridos convencionales, la carga y liberación asistida a demanda de bupivacaina ha sido demostrada sin efectos citotóxicos a concentraciones menores de 0.1 mg/mL.
- Esta liberación pulsada de fármaco también se puede conseguir usando nanogeles híbridos de PNIPAm decorados con nanopartículas plásmonicas de oro (HGNPs) bajo diferentes potencias de irradiación de láser infrarrojo. Una interacción electrostática fuerte entre las nanopartículas plasmónicas y el polímerogarantiza su estabilidad en condiciones fisiológicas. Además, la carga y liberación a demanda del fármaco ha sido validada sin presentar efectos citotóxicos en dosis hasta 0.1 mg/mL en cuatro líneas celulares.
- Micropartículas híbridas termosensibles personalizadas para liberación de fármaco pueden ser satisfactoriamente sintetizadas gracias a un poceso simple de fotopolimerización activado con luz ultravioleta proporcionada por un LED en un

microreactor continuo basado en tecnología flow focusing. Un reactor simple compuesto por tubería de PTFE acoplado a un LED ultravioleta puede ser usado para modificar fácilmente las propiedades de las micropartículas resultando gracias a la alteración de los componentes del microreactor y las condiciones de síntesis. Nanopartículas de oro y fármacos como la bpivacaina pueden ser introducidos en las micropartículas durante la síntesis y posteriormente las propiedades termosensibles se han demostrado. No se han encontrado influencias destacables en el metabolismo celular y el ciclo celular para los materiales obtenidos en dosis menores de 0.5 mg/mL.

- La modificación satisfactoria del fluoróforo IR820 y su anclaje a seis nano y micropartículas polímericas se ha demostrado siendo una opción útil para el estudio de la biodistribución y persistencia local de vectores nanoestructurados. Estos resultados han corroborado la aplicación potencial de los materiales estudiados como reservas locales de fármaco sin mostrar reacciones inflamatorias o degenerativas tras 7 y 14 días tras su administración intramuscular y subcutánea respectivamente. Esto permite superar las desventajas del uso de radiomarcadores o largos métodos de cromatografía para seguir la persistencia local de nanopartículas cargadas de fármaco.
- Gracias a la simulación basada en dinámica molecular, se ha demostrado que la presencia de diferentes grupos funcionales en las cadenas poliméricas puede modificar la temperatura de colapso de los polímeros y por tanto modular su comportamiento como vectores de liberación de fármacos- Además, la farmacocinética de liberación de la bupivacaine se ha comprobado mediante simulaciones de dinámica molecular y se ha confirmado mediante ensayos experimentales que sufre cambios notables cuando diferentes grupos funcionales están presentes en la cadena polimérica. Se ha probado que las interacciones fármaco-polímero determinan la carga y liberación del fármaco abriendo una gran cantidad de oportunidades para personalizar los tratamientos médicos.

APPENDIX I

METHODS & CHARACTERIZATION TECHNIQUES

Appendix I

METHODS & CHARACTERIZATION TECHNIQUES

Appendix I: Methods & Characterization techniques

I. Methods: Biological studies

The final purpose of all micro- and nanoparticles described in this work is their biomedical application as drug delivery vectors. Therefore, *in vitro* biological studies are needed prior their use in real patients and they are present in the experimental chapters of this book. The biocompatibility of micro- and nanoparticles synthetized have been assessed at different levels regarding metabolism, cell nucleus (DNA and cell cycle) and cell membrane (cell apoptosis). Here, the common methodology to carry out these tests is described, though particular cell lines and concentrations are pointed out in each chapter for each specific case.

A. Cell culture

Four to five different cell lines have been used to test the overall biological studies in each situation. Human dermal **fibroblasts** were obtained from Lonza (Belgium) and THP1 human **monocytes** from the American Type Culture Collection (ATCC, USA). Mouse mesenchymal stem cells (**mMSCs**); and human glioblastoma cells (tumor cells **U251MG**) were kindly gifted by Dr. Pilar Martín-Duque. The *in vitro* differentiation of monocytes to **macrophages** was performed by the addition of 1µM phorbol 12-myristate 13-acetate (PMA) to the cell culture medium for 72 h obtaining the characteristic adherent morphology of macrophages.

We chose these cell types in order to test our materials in different groups of cells: *stem cells* (**mMSCs**), *adult somatic cells* (**human dermal fibroblasts**), *tumor cells* (**U251MG**) and the two *phagocytic cell lines*, **monocytes** (circulating cells in blood, marrow and spleen) and **macrophages** (resident cells in tissues). The last ones are the mediators of the immune response and therefore, the first cells that interact with materials when administered in vivo. In addition, stem and somatic cells are the most prevalent ones in normal tissues, whereas tumor cells were assayed to test the effect of our materials on a pathological situation

Fibroblasts and U251MG cells were cultured in DMEM high glucose (Biowest, France) containing 2 mM L-glutamine and supplemented with 10% v/v fetal bovine serum

(FBS; Gibco, UK) and 1% penicillin-streptomycin-amphotericin B (Biowest, France). mMSCs were grown in DMEM-F12 (Biowest, France) containing 1% glutamine (Biowest, France), 10% FBS and 1% penicillin-streptomycin-amphotericin B. Monocytes were cultured in RPMI 1640 (Biowest, France) containing 2 mM L-glutamine and supplemented with 10% v/v FBS, 1% HEPES (Lonza, Belgium), 1% nonessential amino acids, 0.1% 2-mercaptoethanol 50 mM (Gibco, UK), 1% sodium pyruvate 100 mM and 1% penicillin-streptomycin-amphotericin B.

All cell lines were grown in a humidified atmosphere at 37 ºC and 5% CO_2 except for mMSCs which were cultured in hypoxia (3% O_2)

B. Cell viability related to Cell metabolism

The effects in cell metabolism were determined by the blue cell viability (Alamar blue) assay (Abnova).Cells were seeded in a 96-well plate and incubated with the materials at different concentrations for 24 to 48 h. The reagent was then added (10%) and after incubation (4 h, 37 ºC, 5% CO_2), the fluorescence was recorded (535/590 nm ex/em) in a Synergy HT microplate reader (Biotek, USA). Control samples without cells were also run in all cases to evaluate a potential interference in the assay. Cell viability was determined by the interpolation of the emission data obtained from the treated samples and the control samples (untreated cells were assigned with 100% viability).

C. Evaluation of Cell Apoptosis

The effects on cell membrane after treatment for 24 h were determined by the study of cell apoptosis by flow cytometry at the subcytotoxic concentrations obtained from the cell metabolism assay described above. After treatment with the corresponding material's concentration, cells were harvested in PBS and double stained with annexin V-FITC and propidium iodide. In brief, cell suspensions were stained with annexin V-FITC and treated with a solution composed of annexin V-FITC, propidium iodide and annexin V binding buffer to be finnaly incubated with the binding buffer for 15 min before the analysis f the samples in the FACSARIA BD equipment and FACSDIVA BD software (Cell separation and cytometry unit, CIBA, IIS Aragon, Spain). Control samples (not treated samples) were also evaluated to determine the influence of the materials on apoptosis.

D. Study of Cell cycle

The distribution of cell cycle phases was determined by flow cytometry in order to elucidate the effects of the materials in cell cycle and DNA. As described above, cells were exposed for 24 to 48 h to the materials at subcytotoxic concentrations. Then, cells were collected in PBS and fixd in 70% ice-cold ethanol. After 24 h of incubation at 4 ºC, DNA staining was performed by adding RNase A (100 µg/mL) and propidium iodide (50 µg/mL) in PBS. Samples were analyzed in a FACSARIA BD equipment with the MODIFIT 3.0 Verify software. Control samples (not treated cells) were also analyzed to evaluate the normal distribution of cell cycle in all the cell lines assayed.

E. Endotoxin

Endotoxins or lipopolysaccharides (LPS) are bioactive heat-stable molecules present in the outer wall of Gram-negative bacteria. They can induce inflammation and immune response of the host organism or even sepsis[357][358]. During the production and handling of micro- and nanomaterials, these materials can be contaminated with endotoxin with subsequent health risks in a potential future application.[358]. Due to this potential concern, the quantification of the endotoxin content in materials used for in vivo studies was performed prior to their use.

The endpoint chromogenic LAL assay (QCL-1000) (Lonza, Belgium) was developed to quantify the endotoxin content in the different materials (1 mg/mL) according to the manufacturer's indications. In brief, 50 µL of the diluted samples (1:100 to 1:750 dilution in endotoxin free water) was dispensed in duplicate in each well of a microplate. The LAL reagent was then added and subsequently the plate was shaken and incubated (37 ºC, 10 min). Following the incubation, the pre-warmed chromogenic substrate was added and the plate was again incubated (37 ºC, 6 min). Finally the reaction was stopped (10 % SDS solution) and the absorbance was read at 405 nm in a Synergy HT microplate reader (Biotek, USA). The determination of the endotoxin levels in the samples was performed as indicated by the manufacturer.

II. Characterization techniques

This section summarize all characterization techniques used in this work giving a brief theoretical description and measurement conditions.

A. Transmission Electron Microscopy (TEM)

Transmission electron microscopy (TEM) has been used to get high resolution images of the majority of the NPs described in this work. This microscopy technique generates images from transmitted electrons through a specimen. An electron beam is directed to the sample and electrons transmitted are focused in a sensor or photographic film generating a high resolution image of objects thousands of times smaller than objects seen with an optical microscope.

Moreover, elemental analysis for chemical characterization can be done by energy-dispersive X-ray spectroscopy (EDS), where high-energy electrons interacts with the specimen exciting an electron in an inner shell of the atom structure creating electron holes. Then an electron present in the higher energy shell fills the hole emitting the difference energy in form of an X-Ray. Each atom has an specific energy loss when it happens and it allows to differentiate the component of a sample.

In this work, the FEI Tecnai T20, TEM microscope was used operating at 200 kV belonging to the Advanced Microscopy Laboratory (LMA) at University of Zaragoza and Institute of Nanoscience of Aragon (INA). Samples were placed on copper or nickel –carbon grids and dried before taking images.

B. Scanning Transmission Electron Microscopy (STEM)

Scanning transmission electron microscope (STEM) is a particular type of TEM microscope. In this variation, electrons transmitted through the sample are confined to a finer spot before crossing the specimen by using condenser lenses, which allows to scan the spot across the sample. This rastering over the samples makes STEM suitable for analytical characterization.

A singular mode of STEM microscopy is the High-Angle Annular Dark-Field (HAADF). Here, fore-scattered electrons are collected in a high-angle detector not directly aligned to the transmitted electron beam resulting in a dark high-resolution image of the specimen. Fore-scattered electrons are directly related to the atomic number of the sample making possible the analysis of the components in the sample. Moreover, as described in the previous section, EDS analysis can be also carried out in this mode of TEM microscopes.

To obtain high resolution images in this thesis, the STEM; FEI Tecnai F30 microscope has been used operating at 300 kV belonging to the Advanced Microscopy Laboratory (LMA) at University of Zaragoza and Institute of Nanoscience of Aragon (INA). Samples were placed on nickel-carbon grids and dried before taking images.

C. Scanning Electron Microscopy (SEM)

Scanning electron microscopy (SEM) is another type of electron microscope that scans the surface of the samples with an electron beam. These electrons interact with the components of the sample and the scattered ones are collected in a detector giving information about the topology and composition of the specimen studied. This microscope as TEM or STEM must work at low vacuum but with low energy electron beam. High-resolution (until 1 nm) images can be taken with SEM microscopes and elemental analysis of the surface components can be studied by Energy Dispersive X-ray Spectroscopy (EDS). Backscattered electrons are collected in the secondary electrons detector displaying compositional contrast that results from different atomic number elements identified by EDS.

In this work, polymeric micro- and nanoparticles have been studied by SEM in the Inspect F50 (FEI Co., LMA-INA, Spain) equipment operating at an accelerating voltage of 10-15 keV. This systems belongs to the Advanced Microscopy Laboratory (LMA) at University of Zaragoza and Institute of Nanoscience of Aragon (INA). Samples were stained with phosphotungstic acid, thoroughly washed and dried before taking images.

D. Cryogenic Dual Beam

Cryogenic dual beam permits to generate controlled fractures in situ on quenched soft materials, avoiding the mechanical damage associated with room temperature fractures. Cross-sectional surfaces can be created with focused ion beam (FIB) in order to study the internal distribution of the components in the sample together with images generated from STEM modulus, secondary electrons and back scattered electrons. In addition, the equipment includes a EDS software that allows elementary chemical analysis of the component of the sample.

In this work, the Cryogenic Dual Beam Nova 200 (Electron Voltage 200V-30kV; Ion voltage 2kV-30kV) was used. It belongs to the Advanced Microscopy Laboratory (LMA) at

University of Zaragoza and Institute of Nanoscience of Aragon (INA). Lyophilized microparticles with hollow gold nanoparticles (HGNPs) were used as sample.

E. X-Ray Diffraction (XRD)

X-Ray diffraction (XRD) is an analytical technique used for phase identification of a crystalline material. In order to obtain such information, X-rays are generated in a cathode ray tube, concentrated and bombard toward the target material. This may produce the displacement of electrons from inner shells of the atoms in different directions producing a diffracted X-ray beam which direction and intensity depends on the orientation of the crystal lattice with radiation. They are collected in a X-ray detector resulting in a diffraction pattern characteristic of an specific crystalline structure and can be compared to standards.

This diffraction effect occurs when conditions satisfy Bragg's law ($n\lambda = 2d \sin\theta$). This law relates the wavelength of electromagnetic radiation to the diffraction angle and lattice spacing in a crystalline sample. By scanning the sample in all 2θ angles all possible diffraction lattices should be attained.

Copper sulfide nanoparticles finely ground and homogenized were measured in a Philips X-Pert diffractometer equipped with a monochromatized Cu Kα radiation source (40 kV, 20 mA) over the range 0.6−10.0 with a step of 0.02 an analysis time of 5 s.

F. UV-visible Spectroscopy (UV-vis)

Ultraviolet-visible spectroscopy (UV-vis) registers the absorption or reflectance of light through a sample in the UV-vis spectra. Briefly, the equipment measures the intensity (I)of light passing through a sample and compares it to the original source (I_0). This ratio I/I_0 is called transmittance and is directly related with the absorbance through this equation

$$A = -\log(\%T/100\%)$$

This light intensity transmitted through the sample is proportional to the concentration of the component absorbing the light and also characteristic of certain plasmonic nanoparticles to present their plasmonic effect.

A double-beam UV-vis spectrophotometer (PerkinElmer Lambda 35) was used to characterize the dyes and plasmonic nanoparticles in this work.

G. X-Ray Photoelectron Spectroscopy (XPS)

X-ray photoelectron spectroscopy (XPS) is a low-resolution, quantitative technique to measure the elemental composition on the surface of a sample giving information about their empirical formula, chemical and electronic state. X-rays are used to irradiate the material to study at ultra high vacuum and photo-emitted electrons from the top surface of the sample are collected and analyzed. Electrons' quantity and kinetic energy are measured and the difference between the irradiated energy and their kinetic energy gives the ligand energy characteristic for each atom and electronic state.

In this work, the XPS, Axis Ultra DLD, Kratos Tech equipment was used

H. Dynamic Light Scattering (DLS) & Z-Potential

Dynamic light scattering (DLS) is a technique capable to give determine the size distribution of small particles in suspension by measuring the scattered light of a laser beam when it passes through the sample. This scattering is related to the hydrodynamic diameter of the particles and fluctuates due to the Brownian motion of the particles in solution.

On the other hand, Z-potential refers to the electrokinetic potential of particles in a colloidal suspension. The electric potential in the interfacial double layer at the surface of the particle, the potential difference between this layer and the dispersion medium. It is a key indicator of the stability of colloidal dispersions indicating the degree of electrostatic repulsion between adjacent charged particles, the higher, the better. The motion of charged particles is probed with phase analysis light scattering (PALS). Electrophoretic mobility is directly related to the phase shift of the scattered light when particles are in an electric field and is converted to Zeta-potential using a model (Smoluchovski for aqueous solutions).

In this work, the 90Plus Particle Size Analyzer by Brookhaven Instruments Corp., Holtsville, NY, USA was used for DLS measurements. Z-Potential measurements were carried out at pH = 6 (using a KCl buffer to provide with constant ionic strength) in a Zeta Plus, Brookhaven Instruments Corporation, NY, USA.

I. Heating efficiency

was measured with the aid of a 808 nm wavelength laser diode (6 × 8 mm2 spot size; Optilas model MDL-III-808-2W, Changchun New Industries Optoelectronics Technology

Co., Ltd., Changchun, China) and a power controller (Model PD300-3W, Ophir Laser Measurement Group, Logan, UT, USA) with an irradiance of 200 mW/cm^2. Temperature gradients were monitored using a type K thermocouple (RS Amidata, Madrid, Spain) immersed in the dispersion parallel to the path of the laser light but without being intercepted with it.

J. Fourier Transformed Infrared Spectroscopy (FTIR)

Fourier-transformed Infrared spectroscopy (FTIR) is an analytical technique of a material's composition. Samples in solid, liquid or gas state are irradiated with infrared light beam at different frequencies and the absorbed the absorbed light from that beam is measured. Then it does again the same but at different frequencies and so on The absorbed bands are obtained by computer processing with the Fourier-transformed algorithm and are representative to certain bonds. Attenuated total reflectance (ATR) technique is applied to measure non-treated samples. ATR is a crystal that reflects at least once off the internal surface in contact with the sample forming an evanescent wave which extends into the sample.

In this work, a Vertex 70, Bruker with an ATR Golden Gate accessory.

K. Mass spectrometry

Mass spectrometry (MS) is an analytical technique that provides information about chemical structures of molecules and chemical compounds in general. In order obtain this information, the sample, in gas, liquid or solid state, is ionized breaking into charged fragments separated by electric or magnetic fields depending on their mass-to-charge ratio. Results are displayed as a spectrum of the relative abundance of detected ions as a function of their mass-to-charge ratio.

This technique was used in Chapter 4 in order to characterize the IR820-modified probes. Mass spectrometry for the dyes was carried out using the corresponding methanol solutions in a Microtof-Q equipment.

L. Nuclear Magnetic Resonance spectroscopy (NMR)

Nuclear magnetic resonance is a physical phenomenon in which an oscillating magnetic field perturbs the nuclei of atoms and responds by producing an electromagnetic

signal with a frequency characteristic of the magnetic field at the nucleus. This process occurs when oscillation frequency matches to intrinsic frequency of the nuclei, which depends on the chemical environment. The electronic structure of a molecule and its functional groups affects the magnetic field of the molecule and are unique, well-resolved and highly predictable for small molecules or functional groups. The signal is detected with sensitive radio receivers.

NMR spectroscopy is commonly used to determine the structure of organic molecules in a solution. The most common types of NMR are proton (1H) and carbon (13C) NMR spectroscopy. A Bruker AV-400 spectrometer operating at 400 MHz using $CDCl_3$ as solvent was selected for thermoresponsive polymer characterization in this work.

M. Optical Transmittance Measurements (Cloud Point)

One of the possibilities to test the lower critical solution temperature (LCST) of thermoresponsive polymers is by turbidimetry. These polymers tuned their hydrophilic becoming hydrophobic and thus not soluble in water, when temperature increases over their LCST. Then, when a water solution of this materials is heated over this temperature, the intensity of transmitted light through the sample decreases due to the scattering effect of the non-soluble material precipitated in it. The process of continuous measuring of this transmitted light is called turbidimetry.

In this work, optical transmittance measurements were carried out at 670 nm varying the temperature using a Varian Cary® 50 UV–Visible spectrometer (Agilent Technologies, USA) equipped with a fiber optic dip probe. The temperature at which 50% of the transmittance was reached was selected as the LCST of the resulting polymer.

N. Gel Permeation Chromatography (GPC)

This technique is mainly used to characterize polymers depending on their hydrodynamic volume. The sample diluted in an appropriate solvent is injected onto a column where porous beads are packed. The smaller analytes are able to penetrate more in the gaps of the beads and thus their retention time is longer than bigger molecules that interact less and exit the column at shorter times. GPC determine the molecular weight of polymer samples and their distribution

In this work, we used a Waters Alliance 2695 HPLC with an evaporative light scattering detector (Waters 2420) and PLgel 5 µm MIXED-C Aglilent columns (7.5 mm x 300 mm), using THF (HPLC grade) as eluent (flow 1 mL/min). Calibration was made with poly(methyl methacrylate) standards. Samples were analyzed at 1 mg/mL after filtration using a 0.2 µm PTFE filter

O. Thermogravimetric Analysis (TGA)

This characterization technique provides qualitative and quantitative information about physical and chemical phenomena such as thermal decomposition, absorption, or desorption processes. In this system, the mass of a sample is measured over time in a microbalance as the temperature changes in an specific atmosphere directly related to humidity loss, removal of structural agents or materials functionalization.

In this work, a Mettler Toledo TGA/STDA 851e) equipment was used to evaluate the polymeric content in the hybrid nanoparticles of Chapter 3. Samples were analyzed in an N_2 atmosphere (gas flow 50 mL/min) between 30 and 800 ºC with a heating rate of 20 ºC/min

P. Ultra Performance Liquid Chromatography (UPLC)

Ultra-performance liquid chromatography (UPLC) is an advanced separation technique based on High-performance liquid chromatography (HPLC) basis. HPLC is an analytical separation technique that relies on passing pressurized liquid solvent containing the analytes through a solid adsorbent column. Each component in the sample interacts different with the solid and pores depending on their properties eluting at different times in the outlet flow stream. This separated component of the sample are further detected by IR or UV light and compared to certain standards with comparable eluting times at the same operating conditions.

Significant advances in instrumentation and column technology have led to dramatic increases in resolution, speed and sensitivity and gave birth to UPLC® technology by Waters company.

In this work the Ultra Performance Liquid Chromatography system (UPLC; ACQUITY UPLC H-Class system with a PDA detector, Waters) has been used for bupivacaine detection in Chapter 3 using dexamethasone as internal standard.

Q. Gas Chromatography-Mass Spectrometry (GC-MS)

Gas chromatography (GC) coupled to mass spectrometry (MS) is an analytical technique that combines the separation method of GC with components detection via MS, described before. GC uses inert gas flow as carrier and separates the components of a sample based on their volatility and interaction with the stationary. Normally, this is a microscopic layer of liquid on a solid support inside a glass or metal cylinder called column. Compounds eligible to be analyze by GC must be sufficiently volatile and thermally stable due to the analysis conditions because the column of GC is placed in an oven, which temperature can be controlled and changed over time, and temperatures can easily reach 400 ºC.

In GC analysis, a certain volume of the sample is injected in the column and the carrier gas moves forward the molecules through the column. The different interactions with the stationary phase determine the residence time of each molecule inside the column and the outlet stream is connected to a detector capable to identify qualitatively the components depending on their emerging time.

It is very common the coupling of GC with MS, which ionizes the outlet stream of the GC column and separates the fragments of molecules by mass-to-charge ratio enabling the qualitative and quantitative analysis of the analytes.

In this work, a Gas Chromatography-Mass Spectrometry (GC-MS-QP2010 SE, Shimadzu) has been used for Bupivacaine analysis in chapter 3 using limonene as internal standard.

APPENDIX II

MD INPUT DATA

Appendix II

MD INPUT DATA

Appendix II: MD input data

Table VII.1: Modified Van der Waals Non-bonded interactions parameters

C-O_w Van der Waals Non-bonded interactions parameters				
	Standard parameters		Modified parameters	
Atom type	ε_{ij}	$R_{min;ij}/2$	ε_{ij}	$R_{min;ij}/2$
CG331	-0.1089	3.3202	-0.1252	3.8182
CG331b	-0.1089	3.3202	-0.1252	3.8182
CG321	-0.0923	3.2854	-0.1061	3.7782
CG311	0.0698	3.2767	-0.0803	3.7682

Table VII.2: Mulliken charges of Bupivacaine hydrochloride molecule (+1) obtained in Gaussian

Bupivacaine Mulliken charges obtained in Gaussian (Total charge: +1)

Atom	Charge	Atom	Charge	Atom	Charge	Atom	Charge
C1	-0.3776	**N2**	-0.5521	**H6**	0.0028	**H19**	0.3508
C2	0.1849	**C11**	0.0198	**H7**	0.0692	**H20**	0.1915
C3	-0.0548	**C12**	0.2258	**H8**	0.0558	**H21**	0.1418
C4	-0.3592	**C13**	-0.3397	**H9**	0.1593	**H22**	0.1777
N1	0.1484	**C14**	-0.0291	**H10**	0.1225	**H23**	0.1301
C5	-0.1003	**C15**	-0.2914	**H11**	0.1046	**H24**	0.1080
C6	-0.0951	**C16**	0.1914	**H12**	0.1232	**H25**	0.0870
C7	-0.0999	**C17**	-0.3213	**H13**	0.0653	**H26**	0.0887
C8	0.0793	**C18**	-0.3132	**H14**	0.0948	**H27**	0.1161
C9	-0.1990	**H2**	0.0989	**H15**	0.0754	**H28**	0.0905
H1	0.1065	**H3**	0.1014	**H16**	0.0568	**H29**	0.2301
C10	0.6498	**H4**	0.1164	**H17**	0.0446		
O1	-0.5028	**H5**	0.0060	**H18**	0.0204		

NAMD input file: [*NPT.conf* **]**

- ***Polymer systems***

```
#############################################################
## ADJUSTABLE PARAMETERS                                   ##
#############################################################

structure          NAMD_input.psf
coordinates        NAMD_input.pdb

outputName         run

set temperature    295.00

# Continuing a job from the restart files

#set inputname      run
#binCoordinates     $inputname.restart.coor
#binVelocities      $inputname.restart.vel  ;# remove the
"temperature" entry if you use this!
#extendedSystem    $inputname.restart.xsc



#############################################################
## SIMULATION PARAMETERS                                   ##
#############################################################

# Input
paraTypeCharmm      on
parameters          pni_wat_extended_1-15.prm


# NOTE: Do not set the initial velocity temperature if you
# have also specified a .vel restart file!
temperature         $temperature

# Periodic Boundary Conditions
# NOTE: Do not set the periodic cell basis if you have also
# specified an .xsc restart file!

cellBasisVector1     90.    0.   0.
cellBasisVector2     0.   90.   0.
cellBasisVector3     0.    0.   90.
cellOrigin          0.0   0.0   0.0


wrapAll             on
```

```
# Force-Field Parameters
exclude             scaled1-4
1-4scaling          1.0
cutoff              14.
switching           on
switchdist          13.
pairlistdist        16.


# Integrator Parameters
timestep            1.0
nonbondedFreq       1
fullElectFrequency  2
stepspercycle       10

margin 5

#PME (for full-system periodic electrostatics)

PME                 yes
PMEGridSizeX       128
PMEGridSizeY       128
PMEGridSizeZ       128


# Constant Temperature Control
langevin            on    ;# do langevin dynamics
langevinDamping     1     ;# damping coefficient (gamma) of 5/ps
langevinTemp        $temperature
langevinHydrogen    off

# Constant Pressure Control (variable volume)
useGroupPressure      no ;# needed for 2fs steps
useFlexibleCell       no  ;# no for oct box, yes for membrane
useConstantArea       no  ;# no for oct box, yes for membrane

langevinPiston        yes
langevinPistonTarget  1.01325 ;#  in bar -> 1 atm
langevinPistonPeriod  100.
langevinPistonDecay   50.
langevinPistonTemp    $temperature


restartfreq        10000     ;# 1000steps = every 2ps
dcdfreq            1000
xstFreq            10000
outputEnergies     10000
outputPressure     10000


minimize            5000
run  100000000
```

- ***Polymer-bupivacaine systems***

```
#############################################################
## ADJUSTABLE PARAMETERS                                   ##
#############################################################

structure           NAMD_input.psf
coordinates         NAMD_input.pdb

outputName         run

set temperature    315.00

# Continuing a job from the restart files

#set inputname      run
#binCoordinates     $inputname.restart.coor
#binVelocities      $inputname.restart.vel  ;# remove the
"temperature" entry if you use this!
#extendedSystem    $inputname.restart.xsc



#############################################################
## SIMULATION PARAMETERS                                   ##
#############################################################

# Input
paraTypeCharmm      on
parameters          pni_wat_extended_1-15_bup+_new.prm


# NOTE: Do not set the initial velocity temperature if you
# have also specified a .vel restart file!
temperature         $temperature


# Periodic Boundary Conditions
# NOTE: Do not set the periodic cell basis if you have also
# specified an .xsc restart file!

cellBasisVector1    100.    0.   0.
cellBasisVector2     0.   100.   0.
cellBasisVector3     0.    0.  100.
cellOrigin          0.0   0.0   0.0


wrapAll             on


# Force-Field Parameters
```

```
exclude             scaled1-4
1-4scaling          1.0
cutoff              14.
switching           on
switchdist          13.
pairlistdist        16.


# Integrator Parameters
timestep            1.0
nonbondedFreq       1
fullElectFrequency  2
stepspercycle       10

margin 5


#PME (for full-system periodic electrostatics)

PME                 yes
PMEGridSizeX       128
PMEGridSizeY       128
PMEGridSizeZ       128


# Constant Temperature Control
langevin            on    ;# do langevin dynamics
langevinDamping     1     ;# damping coefficient (gamma) of 5/ps
langevinTemp        $temperature
langevinHydrogen    off

# Constant Pressure Control (variable volume)
useGroupPressure      no ;# needed for 2fs steps
useFlexibleCell       no  ;# no for oct box, yes for membrane
useConstantArea       no  ;# no for oct box, yes for membrane

langevinPiston        yes
langevinPistonTarget  1.01325 ;#  in bar -> 1 atm
langevinPistonPeriod  100.
langevinPistonDecay   50.
langevinPistonTemp    $temperature


restartfreq        10000     ;# 1000steps = every 2ps
dcdfreq            1000
xstFreq            10000
outputEnergies     10000
outputPressure     10000


minimize            5000
run  100000000
```

Parameters file: [*pni_wat_extended_1-15_bup+_new.prm* **]**

```
BONDS
!
!V(bond) = Kb(b - b0)**2
!
!Kb: kcal/mole/A**2
!b0: A
!
!atom type Kb          b0

!bonds for NMA
CG331   NG2S1    320.00      1.4300 ! PROT NMA Gas & Liquid Phase IR
Spectra (LK)
CG2O1   CG331    250.00     1.4900 ! PROT Ala Dipeptide (5/91)
CG331   HGA3      322.00       1.1110 ! PROT alkane update, adm jr.,
3/2/92
CG331b HGA3      322.00       1.1110 ! PROT alkane update, adm jr.,
3/2/92
CG2O1   OG2D1    620.00     1.2300 ! PROT Peptide geometry, condensed
phase (LK)
NG2S1   HGP1     440.00     0.9970 ! PROT Alanine Dipeptide ab initio
calc's (LK)
CG2O1   NG2S1    370.00     1.3450 ! PROT Alanine Dipeptide ab initio
calc's (LK)

!bonds for PNI
CG321   HGA2     322.00      1.1110 ! **PROT alkane update, adm jr.,
3/2/92
HGA3    CG321    322.00       1.1110 ! PROT alkane update, adm jr.,
3/2/92
CG321   CG321    222.50       1.5380 ! PROT alkane update, adm jr.,
3/2/92
CG321   CG2O1    200.00     1.5220 ! PROT adm jr. 5/02/91, acetic acid
pure solvent
NG2S1   CG311    320.00      1.4300 ! PROT NMA Gas & Liquid Phase IR
Spectra (LK)
HGA3    CG311    322.00       1.1110 ! PROT alkane update, adm jr.,
3/2/92
HGA2    CG311    322.00       1.1110 ! PROT alkane update, adm jr.,
3/2/92
HGA1    CG311    322.00       1.1110 ! PROT alkane update, adm jr.,
3/2/92
CG331   CG311    222.50       1.5380 ! PROT alkane update, adm jr.,
3/2/92
CG331   CG321    222.50       1.5380 ! PROT alkane update, adm jr.,
3/2/92
CG331b CG311    222.50       1.5380 ! PROT alkane update, adm jr.,
3/2/92
CG331b CG321    222.50       1.5380 ! PROT alkane update, adm jr.,
3/2/92
```

```
CG321   HGA1     322.00      1.1110 ! PROT alkane update, adm jr.,
3/2/92
CG331   HGA2     322.00      1.1110 ! PROT alkane update, adm jr.,
3/2/92
CG331b HGA2     322.00      1.1110 ! PROT alkane update, adm jr.,
3/2/92

!EXTRA PNIPMAM

CG311  CG321   222.50     1.5380 ! Same than CG321 CG321
CG311  CG2O1   200.00     1.5220 ! Same than CG321 CG2O1


!Bonds for Bupivacaine

BC2R61  BC2R61    305.00     1.3750 ! PROT benzene, JES 8/25/89
BC2R61  BNG2S1    305.00     1.4140 ! RETINOL PACP
BC2R61  BCG331    230.00     1.4900 ! PROT toluene, adm jr. 3/7/92
BC2R61  BHGR61    340.00     1.0800 ! PROT phe,tyr JES 8/25/89
BCG331  BHGA3     322.00     1.1110 ! PROT alkane update, adm jr.,
3/2/92
BNG2S1   BHGP1      440.00      0.9970 ! PROT Alanine Dipeptide ab
initio calc's (LK)
BNG2S1   BCG2O1     370.00      1.3450 ! PROT Alanine Dipeptide ab
initio calc's (LK)
BCG2O1  BOG2D1   620.00    1.2300 ! PROT Peptide geometry, condensed
phase (LK)
BCG2O1  BCG314    250.00     1.4900 ! PROT Ala Dipeptide (5/91)
BCG314  BHGA1     309.00     1.1110 ! PROT alkane update, adm jr.,
3/2/92
BCG314  BCG321    222.50     1.5380 ! PROT alkane update, adm jr.,
3/2/92
BCG314   BNG3P1     200.00      1.4800 ! CG324/CG334 NG3P1 FLAVOP
PIP1,2,3
BCG321  BHGA2     309.00     1.1110 ! PROT alkane update, adm jr.,
3/2/92
BCG324  BNG3P1    200.00     1.4800 ! FLAVOP PIP1,2,3
BCG321  BCG321    222.50     1.5300 ! PROT alkane update, adm jr.,
3/2/92
BCG321  BCG324    222.50     1.5300 ! FLAVOP PIP1,2,3
BCG324  BHGA2     284.50     1.1000 ! FLAVOP PIP1,2,3
BCG321  BCG331    222.50     1.5280 ! PROT alkane update, adm jr.,
3/2/92
BNG3P1   BHGP2      403.00      1.0400 ! PROT new stretch and bend;
methylammonium (KK 03/10/92)


!TIP3P
OW     HW      450.0      0.9572 ! TIP3P water

ANGLES
```

```
!
!V(angle) = Ktheta(Theta - Theta0)**2
!
!V(Urey-Bradley) = Kub(S - S0)**2
!
!Ktheta: kcal/mole/rad**2
!Theta0: degrees
!Kub: kcal/mole/A**2 (Urey-Bradley)
!S0: A
!
!atom types     Ktheta    Theta0   Kub     S0


!angles for NMA
CG2O1   CG331   HGA3      33.00     109.50    30.00    2.16300 ! PROT
alanine dipeptide, 5/09/91
HGA3    CG331   HGA3      35.50     108.40     5.40    1.80200 ! PROT
alkane update, adm jr., 3/2/92
CG331   CG2O1   NG2S1    80.00    116.50 ! PROT NMA Vib Modes (LK)
CG331   CG2O1   OG2D1    80.00    121.00 ! PROT Alanine Dipeptide ab
initio calc's (LK)

CG2O1   CG331b   HGA3      33.00     109.50    30.00    2.16300 ! PROT
alanine dipeptide, 5/09/91
HGA3    CG331b   HGA3      35.50     108.40     5.40    1.80200 ! PROT
alkane update, adm jr., 3/2/92
CG331b   CG2O1   NG2S1    80.00    116.50 ! PROT NMA Vib Modes (LK)
CG331b   CG2O1   OG2D1    80.00    121.00 ! PROT Alanine Dipeptide ab
initio calc's (LK)

NG2S1   CG2O1   OG2D1    80.00    122.50 ! PROT NMA Vib Modes (LK)
CG2O1   NG2S1   HGP1     34.00    123.00 ! PROT NMA Vib Modes (LK)
CG331   NG2S1   HGP1     35.00    117.00 ! PROT NMA Vibrational Modes
(LK)
NG2S1   CG331   HGA3     51.50    109.50 ! PROT NMA crystal (JCS)
CG2O1   NG2S1   CG331    50.00    120.00 ! PROT NMA Vib Modes (LK)

CG331b   NG2S1   HGP1     35.00    117.00 ! PROT NMA Vibrational Modes
(LK)
NG2S1   CG331b   HGA3     51.50    109.50 ! PROT NMA crystal (JCS)
CG2O1   NG2S1   CG331b    50.00    120.00 ! PROT NMA Vib Modes (LK)

! PNI
HGA1    CG321   HGA1      33.00     109.50    30.00    2.16300 ! PROT
alanine dipeptide, 5/09/91
HGA1    CG321   HGA3      33.00     109.50    30.00    2.16300 ! PROT
alanine dipeptide, 5/09/91
HGA2    CG321   HGA2      33.00     109.50    30.00    2.16300 ! PROT
alanine dipeptide, 5/09/91
HGA2    CG321   HGA3      33.00     109.50    30.00    2.16300 ! PROT
alanine dipeptide, 5/09/91
```

```
HGA3    CG321   HGA3      33.00     109.50    30.00    2.16300 ! PROT
alanine dipeptide, 5/09/91
HGA2    CG331   HGA3      33.00     109.50    30.00    2.16300 ! PROT
alanine dipeptide, 5/09/91
HGA2    CG331b HGA3       33.00     109.50    30.00    2.16300 ! PROT
alanine dipeptide, 5/09/91
HGA1    CG321   CG321     33.00     109.50    30.00    2.16300 ! PROT
alanine dipeptide, 5/09/91
HGA2    CG321   CG321     33.00     109.50    30.00    2.16300 ! PROT
alanine dipeptide, 5/09/91
CG321   CG321   HGA3      33.00     109.50    30.00    2.16300 ! PROT
alanine dipeptide, 5/09/91

HGA3    CG321   CG2O1     33.00     109.50    30.00    2.16300 ! PROT
alanine dipeptide, 5/09/91
HGA1    CG321   CG2O1     33.00     109.50    30.00    2.16300 ! PROT
alanine dipeptide, 5/09/91
CG2O1   CG321   HGA2      33.00    109.50   30.00   2.16300 ! ''  '''
' ''
CG311   CG331   HGA2      33.00    109.50   30.00   2.16300 ! ''  '''
' ''
CG331   CG321   HGA3      33.00    109.50   30.00   2.16300 ! ''  '''
' ''
CG311   CG331b HGA2       33.00    109.50   30.00   2.16300 ! ''  '''
' ''
CG331b CG321   HGA3       33.00    109.50   30.00   2.16300 ! ''  '''
' ''
CG321   CG321   CG2O1      53.35     114.00     8.00    2.56100 ! PROT
alkane update, adm jr., 3/2/92
CG331   CG321   CG2O1      53.35     114.00     8.00    2.56100 ! PROT
alkane update, adm jr., 3/2/92
CG331b CG321   CG2O1      53.35     114.00     8.00    2.56100 ! PROT
alkane update, adm jr., 3/2/92

CG321   CG2O1   OG2D1     80.00     121.00 ! PROT Alanine Dipeptide ab
initio calc's (LK)
CG321   CG2O1   NG2S1     80.00    116.50 ! PROT NMA Vib Modes (LK)
CG2O1   NG2S1   CG311      42.00     119.50 ! DMF, Dimethylformamide,
xxwy

HGP1    NG2S1   CG311     34.00    123.00 ! PROT NMA Vib Modes (LK)
NG2S1   CG311   HGA1      51.50    109.50 ! PROT NMA crystal (JCS)
NG2S1   CG311   HGA3      51.50    109.50 ! PROT NMA crystal (JCS)
NG2S1   CG311   CG331     70.00     113.50 ! PROT Alanine Dipeptide ab
initio calc's (LK)

HGA1    CG311   CG331      34.60     110.10    22.53    2.17900 ! PROT
alkane update, adm jr., 3/2/92
HGA3    CG331   CG321      34.60     110.10    22.53    2.17900 ! PROT
alkane update, adm jr., 3/2/92
HGA2    CG331   CG321      34.60     110.10    22.53    2.17900 ! PROT
alkane update, adm jr., 3/2/92
```

```
CG331  CG311  CG331    53.35    111.00   8.00   2.56100 ! PROT alkane
update, adm jr., 3/2/92
CG321   CG321   CG331     53.35     111.00    8.00    2.56100 ! **PROT
alkane update, adm jr., 3/2/92

CG311   CG331   HGA3      34.60     110.10    22.53    2.17900 ! PROT
alkane update, adm jr., 3/2/92
CG331   CG311   HGA3      34.60     110.10    22.53    2.17900 ! PROT
alkane update, adm jr., 3/2/92
CG321   CG321   CG321     53.35     111.00    8.00    2.56100 ! **PROT
alkane update, adm jr., 3/2/92

NG2S1  CG311  CG331b    70.00    113.50 ! PROT Alanine Dipeptide ab
initio calc's (LK)

HGA1    CG311   CG331b     34.60     110.10    22.53    2.17900 ! PROT
alkane update, adm jr., 3/2/92
HGA3    CG331b   CG321     34.60     110.10    22.53    2.17900 ! PROT
alkane update, adm jr., 3/2/92
HGA2    CG331b   CG321     34.60     110.10    22.53    2.17900 ! PROT
alkane update, adm jr., 3/2/92

CG331b   CG311   CG331b     53.35     111.00    8.00    2.56100 ! PROT
alkane update, adm jr., 3/2/92
CG331   CG311   CG331b     53.35     111.00    8.00    2.56100 ! PROT
alkane update, adm jr., 3/2/92
CG321   CG321   CG331b     53.35     111.00    8.00    2.56100 ! **PROT
alkane update, adm jr., 3/2/92

CG311   CG331b   HGA3      34.60     110.10    22.53    2.17900 ! PROT
alkane update, adm jr., 3/2/92
CG331b   CG311   HGA3      34.60     110.10    22.53    2.17900 ! PROT
alkane update, adm jr., 3/2/92


!EXTRA PNIPMAM

HGA2   CG321  CG311    33.00    109.50   30.00   2.16300 ! Same than
HGA2 CG321 CG321
CG311  CG321  CG311    53.35    111.00   8.00   2.56100 ! Same than
CG321 CG321 CG321
CG311  CG2O1  NG2S1    80.00    116.50 ! Same than CG321 CG2O1 NG2S1
CG311  CG2O1  OG2D1    80.00    121.00 ! Same than CG321 CG2O1 OG2D1
CG331  CG311  CG2O1    53.35    114.00    8.00   2.56100 ! Same than
CG331 CG321 CG2O1
CG321  CG311  CG2O1    53.35    114.00    8.00   2.56100 ! Same than
CG321 CG321 CG2O1
CG321  CG311  CG331    53.35    111.00   8.00   2.56100 ! Same than
CG321 CG321 CG331
CG321  CG311  CG321    53.35    111.00   8.00   2.56100 ! Same than
CG321 CG321 CG321
```

```
HGA1   CG311  CG2O1    33.00    109.50   30.00   2.16300 ! Same than
HGA1   CG321  CG2O1
HGA1   CG311  CG321    33.00    109.50   30.00   2.16300 ! Same than
HGA1   CG321  CG321

CG331b  CG311  CG2O1    53.35    114.00    8.00   2.56100 ! Same
than CG331 CG321 CG2O1
CG321  CG311  CG331b   53.35    111.00   8.00   2.56100 ! Same than
CG321 CG321 CG331

!EXTRA ACRYLAMIDE
HGP1    NG2S1   HGP1      23.00     120.00 ! PROT adm jr. 8/13/90
geometry and vibrations


!Angles for Bupivacaine


BCG2O1   BNG2S1   BC2R61     50.00    120.00 ! RESI PACP, FRET AND
OTHERS
BC2R61   BNG2S1   BHGP1      34.00    117.00 ! RESI PACP, FRET AND
OTHERS
BC2R61  BC2R61   BCG331    45.80   120.00 ! TOLU, toluene, modified
by kevo
BC2R61   BC2R61   BC2R61     40.00    120.00   35.00   2.41620 !
PROT JES 8/25/89
BC2R61   BCG331   BHGA3     49.30   107.50 ! PROT toluene, adm jr.
3/7/92
BC2R61   BC2R61   BHGR61     30.00    120.00   22.00   2.15250 !
PROT JES 8/25/89 benzene
BC2R61  BC2R61   BNG2S1    40.00   120.00   35.00   2.4162 ! RESI
PACP, FRET AND OTHERS
BHGA3    BCG331   BHGA3      35.50    108.40    5.40   1.80200 !
PROT alkane update, adm jr., 3/2/92
BCG314   BCG2O1   BNG2S1     80.00    116.50 ! PROT NMA Vib Modes
(LK)
BNG2S1   BCG2O1   BOG2D1     80.00    122.50 ! PROT NMA Vib Modes
(LK)
BCG2O1   BNG2S1   BHGP1      34.00    123.00 ! PROT NMA Vib Modes
(LK)
BCG321   BCG321   BHGA2      26.50    110.10   22.53   2.17900 !
PROT alkane update, adm jr., 3/2/92
BCG321   BCG321   BCG321     58.35    113.60   11.16   2.56100 !
PROT alkane update, adm jr., 3/2/92
BCG324   BCG321   BHGA2      26.50    110.10   22.53   2.17900 !
FLAVOP PIP1,2,3
BCG321   BCG324   BNG3P1    100.00    110.00 ! ** or 40.0 110.0
FLAVOP PIP1,2,3
BCG2O1  BCG314  BCG321    52.00   108.00 ! PROT Alanine Dipeptide
ab initio calc's (LK)
```

```
BCG2O1   BCG314   BHGA1      50.00    109.50 ! PROT Alanine Dipeptide
ab initio calc's (LK)
BCG314   BCG2O1   BOG2D1     80.00    121.00 ! PROT Alanine Dipeptide
ab initio calc's (LK)
BCG2O1    BCG314    BNG3P1       43.70     110.00 ! NG3P3 PROT new
aliphatics, adm jr., 2/3/92
BCG314    BNG3P1    BCG324      45.00     115.20 ! NG3P2 Alpha benzyl
gamma 2-methyl piperidine
BCG324    BNG3P1    BCG324      45.00     115.20 ! FLAVOP PIP1,2,3 !
tweaked 115.50 --> 115.20 by kevo
BCG314    BNG3P1    BHGP2       30.00     110.80    27.00    2.07400 !
2MRB, Alph benz gam 2-methyl piperid
BCG324    BNG3P1    BHGP2       30.00     110.80    27.00    2.07400 !
FLAVOP PIP1,2,3
BCG314    BCG321    BCG321      58.35     113.50    11.16    2.56100 !
PROT alkanes
BCG314    BCG321    BHGA1       33.43     110.10    22.53    2.17900 !
PROT alkanes
BNG3P1    BCG314    BHGA1       45.00     102.30    35.00    2.10100 !
NG3P2 Al ben gam 2-methyl piperidine
BCG321    BCG314    BHGA1       34.50     110.10    22.53    2.17900 !
PROT alkane update, adm jr., 3/2/92
BCG321    BCG314    BNG3P1      40.00     110.00 ! NG3P2 2MRB, Alpha
benzyl gamma 2-methyl piperidine
BHGA2    BCG321   BHGA2      35.50    109.00    5.40   1.802  ! PROT
alkane update, adm jr., 3/2/92
BHGA2     BCG324    BHGA2       35.50     109.00     5.40    1.80200 !
PIP1,2,3
BNG3P1    BCG324    BHGA2       45.00     102.30    35.00    2.10100 !
FLAVOP PIP1,2,3
BCG321    BCG321    BCG331      58.00     115.00     8.00    2.56100 !
PROT alkane update, adm jr., 3/2/92
BCG321    BCG331    BHGA3       34.60     110.10    22.53    2.17900 !
PROT alkane update, adm jr., 3/2/92
BCG331    BCG321    BHGA2       34.60     110.10    22.53    2.17900 !
PROT alkane update, adm jr., 3/2/92
BCG321    BCG321    BCG324      58.35     110.50    11.16    2.56100 !
FLAVOP PIP1,2,3
BCG321    BCG324    BHGA2       26.50     111.80    22.53    2.17900 !
FLAVOP PIP1,2,3
BCG314    BCG321    BHGA2       33.43     110.10    22.53    2.17900 !
PROT alkanes



!TIP3P
HW   OW   HW    55.      104.52  !  TIP3P water

DIHEDRALS
!
!V(dihedral) = Kchi(1 + cos(n(chi) - delta))
```

```
!
!Kchi: kcal/mole
!n: multiplicity
!delta: degrees
!
!atom types             Kchi    n   delta


! dihedrals for NMA
CG331   CG2O1   NG2S1   CG331        1.6000   1      0.00 ! PROT NMA
cis/trans energy difference. (LK)
CG331   CG2O1   NG2S1   CG331        2.5000   2    180.00 ! PROT Gives
appropriate NMA cis/trans barrier. (LK)

OG2D1   CG2O1   NG2S1   CG331        2.5000   2    180.00 ! PROT Gives
appropriate NMA cis/trans barrier. (LK)
OG2D1   CG2O1   NG2S1   HGP1         2.5000   2    180.00 ! PROT Gives
appropriate NMA cis/trans barrier. (LK)

CG331   CG2O1   NG2S1   HGP1        1.4000   2    180.00 ! PROT adm jr.
4/10/91, acetamide update
NG2S1   CG2O1   CG331   HGA3         0.0000   3      0.00 ! PROT, sp2-
methyl, no torsion potential
OG2D1   CG2O1   CG331   HGA3        0.0000   3    180.00 ! PROT adm jr.,
8/13/90  geometry and vibrations
HGA3    CG331   NG2S1   HGP1         0.0000   3      0.00 ! PROT, sp2-
methyl, no torsion potential
HGA3    CG331   NG2S1   CG2O1        0.0000   3      0.00 ! PROT, sp2-
methyl, no torsion potential


CG331b   CG2O1   NG2S1   CG331b       1.6000   1      0.00 ! PROT NMA
cis/trans energy difference. (LK)
CG331b   CG2O1   NG2S1   CG331b       2.5000   2    180.00 ! PROT Gives
appropriate NMA cis/trans barrier. (LK)

CG331   CG2O1   NG2S1   CG331b        1.6000   1      0.00 ! PROT NMA
cis/trans energy difference. (LK)
CG331   CG2O1   NG2S1   CG331b       2.5000   2    180.00 ! PROT Gives
appropriate NMA cis/trans barrier. (LK)

CG331b   CG2O1   NG2S1   CG331        1.6000   1      0.00 ! PROT NMA
cis/trans energy difference. (LK)
CG331b   CG2O1   NG2S1   CG331        2.5000   2    180.00 ! PROT Gives
appropriate NMA cis/trans barrier. (LK)

OG2D1   CG2O1   NG2S1   CG331b       2.5000   2    180.00 ! PROT Gives
appropriate NMA cis/trans barrier. (LK)


CG331b   CG2O1   NG2S1   HGP1        1.4000   2    180.00 ! PROT adm jr.
4/10/91, acetamide update
```

```
NG2S1   CG2O1   CG331b   HGA3        0.0000   3      0.00 ! PROT, sp2-
methyl, no torsion potential
OG2D1   CG2O1   CG331b   HGA3       0.0000   3   180.00 ! PROT adm jr.,
8/13/90  geometry and vibrations
HGA3    CG331b   NG2S1   HGP1        0.0000   3      0.00 ! PROT, sp2-
methyl, no torsion potential
HGA3    CG331b   NG2S1   CG2O1       0.0000   3      0.00 ! PROT, sp2-
methyl, no torsion potential



! dihedrals for PNI
! dihedral 1
CG321   CG321   CG2O1   OG2D1       1.4000   1       0.00  ! PROT ala
dipeptide, new C VDW Rmin, adm jr., 3/3/93c
! dihedral 2
CG321   CG321   CG2O1   NG2S1       0.0000   1       0.00  ! PROT ala
dipeptide, new C VDW Rmin, 4/10/93 (LK)
!dihedral 3
HGA2    CG321   CG321   HGA3       0.2000   3      0.00 ! PROT alkane
update, adm jr., 3/2/92 no need to tune
! dihedral 4
HGA2    CG321   CG321   CG2O1      0.2000   3      0.00 ! PROT alkane
update, adm jr., 3/2/92
! dihedral 5
CG321   CG2O1   NG2S1   HGP1       0.0000   1      0.00 ! PROT Alanine
Dipeptide ab initio calc's (LK)
! dihedral 6
CG321  CG2O1  NG2S1  CG311    1.6000  1    0.00 ! PROT NMA cis/trans
energy difference. (LK)
CG321   CG2O1   NG2S1   CG311      2.5000   2    180.00 ! PROT Gives
appropriate NMA cis/trans barrier. (LK)
! dihedral 7
HGA3    CG321   CG2O1   OG2D1      0.2000   3      0.00 ! PROT adm jr.
3/19/92, from lipid methyl acetate; LIPID acetic Acid
! dihedral 8
HGA3   CG321  CG2O1  NG2S1     0.0000  3     0.00 ! PROT, sp2-methyl,
no torsion potential
! dihedral 9
CG2O1   NG2S1   CG311   HGA1       0.0000   1      0.00 ! PROT Alanine
Dipeptide ab initio calc's (LK)
! dihedral 10
CG2O1   NG2S1   CG311   CG331      1.8000   1       0.00  ! PROT ala
dipeptide, new C VDW Rmin, adm jr., 3/3/93c
CG2O1   NG2S1   CG311   CG331b      1.8000   1       0.00  ! PROT ala
dipeptide, new C VDW Rmin, adm jr., 3/3/93c
! dihedral 11
OG2D1   CG2O1   NG2S1   CG311      2.5000   2    180.00 ! PROT Gives
appropriate NMA cis/trans barrier. (LK)
! dihedral 12
NG2S1   CG311   CG331   HGA3       0.2000   3      0.00 ! PROT alkane
update, adm jr., 3/2/92
```

```
NG2S1   CG311   CG331b   HGA3       0.2000   3      0.00 ! PROT alkane
update, adm jr., 3/2/92
! dihedral 13
HGP1    NG2S1   CG311   HGA1       0.0000   1      0.00 ! PROT Alanine
Dipeptide ab initio calc's (LK)
! dihedral 14
HGP1    NG2S1   CG311   CG331      0.0000   1      0.00 ! PROT Alanine
dipeptide; NMA; acetate; etc. backbone param. RLD 3/22/92
HGP1    NG2S1   CG311   CG331b     0.0000   1      0.00 ! PROT Alanine
dipeptide; NMA; acetate; etc. backbone param. RLD 3/22/92
! dihedral 15
CG331   CG311   CG331   HGA3       0.2000   3      0.00 ! PROT alkane
update, adm jr., 3/2/921
CG331b  CG311   CG331b  HGA3       0.2000   3      0.00 ! PROT alkane
update, adm jr., 3/2/921
CG331   CG311   CG331b  HGA3       0.2000   3      0.00 ! PROT alkane
update, adm jr., 3/2/921
CG331b  CG311   CG331   HGA3       0.2000   3      0.00 ! PROT alkane
update, adm jr., 3/2/921
! dihedral 16
HGA1    CG311   CG331   HGA3       0.1600   3      0.00 ! PROT rotation
barrier in Ethane (SF)
HGA1    CG311   CG331b  HGA3       0.1600   3      0.00 ! PROT rotation
barrier in Ethane (SF)
! dihedral 17
HGA1   CG321   CG321   HGA3       0.1600   3      0.00 ! PROT rotation
barrier in Ethane (SF)
! dihedral 18
HGA1   CG321   CG321   CG321       0.2000   3      0.00 ! PROT alkane
update, adm jr., 3/2/921
! dihedral 19
HGA1   CG321   CG2O1   OG2D1       0.2000   3    0.00 ! PROT adm jr.
3/19/92, from lipid methyl acetate; LIPID acetic Acid
HGA1   CG321   CG2O1   OG2D1       0.2000   3    0.00 ! PROT adm jr.
3/19/92, from lipid methyl acetate; LIPID acetic Acid
! dihedral 20
HGA1  CG321  CG2O1  NG2S1     0.0000  3     0.00 ! PROT, sp2-methyl,
no torsion potential

! dihedral 21
CG321   CG321   CG321   HGA3       0.2000   3      0.00 ! PROT alkane
update, adm jr., 3/2/921
! dihedral 22
CG321   CG321   CG321   CG321      0.2000   3      0.00 ! PROT alkane
update, adm jr., 3/2/92
! dihedral 23
CG321   CG321   CG321   CG2O1      0.2000   3      0.00 ! PROT alkane
update, adm jr., 3/2/92 can be changed
! dihedral 24
CG321   CG321   CG321   HGA2       0.2000   3      0.00 ! PROT alkane
update, adm jr., 3/2/921
! dihedral 25
```

```
CG2O1   NG2S1   CG311   HGA3        0.0000   1      0.00 ! PROT Alanine
Dipeptide ab initio calc's (LK)
! dihedral 26
CG2O1   CG321   CG321   HGA3        0.2000   3      0.00 ! PROT alkane
update, adm jr., 3/2/92
! dihedral 27
HGA3   CG321   CG321   HGA3        0.1600   3      0.00 ! PROT rotation
barrier in Ethane (SF)
! dihedral 28
HGP1   NG2S1   CG311   HGA3        0.0000   1      0.00 ! PROT Alanine
Dipeptide ab initio calc's (LK)
! dihedral 29
HGA3   CG311   CG331   HGA3        0.1600   3      0.00 ! PROT rotation
barrier in Ethane (SF)
HGA3   CG311   CG331b   HGA3        0.1600   3      0.00 ! PROT rotation
barrier in Ethane (SF)
! dihedral 30
HGA2   CG321   CG321   HGA2        0.1600   3      0.00 ! PROT rotation
barrier in Ethane (SF)
! dihedral 31
OG2D1   CG2O1   CG321   HGA2        0.2000   3      0.00 ! PROT adm jr.
3/19/92, from lipid methyl acetate; LIPID acetic Acid
! dihedral 32
NG2S1   CG2O1   CG321   HGA2        0.2000   3      0.00 ! PROT alkane
update, adm jr., 3/2/92
! dihedral 33
CG321   CG321   CG321   CG331       0.2000   3      0.00 ! PROT alkane
update, adm jr., 3/2/92
CG321   CG321   CG321   CG331b      0.2000   3      0.00 ! PROT alkane
update, adm jr., 3/2/92
! dihedral 34
CG321   CG321   CG331   HGA3        0.2000   3      0.00 ! **PROT alkane
update, adm jr., 3/2/92
CG321   CG321   CG331b   HGA3       0.2000   3      0.00 ! **PROT alkane
update, adm jr., 3/2/92
! dihedral 35
CG321   CG321   CG331   HGA2        0.2000   3      0.00 ! **PROT alkane
update, adm jr., 3/2/92
CG321   CG321   CG331b   HGA2       0.2000   3      0.00 ! **PROT alkane
update, adm jr., 3/2/92
! dihedral 36
CG331   CG321   CG321   HGA2        0.2000   3      0.00 ! PROT alkane
update, adm jr., 3/2/92
CG331b   CG321   CG321   HGA2       0.2000   3      0.00 ! PROT alkane
update, adm jr., 3/2/92
! dihedral 37
CG331   CG321   CG2O1   OG2D1       1.4000   1      0.00 ! PROT ala
dipeptide, new C VDW Rmin, adm jr., 3/3/93c
CG331b   CG321   CG2O1   OG2D1      1.4000   1      0.00 ! PROT ala
dipeptide, new C VDW Rmin, adm jr., 3/3/93c
! dihedral 38
```

```
CG331   CG321   CG2O1   NG2S1       0.0000   1       0.00 ! PROT ala
dipeptide, new C VDW Rmin, 4/10/93 (LK)
CG331b   CG321   CG2O1   NG2S1      0.0000   1       0.00 ! PROT ala
dipeptide, new C VDW Rmin, 4/10/93 (LK)


! dihedral 39
CG2O1   CG321   CG331   HGA3       0.2000   3      0.00 ! PROT alkane
update, adm jr., 3/2/92
CG2O1   CG321   CG331   HGA2       0.2000   3      0.00 ! PROT alkane
update, adm jr., 3/2/92
NG2S1   CG311   CG331   HGA2       0.2000   3      0.00 ! PROT alkane
update, adm jr., 3/2/92
CG331   CG311   CG331   HGA2       0.2000   3      0.00 ! PROT alkane
update, adm jr., 3/2/92
HGA2   CG331   CG321   HGA3       0.1600   3     0.00 ! PROT rotation
barrier in Ethane (SF)
HGA3   CG331   CG321   HGA3       0.1600   3     0.00 ! PROT rotation
barrier in Ethane (SF)
HGA1   CG311   CG331   HGA2       0.1600   3     0.00 ! PROT rotation
barrier in Ethane (SF)

CG2O1   CG321   CG331b HGA3       0.2000   3      0.00 ! PROT alkane
update, adm jr., 3/2/92
CG2O1   CG321   CG331b   HGA2       0.2000   3      0.00 ! PROT alkane
update, adm jr., 3/2/92
NG2S1   CG311   CG331b   HGA2       0.2000   3      0.00 ! PROT alkane
update, adm jr., 3/2/92
CG331b   CG311   CG331b   HGA2       0.2000   3      0.00 ! PROT alkane
update, adm jr., 3/2/92
HGA2   CG331b   CG321   HGA3       0.1600   3     0.00 ! PROT rotation
barrier in Ethane (SF)
HGA3   CG331b   CG321   HGA3       0.1600   3     0.00 ! PROT rotation
barrier in Ethane (SF)
HGA1   CG311   CG331b   HGA2       0.1600   3     0.00 ! PROT rotation
barrier in Ethane (SF)

CG331b   CG311   CG331   HGA2       0.2000   3      0.00 ! PROT alkane
update, adm jr., 3/2/92
CG331   CG311   CG331b   HGA2       0.2000   3      0.00 ! PROT alkane
update, adm jr., 3/2/92


!EXTRA PNIPMAM

CG311   CG321   CG311   CG321     0.2000   3     0.00 ! Same than CG321
CG321   CG321   CG321
CG311   CG321   CG311   CG331     0.2000   3     0.00 ! Same than CG321
CG321   CG321   CG331
CG311   CG321   CG311   CG331b     0.2000   3     0.00 ! Same than CG321
CG321   CG321   CG331
```

```
CG311  CG321  CG311  CG2O1     0.2000  3     0.00 ! Same than CG321
CG321  CG321  CG2O1
CG311  CG2O1  NG2S1  HGP1      0.0000  1     0.00 ! Same than CG321
CG2O1  NG2S1  HGP1
! dihedral 6
CG311  CG2O1  NG2S1  CG311     1.6000  1     0.00 !
CG311  CG2O1  NG2S1  CG311     2.5000  2   180.00 ! Same than CG321
CG2O1  NG2S1  CG311

CG331  CG311  CG321  HGA2      0.2000  3     0.00 ! Same than CG331
CG321  CG321  HGA2
CG331  CG311  CG2O1  OG2D1     1.4000  1     0.00 ! Same than CG331
CG321  CG2O1  OG2D1
CG331  CG311  CG2O1  NG2S1     0.0000  1     0.00 ! Same than CG331
CG321  CG2O1  NG2S1
CG331b  CG311  CG321  HGA2      0.2000  3     0.00 ! Same than CG331
CG321  CG321  HGA2
CG331b  CG311  CG2O1  OG2D1     1.4000  1     0.00 ! Same than CG331
CG321  CG2O1  OG2D1
CG331b  CG311  CG2O1  NG2S1     0.0000  1     0.00 ! Same than CG331
CG321  CG2O1  NG2S1
HGA2   CG321  CG311  CG2O1     0.2000  3     0.00 ! Same than HGA2
CG321  CG321  CG2O1
CG2O1  CG311  CG331  HGA3      0.2000  3     0.00 ! Same than CG2O1
CG321  CG331  HGA3
CG2O1  CG311  CG331b  HGA3      0.2000  3     0.00 ! Same than CG2O1
CG321  CG331  HGA3
CG321  CG311  CG2O1  OG2D1     1.4000  1     0.00 ! Same than CG321
CG321  CG2O1  OG2D1
CG321  CG311  CG2O1  NG2S1     0.0000  1     0.00 ! Same than CG321
CG321  CG2O1  NG2S1
CG321  CG311  CG331  HGA3      0.2000  3     0.00 ! Same than CG321
CG321  CG331  HGA3
CG321  CG311  CG331b  HGA3      0.2000  3     0.00 ! Same than CG321
CG321  CG331  HGA3
CG321  CG311  CG321  HGA2      0.2000  3     0.00 ! Same than CG321
CG321  CG321  HGA2
HGA1  CG311  CG321  CG311      0.2000  3     0.00 ! Same than HGA1
CG321  CG321  CG321
HGA1  CG311  CG2O1  OG2D1       0.2000  3    0.00 ! Same than HGA1
CG321  CG2O1  OG2D1
HGA1  CG311  CG2O1  NG2S1      0.0000  3     0.00 ! Same than HGA1
CG321  CG2O1  NG2S1
HGA1  CG311  CG321  HGA2       0.1600  3     0.00 ! Same than HGA1
CG311  CG331  HGA2



! Dihedrals for Bupivacaine
```

```
BC2R61   BC2R61    BC2R61    BC2R61    3.1000  2   180.00 ! PROT JES
8/25/89
BC2R61   BC2R61    BC2R61    BHGR61    4.2000  2   180.00 ! PROT JES
8/25/89 benzene
BC2R61   BC2R61    BCG331    BHGA3     0.0020  6     0.00 ! PYRIDINE
toluene Kenno: 180 -> 0
BCG331    BC2R61     BC2R61     BC2R61     2.4000  2    180.00 ! PROT
toluene, adm jr., 3/7/92 K:4.2 -> 2.4
BC2R61   BC2R61    BC2R61    BNG2S1    3.1000  2   180.00 ! RETINOL
PACP
BCG331   BC2R61    BC2R61    BNG2S1    2.4000  2   180.00 ! 3A2MPD,
3-amino-2-methyl-pyridine CDCA
BCG331    BC2R61     BC2R61     BHGR61     2.4000  2    180.00 ! PROT
toluene, adm jr.,3/7/92 Ke:4.2 -> 2.4
BHGR61   BC2R61    BC2R61    BHGR61    2.4000  2   180.00 ! PROT JES
8/25/89 benzene
BNG2S1    BCG2O1     BCG314     BHGA1      0.0000  1      0.00 ! PROT
Alanine Dipeptide ab initio calc (LK)
BNG2S1   BCG2O1    BCG314    BNG3P1    0.6000  1     0.00 ! PROT ala
dipeptide, new C VDW Rmin,
BOG2D1    BCG2O1     BNG2S1     BHGP1      2.5000  2    180.00 ! PROT
Gives appropriate NMA cis/trans barr
BCG314    BCG2O1     BNG2S1     BHGP1      2.5000  2    180.00 ! PROT
Gives appropriate NMA cis/trans barr
BCG2O1    BCG314     BCG321     BHGA2      0.2000  3      0.00 ! PROT
alkane update, adm jr., 3/2/92
BCG2O1    BCG314     BCG321     BCG321     0.2000  3      0.00 ! PROT
alkane update, adm jr., 3/2/92
BCG2O1   BCG314    BNG3P1    BCG324    0.1000  3     0.00 ! Gamm-3
methyl piperidine, alph-ben amide
BOG2D1    BCG2O1     BCG314     BHGA1      0.0000  1      0.00 ! PROT
Alanine Dipeptide ab initio cal (LK)
BOG2D1   BCG2O1    BCG314    BCG321    1.4000  1     0.00 ! PROT ala
dipeptide, new C VDW Rmin, admjr.
BOG2D1    BCG2O1     BCG314     BNG3P1     0.0000  1      0.00 ! PROT
Backbone param set made complete RLD
BCG321   BCG324    BNG3P1    BCG314    0.4000  1     0.00 ! NG3P2***
Developmental params for PEI polymers and PIP. Will be tweaked, then
applied to existing PIP derivatives *** kevo
BCG321   BCG324    BNG3P1    BCG314    0.2500  2     0.00
BCG321   BCG324    BNG3P1    BCG314    0.6000  3     0.00
BHGA2     BCG324     BNG3P1     BCG314     0.1000  3      0.00 ! NG3P2
Gam-3 methyl piperidine, alpha-benz
BCG314   BCG321    BCG321    BHGA2     0.1950  3     0.00 ! NA abasic
nucleoside
BCG314   BCG321    BCG321    BCG321    0.5000  3     0.00 ! CARBOCY
carbocyclic sugars
BCG314   BCG321    BCG321    BCG321    0.5000  6   180.00 ! CARBOCY
carbocyclic sugars
BHGA1     BCG314     BCG321     BHGA2      0.1950  3      0.00 ! NA,
sugar
```

```
BHGA1    BCG314    BCG321    BCG321    0.1950  3     0.00 ! NA abasic
nucleoside
BHGA1    BCG314    BNG3P1    BCG324    0.1000  3     0.00 ! FLAVOP
PIP1,2,3; PEI polymers, kevo
BCG314   BNG3P1    BCG324    BHGA2     0.1000  3     0.00 ! NG3P2,Gamm-
3 methyl piperidine, alph-benzy
BHGA2    BCG324    BCG321    BCG321    0.1950  3     0.00 ! FLAVOP
PIP1,2,3
BCG321   BCG321    BCG321    BCG324    0.1950  3     0.00 ! FLAVOP
PIP1,2,3
BCG321   BCG324    BNG3P1    BCG324    0.1000  3     0.00 ! FLAVOP
PIP1,2,3; PEI polymers, kevo
BCG321   BCG314    BNG3P1    BCG324    0.1000  3     0.00 ! 3MRB,Gam-
3 methyl piperidine, alpha-benzyl
BHGA2    BCG321    BCG314    BNG3P1    0.1950  3     0.00 ! PIP,
piperidine
BHGA2    BCG321    BCG321    BHGA2     0.2200  3     0.00 ! LIPID
alkanes
BHGA2    BCG321    BCG324    BHGA2     0.1950  3     0.00 ! FLAVOP
PIP1,2,3
BCG321   BCG321    BCG324    BNG3P1    1.0000  3     0.00 ! FLAVOP
PIP1,2,3 ! Kenno: 0.1950 -> 1.0000
BNG3P1   BCG314    BCG321    BCG321    0.1950  3     0.00 ! 3MRB,
Gam-3 methyl piperidine, alpha-benzy
BHGA2    BCG321    BCG324    BNG3P1    0.1950  3     0.00 ! FLAVOP
PIP1,2,3
BCG321   BCG321    BCG331    BHGA3     0.1600  3     0.00 ! PROT
rotation barrier in Ethane (SF)
BCG324   BCG321    BCG321    BCG331    0.15051 2     0.00 ! CG324=CG321
LIPID alkane, 4/04, jbk (Jeff Klauda)
BCG324   BCG321    BCG321    BCG331    0.08133 3   180.00 ! *LIPID
alkane, 4/04, jbk
BCG324   BCG321    BCG321    BCG331    0.10824 4     0.00 ! *LIPID
alkane, 4/04, jbk
BCG324   BCG321    BCG321    BCG331    0.20391 5     0.00 ! *LIPID
alkane, 4/04, jbk
BCG324   BCG321    BCG321    BHGA2     0.1950  3     0.00 ! FLAVOP
PIP1,2,3
BCG321   BCG321    BCG321    BHGA2     0.1950  3     0.00 ! LIPID
alkanes
BCG331   BCG321    BCG321    BHGA2     0.1800  3     0.00 ! LIPID
alkane
BHGA3    BCG331    BCG321    BHGA2     0.1600  3     0.00 ! PROT
rotation barrier in Ethane (SF)
BOG2D1   BCG2O1    BNG2S1    BC2R61    2.5000  2   180.00 ! RETINOL
PACP
BCG314    BCG2O1     BNG2S1     BC2R61     1.6000   1       0.00 !
cg2r61=CG321 PROT NMA cis/trans energy difference. (LK)
BCG314    BCG2O1     BNG2S1     BC2R61     2.5000   2     180.00 !
cg2r61=CG321 PROT Gives appropr NMA cis/trans barrier.
BC2R61   BC2R61    BNG2S1    BHGP1     2.5000  2   180.00 ! PROT
Gives appropriate NMA cis/trans barr
```

```
BC2R61   BC2R61    BNG2S1    BCG2O1    1.2000  2   180.00 ! RETINOL
PACP
BNG2S1   BCG2O1    BCG314    BCG321    0.0000  1     0.00 ! PROT ala
dipeptide, new C VDW Rmin, (LK)
BCG2O1    BCG314     BCG321     BHGA2      0.2000   3      0.00 ! PROT
alkane update, adm jr., 3/2/92
BCG2O1    BCG314     BNG3P1     BHGP2      0.1000   3      0.00 ! NG3P3
PROT N-terminal AA - stand parameter
BCG321    BCG314     BNG3P1     BHGP2      0.1000   3      0.00 ! PROT
0.715->0.10 METHYLAMMONIUM (KK)
BHGA1     BCG314     BNG3P1     BHGP2      0.1000   3      0.00 ! 3MRB,
Gam-3 methyl piperidine, alpha-benzy
BCG321    BCG324     BNG3P1     BHGP2      0.1000   3      0.00 ! FLAVOP
PIP1,2,3
BHGA2     BCG324     BNG3P1     BHGP2      0.1000   3      0.00 ! FLAVOP
PIP1,2,3
BHGA2     BCG324     BNG3P1     BCG324     0.1000   3      0.00 ! FLAVOP
PIP1,2,3; PEI polymers, kevo

IMPROPER
!
!V(improper) = Kpsi(psi - psi0)**2
!
!Kpsi: kcal/mole/rad**2
!psi0: degrees
!note that the second column of numbers (0) is ignored
!
!atom types           Kpsi                   psi0
!
! Impropers for heterocyclic ring

!NMA
CG2O1   X   X   OG2D1     120.0000   0      0.00 ! PROT NMA Vibrational
Modes (LK)
NG2S1   X   X   HGP1       20.0000   0      0.00 ! PROT NMA Vibrational
Modes (LK)


! Impropers for heterocyclic ring BUPIVACAINE

BOG2D1    X    X    BCG2O1    120.0000         0      0.0000 ! ALLOW
PEP POL ARO


NONBONDED nbxmod  5 atom cdiel shift vatom vdistance vswitch -
cutnb 14.0 ctofnb 12.0 ctonnb 10.0 eps 1.0 e14fac 1.0 wmin 1.5
                !adm jr., 5/08/91, suggested cutoff scheme
!
!V(Lennard-Jones)       =       Eps,i,j[(Rmin,i,j/ri,j)**12       -
2(Rmin,i,j/ri,j)**6]
!
!epsilon: kcal/mole, Eps,i,j = sqrt(eps,i * eps,j)
```

```
!Rmin/2: A, Rmin,i,j = Rmin/2,i + Rmin/2,j
!
!atom  ignored   epsilon     Rmin/2  ignored  eps,1-4      Rmin/2,1-
4
!

! There aren't NONBONDED parameters for Bupivacaine
!NMA
CG331    0.0       -0.0780     2.0500   0.0 -0.01 1.9 ! alkane (CT3),
4/98, yin, adm jr; Rmin/2 modified from 2.04 to 2.05
CG331b   0.0       -0.0780     2.0500   0.0 -0.01 1.9 ! increase 20%
!!!!
HGA3     0.0        -0.0240     1.3400 ! alkane, yin and mackerell,
4/98
CG2O1    0.0        -0.1100     2.0000 ! NMA pure solvent, adm jr.,
3/3/93
OG2D1    0.0       -0.1200     1.7000   0.0  -0.12 1.40 ! carbonyl.
Also consistent with adm, acetaldehyde, 11/08
NG2S1    0.0        -0.2000     1.8500   0.0  -0.20 1.55 ! 1,4 vdW
allows the C5 dipeptide minimum to exist
HGP1     0.0       -0.0460     0.2245 ! polar H

! PNI
HGA1     0.0       -0.0450     1.3400 ! alkane, igor, 6/05
HGA2     0.0       -0.0350     1.3400 ! alkane, igor, 6/05
CG321    0.0      -0.0560     2.0100   0.0 -0.01 1.9 ! alkane (CT2),
4/98, yin, adm jr, also used by viv
CG311    0.0      -0.0320     2.0000   0.0 -0.01 1.9 ! alkane (CT1),
isobutane, 6/05 viv



! Bupivacaine

BHGA1  0.0       -0.0450     1.3400 ! alkane, igor, 6/05
BHGA2  0.0       -0.0350     1.3400 ! alkane, igor, 6/05
BHGA3   0.0        -0.0240      1.3400 ! alkane, yin and mackerell,
4/98
BHGP1  0.0       -0.0460     0.2245 ! polar H
BHGP2  0.0       -0.0460     0.2245 ! small polar Hydrogen, charged
systems
BHGR61 0.0       -0.0300     1.3582 ! benzene
BCG321 0.0       -0.0560     2.0100   0.0 -0.01 1.9 ! alkane (CT2),
4/98, yin, adm jr,
BCG331 0.0       -0.0780     2.0500   0.0 -0.01 1.9 ! alkane (CT3),
4/98, yin, adm jr;
BCG314 0.0       -0.0310     2.1650   0.0 -0.01 1.9 ! extrapolation
based on CG311, CG321 and CG324,
BCG324 0.0       -0.0550     2.1750   0.0 -0.01 1.9 ! PIP1,2,3
BCG2O1 0.0        -0.1100      2.0000 ! NMA pure solvent, adm jr.,
3/3/93
BC2R61 0.0       -0.0700     1.9924 ! INDO/TRP
```

```
BNG3P1 0.0       -0.2000     1.8500 ! PIP, tertiary amine
BNG2S1 0.0        -0.2000      1.8500    0.0   -0.20 1.55 ! 1,4 vdW
allows the C5 dipeptide min to exist
BOG2D1 0.0       -0.1200     1.7000   0.0 -0.12 1.40 ! carbonyl.


!For chloride ion. From toppar_water_ions file
CLA    0.0         -0.150       2.27     ! Chloride


!TIP3P water
OW       0.0       -0.1521     1.7682 ! TIP3P water
HW       0.0       -0.0460     0.2245 ! TIP3P water

NBFIX
CG331    OW    -0.1252    3.8182
CG331b   OW    -0.1252    3.8182
CG321    OW    -0.1061    3.7782
CG311    OW    -0.0803    3.7682


END
```

REFERENCES

SCIENTIFIC PAPERS & BOOKS

References

[1] A. S. Hoffman, “The origins and evolution of ‘controlled’ drug delivery systems,” *J. Control. Release*, vol. 132, no. 3, pp. 153–163, 2008.

[2] M. W. Tibbitt, J. E. Dahlman, and R. Langer, “Emerging Frontiers in Drug Delivery,” *J. Am. Chem. Soc.*, vol. 138, no. 3, pp. 704–717, 2016.

[3] J. Folkman and D. M. Long, “The use of silicone rubber as a carrier for prolonged drug therapy,” *J. Surg. Res.*, vol. 4, no. 3, pp. 139–142, 1964.

[4] A. Zaffaroni, “Bandage for administering drugs,” 3,598,122, 1971.

[5] G. Boswell and R. Scribner, “Polylactide-drugmixtures,” 3,773,919, 1973.

[6] J. Kent, D. Lewis, L. Sanders, and T. Tice, “Microencapsulation of water soluble active polypeptides,” 4,675,189, 1987.

[7] Y. Kawashima, “Nanoparticulate systems for improved drug delivery,” *Adv. Drug Deliv. Rev.*, vol. 47, no. 1, pp. 1–2, 2001.

[8] P. Couvreur, “Nanoparticles in drug delivery: Past, present and future,” *Adv. Drug Deliv. Rev.*, vol. 65, no. 1, pp. 21–23, 2013.

[9] B. K. Lee, Y. H. Yun, and K. Park, “Smart nanoparticles for drug delivery: Boundaries and opportunities,” *Chem. Eng. Sci.*, vol. 125, pp. 158–164, 2015.

[10] K. M. El-Say and H. S. El-Sawy, “Polymeric nanoparticles: Promising platform for drug delivery,” *Int. J. Pharm.*, vol. 528, no. 1–2, pp. 675–691, 2017.

[11] J. P. Rao and K. E. Geckeler, “Polymer nanoparticles: Preparation techniques and size-control parameters,” *Prog. Polym. Sci.*, vol. 36, no. 7, pp. 887–913, Jul. 2011.

[12] G. Agrawal and R. Agrawal, “Stimuli-responsive microgels and microgel-based systems: Advances in the exploitation of microgel colloidal properties and their interfacial activity,” *Polymers (Basel).*, vol. 10, no. 4, 2018.

[13] Q. Xu, M. Hashimoto, T. T. Dang, T. Hoare, D. S. Kohane, G. M. Whitesides, R. Langer, and D. G. Anderson, “Preparation of Monodisperse Biodegradable Polymer

Microparticles Using a Microfluidic Flow-focusing Device for Controlled Drug Delivery," *Natl. Inst. Heal. Public Access*, vol. 5, no. 13, pp. 1575–1581, 2010.

[14] S. Rezvantalab, N. I. Drude, M. K. Moraveji, N. Güvener, E. K. Koons, Y. Shi, T. Lammers, and F. Kiessling, "PLGA-based nanoparticles in cancer treatment," *Front. Pharmacol.*, vol. 9, no. NOV, pp. 1–19, 2018.

[15] J. Cheng, B. A. Teply, I. Sherifi, J. Sung, G. Luther, F. X. Gu, E. Levy-Nissenbaum, A. F. Radovic-Moreno, R. Langer, and O. C. Farokhzad, "Formulation of Functionalized PLGA-PEG Nanoparticles for In Vivo Targeted Drug Delivery," *Biomaterials*, vol. 28, no. 5, pp. 869–876, 2007.

[16] Y. Panahi, M. Farshbaf, M. Mohammadhosseini, M. Mirahadi, R. Khalilov, S. Saghfi, and A. Akbarzadeh, "Recent advances on liposomal nanoparticles: synthesis, characterization and biomedical applications," *Artif. Cells, Nanomedicine Biotechnol.*, vol. 45, no. 4, pp. 788–799, 2017.

[17] R. R. Sawant and V. P. Torchilin, "Challenges in Development of Targeted Liposomal Therapeutics," *AAPS J.*, vol. 14, no. 2, pp. 303–315, 2012.

[18] Y. Patil, Y. Amitay, P. Ohana, H. Shmeeda, and A. Gabizon, "Targeting of pegylated liposomal mitomycin-C prodrug to the folate receptor of cancer cells: Intracellular activation and enhanced cytotoxicity," *J. Control. Release*, vol. 225, pp. 87–95, 2016.

[19] J. Rios-Doria, N. Durham, L. Wetzel, R. Rothstein, J. Chesebrough, N. Holoweckyj, W. Zhao, C. C. Leow, and R. Hollingsworth, "Doxil Synergizes with Cancer Immunotherapies to Enhance Antitumor Responses in Syngeneic Mouse Models," *Neoplasia*, vol. 17, no. 8, pp. 661–670, 2015.

[20] J. J. Giner-Casares, M. Henriksen-Lacey, M. Coronado-Puchau, and L. M. Liz-Marzán, "Inorganic nanoparticles for biomedicine: Where materials scientists meet medical research," *Mater. Today*, vol. 19, no. 1, pp. 19–28, 2016.

[21] Y. Chang, X. Meng, Y. Zhao, K. Li, B. Zhao, M. Zhu, X. Li, YapengChen, and J. Wang, "Novel water-soluble and pH-responsive anticancer drug nanocarriers: Doxorubicin–PAMAM dendrimer conjugates attached to superparamagnetic iron

oxide nanoparticles (IONPs)," *J. Colloid Interface Sci.*, vol. 363, no. 1, pp. 403–409, 2011.

[22] F. Karchemski, D. Zucker, Y. Barenholz, and O. Regev, "Carbon nanotubes-liposomes conjugate as a platform for drug delivery into cells," *J. Control. Release*, vol. 160, no. 2, pp. 339–345, 2012.

[23] P. A. Tran, L. Zhang, and T. J. Webster, "Carbon nanofibers and carbon nanotubes in regenerative medicine," *Adv. Drug Deliv. Rev.*, vol. 61, no. 12, pp. 1097–1114, 2009.

[24] D. Pantarotto, J.-P. Briand, M. Prato, and A. Bianco, "Translocation of bioactive peptides across cell membranes by carbon nanotubes.," *Chem. Commun.*, no. 1, pp. 16–7, 2004.

[25] C. Bharti, N. Gulati, U. Nagaich, and A. Pal, "Mesoporous silica nanoparticles in target drug delivery system: A review," *Int. J. Pharm. Investig.*, vol. 5, no. 3, p. 124, 2015.

[26] W. Zeng, X. F. Qian, Y. B. Zhang, J. Yin, and Z. K. Zhu, "Organic modified mesoporous MCM-41 through solvothermal process as drug delivery system," *Mater. Res. Bull.*, vol. 40, no. 5, pp. 766–772, 2005.

[27] S. W. Song, K. Hidajat, and S. Kawi, "Functionalized SBA-15 materials as carriers for controlled drug delivery: Influence of surface properties on matrix-drug interactions," *Langmuir*, vol. 21, no. 21, pp. 9568–9575, 2005.

[28] D. J. Savage, X. Liu, S. A. Curley, M. Ferrari, and R. E. Serda, "Porous silicon advances in drug delivery and immunotherapy," *Curr. Opin. Pharmacol.*, vol. 13, no. 5, pp. 834–841, 2013.

[29] E. Vyskocilová, I. Luštická, I. Paterová, L. MacHová, and L. Cervený, "Modified MCM-41 as a drug delivery system for acetylsalicylic acid," *Solid State Sci.*, vol. 38, pp. 85–89, 2014.

[30] Z. Khan, S. A. Al-Thabaiti, A. Y. Obaid, and A. O. Al-Youbi, "Preparation and characterization of silver nanoparticles by chemical reduction method," *Colloids Surfaces B Biointerfaces*, vol. 82, no. 2, pp. 513–517, 2011.

[31] H. Huang and X. Yang, “Synthesis of polysaccharide-stabilized gold and silver nanoparticles: A green method,” *Carbohydr. Res.*, vol. 339, no. 15, pp. 2627–2631, 2004.

[32] S. Marre and K. F. Jensen, “Synthesis of micro and nanostructures in microfluidic systems,” *Chem. Soc. Rev.*, vol. 39, no. 3, pp. 1183–1202, 2010.

[33] M. Hamidi, A. Azadi, and P. Rafiei, “Hydrogel nanoparticles in drug delivery,” *Adv. Drug Deliv. Rev.*, vol. 60, pp. 1638–1649, 2008.

[34] O. Lyass, B. Uziely, R. Ben-Yosef, D. Tzemach, N. I. Heshing, M. Lotem, G. Brufman, and A. Bagizon, “Correlation of Toxicity with Pharmacokinetics of Breast Carcinoma,” *Cancer*, vol. 89, no. 5, pp. 1037–1047, 2000.

[35] J. Oberholzer, E. Langan, N. Dholakia, D. G. Anderson, R. Thakrar, M. Chen, H. H. Tam, J. Li, O. Veiseh, M. Qi, S. Jhunjhunwala, S. Siebert, M. Ma, J. Wyckoff, R. Langer, Y. Wang, M. Bochenek, D. L. Greiner, G. C. Weir, J. Hollister-Lock, I. Lacík, S. Aresta-Dasilva, J. C. Doloff, D. M. Lavin, A. R. Bader, A. Chiu, W. S. Loo, A. J. Vegas, J. Mendoza-Elias, and K. Tang, “Size- and shape-dependent foreign body immune response to materials implanted in rodents and non-human primates,” *Nat. Mater.*, vol. 14, no. 6, pp. 643–651, 2015.

[36] P. Brooks, O. Barzilay, Z. Sheikh, M. Glogauer, and N. Fine, “Macrophages, Foreign Body Giant Cells and Their Response to Implantable Biomaterials,” *Materials (Basel).*, vol. 8, no. 9, pp. 5671–5701, 2015.

[37] F. Alexis, E. Pridgen, and L. K. Molnar, “Factors Affecting the Clearance and Biodistribution of Polymeric Nanoparticles,” *Mol. Pharm.*, vol. 5, no. 4, pp. 505–515, 2015.

[38] H. Maeda, H. Nakamura, and J. Fang, “The EPR effect for macromolecular drug delivery to solid tumors: Improvement of tumor uptake, lowering of systemic toxicity, and distinct tumor imaging in vivo,” *Adv. Drug Deliv. Rev.*, vol. 65, no. 1, pp. 71–79, 2013.

[39] S. Wilhelm, A. J. Tavares, Q. Dai, S. Ohta, J. Audet, H. F. Dvorak, and W. C. W.

Chan, “Analysis of nanoparticle delivery to tumours,” *Nat. Rev. | Mater.*, vol. 1, pp. 1–12, 2016.

[40] G. Sonavane, K. Tomoda, and K. Makino, “Biodistribution of colloidal gold nanoparticles after intravenous administration: Effect of particle size,” *Colloids Surfaces B Biointerfaces*, vol. 66, no. 2, pp. 274–280, 2008.

[41] B. T. T. Pham, E. K. Colvin, N. T. H. Pham, B. J. Kim, E. S. Fuller, E. A. Moon, R. Barbey, S. Yuen, B. H. Rickman, N. S. Bryce, S. Bickley, M. Tanudji, S. K. Jones, V. M. Howell, and B. S. Hawkett, “Biodistribution and clearance of stable superparamagnetic maghemite iron oxide nanoparticles in mice following intraperitoneal administration,” *Int. J. Mol. Sci.*, vol. 19, no. 1, 2018.

[42] L. Guo, I. Panderi, D. D. Yan, K. Szulak, Y. Li, Y. T. Chen, H. Ma, D. B. Niesen, N. Seeram, A. Ahmed, B. Yan, D. Pantazatos, and W. Lu, “A comparative study of hollow copper sulfide nanoparticles and hollow gold nanospheres on degradability and toxicity,” *ACS Nano*, vol. 7, no. Xx, pp. 8780–8793, 2013.

[43] C. Fang, B. Shi, Y. Y. Pei, M. H. Hong, J. Wu, and H. Z. Chen, “In vivo tumor targeting of tumor necrosis factor-α-loaded stealth nanoparticles: Effect of MePEG molecular weight and particle size,” *Eur. J. Pharm. Sci.*, vol. 27, no. 1, pp. 27–36, 2006.

[44] D. E. Owens, N. A. Peppas, S.-D. Li, and L. Huang, “Pharmacokinetics and biodistribution of nanoparticles.,” *Mol. Pharm.*, vol. 5, no. 4, pp. 496–504, 2008.

[45] X. Gao, Y. Cui, R. M. Levenson, L. W. K. Chung, and S. Nie, “In vivo cancer targeting and imaging with semiconductor quantum dots,” *Nat. Biotechnol.*, vol. 22, no. 8, pp. 969–976, 2004.

[46] J. Elkhader, K. D. Wittrup, S. A. Gai, D. J. Irvine, and B. Kwong, “Localized Immunotherapy via Liposome-Anchored Anti-CD137 + IL-2 Prevents Lethal Toxicity and Elicits Local and Systemic Antitumor Immunity,” *Cancer Res.*, vol. 73, no. 5, pp. 1547–1558, 2013.

[47] and A. D. M. J. . K. Vanommeslaeghe, E. Hatcher, C. Acharya, S. Kundu, S. Zhong,

J. Shim, E. Darian, O. Guvench, P. Lopes, I. Vorobyov, and A. D. MacKerell Jr.*K. Vanommeslaeghe, E. Hatcher, C. Acharya, S. Kundu, S. Zhong, J. Shim, E. Darian, O. Guvench, P. Lopes, I. Vorob, "CHARMM General Force Field (CGenFF): A force field for drug-like molecules compatible with the CHARMM all-atom additive biological force fields(NIH Public Access)," vol. 31, no. 4, pp. 671–690, 2011.

[48] M. Mangoni, D. Roccatano, and A. Di Nola, "Docking of flexible ligands to flexible receptors in solution by molecular dynamics simulation," *Proteins Struct. Funct. Genet.*, vol. 35, no. 2, pp. 153–162, 1999.

[49] A. Müller, B. Homey, H. Soto, N. Ge, D. Catron, M. e. Buchanan, T. McClanahan, E. Murphy, W. Yuan, S. N. Wagner, J. L. Barrera, A. Mohar, E. Verástegui, and A. Zlotnik, "Involvement of chemokine receptors in breast cancer metastasis," *Nature*, vol. 410, pp. 50–56, 2001.

[50] X. Huang, J. Shen, M. Cui, L. Shen, X. Luo, K. Ling, G. Pei, H. Jiang, and K. Chen, "Molecular dynamics simulations on SDF-1a: Binding with CXCR4 receptor," *Biophys. J.*, vol. 84, pp. 171–184, 2003.

[51] S. Agarwal, E. Verma, V. Kumar, N. Lall, S. Sau, A. K. Iyer, and S. K. Kashaw, "An integrated computational approach of molecular dynamics simulations, receptor binding studies and pharmacophore mapping analysis in search of potent inhibitors against tuberculosis," *J. Mol. Graph. Model.*, vol. 83, pp. 17–32, 2018.

[52] S. Chowdhury, L. K. Beitel, R. Lumbroso, E. O. Purisima, M. Paliouras, and M. Trifiro, "A Targeted Bivalent Androgen Receptor Binding Compound for Prostate Cancer Therapy," *Horm. Cancer*, vol. 10, no. 1, pp. 24–35, 2019.

[53] D. W. Borhani and D. E. Shaw, "The future of molecular dynamics simulations in drug discovery," *J. Comput. Aided. Mol. Des.*, vol. 26, no. 1, pp. 15–26, 2012.

[54] M. Subashini, P. V. Devarajan, G. S. Sonavane, and M. Doble, "Molecular dynamics simulation of drug uptake by polymer," *J. Mol. Model.*, vol. 17, no. 5, pp. 1141–1147, 2011.

[55] P. Arendt, W. Chen, and W. Liu, "Simulation of the Diffusion of Doxorubicin (DOX)

in Polymer Pores for a Multiscale Nanodiamond Based Drug Delivery System," pp. 1–2, 2010.

[56] J. Lange, F. G. De Souza, M. Nele, F. W. Tavares, I. S. V. Segtovich, G. C. Q. Da Silva, and J. C. Pinto, "Molecular dynamic simulation of oxaliplatin diffusion in poly(lactic acid-co-glycolic acid). Part A: Parameterization and validation of the force-field CVFF," *Macromol. Theory Simulations*, vol. 25, no. 1, pp. 45–62, 2016.

[57] Z. Luo and J. Jiang, "PH-sensitive drug loading/releasing in amphiphilic copolymer PAE-PEG: Integrating molecular dynamics and dissipative particle dynamics simulations," *J. Control. Release*, vol. 162, no. 1, pp. 185–193, 2012.

[58] E. Ghobadi, M. Heuchel, K. Kratz, and A. Lendlein, "Simulation of volumetric swelling of degradable poly[(rac-lactide)-co-glycolide] based polyesterurethanes containing different urethane-linkers," *J. Appl. Biomater. Funct. Mater.*, vol. 10, no. 3, pp. 293–301, 2012.

[59] J. Walter, J. Sehrt, J. Vrabec, and H. Hasse, "Molecular Dynamics and Experimental Study of Conformation Change of Poly(N -isopropylacrylamide) Hydrogels in Mixtures of Water and Methanol," *J. Phys. Chem. B*, vol. 116, no. 17, pp. 5251–5259, 2012.

[60] T. Panczyk, P. Wolski, and L. Lajtar, "Coadsorption of Doxorubicin and Selected Dyes on Carbon Nanotubes. Theoretical Investigation of Potential Application as a pH-Controlled Drug Delivery System," *Langmuir*, vol. 32, no. 19, pp. 4719–4728, 2016.

[61] B. E. Smith, P. B. Roder, X. Zhou, and P. J. Pauzauskie, "Nanoscale materials for hyperthermal theranostics," *Nanoscale*, vol. 7, no. 16, pp. 7115–7126, 2015.

[62] J. Kolny-Olesiak, "Synthesis of copper sulphide-based hybrid nanostructures and their application in shape control of colloidal semiconductor nanocrystals," *CrystEngComm*, vol. 16, no. 40, pp. 9381–9390, 2014.

[63] H. Lee, S. W. Yoon, E. J. Kim, and J. Park, "In-Situ Growth of Copper Sulfide Nanocrystals on Multiwalled Carbon Nanotubes and Their Application as Novel Solar

Cell and Amperometric Glucose Sensor Materials," vol. 7, no. 3, pp. 778–784, 2007.

[64] G. Ku, M. Zhou, S. Song, Q. Huang, J. Hazle, and C. Li, "Copper sulfide nanoparticles as a new class of photoacoustic contrast agent for deep tissue imaging at 1064 nm," *ACS Nano*, vol. 6, no. 8, pp. 7489–7496, 2012.

[65] M. Zhou, R. Zhang, M. Huang, W. Lu, S. Song, M. P. Melancon, M. Tian, D. Liang, and C. Li, "A chelator-free multifunctional [64Cu]CuS nanoparticle platform for simultaneous micro-PET/CT imaging and photothermal ablation therapy," *J. Am. Chem. Soc.*, vol. 132, no. 16, pp. 15351–15358, 2010.

[66] X. Ding, C. H. Liow, M. Zhang, R. Huang, C. Li, H. Shen, M. Liu, Y. Zou, N. Gao, Z. Zhang, Y. Li, Q. Wang, S. Li, and J. Jiang, "Surface plasmon resonance enhanced light absorption and photothermal therapy in the second near-infrared window," *J. Am. Chem. Soc.*, vol. 136, no. 44, pp. 15684–15693, 2014.

[67] Q. Tian, M. Tang, Y. Sun, R. Zou, Z. Chen, M. Zhu, S. Yang, J. Wang, J. Wang, and J. Hu, "Hydrophilic flower-like cus superstructures as an efficient 980 nm laser-driven photothermal agent for ablation of cancer cells," *Adv. Mater.*, vol. 23, no. 31, pp. 3542–3547, 2011.

[68] Y. Li, W. Lu, Q. Huang, C. Li, and W. Chen, "Copper sulfide nanoparticles for photothermal ablation of tumor cells," *Nanomedicine*, vol. 5, no. 8, pp. 1161–1171, 2010.

[69] I. Ortiz de Solorzano, T. Alejo, M. Abad, C. Bueno-Alejo, G. Mendoza, V. Andreu, S. Irusta, V. Sebastian, and M. Arruebo, "Cleavable and thermo-responsive hybrid nanoparticles for on-demand drug delivery," *J. Colloid Interface Sci.*, vol. 533, pp. 171–181, 2019.

[70] J.-H. Lee and J.-W. Choi, "Application of Plasmonic Gold Nanoparticle for Drug Delivery System," *Curr. Drug Targets*, vol. 19, no. 3, pp. 271–278, 2017.

[71] B. E. Smith, P. B.Roder., X. Zhou., and Peter J. Pauzauskie., "Nanoscale materials for hyperthermal theranostics," *Optoelectron. Adv. Mater. Rapid Commun.*, vol. 4, no. 8, pp. 1166–1169, 2010.

[72] S. K. Libutti, G. F. Paciotti, A. A. Byrnes, H. R. Alexander, W. E. Gannon, M. Walker, G. D. Seidel, N. Yuldasheva, and L. Tamarkin, “Phase I and pharmacokinetic studies of CYT-6091, a novel PEGylated colloidal gold-rhTNF nanomedicine,” *Clin. Cancer Res.*, vol. 16, no. 24, pp. 6139–6149, 2010.

[73] J. M. Stern, V. V. Kibanov Solomonov, E. Sazykina, J. A. Schwartz, S. C. Gad, and G. P. Goodrich, “Initial Evaluation of the Safety of Nanoshell-Directed Photothermal Therapy in the Treatment of Prostate Disease,” *Int. J. Toxicol.*, vol. 35, no. 1, pp. 38–46, 2016.

[74] G. Hong, S. Diao, J. Chang, A. L. Antaris, C. Chen, B. Zhang, S. Zhao, D. N. Atochin, P. L. Huang, K. I. Andreasson, C. J. Kuo, and H. Dai, “Through-skull fluorescence imaging of the brain in a new near-infrared window,” *Nat. Photonics*, vol. 8, no. 9, pp. 723–730, 2014.

[75] S. B. Lakshmanan, X. Zou, M. Hossu, L. Ma, C. Yang, and W. Chen, “Local field enhanced Au/CuS nanocomposites as efficient photothermal transducer agents for cancer treatment,” *J. Biomed. Nanotechnol.*, vol. 8, no. 6, pp. 883–890, 2012.

[76] X. Liu, H. Qian, Y. Ji, Z. Li, Y. Shao, Y. Hu, G. Tong, L. Li, W. Guo, and H. Guo, “Mesoporous silica-coated NaYF4 nanocrystals: Facile synthesis, in vitro bioimaging and photodynamic therapy of cancer cells,” *RSC Adv.*, vol. 2, no. 32, pp. 12263–12268, 2012.

[77] H. J. Seo, S. H. Nam, H. J. Im, J. Y. Park, J. Y. Lee, B. Yoo, Y. S. Lee, J. M. Jeong, T. Hyeon, J. W. Kim, J. S. Lee, I. J. Jang, J. Y. Cho, D. W. Hwang, Y. D. Suh, and D. S. Lee, “Rapid Hepatobiliary Excretion of Micelle-Encapsulated/Radiolabeled Upconverting Nanoparticles as an Integrated Form,” *Sci. Rep.*, vol. 5, no. October, pp. 1–12, 2015.

[78] Y. Sato, A. Yokoyama, Y. Nodasaka, T. Kohgo, K. Motomiya, H. Matsumoto, E. Nakazawa, T. Numata, M. Zhang, M. Yudasaka, H. Hara, R. Araki, O. Tsukamoto, H. Saito, T. Kamino, F. Watari, and K. Tohji, “Long-term biopersistence of tangled oxidized carbon nanotubes inside and outside macrophages in rat subcutaneous tissue,” *Sci. Rep.*, vol. 3, pp. 1–10, 2013.

[79] C. M. Girish, A. Sasidharan, G. S. Gowd, S. Nair, and M. Koyakutty, “Confocal raman imaging study showing macrophage mediated biodegradation of graphene in vivo,” *Adv. Healthc. Mater.*, vol. 2, no. 11, pp. 1489–1500, 2013.

[80] L. Guo, I. Panderi, D. D. Yan, K. Szulak, Y. Li, Y. T. Chen, H. Ma, D. B. Niesen, N. Seeram, A. Ahmed, B. Yan, D. Pantazatos, and W. Lu, “A comparative study of hollow copper sulfide nanoparticles and hollow gold nanospheres on degradability and toxicity,” *ACS Nano*, vol. 7, no. 10, pp. 8780–8793, 2013.

[81] L. Guo, D. D. Yan, D. Yang, Y. Li, X. Wang, O. Zalewski, B. Yan, and W. Lu, “Combinatorial photothermal and immuno cancer therapy using chitosan-coated hollow copper sulfide nanoparticles,” *ACS Nano*, vol. 8, no. 6, pp. 5670–5681, 2014.

[82] D. Elgrabli, W. Dachraoui, C. Ménard-Moyon, X. J. Liu, D. Bégin, S. Bégin-Colin, A. Bianco, F. Gazeau, and D. Alloyeau, “Carbon Nanotube Degradation in Macrophages: Live Nanoscale Monitoring and Understanding of Biological Pathway,” *ACS Nano*, vol. 9, no. 10, pp. 10113–10124, 2015.

[83] A. M. Goodman, Y. Cao, C. Urban, O. Neumann, C. Ayala-orozco, M. W. Knight, A. Joshi, P. Nordlander, and N. J. Halas, “The Surprising in Vivo Instability of Near-IR-Absorbing Hollow Au À Ag Nanoshells,” no. 4, pp. 3222–3231, 2015.

[84] J. P. McMullen and K. F. Jensen, “Integrated Microreactors for Reaction Automation: New Approaches to Reaction Development,” *Annu. Rev. Anal. Chem.*, vol. 3, no. 1, pp. 19–42, 2010.

[85] R. C. R. Wootton, P. S. Doyle, C. Hansen, D. T. Chiu, D. Di Carlo, R. M. Maceiczyk, and A. J. deMello, “Small but Perfectly Formed? Successes, Challenges, and Opportunities for Microfluidics in the Chemical and Biological Sciences,” *Chem*, vol. 2, no. 2, pp. 201–223, 2017.

[86] P. Watts and C. Wiles, “Recent advances in synthetic micro reaction technology,” *Chem. Commun.*, no. 5, pp. 443–467, 2007.

[87] S. J. Haswell and P. Watts, “Green chemistry: Synthesis in micro reactors,” *Green Chem.*, vol. 5, no. 2, pp. 240–249, 2003.

[88] H. Wang, K. Liu, K. Chen, Y. Lu, S. Wang, W. Lin, F. Guo, K. Kamei, Y. Chen, M. Ohashi, and M. Wang, “A Rapid Pathway Toward a Superb Gene Delivery System : Programming Structural and Functional Diversity into a Supramolecular Nanoparticle Library,” vol. 4, no. 10, pp. 6235–6243, 2010.

[89] L. Gomez, V. Sebastian, S. Irusta, A. Ibarra, and J. Santamaria, “Scaled-up production of plasmonic nanoparticles using microfluidics : from metal precursors to functionalized and sterilized nanoparticles,” *Lab Chip*, vol. 14, pp. 325–332, 2014.

[90] S. Krishnadasan, R. J. C. Brown, A. J. DeMello, and J. C. DeMello, “Intelligent routes to the controlled synthesis of nanoparticles,” *Lab Chip*, vol. 7, no. 11, pp. 1434–1441, 2007.

[91] J. Lim, A. Swami, L. M. Gilson, S. Chopra, S. Choi, J. Wu, R. Langer, R. Karnik, O. C. Farokhzad, U. States, W. Hospital, U. States, U. States, U. States, and S. Arabia, “Ultra-High Throughput Synthesis of Nanoparticles with Homogeneous Size Distribution Using a Coaxial,” no. 6, pp. 6056–6065, 2014.

[92] F. Bally, D. K. Garg, C. A. Serra, Y. Hoarau, N. Anton, C. Brochon, D. Parida, T. Vandamme, and G. Hadziioannou, “Improved size-tunable preparation of polymeric nanoparticles by microfluidic nanoprecipitation,” *Polymer (Guildf).*, vol. 53, no. 22, pp. 5045–5051, 2012.

[93] E. Kastner, V. Verma, D. Lowry, and Y. Perrie, “Microfluidic-controlled manufacture of liposomes for the solubilisation of a poorly water soluble drug,” *Int. J. Pharm.*, vol. 485, no. 1–2, pp. 122–130, 2015.

[94] H. M. Xia, Y. P. Seah, Y. C. Liu, W. Wang, A. G. G. Toh, and Z. P. Wang, “Anti-solvent precipitation of solid lipid nanoparticles using a microfluidic oscillator mixer,” *Microfluid. Nanofluidics*, vol. 19, no. 2, pp. 283–290, 2015.

[95] L. Gomez, V. Sebastian, S. Irusta, A. Ibarra, M. Arruebo, and J. Santamaria, “Scaled-up production of plasmonic nanoparticles using microfluidics: from metal precursors to functionalized and sterilized nanoparticles,” *Lab Chip*, vol. 14, no. 2, pp. 325–332, 2014.

[96] L. Gomez, M. Arruebo, V. Sebastian, L. Gutierrez, and J. Santamaria, “Facile synthesis of SiO2-Au nanoshells in a three-stage microfluidic system,” *J. Mater. Chem.*, vol. 22, no. 40, pp. 21420–21425, 2012.

[97] T.-L. Cheung, L. Hong, N. Rao, C. Yang, L. Wang, W. J. Lai, P. H. J. Chong, W.-C. Law, and K.-T. Yong, “The non-aqueous synthesis of shape controllable Cu $_{2-x}$ S plasmonic nanostructures in a continuous-flow millifluidic chip for the generation of photo-induced heating,” *Nanoscale*, vol. 8, no. 12, pp. 6609–6622, 2016.

[98] S. Ramadan, L. Guo, Y. Li, B. Yan, and W. Lu, “Hollow copper sulfide nanoparticle-mediated transdermal drug delivery,” *Small*, vol. 8. pp. 3143–3150, 2012.

[99] Y. Xie, L. Carbone, C. Nobile, V. Grillo, S. D’Agostino, F. Della Sala, C. Giannini, D. Altamura, C. Oelsner, C. Kryschi, and P. D. Cozzoli, “Metallic-like stoichiometric copper sulfide nanocrystals: Phase- and shape-selective synthesis, near-infrared surface plasmon resonance properties, and their modeling,” *ACS Nano*, vol. 7, no. 8, pp. 7352–7369, 2013.

[100] Y. Zhao, H. Pan, Y. Lou, X. Qiu, J. Zhu, and C. Burda, “Plasmonic Cu 2-xS nanocrystals: Optical and structural properties of copper-deficient copper(I) sulfides,” *J. Am. Chem. Soc.*, vol. 131, no. I, pp. 4253–4261, 2009.

[101] R. Weissleder, “A clearer vision for in vivo imaging,” *Nat. Biotechnol.*, vol. 19, pp. 316–317, 2001.

[102] A. Matas, M. G. Sowa, G. Taylor, and H. H. Mantsch, “Melanin as a confounding factor in near infrared spectroscopy of skin,” *Vib. Spectrosc.*, vol. 28, no. 1, pp. 45–52, 2002.

[103] G. W. Luther, S. M. Theberge, T. F. Rozan, D. Rickard, C. C. Rowlands, and A. Oldroyd, “Aqueous copper Sulfide clusters as intermediates during copper sulfidek formation,” *Environ. Sci. Technol.*, vol. 36, no. 3, pp. 394–402, 2002.

[104] R. a. D. Pattrick, J. F. W. Mosselmans, J. M. Charnock, K. E. R. England, G. R. Helz, C. D. Garner, and D. J. Vaughan, “The structure of amorphous copper sulfide precipitates: An X-ray absorption study,” *Geochim. Cosmochim. Acta*, vol. 61, no. 10,

pp. 2023–2036, 1997.

[105] H. Zhu, J. Wang, and D. Wu, “Fast synthesis, formation mechanism, and control of shell thickness of cus hollow spheres,” *Inorg. Chem.*, vol. 48, no. 24, pp. 7099–7104, 2009.

[106] S. Bang, D. Yoon, J. Kim, H. Baik, H. Yang, and K. Lee, “Formation of double layer hollow nanostars of Pd/CuIr by utilizing a Kirkendall effect and a facile Cu atom movement along twinning boundaries and their usage as efficient water splitting catalysts,” *CrystEngComm*, vol. 17, no. 22, pp. 4084–4088, 2015.

[107] E. A. Magee, R. Curno, L. M. Edmond, and J. H. Cummings, “Contribution of dietary protein and inorganic sulfur to urinary sulfate: Toward a biomarker of inorganic sulfur intake,” *Am. J. Clin. Nutr.*, vol. 80, no. 1, pp. 137–142, 2004.

[108] W. Feng, W. Nie, Y. Cheng, X. Zhou, L. Chen, K. Qiu, Z. Chen, M. Zhu, and C. He, “In vitro and in vivo toxicity studies of copper sulfide nanoplates for potential photothermal applications,” *Nanomedicine Nanotechnology, Biol. Med.*, vol. 11, no. 4, pp. 901–912, 2015.

[109] L. Han, Y. Zhang, X. Chen, Y. Shu, and J.-H. Wang, “Protein-modified hollow copper sulfide nanoparticles carrying indocyanine green for photothermal and photodynamic therapy,” *J. Mater. Chem. B*, vol. 4, pp. 105–112, 2015.

[110] Y. Huang, Y. Lai, S. Shi, S. Hao, J. Wei, and X. Chen, “Copper sulfide nanoparticles with phospholipid-PEG coating for in vivo near-infrared photothermal cancer therapy,” *Chem. - An Asian J.*, vol. 10, no. 2, pp. 370–376, 2015.

[111] Laser Institute of America, *ANSI. American National Standard for safe use of lasers*. Orlando, FL, 2000.

[112] C. G. Pitt, Z.-W. Gu, R. W. Hendren, J. Thompson, and M. C. Wani, “Triggered drug delivery systems,” *J. Control. Release*, vol. 2, pp. 363–374, 1985.

[113] E. Ruvinov, J. Leor, and S. Cohen, “The promotion of myocardial repair by the sequential delivery of IGF-1 and HGF from an injectable alginate biomaterial in a model of acute myocardial infarction,” *Biomaterials*, vol. 32, no. 2, pp. 565–578,

2011.

[114] P. J.D., A. K., and M. S.H., “Pulsatile drug delivery system: An user-friendly dosage form,” *J. Pharm. Res. Heal. Care*, vol. 2, no. 2, pp. 204–215, 2010.

[115] S. A. Rovers, M. F. Kemmere, J. T. F. Keurentjes, and R. Hoogenboom, “Repetitive on-demand drug release from polymeric matrices containing a macroscopic spherical iron core,” *J. Mater. Sci. Mater. Med.*, vol. 28, no. 10, p. 163, 2017.

[116] M. Soleymani, M. Edrissi, and A. M. Alizadeh, “Thermosensitive polymer-coated La0.73Sr0.27MnO3 nanoparticles: potential applications in cancer hyperthermia therapy and magnetically activated drug delivery systems,” *Polym. J.*, vol. 47, p. 797, Sep. 2015.

[117] C. Aschkenasy and J. Kost, “On-demand release by ultrasound from osmotically swollen hydrophobic matrices,” *J. Control. Release*, vol. 110, no. 1, pp. 58–66, 2005.

[118] Y. Jing, Y. Zhu, X. Yang, J. Shen, and C. Li, “Ultrasound-triggered smart drug release from multifunctional core-shell capsules one-step fabricated by coaxial electrospray method,” *Langmuir*, vol. 27, no. 3, pp. 1175–1180, 2011.

[119] T. Kawano, Y. Niidome, T. Mori, Y. Katayama, and T. Niidome, “PNIPAM gel-coated gold nanorods for targeted delivery responding to a near-infrared laser,” *Bioconjug. Chem.*, vol. 20, no. 2, pp. 209–212, 2009.

[120] H. Nakatsuji, T. Numata, N. Morone, S. Kaneko, Y. Mori, H. Imahori, and T. Murakami, “Thermosensitive Ion Channel Activation in Single Neuronal Cells by Using Surface-Engineered Plasmonic Nanoparticles,” *Angew. Chemie - Int. Ed.*, vol. 54, no. 40, pp. 11725–11729, 2015.

[121] H. Kearns, N. C. Shand, K. Faulds, and D. Graham, “Laser induced SERS switching using plasmonic heating of PNIPAM coated HGNs.,” *Chem. Commun. (Camb).*, vol. 51, no. 38, pp. 8138–41, 2015.

[122] Z. Chen, Z. Cui, C. Cao, W. He, L. Jiang, and W. Song, “Temperature-Responsive Smart Nanoreactors: Poly(N-isopropylacrylamide)-Coated Au@Mesoporous-Si)2 Hollow Nanospheres,” *Langmuir*, vol. 28, pp. 13452–13458, 2012.

[123] T. T. T. Mai, T. H. P. Le, H. N. Pham, H. M. Do, and X. P. Nguyen, “Synthesis and magnetic heating characteristics of thermoresponsive poly (N-isopropylacrylamide-co-acrylic acid)/nano Fe 3 O 4 nanparticles,” *Adv. Nat. Sci. Nanosci. Nanotechnol.*, vol. 5, no. 4, p. 045007, 2014.

[124] F. Ye, J. Qin, M. S. Toprak, and M. Muhammed, “Multifunctional core-shell nanoparticles: Superparamagnetic, mesoporous, and thermosensitive,” *J. Nanoparticle Res.*, vol. 13, no. 11, pp. 6157–6167, 2011.

[125] P. Ji, B. Zhou, Y. Zhan, Y. Wang, Y. Zhang, Y. Li, and P. He, “Multistimulative Nanogels with Enhanced Thermosensitivity for Intracellular Therapeutic Delivery,” *ACS Appl. Mater. Interfaces*, vol. 9, no. 45, pp. 39143–39151, 2017.

[126] X. Xu, X. Wang, W. Luo, Q. Qian, Q. Li, B. Han, and Y. Li, “Triple cell-responsive nanogels for delivery of drug into cancer cells,” *Colloids Surfaces B Biointerfaces*, vol. 163, pp. 362–368, 2018.

[127] S. Shen, B. Ding, S. Zhang, X. Qi, K. Wang, J. Tian, Y. Yan, Y. Ge, and L. Wu, “Near-infrared light-responsive nanoparticles with thermosensitive yolk-shell structure for multimodal imaging and chemo-photothermal therapy of tumor,” *Nanomedicine Nanotechnology, Biol. Med.*, vol. 13, no. 5, pp. 1607–1616, 2017.

[128] W. Wu, Z. Lin, Y. Liu, X. Xu, C. Ding, and J. Li, “Thermoresponsive hydrogels based on a phosphorylated star-shaped copolymer: mimicking the extracellular matrix for in situ bone repair,” *J. Mater. Chem. B*, vol. 5, no. 3, pp. 428–434, 2017.

[129] P. Y. Chou, S. H. Chen, C. H. Chen, S. H. Chen, Y. T. Fong, and J. P. Chen, “Thermo-responsive in-situ forming hydrogels as barriers to prevent post-operative peritendinous adhesion,” *Acta Biomater.*, vol. 63, pp. 85–95, 2017.

[130] G. Vancoillie, D. Frank, and R. Hoogenboom, “Thermoresponsive poly(oligo ethylene glycol acrylates),” *Prog. Polym. Sci.*, vol. 39, no. 6, pp. 1074–1095, 2014.

[131] J. F. Lutz and A. Hoth, “Preparation of ideal PEG analogues with a tunable thermosensitivity by controlled radical copolymerization of 2-(2-methoxyethoxy)ethyl methacrylate and oligo(ethylene glycol) methacrylate,”

Macromolecules, vol. 39, no. 2, pp. 893–896, 2006.

[132] J. F. Lutz, Ö. Akdemir, and A. Hoth, "Point by point comparison of two thermosensitive polymers exhibiting a similar LCST: Is the age of poly(NIPAM) over?," *J. Am. Chem. Soc.*, vol. 128, no. 40, pp. 13046–13047, 2006.

[133] I. Bjornsdottir, O. Sternebring, W. A. Kappers, H. Selvig, H. T. Korno, J. B. Kristensen, and M. A. Bagger, "Pharmacokinetics, tissue distribution and excretion of 40 kDa PEG and PEGylated rFVIII (N8-GP) in rats," *Eur. J. Pharm. Sci.*, vol. 87, pp. 58–68, 2016.

[134] J. F. Lutz, J. Andrieu, S. Üzgün, C. Rudolph, and S. Agarwal, "Biocompatible, thermoresponsive, and biodegradable: Simple preparation of 'All-in-one' biorelevant polymers," *Macromolecules*, vol. 40, no. 24, pp. 8540–8543, 2007.

[135] P. Yi, Y. Wang, S. Zhang, Y. Zhan, Y. Zhang, Z. Sun, Y. Li, and P. He, "Stimulative nanogels with enhanced thermosensitivity for therapeutic delivery via β-cyclodextrin-induced formation of inclusion complexes," *Carbohydr. Polym.*, vol. 166, pp. 219–227, 2017.

[136] S. Kim, E. H. Chung, M. Gilbert, and K. E. Healy, "Synthetic MMP-13 degradable ECMs based on poly(N-isopropylacrylamide-co- acrylic acid) semi-interpenetrating polymer networks. I. Degradation and cell migration," *J. Biomed. Mater. Res. - Part A*, vol. 75, no. 1, pp. 73–88, 2005.

[137] H. G. Schild, "Poly(N-isopropylacrylamide): experiment, theory and application," *Prog. Polym. Sci.*, vol. 17, no. 2, pp. 163–249, Jan. 1992.

[138] I. Ankareddi, M. M. Bailey, C. S. Brazel, J. F. Rasco, and R. D. Hood, "Developmental toxicity assessment of thermoresponsive poly(N-isopropylacrylamide-co-acrylamide) oligomers in CD-1 mice.," *Birth Defects Res. B. Dev. Reprod. Toxicol.*, vol. 83, no. 2, pp. 112–6, 2008.

[139] K. Kono, A. Henmi, H. Yamashita, H. Hayashi, and T. Takagishi, "Improvement of temperature-sensitivity of poly(N-isopropylacrylamide)-modified liposomes," *J. Control. Release*, vol. 59, no. 1, pp. 63–75, 1999.

[140] H. Hayashi, K. Kono, and T. Takfagishi, “Temperature sensitization of liposomes using copolymers of N-isopropylacrylamide,” *Bioconjug. Chem.*, vol. 10, no. 3, pp. 412–418, 1999.

[141] N. Shamim, L. Hong, K. Hidajat, and M. S. Uddin, “Thermosensitive polymer (N-isopropylacrylamide) coated nanomagnetic particles: Preparation and characterization,” *Colloids Surfaces B Biointerfaces*, vol. 55, no. 1, pp. 51–58, 2007.

[142] S. A. Shah, M. H. Asdi, M. U. Hashmi, M. F. Umar, and S. U. Awan, “Thermo-responsive copolymer coated MnFe 2O 4 magnetic nanoparticles for hyperthermia therapy and controlled drug delivery,” *Mater. Chem. Phys.*, vol. 137, no. 1, pp. 365–371, 2012.

[143] A. Sánchez-Iglesias, M. Grzelczak, B. Rodríguez-González, P. Guardia-Girós, I. Pastoriza-Santos, J. Pérez-Juste, M. Prato, and L. M. Liz-Marzán, “Synthesis of multifunctional composite microgels via in situ Ni growth on pNIPAM-coated au nanoparticles,” *ACS Nano*, vol. 3, no. 10, pp. 3184–3190, Oct. 2009.

[144] Y. Li, D. Maciel, J. Rodrigues, X. Shi, and H. Tomás, “Biodegradable polymer nanogels for drug/nucleic acid delivery,” *Chem. Rev.*, vol. 115, no. 16, pp. 8564–8608, 2015.

[145] G. Wang, Y. Chen, P. Wang, Y. Wang, H. Hong, Y. Li, J. Qian, Y. Yuan, B. Yu, and C. Liu, “Preferential tumor accumulation and desirable interstitial penetration of poly(lactic-co-glycolic acid) nanoparticles with dual coating of chitosan oligosaccharide and polyethylene glycol-poly(d,l-lactic acid),” *Acta Biomater.*, vol. 29, pp. 248–260, 2016.

[146] Y. Li and C. Liu, “Nanomaterial-based bone regeneration,” *Nanoscale*, vol. 9, no. 15, pp. 4862–4874, 2017.

[147] Y. Li, Y. Xiao, and C. Liu, “The Horizon of Materiobiology: A Perspective on Material-Guided Cell Behaviors and Tissue Engineering,” *Chem. Rev.*, vol. 117, no. 5, pp. 4376–4421, 2017.

[148] B. Zhou, B. Wu, J. Wang, Q. Qian, J. Wang, H. Xu, S. Yang, P. Feng, W. Chen, Y.

Li, J. Jiang, and B. Han, “Drug-mediation formation of nanohybrids for sequential therapeutic delivery in cancer cells,” *Colloids Surfaces B Biointerfaces*, vol. 163, pp. 284–290, 2018.

[149] X. Xu, J. Wang, Y. Wang, L. Zhao, Y. Li, and C. Liu, “Formation of graphene oxide-hybridized nanogels for combinative anticancer therapy,” *Nanomedicine Nanotechnology, Biol. Med.*, pp. 1–9, 2016.

[150] Z. Zha, S. Zhang, Z. Deng, Y. Li, C. Li, and Z. Dai, “Enzyme-responsive copper sulphide nanoparticles for combined photoacoustic imaging, tumor-selective chemotherapy and photothermal therapy,” *Chem. Commun.*, vol. 49, no. 33, p. 3455, 2013.

[151] L. Guo, D. D. Yan, D. Yang, Y. Li, X. Wang, O. Zalewski, B. Yan, and W. Lu, “Combinatorial Photothermal and Immuno Cancer Therapy Using Chitosan-Coated Hollow Copper Sulfide Nanoparticles,” *ACS Nano*, vol. 8, no. 6, pp. 5670–5681, Jun. 2014.

[152] S. Huang, J. Liu, Q. He, H. Chen, J. Cui, S. Xu, Y. Zhao, C. Chen, and L. Wang, “Smart Cu1.75S nanocapsules with high and stable photothermal efficiency for NIR photo-triggered drug release,” *Nano Res.*, vol. 8, no. 12, pp. 4038–4047, 2015.

[153] Z. Meng, F. Wei, R. Wang, M. Xia, Z. Chen, H. Wang, and M. Zhu, “NIR-Laser-Switched in Vivo Smart Nanocapsules for Synergic Photothermal and Chemotherapy of Tumors,” *Adv. Mater.*, vol. 28, no. 2, pp. 245–253, 2016.

[154] J. L. Apfelbaum, C. Chen, S. S. Mehta, and and T. J. Gan, “Postoperative Pain Experience: Results from a National Survey Suggest Postoperative Pain Continues to Be Undermanaged,” *Anesth. Analg.*, vol. 97, no. 2, pp. 534–540, 2003.

[155] C. M. Santamaria, A. Woodruff, R. Yang, and D. S. Kohane, “Drug delivery systems for prolonged duration local anesthesia,” *Mater. Today*, vol. 20, no. 1, pp. 22–31, 2017.

[156] H. Zhang, Y. Lu, G. Zhang, S. Gao, D. Sun, and Y. Zhong, “Bupivacaine-loaded biodegradable poly(lactic-co-glycolic) acid microspheres. I. Optimization of the drug

incorporation into the polymer matrix and modelling of drug release," *Int. J. Pharm.*, vol. 351, no. 1–2, pp. 244–249, 2008.

[157] J. B. McAlvin, R. F. Padera, S. A. Shankarappa, G. Reznor, A. H. Kwon, H. H. Chiang, J. Yang, and D. S. Kohane, "Multivesicular liposomal bupivacaine at the sciatic nerve," *Biomaterials*, vol. 35, no. 15, pp. 4557–4564, 2014.

[158] S. Nadri, H. Mahmoudvand, and A. Eatemadi, "Magnetic nanogel polymer of bupivacaine for ankle block in rats," *J. Microencapsul.*, vol. 33, no. 7, pp. 656–662, 2016.

[159] S. Radin, T. Chen, and P. Ducheyne, "The controlled release of drugs from emulsified, sol gel processed silica microspheres," *Biomaterials*, vol. 30, no. 5, pp. 850–858, 2009.

[160] G. Colombo, R. Padera, R. Langer, and D. S. Kohane, "Prolonged duration local anesthesia with lipid-protein-sugar particles containing bupivacaine and dexamethasone," *J. Biomed. Mater. Res. - Part A*, vol. 75, no. 2, pp. 458–464, 2005.

[161] C. Zhan, W. Wang, C. Santamaria, B. Wang, A. Rwei, B. P. Timko, and D. S. Kohane, "Ultrasensitive Phototriggered Local Anesthesia," *Nano Lett.*, vol. 17, no. 2, pp. 660–665, 2017.

[162] N. Guarrotxena and I. Quijada-Garrido, "Optical and Swelling Stimuli-Response of Functional Hybrid Nanogels: Feasible Route to Achieve Tunable Smart Core@Shell Plasmonic@Polymer Nanomaterials," *Chem. Mater.*, vol. 28, no. 5, pp. 1402–1412, 2016.

[163] M. Liras, E. Peinado, P. Cañamero, I. Quijada-Garrido, and O. García, "Smart photoluminescent nanohybrids based on CdSe quantum dots capped with multidentate thiolated pH-responsive and thermoresponsive polymers for nanosensing," *J. Polym. Sci. Part A Polym. Chem.*, vol. 52, no. 21, pp. 3087–3095, 2014.

[164] E. Cazares-Cortes, A. Espinosa, J. M. Guigner, A. Michel, N. Griffete, C. Wilhelm, and C. Ménager, "Doxorubicin Intracellular Remote Release from Biocompatible Oligo(ethylene glycol) Methyl Ether Methacrylate-Based Magnetic Nanogels

Triggered by Magnetic Hyperthermia," *ACS Appl. Mater. Interfaces*, vol. 9, no. 31, pp. 25775–25788, 2017.

[165] A. M. Santiago, T. Ribeiro, A. S. Rodrigues, B. Ribeiro, R. F. M. Frade, C. Baleizão, and J. P. S. Farinha, "Multifunctional Hybrid Silica Nanoparticles with a Fluorescent Core and Active Targeting Shell for Fluorescence Imaging Biodiagnostic Applications," *Eur. J. Inorg. Chem.*, vol. 2015, no. 27, pp. 4579–4587, 2015.

[166] V. B. Sadhu, J. Pionteck, D. Voigt, H. Komber, D. Fischer, and B. Voit, "Atom-transfer radical polymerization: A strategy for the synthesis of halogen-free amino-functionalized poly(methyl methacrylate) in a one-pot reaction," *Macromol. Chem. Phys.*, vol. 205, no. 17, pp. 2356–2365, 2004.

[167] M. Alejo, T.; Prieto, M.; García-Juan, H.; Andreu, V.; Mendoza, G.; Sebastian, V.; Arruebo, "A facile method for the controlled polymerization of biocompatible and thermoresponsive oligo(ethylene glycol) methyl ether methacrylate copolymers," *Polym. J.*, 2017.

[168] F. M. Aseyev, V., Tenhu, H. & Winnik, *Self Organized Nanostructures of Amphiphilic Block Copolymers II*. Springer Berlin Heidelberg, 2010.

[169] J. Lei, C. Mayer, V. Freger, and M. Ulbricht, "Synthesis and characterization of poly(ethylene glycol) methacrylate based hydrogel networks for anti-biofouling applications," *Macromol. Mater. Eng.*, vol. 298, no. 9, pp. 967–980, 2013.

[170] L. S. Starkey, "H-NMR Chemical Shifts," *Calif. State Polytech. Univ. Pomona* , p. 318.

[171] A. G. Kumbhar and K. Kishore, "Redox reactions of Cu (II) -amine complexes in aqueous solutions," vol. 66, pp. 275–280, 2003.

[172] P. G. Ganesan, G. Cui, K. Vijayamohanan, M. Lane, and G. Ramanath, "Effects of amine- and pyridine-terminated molecular nanolayers on adhesion at Cu–SiO[sub 2] interfaces," *J. Vac. Sci. Technol. B Microelectron. Nanom. Struct.*, vol. 23, no. 1, p. 327, 2005.

[173] I. Ortiz De Solorzano, M. Prieto, G. Mendoza, T. Alejo, S. Irusta, V. Sebastian, and

M. Arruebo, “Microfluidic Synthesis and Biological Evaluation of Photothermal Biodegradable Copper Sulfide Nanoparticles,” *ACS Appl. Mater. Interfaces*, vol. 8, no. 33, pp. 21545–21554, 2016.

[174] C. Harford and B. Sarkar, “Amino Terminal Cu(II)-and Ni(II)-Binding (ATCUN) Motif of Proteins and Peptides: Metal Binding, DNA Cleavage, and Other Properties,” *Acc. Chem. Res.*, vol. 30, no. 3, pp. 123–130, 1997.

[175] A. Y. Rwei, J.-J. Lee, C. Zhan, Q. Liu, M. T. Ok, S. A. Shankarappa, R. Langer, and D. S. Kohane, “Repeatable and adjustable on-demand sciatic nerve block with phototriggerable liposomes,” *Proc. Natl. Acad. Sci.*, vol. 112, no. 51, pp. 15719–15724, 2015.

[176] M. B. Browning, S. N. Cereceres, P. T. Luong, and E. M. Cosgriff-Hernandez, “Determination of the in vivo degradation mechanism of PEGDA hydrogels,” *J. Biomed. Mater. Res. - Part A*, vol. 102, no. 12, pp. 4244–4251, 2014.

[177] P. Ma, T. Li, H. Xing, S. Wang, Y. Sun, X. Sheng, and K. Wang, “Local anesthetic effects of bupivacaine loaded lipid-polymer hybrid nanoparticles: In vitro and in vivo evaluation,” *Biomed. Pharmacother.*, vol. 89, no. October 2011, pp. 689–695, 2017.

[178] J. M. Maurice, Y. Gan, F. MA, Y. Chang, M. Hibner, and Y. Huang, “Bupivacaine causes cytotoxicity in mouse C2C12 myoblast cells: involvement of ERK and Akt signaling pathways,” *Acta Pharmacol. Sin.*, vol. 31, no. 4, pp. 493–500, 2010.

[179] R. Grillo, N. F. S. de Melo, D. R. de Araújo, E. de Paula, A. H. Rosa, and L. F. Fraceto, “Polymeric alginate nanoparticles containing the local anesthetic bupivacaine,” *J. Drug Target.*, vol. 18, no. 9, pp. 688–699, 2010.

[180] B. C. Wang, N. T. Flynn, and R. Langer, “Controlled Structure and Properties of Thermoresponsive Nanoparticle - Hydrogel Composites,” vol. 16, no. 13, pp. 1074–1079, 2004.

[181] Y. Guang and Y. Zhang, “PNIPAM microgels for biomedical applications : from dispersed particles to 3D assemblies,” *Soft Matter*, vol. 7, pp. 6375–6384, 2011.

[182] M. R. Islam, A. Ahiabu, X. Li, and M. J. Serpe, “Poly (N-isopropylacrylamide)

Microgel-Based Optical Devices for Sensing and Biosensing," *Sensors (basel)*, vol. 14, no. 5, pp. 8984–8995, 2014.

[183] D. E. Bergbreiter, B. L. Case, Y. Liu, and J. W. Caraway, "Poly (N - isopropylacrylamide) Soluble Polymer Supports in Catalysis and Synthesis," *Macromolecules*, vol. 31, no. 98, pp. 6053–6062, 1998.

[184] Q. Zhao, N. Chen, D. Zhao, and X. Lu, "Thermoresponsive Magnetic Nanoparticles for Seawater Desalination," *ACS Appl. Mater. Interfaces*, vol. 5, no. 21, pp. 11453–11461, 2013.

[185] C. E. Reese, A. V Mikhonin, M. Kamenjicki, A. Tikhonov, and S. A. Asher, "Nanogel Nanosecond Photonic Crystal Optical Switching," *J. Am. Chem. Soc.*, vol. 126, pp. 1493–1496, 2004.

[186] Y. Shi, L. Peng, and G. Yu, "Conductive ' Smart ' Hybrid Hydrogels with PNIPAM and Nanostructured Conductive Polymers," *Adv. Funct. Mater.*, vol. 25, no. 8, pp. 1219–1225, 2015.

[187] J. L. Paris, M. V. Cabañas, M. Manzano, and M. Vallet-Regi, "Polymer-Grafted Mesoporous Silica Nanoparticles as Ultrasound-Responsive Drug Carriers," *ACS Nano*, vol. 9, no. 11, pp. 11023–11033, 2015.

[188] L. Chu, T. Niitsuma, T. Yamaguchi, and S. Nakao, "Thermoresponsive Transport through Porous Membranes with Grafted PNIPAM Gates," *AIChE J.*, vol. 49, no. 4, pp. 896–909, 2003.

[189] T. Hoare and R. Pelton, "Engineering Glucose Swelling Responses in Poly (N - isopropylacrylamide) -Based Microgels," *Macromolecules*, vol. 40, pp. 670–678, 2007.

[190] G. Li, S. E. N. Song, L. E. I. Guo, and S. Ma, "Self-Assembly of Thermo- and pH-Responsive Poly (acrylic acid) - b -poly (N -isopropylacrylamide) Micelles for Drug Delivery," *J. Polym. Sci. Part A Polym. Chem.*, vol. 46, no. 15, pp. 5028–5035, 2008.

[191] S. Kumar, Y. L. Dory, M. Lepage, and Y. Zhao, "Surface-Grafted Stimuli-Responsive Block Copolymer Brushes for the Thermo- , Photo- and pH-Sensitive Release of Dye

Molecules," *Macromolecules*, vol. 44, no. 18, pp. 7385–7393, 2011.

[192] G. Huang, J. Gao, Z. Hu, J. V St, B. C. Ponder, and D. Moro, "Controlled drug release from hydrogel nanoparticle networks," *J. Control. Release*, vol. 94, no. 2–3, pp. 303–311, 2004.

[193] J. C. Garbern, A. S. Hoffman, and P. S. Stayton, "Injectable pH- and temperature-responsive poly (N-isopropylacrylamide- co -propylacrylic acid) Copolymers for Delivery of Angiogenic Growth Factors," *Biomacromolecules*, vol. 11, no. 7, pp. 1833–1839, 2010.

[194] L. Zhang, L. Wang, B. Guo, and P. X. Ma, "Cytocompatible injectable carboxymethyl chitosan / N -isopropylacrylamide hydrogels for localized drug delivery," *Carbohydr. Polym.*, vol. 103, pp. 110–118, 2014.

[195] B. P. Timko, M. Arruebo, S. A. Shankarappa, J. B. McAlvin, O. S. Okonkwo, B. Mizrahi, C. F. Stefanescu, L. Gomez, J. Zhu, A. Zhu, J. Santamaria, R. Langer, and D. S. Kohane, "Near-infrared-actuated devices for remotely controlled drug delivery.," *Proc. Natl. Acad. Sci. U. S. A.*, vol. 111, no. 4, pp. 1349–54, 2014.

[196] C. Zhu, Y. Lu, J. Peng, J. Chen, and S. Yu, "Photothermally Sensitive Poly (N -isopropylacrylamide)/ Graphene Oxide Nanocomposite Hydrogels as Remote Light-Controlled Liquid Microvalves," *Adv. Funct. Mater.*, vol. 22, no. 19, pp. 4017–4022, 2012.

[197] S. Purushotham and R. V. Ramanujan, "Thermoresponsive magnetic composite nanomaterials for multimodal cancer therapy," *Acta Biomater.*, vol. 6, no. 2, pp. 502–510, 2010.

[198] S. Deshpande, S. Sharma, V. Koul, and N. Singh, "Core − Shell Nanoparticles as an Efficient, Sustained, and Triggered Drug-Delivery System," *ACS Omega*, vol. 2, pp. 6455–6463, 2017.

[199] J. Sun, R. Gui, H. Jin, and X. Wang, "CuS nanocrystal@microgel nanocomposites for light-regulated release of dual-drugs and chemo-photothermal synergistic therapy in vitro," *RSC Adv.*, vol. 6, pp. 8722–8728, 2016.

[200] J. You, G. Zhang, and C. Li, “Exceptionally High Payload of docorubicin in hollow gold nanospheres for near-infrared light-triggered drug release,” *ACS Nano*, vol. 4, no. 2, pp. 1033–1041, 2010.

[201] D. Bartczak, O. L. Muskens, S. Nitti, T. Sanchez-elsner, T. M. Millar, and A. G. Kanaras, “Interactions of Human Endothelial Cells with Gold Nanoparticles of Different Morphologies,” *Small*, vol. 8, no. 1, pp. 122–130, 2012.

[202] W. Lu, Q. Huang, G. Ku, X. Wen, M. Zhou, D. Guzatov, R. Su, A. Oraevsky, L. V Wang, and C. Li, “Photoacoustic imaging of living mouse brain vasculature using hollow gold nanospheres,” *Biomaterials*, vol. 31, no. 9, pp. 2617–2626, 2010.

[203] A. Mulgaonkar, S. Moeendarbari, W. Silvers, G. Hassan, X. Sun, Y. Hao, and W. Mao, “Hollow Gold Nanoparticles as Efficient In Vivo Radiosensitizing Agents for Radiation Therapy of Breast Cancer,” *J. Biomed. Nanotechnol.*, vol. 13, no. 5, pp. 566–574, 2017.

[204] F. M. Martin-saavedra, V. Cebrian, L. Gomez, D. Lopez, M. Arruebo, C. G. Wilson, R. T. Franceschi, R. Voellmy, J. Santamaria, and N. Vilaboa, “Temporal and spatial patterning of transgene expression by near-infrared irradiation,” *Biomaterials*, vol. 35, no. 28, pp. 8134–8143, 2014.

[205] M. Karg, I. Pastoriza-Santos, J. Pérez-Juste, T. Hellweg, and L. M. Liz-Marzán, “Nanorod-coated PNIPAM microgels: Thermoresponsive optical properties,” *Small*, vol. 3, no. 7, pp. 1222–1229, 2007.

[206] S. A. Jadhav, V. Brunella, I. Miletto, G. Berlier, and D. Scalarone, “Synthesis of poly(N -isopropylacrylamide) by distillation precipitation polymerization and quantitative grafting on mesoporous silica,” vol. 133, p. 44181, 2016.

[207] Y. Katsumoto, T. Tanaka, H. Sato, and Y. Ozaki, “Conformational Change of Poly (N -isopropylacrylamide) during the Coil - Globule Transition Investigated by Attenuated Total Reflection / Infrared Spectroscopy and Density,” *J. Phys. Chem. A*, vol. 106, no. 14, pp. 3429–3435, 2002.

[208] H. Kolya and T. Tripathy, “Biodegradable flocculants based on polyacrylamide and

poly (N , N-dimethylacrylamide) grafted amylopectin," *Int. J. Biol. Macromol.*, vol. 70, pp. 26–36, 2014.

[209] S. Carter, B. Hunt, and S. Rimmer, "Highly branched poly(N-isopropylacrylamide)s with imidazole end groups prepared by radical polymerization in the presence of a styryl monomer containing a dithioester group," *Macromolecules*, vol. 38, no. 11, pp. 4595–4603, 2005.

[210] S. Rimmer, S. Carter, R. Rutkaite, J. W. Haycock, and L. Swanson, "Highly branched poly-(N-isopropylacrylamide)s with arginine-glycine- aspartic acid (RGD)- or COOH-chain ends that form sub-micron stimulus-responsive particles above the critical solution temperature," *Soft Matter*, vol. 3, no. 8, pp. 971–973, 2007.

[211] B. J. Chen, B. Wiley, Z. Li, D. Campbell, F. Saeki, H. Cang, L. Au, J. Lee, X. Li, and Y. Xia, "Gold Nanocages : Engineering Their Structure for Biomedical Applications," *Adv. Mater.*, vol. 17, pp. 2255–2261, 2005.

[212] S. K. Kailasa and H.-F. Wu, "One-pot synthesis of dopamine dithiocarbamate functionalized gold nanoparticles for quantitative analysis of small molecules and phosphopeptides in SALDI- and MALDI-MS," *Analyst*, vol. 137, pp. 1629–1638, 2012.

[213] V. N. Mehta, M. A. Kumar, and S. K. Kailasa, "Colorimetric Detection of Copper in Water Samples Using Dopamine Dithiocarbamate-Functionalized Au Nanoparticles," *Ind. Eng. Chem. Res.*, vol. 52, pp. 4414–4420, 2013.

[214] H. Chen, L. Shao, T. Ming, Z. Sun, C. Zhao, and B. Yang, "Understanding the Photothermal Conversion Effi ciency of Gold Nanocrystals," vol. 6, no. 20, pp. 2272–2280, 2010.

[215] T. Hoare, B. P. Timko, J. Santamaria, G. F. Goya, S. Irusta, S. Lau, C. F. Stefanescu, D. Lin, R. Langer, and D. S. Kohane, "Magnetically Triggered Nanocomposite Membranes : A Versatile Platform for Triggered Drug Release," *Nano Lett.*, vol. 11, pp. 1395–1400, 2011.

[216] M. Verderame, *Handbook of CNS Agents and Local Anesthetics*. 1986.

[217] A. El-Toni, T. Khan, A. Aldalbahi, T. Ahamad, M. Ahamed, A. Khan, and J. Alam, "Temperature-Responsive Polymer Microgel-Gold Nanorods Composite Particles: Physicochemical Characterization and Cytocompatibility," *Polymers (Basel).*, vol. 10, no. 1, p. 99, 2018.

[218] M. Ghorbani and H. Hamishehkar, "A novel multi stimuli-responsive PEGylated hybrid gold/nanogels for co-delivery of doxorubicin and 6-mercaptopurine," *Mater. Sci. Eng. C*, vol. 92, no. November 2017, pp. 599–611, 2018.

[219] Y. P. Jia, B. Y. Ma, X. W. Wei, and Z. Y. Qian, "The in vitro and in vivo toxicity of gold nanoparticles," *Chinese Chem. Lett.*, vol. 28, no. 4, pp. 691–702, 2017.

[220] E. Marsich, A. Travan, I. Donati, A. Di Luca, M. Benincasa, M. Crosera, and S. Paoletti, "Biological response of hydrogels embedding gold nanoparticles," *Colloids Surfaces B Biointerfaces*, vol. 83, pp. 331–339, 2011.

[221] Y. C. Chang, C. L. Liu, M. J. Chen, Y. W. Hsu, S. N. Chen, C. H. Lin, C. M. Chen, F. M. Yang, and M. C. Hu, "Local anesthetics induce apoptosis in human breast tumor cells," *Anesth. Analg.*, vol. 118, no. 1, pp. 116–124, 2014.

[222] Y. C. Chang, Y. C. Hsu, C. L. Liu, S. Y. Huang, M. C. Hu, and S. P. Cheng, "Local anesthetics induce apoptosis in human thyroid cancer cells through the mitogen-activated protein kinase pathway," *PLoS One*, vol. 9, no. 2, 2014.

[223] W. Xuan, H. Zhao, J. Hankin, L. Chen, S. Yao, and D. Ma, "Local anesthetic bupivacaine induced ovarian and prostate cancer apoptotic cell death and underlying mechanisms in vitro," *Sci. Rep.*, vol. 6, no. April, pp. 1–12, 2016.

[224] W. Xue, Z. Guo, J. Wu, C. Wang, B. Kirk, J. Xu, S. Li, and Z. Liu, " Biocompatibility and cellular uptake mechanisms of poly(N -isopropylacrylamide) in different cells ," *J. Bioact. Compat. Polym.*, vol. 32, no. 1, pp. 17–31, 2016.

[225] A. Choi, K. D. Seo, D. W. Kim, B. C. Kim, and D. S. Kim, "Recent advances in engineering microparticles and their nascent utilization in biomedical delivery and diagnostic applications," *Lab Chip*, vol. 17, no. 4, pp. 591–613, 2017.

[226] S. Jung, C. H. Choi, C. S. Lee, and H. Yi, "Integrated fabrication-conjugation methods

for polymeric and hybrid microparticles for programmable drug delivery and biosensing applications," *Biotechnol. J.*, vol. 11, no. 12, pp. 1561–1571, 2016.

[227] W. Jiang, M. Li, Z. Chen, and K. W. Leong, "Cell-laden microfluidic microgels for tissue regeneration," *Lab Chip*, vol. 16, no. 23, pp. 4482–4506, 2016.

[228] C. Berkland, M. King, A. Cox, K. Kim, and D. W. Pack, "Precise control of PLG microsphere size provides enhanced control of drug release rate," *J. Control. Release*, vol. 82, no. 1, pp. 137–147, 2002.

[229] K. M. C. Chan, R. H. Li, J. W. Chapman, E. M. Trac, J. B. Kobler, S. M. Zeitels, R. Langer, and S. S. Karajanagi, "Functionalizable hydrogel microparticles of tunable size and stiffness for soft-tissue filler applications," *Acta Biomater.*, vol. 10, no. 6, pp. 2563–2573, 2014.

[230] G. Cirillo, F. Iemma, U. G. Spizzirri, F. Puoci, M. Curcio, O. I. Parisi, and N. Picci, "Synthesis of stimuli-responsive microgels for in vitro release of diclofenac diethyl ammonium," *J. Biomater. Sci. Polym. Ed.*, vol. 22, no. 4–6, pp. 823–844, 2011.

[231] M. Bazzano, D. Latorre, R. Pisano, M. Sangermano, and M. Woerner, "Nano-structured polymeric microparticles produced via cationic aerosol photopolymerization," *J. Photochem. Photobiol. A Chem.*, vol. 346, pp. 364–371, 2017.

[232] G. T. Vladisavljević and R. A. Williams, "Recent developments in manufacturing emulsions and particulate products using membranes," *Adv. Colloid Interface Sci.*, vol. 113, no. 1, pp. 1–20, 2005.

[233] C. Charcosset; and H. Fessi, "MEMBRANE EMULSIFICATION AND MICROCHANNEL EMULSIFICATION PROCESSES," *Rev. Chem. Eng.*, vol. 21, pp. 1–32, 2005.

[234] B. G. De Geest, J. P. Urbanski, T. Thorsen, J. Demeester, and S. C. De Smedt, "Synthesis of monodisperse biodegradable microgels in microfluidic devices," *Langmuir*, vol. 21, no. 23, pp. 10275–10279, 2005.

[235] C. H. Choi, D. A. Weitz, and C. S. Lee, "One step formation of controllable complex

emulsions: From functional particles to simultaneous encapsulation of hydrophilic and hydrophobic agents into desired position," *Adv. Mater.*, vol. 25, no. 18, pp. 2536–2541, 2013.

[236] S. Ma, J. Thiele, X. Liu, Y. Bai, C. Abell, and W. T. S. Huck, "Fabrication of microgel particles with complex shape via selective polymerization of aqueous two-phase systems," *Small*, vol. 8, no. 15, pp. 2356–2360, 2012.

[237] Z. Nosrati, N. Li, F. Michaud, S. Ranamukhaarachchi, S. Karagiozov, G. Soulez, S. Martel, K. Saatchi, and U. O. Häfeli, "Development of a Coflowing Device for the Size-Controlled Preparation of Magnetic-Polymeric Microspheres as Embolization Agents in Magnetic Resonance Navigation Technology," *ACS Biomater. Sci. Eng.*, vol. 4, no. 3, pp. 1092–1102, 2018.

[238] J. H. Xu, H. Zhao, W. J. Lan, and G. S. Luo, "A novel microfluidic approach for monodispersed chitosan microspheres with controllable structures," *Adv. Healthc. Mater.*, vol. 1, no. 1, pp. 106–111, 2012.

[239] V. Sebastian and M. Arruebo, *Microfluidic production of inorganic nanomaterials for biomedical applications*. Elsevier Inc., 2018.

[240] H. Dong, G. Tang, T. Ma, and X. Cao, "One-step fabrication of inorganic/organic hybrid microspheres with tunable surface texture for controlled drug release application," *J. Mater. Sci. Mater. Med.*, vol. 27, no. 1, p. 7, Jan. 2016.

[241] K. D. Seo, D. S. Kim, and S. Sánchez, "Fabrication and applications of complex-shaped microparticles via microfluidics," *Lab Chip*, vol. 15, no. 18, pp. 3622–3626, 2015.

[242] C.-H. Choi, J.-H. Jung, D.-W. Kim, Y.-M. Chung, and C.-S. Lee, "Novel one-pot route to monodisperse thermosensitive hollow microcapsules in a microfluidic system.," *Lab Chip*, vol. 8, no. 9, pp. 1544–1551, 2008.

[243] T. Kanai, K. Ohtani, M. Fukuyama, T. Katakura, and M. Hayakawa, "Preparation of monodisperse PNIPAM gel particles in a microfluidic device fabricated by stereolithography," *Polym. J.*, vol. 43, no. 12, pp. 987–990, 2011.

[244] W. Xi, F. Kong, J. C. Yeo, L. Yu, S. Sonam, M. Dao, X. Gong, and C. T. Lim, "Soft tubular microfluidics for 2D and 3D applications," *Proc. Natl. Acad. Sci.*, vol. 114, no. 40, pp. 10590–10595, 2017.

[245] K. Ren, W. Dai, J. Zhou, J. Su, and H. Wu, "Whole-Teflon microfluidic chips," *Proc. Natl. Acad. Sci.*, vol. 108, no. 20, pp. 8162–8166, 2011.

[246] P. N. Nge, C. I. Rogers, and A. T. Woolley, "Advances in Microfluidic Materials, Functions, Integration and Applications," *Chem. Rev.*, vol. 113, no. 4, pp. 2550–2583, 2013.

[247] Y. Hu, S. Wang, A. Abbaspourrad, and A. M. Ardekani, "Fabrication of Shape Controllable Janus Alginate/pNIPAAm Microgels via Microfluidics Technique and Off-Chip Ionic Cross-Linking," *Langmuir*, vol. 31, no. 6, pp. 1885–1891, Feb. 2015.

[248] D. Velasco, E. Tumarkin, and E. Kumacheva, "Microfluidic encapsulation of cells in polymer microgels," *Small*, vol. 8, no. 11, pp. 1633–1642, 2012.

[249] S. Seiffert and D. A. Weitz, "Controlled fabrication of polymer microgels by polymer-analogous gelation in droplet microfluidics," *Soft Matter*, vol. 6, no. 14, p. 3184, 2010.

[250] W. Li, L. Zhang, X. Ge, B. Xu, W. Zhang, L. Qu, C. H. Choi, J. Xu, A. Zhang, H. Lee, and D. A. Weitz, "Microfluidic fabrication of microparticles for biomedical applications," *Chem. Soc. Rev.*, vol. 47, no. 15, pp. 5646–5683, 2018.

[251] C. Dietlin, S. Schweizer, P. Xiao, J. Zhang, F. Morlet-Savary, B. Graff, J. P. Fouassier, and J. Lalevée, "Photopolymerization upon LEDs: New photoinitiating systems and strategies," *Polym. Chem.*, vol. 6, no. 21, pp. 3895–3912, 2015.

[252] D. Sivakumaran, E. Mueller, and T. Hoare, "Microfluidic production of degradable thermoresponsive poly(: N -isopropylacrylamide)-based microgels," *Soft Matter*, vol. 13, no. 47, pp. 9060–9070, 2017.

[253] Y. S. Kim, H. M. Lee, J. H. Kim, J. Joo, and I. W. Cheong, "Hydrogel adsorbents of poly(N-isopropylacrylamide-co-methacryloyloxymethyl-12-crown-4) for Li+recovery prepared by droplet microfluidics," *RSC Adv.*, vol. 5, no. 14, pp. 10656–10661, 2015.

[254] C. J. Cheng, L. Y. Chu, P. W. Ren, J. Zhang, and L. Hu, “Preparation of monodisperse thermo-sensitive poly(N-isopropylacrylamide) hollow microcapsules,” *J. Colloid Interface Sci.*, vol. 313, no. 2, pp. 383–388, 2007.

[255] X. H. Ge, J. P. Huang, J. H. Xu, and G. S. Luo, “Controlled stimulation-burst targeted release by smart decentered core-shell microcapsules in gravity and magnetic field,” *Lab Chip*, vol. 14, no. 23, pp. 4451–4454, 2014.

[256] C. L. Mou, X. J. Ju, L. Zhang, R. Xie, W. Wang, N. N. Deng, J. Wei, Q. Chen, and L. Y. Chu, “Monodisperse and fast-responsive poly(N -isopropylacrylamide) microgels with open-celled porous structure,” *Langmuir*, vol. 30, no. 5, pp. 1455–1464, 2014.

[257] S. Park, D. Kim, S. Y. Ko, J. O. Park, S. Akella, B. Xu, Y. Zhang, and S. Fraden, “Controlling uniformity of photopolymerized microscopic hydrogels,” *Lab Chip*, vol. 14, no. 9, pp. 1551–1563, 2014.

[258] N. A. Filatov, D. V. Nozdriukhin, and A. S. Bukatin, “The kinetic study of solidification PEGDA microparticles in flow-focusing microfluidic chip,” *J. Phys. Conf. Ser.*, vol. 917, no. 4, pp. 1–5, 2017.

[259] J. Chen, K. Huang, Q. Chen, C. Deng, J. Zhang, and Z. Zhong, “Tailor-Making Fluorescent Hyaluronic Acid Microgels via Combining Microfluidics and Photoclick Chemistry for Sustained and Localized Delivery of Herceptin in Tumors,” *ACS Appl. Mater. Interfaces*, vol. 10, no. 4, pp. 3929–3937, 2018.

[260] W. C. Jeong, S. H. Kim, and S. M. Yang, “Photothermal control of membrane permeability of microcapsules for on-demand release,” *ACS Appl. Mater. Interfaces*, vol. 6, no. 2, pp. 826–832, 2014.

[261] B. Homayun, C. Sun, A. Kumar, C. Montemagno, and H. J. Choi, “Facile fabrication of microparticles with pH-responsive macropores for small intestine targeted drug formulation,” *Eur. J. Pharm. Biopharm.*, vol. 128, no. March, pp. 316–326, 2018.

[262] S. Huang, B. Lin, and J. Qin, “Microfluidic synthesis of tunable poly-(N-isopropylacrylamide) microparticles via PEG adjustment,” *Electrophoresis*, vol. 32, no. 23, pp. 3364–3370, 2011.

[263] K. Zhang, W. Wu, K. Guo, J. Chen, and P. Zhang, “Synthesis of temperature-responsive poly(N-isopropyl acrylamide)/ poly(methyl methacrvlate)/silica hybrid capsules from inverse pickering emulsion polymerization and their application in controlled drug release,” *Langmuir*, vol. 26, no. 11, pp. 7971–7980, 2010.

[264] B. M. Budhlall, M. Marquez, and O. D. Velev, “Microwave, photo- And thermally responsive PNIPAm-gold nanoparticle microgels,” *Langmuir*, vol. 24, no. 20, pp. 11959–11966, 2008.

[265] T. Heida, J. W. Neubauer, M. Seuss, N. Hauck, J. Thiele, and A. Fery, “Mechanically Defined Microgels by Droplet Microfluidics,” *Macromol. Chem. Phys.*, vol. 218, no. 2, pp. 1–19, 2017.

[266] S. Ekici, P. Ilgin, S. Yilmaz, N. Aktas, and N. Sahiner, “Temperature and magnetic field responsive hyaluronic acid particles with tunable physical and chemical properties,” *Appl. Surf. Sci.*, vol. 257, no. 7, pp. 2669–2676, 2011.

[267] S. Seiffert, J. Thiele, A. R. Abate, and D. A. Weitz, “Smart Microgel Capsules from Macromolecular Precursors,” vol. 01238, no. 14, pp. 1–9, 2010.

[268] S. Akbari, T. Pirbodaghi, R. D. Kamm, and P. T. Hammond, “A versatile microfluidic device for high throughput production of microparticles and cell microencapsulation,” *Lab Chip*, vol. 17, no. 12, pp. 2067–2075, 2017.

[269] D. Steinhilber, T. Rossow, S. Wedepohl, F. Paulus, S. Seiffert, and R. Haag, “A microgel construction kit for bioorthogonal encapsulation and pH-controlled release of living cells,” *Angew. Chemie - Int. Ed.*, vol. 52, no. 51, pp. 13538–13543, 2013.

[270] G. Celetti, C. Di Natale, F. Causa, E. Battista, and P. A. Netti, “Functionalized poly(ethylene glycol) diacrylate microgels by microfluidics: In situ peptide encapsulation for in serum selective protein detection,” *Colloids Surfaces B Biointerfaces*, vol. 145, pp. 21–29, 2016.

[271] W. Wang, L. Liu, X. J. Ju, D. Zerrouki, R. Xie, L. Yang, and L. Y. Chu, “A novel thermo-induced self-bursting microcapsule with magnetictargeting property,” *ChemPhysChem*, vol. 10, no. 14, pp. 2405–2409, 2009.

[272] J. Wang, X. Zhu, L. Wei, Y. Ye, Y. Liu, J. Li, T. Mei, X. Wang, and L. Wang, "Controlled Shape Transformation and Loading Release of Smart Hemispherical Hybrid Microgels Triggered by 'Inner Engines,'" *ChemistrySelect*, vol. 3, no. 15, pp. 4067–4074, 2018.

[273] B. Kim, H. Soo Lee, J. Kim, and S. H. Kim, "Microfluidic fabrication of photo-responsive hydrogel capsules," *Chem. Commun.*, vol. 49, no. 18, pp. 1865–1867, 2013.

[274] C.-H. Choi, J.-H. Jung, D.-W. Kim, Y.-M. Chung, and C.-S. Lee, "Novel one-pot route to monodisperse thermosensitive hollow microcapsules in a microfluidic system," *Lab Chip*, vol. 8, no. 9, p. 1544, 2008.

[275] H. Gu, M. H. G. Duits, and F. Mugele, "Droplets formation and merging in two-phase flow microfluidics," *Int. J. Mol. Sci.*, vol. 12, no. 4, pp. 2572–2597, 2011.

[276] N.-T. Nguyen, S. T. Wereley, and S. A. M. Shaegh, *Fundamentals and Applications of Microfluidics*, Third Edit. 2019.

[277] I. U. Khan, L. Stolch, C. A. Serra, N. Anton, R. Akasov, and T. F. Vandamme, "Microfluidic conceived pH sensitive core-shell particles for dual drug delivery," *Int. J. Pharm.*, vol. 478, no. 1, pp. 78–87, 2015.

[278] H. Feil, Y. H. Bae, J. Feijen, and S. W. Kim, "Effect of Comonomer Hydrophilicity and Ionization on the Lower Critical Solution Temperature of N-Isopropylacrylamide Copolymers," *Macromolecules*, vol. 26, no. 10, pp. 2496–2500, 1993.

[279] Y. J. Yang, B. Tang, L. Zhang, C. Wang, H. T. Ma, D. W. Pang, and Z. L. Zhang, "On-demand one-step synthesis of small-sized fluorescent-magnetic bifunctional microparticles on a droplet-splitting chip," *J. Mater. Chem. B*, vol. 6, no. 6, pp. 961–965, 2018.

[280] "ISO 10993-5:2009 - Biological evaluation of medical devices – Part 5: Tests for in vitro cytotoxicity. http://www.iso.org/ iso/catalogue_detail.htm?csnumber=36406." .

[281] R. Korsmeyer, "Critical questions in development of targeted nanoparticle therapeutics," *Regen. Biomater.*, vol. 3, no. 2, pp. 143–147, 2016.

[282] A. Gaudin, S. Lepetre-Mouelhi, J. Mougin, M. Parrod, G. Pieters, S. Garcia-Argote, O. Loreau, J. Goncalves, H. Chacun, Y. Courbebaisse, P. Clayette, D. Desmaële, B. Rousseau, K. Andrieux, and P. Couvreur, "Pharmacokinetics, biodistribution and metabolism of squalenoyl adenosine nanoparticles in mice using dual radio-labeling and radio-HPLC analysis," *J. Control. Release*, vol. 212, pp. 50–58, 2015.

[283] E. R. Gardner, *Handbook of Anticancer Pharmacokinetics and Pharmacodynamics*, 2nd ed. Springer US, 2014.

[284] A. Lăpădat, S. Sovaila, I. Gheonea, D. Gheonea, L. Florescu, B. Ungureanu, and I. Jianu, "Non-invasive imaging techniques in assessing non-alcoholic fatty liver disease: a current status of available methods," *J. Med. Life*, vol. 10, no. 1, pp. 19–26, 2017.

[285] H. Chen and S. H. Thorne, "Practical methods for molecular in vivo optical imaging," *Curr. Protoc. Cytom.*, vol. 59, no. SUPPL.59, pp. 1–15, 2012.

[286] A. R. Patel, E. Lim, K. P. Francis, and M. Singh, "Opening Up the Optical Imaging Window Using Nano-Luciferin," *Pharm. Res.*, vol. 31, pp. 3073–3084, 2014.

[287] J. K. Willmann, N. van Bruggen, L. M. Dinkelborg, and S. S. Gambhir, "Molecular imaging in drug development," *Nat. Rev. Drug Discov.*, vol. 7, no. 7, pp. 591–607, 2008.

[288] C. E. Badr and B. A. Tannous, "BIOLUMINESCENCE IMAGING: PROGRESS AND APPLICATIONS," *Trends Biotechnol.*, vol. 29, no. 12, pp. 624–633, 2011.

[289] A. C. Freise and A. M. Wu, "In vivo Imaging with Antibodies and Engineered Fragments," *Mol. Immunol.*, vol. 67, pp. 142–152, 2015.

[290] B. Lim, Y. Yao, A. L. i. Huang, M. L. Yap, U. Flierl, J. Palasubramaniam, M. T. K. Zaldivia, X. Wang, and K. Peter, "A unique recombinant fluoroprobe targeting activated platelets allows in vivo detection of arterial thrombosis and pulmonary embolism using a novel three-dimensional fluorescence emission computed tomography (FLECT) technology," *Theranostics*, vol. 7, no. 5, pp. 1047–1061, 2017.

[291] M. Ptaszek, "Rational Design of Fluorophores for In vivo Applications," *Prog. Mol.*

Biol. Transl. Sci., vol. 113, pp. 59–108, 2013.

[292] M. Sun, K. Müllen, and M. Yin, "Water-soluble perylenediimides: Design concepts and biological applications," *Chem. Soc. Rev.*, vol. 45, no. 6, pp. 1513–1528, 2016.

[293] J. O. Escobedo, O. Rusin, S. Lim, and R. M. Strongin, "NIR Dyes for Bioimaging Applications Jorge," *Curr. Opin. Chem. Biol.*, vol. 14, no. 1, p. 64, 2010.

[294] Summer L. Gibbs, "Near infrared fluorescence for image-guided surgery," *Quant Imaging Med Surg*, vol. 2, no. 3, pp. 177–187, 2012.

[295] Y. Yang, C. Yue, Y. Han, W. Zhang, A. He, C. Zhang, T. Yin, Q. Zhang, J. Zhang, Y. Yang, J. Ni, J. Sun, and D. Cui, "Tumor-Responsive Small Molecule Self-Assembled Nanosystem for Simultaneous Fluorescence Imaging and Chemotherapy of Lung Cancer," *Adv. Funct. Mater.*, vol. 26, no. 47, pp. 8735–8745, 2016.

[296] Q. T. Nguyen and R. Y. Tsien, "Fluorescence-guided surgery with live molecular navigation — a new cutting edge," *Naure Rev. cancer*, vol. 13, no. 9, pp. 653–662, 2013.

[297] M. Chen and M. Yin, "Design and development of fluorescent nanostructures for bioimaging," *Prog. Polym. Sci.*, vol. 39, no. 2, pp. 365–395, 2014.

[298] J. Pauli, T. Vag, R. Haag, M. Spieles, M. Wenzel, W. A. Kaiser, U. Resch-Genger, and I. Hilger, "An in vitro characterization study of new near infrared dyes for molecular imaging," *Eur. J. Med. Chem.*, vol. 44, no. 9, pp. 3496–3503, 2009.

[299] A. Fernandez-Fernandez, R. Manchanda, T. Lei, D. A. Carvajal, Y. Tang, S. Z. R. Kazmi, and A. J. McGoron, "Comparative study of the optical and heat generation properties of IR820 and indocyanine green," *Mol. Imaging*, vol. 11, no. 2, pp. 99–113, 2012.

[300] A. Fernandez-Fernandez, R. Manchanda, D. A. Carvajal, T. Lei, S. Srinivasan, and A. J. McGoron, "Covalent IR820-PEG-diamine nanoconjugates for theranostic applications in cancer," *Int. J. Nanomedicine*, vol. 9, no. 1, pp. 4631–4648, 2014.

[301] W. Hou, F. Xia, C. S. Alves, X. Qian, Y. Yang, and D. Cui, "MMP2-Targeting and

Redox-Responsive PEGylated Chlorin e6 Nanoparticles for Cancer Near-Infrared Imaging and Photodynamic Therapy," *ACS Appl. Mater. Interfaces*, vol. 8, no. 2, pp. 1447–1457, 2016.

[302] C. Yue, C. Zhang, G. Alfranca, Y. Yang, X. Jiang, Y. Yang, F. Pan, J. M. de la Fuente, and D. Cui, "Near-infrared light triggered ros-activated theranostic platform based on ce6-cpt-ucnps for simultaneous fluorescence imaging and chemo-photodynamic combined therapy," *Theranostics*, vol. 6, no. 4, pp. 456–469, 2016.

[303] S. Zhang, W. Guo, J. Wei, C. Li, X.-J. Liang, and M. Yin, "Terrylenediimide-Based Intrinsic Theranostic Nanomedicines with High Photothermal Conversion Efficiency for Photoacoustic Imaging-Guided Cancer Therapy," *ACS Nano*, vol. 11, no. 4, pp. 3797–3805, 2017.

[304] E. P. Porcu, A. Salis, E. Gavini, G. Rassu, M. Maestri, and P. Giunchedi, "Indocyanine green delivery systems for tumour detection and treatments," *Biotechnol. Adv.*, vol. 34, no. 5, pp. 768–789, 2016.

[305] V. Saxena, M. Sadoqi, S. Kumar, and J. Shao, *Novel multifunctional near-infrared fluorescent nanoparticles: integrating nanotechnology and biophotonics*. A. N. Cartwright, International Society for Optics and Photonics, 2004.

[306] V. Saxena, M. Sadoqi, and J. Shao, "Polymeric nanoparticulate delivery system for Indocyanine green: Biodistribution in healthy mice," *Int. J. Pharm.*, vol. 308, no. 1–2, pp. 200–204, 2006.

[307] R. Manchanda, A. Fernandez-Fernandez, A. Nagesetti, and A. J. McGoron, "Preparation and characterization of a polymeric (PLGA) nanoparticulate drug delivery system with simultaneous incorporation of chemotherapeutic and thermo-optical agents," *Colloids Surfaces B Biointerfaces*, vol. 75, no. 1, pp. 260–267, 2010.

[308] S. Srinivasan, R. Manchanda, T. Lei, A. Nagesetti, A. Fernandez-Fernandez, and A. J. McGoron, "Targeted nanoparticles for simultaneous delivery of chemotherapeutic and hyperthermia agents – An in vitro study," *J. Photochem. Photobiol. B Biol.*, vol. 136, pp. 81–90, 2014.

[309] B. P. Timko, T. Dvir, and D. S. Kohane, “Remotely triggerable drug delivery systems,” *Adv. Mater.*, vol. 22, no. 44, pp. 4925–4943, 2010.

[310] H. J. Sung, C. Meredith, C. Johnson, and Z. S. Galis, “The effect of scaffold degradation rate on three-dimensional cell growth and angiogenesis,” *Biomaterials*, vol. 25, no. 26, pp. 5735–5742, 2004.

[311] Z. Ge and S. Liu, “Functional block copolymer assemblies responsive to tumor and intracellular microenvironments for site-specific drug delivery and enhanced imaging performance,” *Chem. Soc. Rev.*, vol. 42, no. 17, pp. 7289–7325, 2013.

[312] A. K. Mohammad and J. J. Reineke, “Quantitative detection of PLGA nanoparticle degradation in tissues following intravenous administration,” *Mol. Pharm.*, vol. 10, no. 6, pp. 2183–2189, 2013.

[313] E. Lu, W. Zhou, X. Peng, F. Song, Y. Wang, Y. Gao, and J. Fan, “Heptamethine Cyanine Dyes with a Large Stokes Shift and Strong Fluorescence: A Paradigm for Excited-State Intramolecular Charge Transfer,” *J. Am. Chem. Soc.*, vol. 127, no. 12, pp. 4170–4171, 2005.

[314] X. Peng, F. Song, E. Lu, Y. Wang, W. Zhou, J. Fan, and Y. Gao, “Heptamethine cyanine dyes with a large {S}tokes shift and strong fluoresence: a paradigm for excited-state intramolecular charge transfer,” *J. Am. Chem. Soc.*, vol. 127, no. Figure 4, pp. 4170–4171, 2005.

[315] J. Gregory, M. S. Riasi, J. Cannell, H. Arora, L. Yeghiazarian, and V. Nistor, “Remote-controlled peristaltic locomotion in free-floating PNIPAM hydrogels,” *J. Appl. Polym. Sci.*, vol. 131, no. 20, pp. 2–7, 2014.

[316] M. Guvendiren and J. A. Burdick, “Engineering synthetic hydrogel microenvironments to instruct stem cells,” *Curr. Opin. Biotechnol.*, vol. 24, no. 5, pp. 841–846, 2013.

[317] S. S. HO, K. C. MURPHY, B. Y. K. BINDER, C. B. VISSERS, and J. K. LEACH, “Increased Survival and Function of Mesenchymal Stem Cell Spheroids Entrapped in Instructive Alginate Hydrogels,” *Stemcells Transl. Med.*, vol. 5, pp. 773–781, 2016.

[318] P. Chiarugi and E. Giannoni, “Anoikis: A necessary death program for anchorage-dependent cells,” *Biochem. Pharmacol.*, vol. 76, no. 11, pp. 1352–1364, 2008.

[319] L. Yang, F. Cheng, T. Liu, J. R. Lu, K. Song, L. Jiang, S. Wu, and W. Guo, “Comparison of mesenchymal stem cells released from poly(N- isopropylacrylamide) copolymer film and by trypsinization,” *Biomed. Mater.*, vol. 7, no. 3, 2012.

[320] S. I. Prajapati, C. O. Martinez, A. N. Bahadur, I. Q. Wu, W. Zheng, J. D. Lechleiter, L. M. McManus, G. B. Chisholm, J. E. Michalek, P. K. Shireman, and C. Keller, “Near-Infrared Imaging of Injured Tissue in Living Subjects Using IR-820,” *Mol. Imaging*, vol. 8, no. 1, pp. 45–54, 2009.

[321] A. Hospital, J. R. Goñi, M. Orozco, and J. L. Gelpí, “Molecular Dynamics Simulations: advances and applications,” *Adv. Appl. Bioinforma. Chem.*, vol. 8, pp. 37–47, 2015.

[322] D. C. Rapaport, “Molecular dynamics study of a polymer chain in solution,” *J. Chem. Phys.*, vol. 71, no. 8, pp. 3299–3303, 1979.

[323] B. Dünweg and K. Kremer, “Molecular dynamics simulation of a polymer chain in solution,” *J. Chem. Phys.*, vol. 99, no. 9, pp. 6983–6997, 1993.

[324] P. M. Anderson and M. R. Wilson, “Molecular dynamics simulations of amphiphilic graft copolymer molecules at a water/air interface,” *J. Chem. Phys.*, vol. 121, no. 17, pp. 8503–8510, 2004.

[325] J. Lin, J. Zhu, T. Chen, S. Lin, C. Cai, L. Zhang, Y. Zhuang, and X. S. Wang, “Drug releasing behavior of hybrid micelles containing polypeptide triblock copolymer,” *Biomaterials*, vol. 30, no. 1, pp. 108–117, 2009.

[326] W. Ding, S. Lin, J. Lin, and L. Zhang, “Effect of chain conformational change on micelle structures: Experimental studies and molecular dynamics simulations,” *J. Phys. Chem. B*, vol. 112, no. 3, pp. 776–783, 2008.

[327] S. A. Oelmeier, F. Dismer, and J. Hubbuch, “Molecular dynamics simulations on aqueous two-phase systems - Single PEG-molecules in solution,” *BMC Biophys.*, vol. 5, no. 1, 2012.

[328] M. L. O'Mara, P. P. T. Surawski, A. E. Mark, M. Trau, and Y. Xue, "Effect of Poly(ethylene glycol) (PEG) Spacers on the Conformational Properties of Small Peptides: A Molecular Dynamics Study," *Langmuir*, vol. 27, no. 1, pp. 296–303, 2010.

[329] C. Sanchez, B. Julián, P. Belleville, and M. Popall, "Applications of hybrid organic-inorganic nanocomposites," *J. Mater. Chem.*, vol. 15, no. 35–36, pp. 3559–3592, 2005.

[330] H. Vihola, A. Laukkanen, L. Valtola, H. Tenhu, and J. Hirvonen, "Cytotoxicity of thermosensitive polymers poly(N-isopropylacrylamide), poly(N-vinylcaprolactam) and amphiphilically modified poly(N-vinylcaprolactam)," *Biomaterials*, vol. 26, no. 16, pp. 3055–3064, 2005.

[331] S. Lanzalaco and E. Armelin, "Poly(N-isopropylacrylamide) and Copolymers: A Review on Recent Progresses in Biomedical Applications," *Gels*, vol. 3, no. 4, p. 36, 2017.

[332] G. Fundueanu, M. Constantin, and P. Ascenzi, "Poly(N-isopropylacrylamide-co-acrylamide) cross-linked thermoresponsive microspheres obtained from preformed polymers: Influence of the physico-chemical characteristics of drugs on their release profiles," *Acta Biomater.*, vol. 5, no. 1, pp. 363–373, 2009.

[333] M. Keerl, J. S. Pedersen, and W. Richtering, "Temperature sensitive copolymer microgels with nanophase separated structure," *J. Am. Chem. Soc.*, vol. 131, no. 8, pp. 3093–3097, 2009.

[334] S. Fujishige, K. Kubota, and I. Ando, "Phase transition of aqueous solutions of poly(N-isopropylacrylamide) and poly(N-isopropylmethacrylamide)," *J. Phys. Chem.*, vol. 93, no. 8, pp. 3311–3313, 1989.

[335] E. Djokpé and W. Vogt, "N-isopropylacrylamide and N-isopropylmethacrylamide: Cloud points of mixtures and copolymers," *Macromol. Chem. Phys.*, vol. 202, no. 5, pp. 750–757, 2001.

[336] M. L. Galbraith and J. D. Madura, "Identifying trends in hydration behavior for modifications to the hydrophobicity of poly(n-isopropylacrylamide)," *J. Mol. Graph.*

Model., vol. 78, pp. 168–175, 2017.

[337] K. Kubota, K. Hamano, N. Kuwahara, S. Fujishige, and I. Ando, "Characterization of Poly(N-isopropylmethacrylamide) in water," *Polym. J.*, vol. 22, no. 12, pp. 1051–1057, 1990.

[338] J. PANG, H. YANG, J. MA, and R. CHENG, "Understanding Different Lcst Levels of Poly(N-Alkylacrylamide)S By Molecular Dynamics Simulations and Quantum Mechanics Calculations," *J. Theor. Comput. Chem.*, vol. 10, no. 03, pp. 359–370, 2011.

[339] G. Heun, N. Lambov, and R. Gröning, "Experimental and molecular modeling studies on interactions between drugs and Eudragit® RL/RS resins in aqueous environment," *Pharm. Acta Helv.*, vol. 73, no. 1, pp. 57–62, 1998.

[340] M. Mahdavi, F. Rahmani, and S. Nouranian, "Molecular simulation of pH-dependent diffusion, loading, and release of doxorubicin in graphene and graphene oxide drug delivery systems," *J. Mater. Chem. B*, vol. 4, no. 46, pp. 7441–7451, 2016.

[341] S. Patel, A. Lavasanifar, and P. Choi, "Application of Molecular Dynamics Simulation To Predict the Compatability between Water-Insoluble Drugs and Self-Associating Poly (ethylene oxide) - b -poly (ε -caprolactone)," pp. 3014–3023, 2008.

[342] S. K. Patel, A. Lavasanifar, and P. Choi, "Molecular dynamics study of the encapsulation capability of a PCL-PEO based block copolymer for hydrophobic drugs with different spatial distributions of hydrogen bond donors and acceptors," *Biomaterials*, vol. 31, no. 7, pp. 1780–1786, 2010.

[343] W. L. Jorgensen, J. Chandrasekhar, J. D. Madura, R. W. Impey, and M. L. . Klein, "Comparison of simple potential functions for simulating liquid water," *J. Chem. Phys.*, vol. 79, no. 2, pp. 926–935, Jul. 1983.

[344] J. C. Phillips, R. Braun, W. Wang, J. Gumbart, E. Tajkhorshid, E. Villa, and K. , Christophe Chipot, Robert D. Skeel, Laxmikant Kalé, and Schulten, "Scalable Molecular Dynamics with NAMD," *J. Comput. Chem.*, vol. 26, no. 16, pp. 1781–1802, 2005.

[345] T. Darden, D. York, and L. Pedersen, “Particle mesh Ewald: An N ·log(N) method for Ewald sums in large systems,” *J. Chem. Phys.*, vol. 98, no. 12, pp. 10089–10092, Jun. 1993.

[346] D. R. Roe and T. E. Cheatham, “PTRAJ and CPPTRAJ: Software for Processing and Analysis of Molecular Dynamics Trajectory Data,” *J. Chem. Theory Comput.*, vol. 9, no. 7, pp. 3084–3095, Jul. 2013.

[347] W. Humphrey, A. Dalke, and K. Schulten, “VMD: Visual molecular dynamics,” *J. Mol. Graph.*, vol. 14, no. 1, pp. 33–38, Feb. 1996.

[348] Y. Tamai, H. Tanaka, and K. Nakanishi, “Molecular dynamics study of polymer-water interaction in hydrogels. 2. Hydrogen-bond dynamics,” *Macromolecules*, vol. 29, no. 21, pp. 6761–6769, 1996.

[349] P. A. Netz and T. Dorfmüller, “Computer Simulation Studies on the Polymer-Induced Modification of Water Properties in Polyacrylamide Hydrogels,” *J. Phys. Chem. B*, vol. 102, no. 25, pp. 4875–4886, 1998.

[350] S. A. Deshmukh, S. K. R. S. Sankaranarayanan, K. Suthar, and D. C. Mancini, “Role of Solvation Dynamics and Local Ordering of Water in Inducing Conformational Transitions in Poly(N -isopropylacrylamide) Oligomers through the LCST,” *J. Phys. Chem. B*, vol. 116, no. 9, pp. 2651–2663, Mar. 2012.

[351] A. Luzar and D. Chandler, “Structure and hydrogen bond dynamics of water-dimethyl sulfoxide mixtures by computer simulations,” *J. Chem. Phys.*, vol. 98, no. 10, pp. 8160–8173, 1993.

[352] D. C. Rapaport, “Hydrogen bonds in water,” *Mol. Phys.*, vol. 50, no. 5, pp. 1151–1162, Dec. 1983.

[353] M. Keerl, V. Smirnovas, R. Winter, and W. Richtering, “Copolymer microgels from mono- And disubstituted acrylamides: Phase behavior and hydrogen bonds,” *Macromolecules*, vol. 41, no. 18, pp. 6830–6836, 2008.

[354] A. Gandhi, A. Paul, S. O. Sen, and K. K. Sen, “Studies on thermoresponsive polymers: Phase behaviour, drug delivery and biomedical applications,” *Asian J. Pharm. Sci.*,

vol. 10, no. 2, pp. 99–107, 2015.

[355] E. Chiessi and G. Paradossi, “Influence of Tacticity on Hydrophobicity of Poly(N - isopropylacrylamide): A Single Chain Molecular Dynamics Simulation Study,” *J. Phys. Chem. B*, vol. 120, no. 15, pp. 3765–3776, Apr. 2016.

[356] Y. Kang, H. Joo, and J. S. Kim, “Collapse − Swelling Transitions of a Thermoresponsive, Single Poly(N - isopropylacrylamide) Chain in Water,” *J. Phys. Chem. B*, vol. 120, pp. 13184–13192, 2016.

[357] J. C. Hurley, “Endotoxemia: Methods of detection and clinical correlates,” *Clin. Microbiol. Rev.*, vol. 8, no. 2, pp. 268–292, 1995.

[358] S. Smulders, J.-P. Kaiser, S. Zuin, K. L. Van Landuyt, L. Golanski, J. Vanoirbeek, P. Wick, and P. H. Hoet, “Contamination of nanoparticles by endotoxin: evaluation of different test methods,” *Part. Fibre Toxicol.*, vol. 9, no. 1, p. 41, 2012.

PUBLICATIONS

PUBLISHED SCIENTIFIC PAPERS

Published scientific papers

1.

Ortiz de Solorzano, I[¥]., Uson, L[¥]., Larrea, A[¥]., Miana, M., Sebastian, V., Arruebo, M.
([¥] These authors contributed equally to this work)

"Continuous synthesis of drug-loaded nanoparticles using microchannel emulsification and numerical modeling: effect of passive mixing"

Int. J. Nanomedicine, **2016**, 11: 3397-3416; DOI: 10.2147/IJN.S108812

2.

Ortiz de Solorzano, I., Prieto, M., Mendoza, G., Alejo, T., Irusta, S., Sebastian, V., Arruebo, M.

"Microfluidic synthesis and biological evaluation of photothermal biodegradable copper sulfide nanoparticles"

ACS Appl. Mater. Interfaces, **2016**, 8: p. 21545−21554; DOI: 10.1021/acsami.6b05727

3.

Mendoza, G.[¥], Ortiz de Solorzano, I.[¥], Pintre, I., Garcia-Salinas, S., Sebastian, V., Andreu, V., Gimeno, M., Arruebo, M. *([¥] Both authors contributed equally to this work)*

"Near infrared dye-labelled polymeric micro- and nanomaterials: *in vivo* imaging and evaluation of their local persistence"

Nanoscale, **2018**, 10: p. 2970−2982; DOI: 10.1039/c7nr07345c

4.

Ortiz de Solorzano, I.[*], Alejo, T., Abad, M., Bueno-Alejo, C., Mendoza, G., Andreu, V., Irusta, S., Sebastian, V., Arruebo, M. *([*]Corresponding autor)*

"Cleavable and thermo-responsive hybrid nanoparticles for on-demand drug delivery"

J. Colloid Interface Sci., **2019**, 533: p. 171-181; DOI: 10.1016/j.jcis.2018.08.069

Participation in Conferences

1.

Title: *"Numerical simulations of continuous mixing reactors for synthesis of biodegradable polymeric nanoparticles"*

Authors: Miana, M; Usón, L; Ortiz de Solorzano, I; Sebastián, V; Aruebo, M.

Contribution: *Oral presentation*

Event & Organization: *NanoMath 2014;* Instituto Universitario de Investigación en Matemáticas y Aplicaciones (IUMA)

Scope: *International*

Place & Date: Facultad de Ciencias de la Universidad de Zaragoza; October 1st-3rd, 2014

2.

Title: *"Síntesis continua de nanomateriales poliméricos biodegradables para aplicaciones biomédicas mediante tecnología basada en microfluídica"*

Authors: Ortiz de Solorzano, I; Larrea, A; Sebastián, V; Aruebo, M; Santamaría, J.

Contribution: *Poster*

Event & Organization: *6ª Jornada de Jóvenes Investigadores en Física y Química de Aragón;* Real Sociedad Española de Química y Física

Scope: *National*

Place & Date: Escuela de Ingeniería y Arquitectura de la Universidad de Zaragoza; November, 20th 2014.

3.

Title: *"Microfluidic-assisted synthesis of CuS nanoparticles used in photothermal therapy."*

Authors: Prieto, M; Ortiz de Solorzano, I.; Andreu, V; Mendoza, G; Sebastián, V; Aruebo, M; Santamaría, J.

Contribution: *Poster*

Event & Organization: *Fourth International Conference on Multifunctional, Hybrid and Nanomaterials;* Elsevier Editorial

Scope: International

Place & Date: Sitges, Spain; March, 9th- 13th 2015

4.

Title: *"Microfluidic-assisted synthesis of PLGA nanoparticles used as drug delivery vectors"*

Authors: Ortiz de Solorzano, I.; Larrea, A; Prieto, M; Sebastián, V; Aruebo, M; Santamaría, J.

Contribution: *Poster*

Event & Organization: *Fourth International Conference on Multifunctional, Hybrid and Nanomaterials;* Elsevier Editorial

Scope: International

Place & Date: Sitges, Spain; March, 9th- 13th 2015

5.

Title: *"Synthesis of nanomaterials with multiple applications in Biomedicine"*

Authors: Usón, L; Ortiz de Solorzano, I.; Santamaría, J.

Contribution: *Poster*

Event & Organization: *CIBER-BBN Annual Conference;* CIBER-BBN

Scope: National

Place & Date: Valencia, Spain; 30th November to 1st December 2015

6.

Title: *"Synthesis of nanomaterials with multiple applications in Biomedicine"*

Authors: Ortiz de Solorzano, I.; Usón, L; Santamaría, J.

Contribution: *Poster*

Event & Organization: *NanoBio&Med 2015;* Phantoms foundation, Institute of Bioengineering of Catalonia (IBEC), BOKU

Scope: International

Place & Date: Barcelona, Spain; November 18th -20th 2015.

7.

Title: *"High troughput synthesis of polymer biodegradable nanoparticles using microchannel emulsification of drugs and inorganic nanoparticles."*

Authors: Santamaría, J; Sebastian, V; Arruebo, M, Larrea, A; Ortiz de Solorzano, I.; Usón, L

Contribution: *Abstract*

Event & Organization: *11th International Symposium on Polymer Therapeutics;* Centro de investigación Principe Felipe

Scope: International

Place & Date: Valencia, Spain; May 23rd -25th 2016

8.

Title: *"Microfluidic synthesis and biological evaluation of photothermal biodegradable copper sulphide nanoparticles."*

Authors: Ortiz de Solorzano, I.; Prieto, M.; Mendoza, G.; Alejo, T.; Irusta, S.; Sebastian, V.; Arruebo, M.

Contribution: *Oral presentation*

Event & Organization: *International Conference on Nanomedicine and Nanobiotechnology (ICONAN 2016);* PremC Conferences, Events & Workshops

Scope: International

Place & Date: Paris, France; September 28th -30th 2016

9.

Title: *"In vivo imaging and local persistence of polymeric micro- and nanomaterials labelled with the near infrared dye IR820"*

Authors: Ortiz de Solorzano, I.; Mendoza, G.; Pintre, I.; García-Salinas, S.; Sebastian, V.; Andreu, V.; Gimeno, M.; Arruebo, M.

Contribution: *Poster*

Event & Organization: *International Conference on Nanomedicine and Nanobiotechnology (ICONAN 2017);* PremC Conferences, Events & Workshops

Scope: International

Place & Date: Barcelona, Spain; September 25th -27th 2017

10.

Title: *"Near infrared dye-labeled polymeric micro- and nanomaterials: in vivo imaging and evaluation of their local persistence"*

Authors: Arruebo, M; Mendoza, G; Ortiz de Solórzano, I; Pintre, I; García-Salinas, S; Sebastian, V; Andreu, V; Gimeno, M.

Contribution: *Invited communication*

Event & Organization: *XII Spanish-Portuguese Conference on Controlled Drug Delivery;* University of Coimbra

Scope: International

Place & Date: Coimbra, Portugal; January 14th -16th 2018

11.

Title: *"Advanced production of vectors forgrug delivery applications using continuous flow"*

Authors: Sebastian, V; Ortiz de Solórzano, I; García-Salinas, S; Albisa, A; Larrea, A; Uson, L; Piacentini, E; Giorno, L; Arruebo, M

Contribution: *Poster*

Event & Organization: *XII Spanish-Portuguese Conference on Controlled Drug Delivery;* University of Coimbra

Scope: International

Place & Date: Coimbra, Portugal; January 14th -16th 2018

12.

Title: *"Continuous microflow synthesis of Photothermal Nanoparticles: Au nanorods and Biodegradable Copper Sulfide hollow nanospheres"*

Authors: Sebastian, V; Ortiz de Solórzano, I; Uson, L., Prieto, M., Mendoza, G., Alejo, T., Irusta, S., Santamaria, J., Arruebo, M

Contribution: *Poster*

Event & Organization: *15th International conference on Micro reaction technology;* DECHEMA

Scope: International

Place & Date: Karlsruhe, Germany; October 21st -24th 2018

13.

Title: *"NIR Photo-triggered hybrid copper sulfide nanoparticles functionalized with thermos-responsive polymers for on-demand drug delivery"*

Authors: Ortiz de Solorzano, I.; Alejo, T.; Abad, M.; Bueno Alejo, C.; Mendoza, G.; Andreu, V.; Irusta, S.; Sebastian, V.; Arruebo, M.

Contribution: *Oral presentation*

Event & Organization: *NanoMed 2018;* SETCOR Conferences & Exhibitions

Scope: *International*

Place & Date: Venice, Italy; October 23rd – 25th 2018.

14.

Title: *"Microreactors, a versatile tool in process intensification to produce high quality nanomaterials in continuous flow"*

Authors: Sebastian, V.; Ortiz de Solorzano, I.; Uson, L.; Arruebo, M.

Contribution: *Oral presentation*

Event & Organization: *IPIC.* The Second international process intensification conference

Scope: *International*

Place & Date: Leuven, Belgium; May 27th – 29th 2019.